Analysis tools for precision studies of hadronic three-body decays and transition form factors

Dissertation

zur

Erlangung des Doktorgrades (Dr. rer. nat.)

der

Mathematisch-Naturwissenschaftlichen Fakultät

der

Rheinischen Friedrich-Wilhelms-Universität Bonn

vorgelegt von

Sebastian Philipp Schneider

aus

Engelskirchen

Bonn, Dezember 2012

Angefertigt mit Genehmigung der
Mathematisch-Naturwissenschaftlichen Fakultät der
Rheinischen Friedrich-Wilhelms-Universität Bonn

1. Gutachter: PD Dr. Bastian Kubis
2. Gutachter: Prof. Dr. Ulf-G. Meißner
Tag der Promotion: 14.02.2013
Erscheinungsjahr: 2013

Abstract

Due to the running coupling constant of Quantum Chromodynamics one of the pillars of the Standard Model, the strong interactions, is still insufficiently understood at low energies. In order to describe the interactions of hadrons that form in this physical regime, one has to devise methods that are non-perturbative in the strong coupling constant. In particular hadronic three-body decays and transition form factors present a great challenge due to the complex analytic structure ensued by strong final-state interactions. In this thesis we present two approaches to tackle these processes.

In the first part we use a modified version of non-relativistic effective field theory to analyze the decay $\eta \to 3\pi$. This perturbative low-energy expansion is ideally suited to study the effects of $\pi\pi$ rescattering and contributes greatly to the understanding of the slope parameter of the $\eta \to 3\pi^0$ Dalitz plot, a quantity that is strongly influenced by final-state interactions and has presented a long-standing puzzle for theoretical approaches.

In the second part we present dispersion relations as a non-perturbative means to study three-particle decays. Using the example of $\eta' \to \eta\pi\pi$ we give a detailed introduction to the framework and its numerical implementation. We confront our findings with recent experimental data from the BES-III and VES collaborations and discuss whether the extraction of $\pi\eta$ scattering parameters, one of the prime motives to study this decay channel, is feasible in such an approach.

A more clear-cut application will be given in our study of the decays $\omega/\phi \to 3\pi$ due to the relative simplicity of this decay channel: our results are solely dependent on the $\pi\pi$ P-wave scattering phase shift. We give predictions for the Dalitz plot distributions and compare our findings to very precise data on $\phi \to 3\pi$ by the KLOE and CMD-2 collaborations. We also predict Dalitz plot parameters that may be determined in future high-precision measurements of $\omega \to 3\pi$ and present a calculation of the $\pi\pi$ P-wave inelasticity from $\omega\pi$ intermediate states.

Finally, we extend the framework and discuss the $\omega/\phi \to \pi^0\gamma^*$ transition form factor. For that we use the previously determined $\omega/\phi \to 3\pi$ partial-wave amplitude and the well-known pion vector form factor as input. Our findings are compared to recent measurements of $\omega \to \pi^0\mu^+\mu^-$ by the NA60 collaboration. We also suggest that a precise measurement of the Okubo–Zweig–Iizuka-forbidden $\phi \to \pi^0\ell^+\ell^-$ decay may help to understand the strong deviations found between recent theoretical determinations and transition form factor data.

Parts of this thesis have been published in the following articles:

- S. P. Schneider, B. Kubis and C. Ditsche, *Rescattering effects in $\eta \to 3\pi$ decays*, JHEP **1102** (2011) 028
- F. Niecknig, B. Kubis and S. P. Schneider, *Dispersive analysis of $\omega \to 3\pi$ and $\phi \to 3\pi$ decays*, Eur. Phys. J. C **72** (2012) 2014
- S. P. Schneider, B. Kubis and F. Niecknig, *The $\omega \to \pi^0\gamma^*$ and $\phi \to \pi^0\gamma^*$ transition form factors in dispersion theory*, Phys. Rev. D **86** (2012) 054013
- S. P. Schneider, B. Kubis and F. Niecknig, *Dispersive analysis of $\omega/\phi \to 3\pi$ decays and the $\omega/\phi \to \pi^0\gamma^*$ transition form factors*, arXiv:1212.0654 [hep-ph].

Contents

Chapter 1

Introduction

Ever since its inception in the late 1960s and early 1970s the Standard Model of elementary particle physics [1–4] has formidably withstood detailed experimental scrutiny. Only recently a non-vector boson with a measured mass between 125 and 126 GeV has been discovered by the ATLAS [5] and CMS [6] collaborations at CERN. This particle that appears to have all the makings of a Standard-Model Higgs boson [7–9] eluded experimental physicists for almost four decades and endeavors yet to be another pillar of this very successful theory that unites electromagnetic, weak and strong interactions. As far as the understanding of particle physics in general and the strong interactions based on the theory of Quantum Chromodynamics (QCD) in particular has progressed at the high-energy frontier, it is rather remarkable that the low-energy end of the QCD spectrum is still insufficiently understood. This is a consequence of the running of the QCD coupling constant.

The interactions between quarks and gluons are subsumed in the QCD Lagrangian, which was first formulated in terms of a Yang-Mills theory by Fritzsch, Gell-Mann, and Leutwyler [10]. Shortly after it was found that the coupling constant that determines the strength of these interactions is actually not constant, but dependent on the energy scale, obeying the renormalization group equation (see e.g. [11] and references therein),[#1]

$$Q^2 \frac{\partial \alpha_s(Q^2)}{\partial Q^2} = \beta\big(\alpha_s\big) \ , \qquad \beta\big(\alpha_s\big) = -\frac{\alpha_s^2}{12\pi}(33 - 2n_f) + \mathcal{O}(\alpha_s^3) \ , \tag{1.1}$$

where n_f is the number of active quark flavors at energy scale Q, see Fig. 1.1 for an illustration. In particular it was discovered that the coupling constant decreases as the energy increases giving rise to a phenomenon called asymptotic freedom [13, 14], for which Gross, Politzer, and Wilczek were awarded the Nobel Prize in 2004. In this regime a perturbative expansion in terms of the coupling constant thus allows to calculate scattering and decay processes.

On the other hand the coupling constant significantly increases as one approaches the lower end of the spectrum: quarks are confined in hadrons rendering any attempt to perform a perturbative calculation in terms of α_s futile. It is obvious that one has to devise other methods to study the interactions of mesons and baryons. Over the last decades Chiral Perturbation Theory (ChPT), the systematization of current algebra into an effective field-theory pioneered by the works of Weinberg [15], and Gasser and Leutwyler [16–18], has proven

[#1] The running of the coupling constant is not a unique phenomenon of the strong interaction: the electromagnetic and weak couplings are also dependent on the energy scale, but the effect is less pronounced compared to the strong coupling. The β function of the electromagnetic interactions is positive, so that QED is strongly coupled at high energies [12].

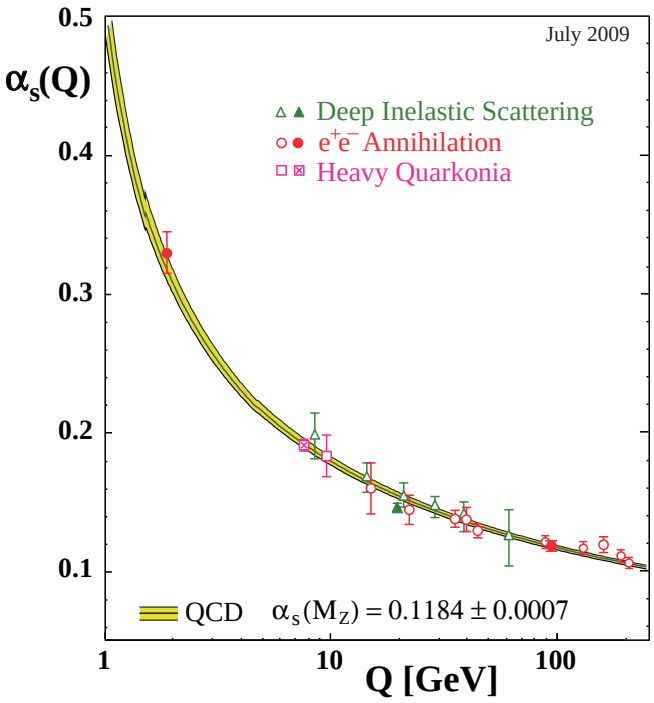

Figure 1.1: Running of the strong coupling constant α_s as a function of the energy scale Q as compared to several experimental determinations from deep inelastic scattering, e^+e^- annihilation, and heavy quarkonia. Figure taken from Ref. [11] with kind permission from Springer and S. Bethke.

a very successful tool in the meson sector.[#2] However, an expansion in small momenta and pion masses, ChPT reaches its limits as soon as the energies of the interacting particles are close to the chiral scale (and even earlier, as for example in the isospin-zero $\pi\pi$ scattering channel). But also in precision studies of decay and scattering processes, where the final-state interactions are strong, ChPT has limitations as we shall see. It is evident that new analysis tools have to be developed that are fit to tighten our grasp around these kinds of physics.

In this thesis we shall present two very distinct tools that are specifically tailored to treat final-state interactions in hadronic three-body decays and transition form factors: a perturbative method in *modified non-relativistic effective field theory* (NREFT), and a non-perturbative method in *dispersion relations*. The outline is as follows: we shall in the following give a very brief introduction to the two methods. The main part of the thesis is then divided into two parts, each attempting to show the potential of the respective method. Chapter 2 is an application of NREFT to the decay $\eta \to 3\pi$ and discloses a way to solve the long-standing puzzle of the slope parameter in the neutral decay channel. The second part deals with dispersion relations and their application in several decays, starting with $\eta' \to \eta\pi\pi$ in Chapter 3, followed by an analysis of $\omega/\phi \to 3\pi$ in Chapter 4, and concludes with a study of the transition form factor $\omega/\phi \to \pi^0 l^+ l^-$ in Chapter 5. We will give a summary and outlook in Chapter 6. Several technical details of Parts I and II are relegated to Appendices A and B.6.

[#2] Since Chiral Perturbation Theory is not the main topic of this work but will nevertheless be an important ingredient to several of our calculations, we refer to Refs. [19–23] for more introductions.

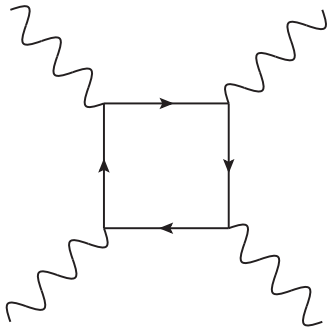

Figure 1.2: Feynman diagram for the electron loop contribution in light-by-light scattering.

1.1 Perturbative methods – Effective field theories

The idea behind an effective field theory is rooted in Weinberg's conjecture, which states that a quantum field theory has no content besides unitarity, analyticity, cluster decomposition, and symmetries [15]. One constructs the most general effective Lagrangian for the low-energy degrees-of-freedom consistent with the symmetry principles of the underlying theory. This Lagrangian can be organized as a series of operators that are suppressed by increasing powers of an expansion parameter (or set of expansion parameters). This expansion parameter, that determines the range of applicability of the effective theory, relies on the ratio of the low- to high-energy scales. A small ratio between scales, and thus a strong scale separation, entails a small expansion parameter and thus guarantees a fast convergence of the expansion.

A neat and very simple example that gives some insight into the mechanisms of effective field theories is light-by-light scattering (see also [23]): consider Quantum Electrodynamics (QED), where the only available scale is given by the electron mass m_e. If what we explained before is true, we should be able to write down an effective Lagrangian that contains only photons as degrees of freedom as long as we stay below the scale m_e, where electrons cannot be produced directly,

$$\mathcal{L}_{\rm QED}[\psi, \bar{\psi}, A_\mu] \to \mathcal{L}_{\rm eff}[A_\mu] \ . \tag{1.2}$$

Lorentz and gauge invariance as the symmetries of the underlying theory (QED) tell us that we can only have terms depending on the field-strength tensor $F_{\mu\nu}$, its adjoint $\tilde{F}_{\mu\nu}$ and derivatives thereof. The latter, however, are suppressed by powers of $(\omega/m_e)^n$ since we are only interested in low-energy interactions, $\omega \ll m_e$. Considering only terms with four photon fields, the effective Lagrangian reads

$$\begin{aligned} \mathcal{L}_{\rm eff} &= \frac{1}{4}(F_{\mu\nu}F^{\mu\nu}) + \tilde{a}(F_{\mu\nu}F^{\mu\nu})^2 + \tilde{b}(F_{\mu\nu}\tilde{F}^{\mu\nu})^2 + \dots \\ &= \frac{1}{2}(\mathbf{E}^2 - \mathbf{B}^2) + \frac{\alpha^2}{m_e^4}\Big[a(\mathbf{E}^2 - \mathbf{B}^2)^2 + b(\mathbf{E}\cdot\mathbf{B})^2\Big] + \dots \ , \end{aligned} \tag{1.3}$$

where $\alpha = e^2/4\pi$, e is the electric charge, a and b are low-energy constants that have to be determined from the underlying theory, and the prefactor follows from dimensional analysis. In the case at hand one has to calculate the underlying loop diagram in Fig. 1.2, the result being $7a = b = 14/45$ [24].

While the basic principles of an effective field theory have been nicely illustrated by this brief exercise, the low-energy constants still merit some discussion. Of course calculating loop

diagrams to determine these constants is rather artificial. When considering strong interactions in the low-energy regime, where QCD becomes nonpertubative, such a determination would require the calculation of an infinite amount of diagrams. Effective field theories describing these dynamics, such as Chiral Perturbation Theory, resort to different methods to constrain the low-energy constants: in ChPT one uses experimental information and input from Lattice QCD. This is a formidable task since ChPT is non-renormalizable and thus the number of low-energy constants quickly explodes with every additional order. For higher-order calculations one tries to obtain estimates for the low-energy constants by assuming that the constants are saturated by resonances.

In our analysis of final-state interactions in $\eta \to 3\pi$ we will resort to the modified non-relativistic effective field theory framework. This framework provides a useful tool to investigate low-energy scattering and decay processes: it has found applications in detailed studies of cusp effects in $K \to 3\pi$ [25–27] and $\eta \to 3\pi$ [28] as well as $\eta' \to \eta\pi\pi$ [29] decays, and has been extended to describe near-threshold pion photo- and electroproduction on the nucleon [30, 31] (for an overview on cusp effects in meson decays, see Ref. [32]). In the following subsection we will begin with a very general construction of the framework, specific details to the $\eta \to 3\pi$ decay are laid out in Chapter 2.

1.1.1 Construction of the non-relativistic effective field theory

The following construction of the modified non-relativistic effective field theory closely follows the train of thought that is outlined in Ref. [33]. We are considering a three-particle decay with relatively small excess energy, so that momenta of the final-state particles are small. It makes sense that these momenta constitute the small energy scale of the system summarized in a small power-counting parameter ϵ. The large energy scale is given by the masses of the particles involved, the lowest being the pion mass. The rules for the power counting are as follows:

- three-momenta of the decay products in the rest frame of the decaying particle are counted as $\mathcal{O}(\epsilon)$;
- as a consequence kinetic energies $T_i = p_i^0 - M_i = \frac{\mathbf{p}_i^2}{2M_i^2} + \ldots$ are to be counted as $\mathcal{O}(\epsilon^2)$;
- masses of the particles involved shall be counted as $\mathcal{O}(1)$;
- the excess energy $Q = \sum_i T_i = M_D - \sum_i M_i$ is counted as $\mathcal{O}(\epsilon^2)$.

The above counting rules may give pause since it is quite possible for the maximum pion three-momenta to be of the size of the pion mass in $\eta \to 3\pi$. We will address this point at a later stage.

At the current stage of the discussion our framework has in terms of power-counting all the makings of a non-relativistic effective theory (see Ref. [34]), so the question why we coin the framework 'modified' naturally arises. The standard non-relativistic propagator has a pole at $p_0 = M + \mathbf{p}^2/2M$ and thus obeys a non-relativistic dispersion law. Loop calculations with such a propagator fulfill Lorentz invariance only perturbatively, which is highly inconvenient: the location of singularities in the two-body subsystems, which in general are not in the rest-frame, only approximately agrees with the exact relativistic value. This can be remedied by summing up the higher-order corrections to the propagator, leading to the relativistic dispersion law of the form $p^0 = w(\mathbf{p}) = \sqrt{\mathbf{p}^2 + M^2}$.

We will discuss this issue on the level of the effective Lagrangian that describes scattering of a massive scalar particle in the center-of-mass frame (CM):

$$\mathcal{L}_{\rm NR} = \phi^\dagger \Big(i\partial_t - M + \frac{\Delta}{2M} + \frac{\Delta^2}{8M^3} + \ldots \Big) \phi + c_0 (\phi^\dagger)^2 \phi^2 + c_1 \Big[(\phi^\dagger \overset{\leftrightarrow}{\Delta} \phi^\dagger) \phi^2 + h.c. \Big] + \ldots \ , \quad (1.4)$$

where ϕ is the non-relativistic field operator of the particle with mass M, Δ is the Laplacian, $u \overset{\leftrightarrow}{\Delta} v = u(\Delta v) + (\Delta u) v$ and we have omitted higher orders in the derivative couplings. It is readily observed that Eq. (1.4) is an expansion organized in powers of ϵ. The term containing four fields corresponds to the effective range expansion in the center-of-mass frame. If we consider the effective Lagrangian as the sum of a free dynamical part and an interaction part according to

$$\mathcal{L}_{\rm NR} = \mathcal{L}^0_{\rm NR} + \mathcal{L}^{\rm int}_{\rm NR} \ , \quad (1.5)$$

where the free part is given by $\mathcal{L}^0_{\rm NR} = \phi^\dagger (i\partial_t - M + \frac{\Delta}{2M}) \phi$, we obtain for the two-point function

$$i \langle 0 | \phi(x) \phi^\dagger(y) | 0 \rangle = \int \frac{d^4 p}{(2\pi)^4} \frac{e^{-ip(x-y)}}{M + \frac{\mathbf{p}^2}{2M} - p_0 - i\epsilon} \ , \quad (1.6)$$

which obeys the non-relativistic dispersion law as alluded to before. To arrive at the relativistic dispersion law one has to sum up the additional mass insertions $\Delta^2/8M + \ldots$ into the external legs of the Green's functions, and thus modify the propagator according to

$$\int \frac{d^4 p}{(2\pi)^4} \frac{e^{-ip(x-y)}}{M + \frac{\mathbf{p}^2}{2M} - p_0 - i\epsilon} \to \int \frac{d^4 p}{(2\pi)^4} \frac{e^{-ip(x-y)}}{w(\mathbf{p}) - p_0 - i\epsilon} \ , \quad (1.7)$$

which obeys the desired dispersion law.

There is an additional modification to the classical non-relativistic effective field theory that is tied to the matching between the non-relativistic and the relativistic theory. In the conventional approach, see Ref. [34], the matching condition is given as

$$\prod_{i=1}^{4} (2w(\mathbf{p}_i))^{1/2} T_{\rm NR}(\mathbf{p}_3, \mathbf{p}_4; \mathbf{p}_1, \mathbf{p}_2) = T_{\rm R}(\mathbf{p}_3, \mathbf{p}_4; \mathbf{p}_1, \mathbf{p}_2) \ . \quad (1.8)$$

From Eq. (1.8) one determines the low-energy couplings of the non-relativistic theory in terms of the underlying relativistic theory. The prefactors $(2w(\mathbf{p}_i))^{1/2}$ stem from the normalization of the relativistic asymptotic states. The matching condition is not explicitly covariant, which is illustrated by the following example: consider standard φ^4-theory as the underlying relativistic theory with an interaction piece in the Lagrangian given as $\lambda\varphi^4/24$. At leading order the relativistic amplitude is then given as $T_{\rm R}(\mathbf{p}_3, \mathbf{p}_4; \mathbf{p}_1, \mathbf{p}_2) = \lambda$, so that

$$T_{\rm NR}(\mathbf{p}_3, \mathbf{p}_4; \mathbf{p}_1, \mathbf{p}_2) = \frac{\lambda}{(2w(\mathbf{p}_1) 2w(\mathbf{p}_2) 2w(\mathbf{p}_3) 2w(\mathbf{p}_4))^{1/2}} \ , \quad (1.9)$$

which at threshold simplifies to

$$T_{\rm NR}(\mathbf{p}_3, \mathbf{p}_4; \mathbf{p}_1, \mathbf{p}_2)\Big|_{\text{threshold, CM}} = \frac{\lambda}{4M^2} \ , \quad (1.10)$$

implying $c_0 = \lambda/4M^2$ and $c_1 = c_2 = \ldots = 0$ in the center-of-mass frame. If, however, we move away from the center-of-mass system to an arbitrary reference frame, the matching condition implies for the non-relativistic amplitude at threshold:

$$T_{\mathrm{NR}}(\mathbf{p}_3, \mathbf{p}_4; \mathbf{p}_1, \mathbf{p}_2)\Big|_{\text{threshold, CM}} = \frac{\lambda}{4w^2(\mathbf{P})} = \frac{\lambda}{4M^2} - \frac{\lambda}{16M^2}\mathbf{P}^2 + \ldots \ . \tag{1.11}$$

$\mathbf{P}$ denotes the total 3-momentum of particles 1 and 2 at threshold. An infinite amount of low-energy constants is needed to properly describe the system. Of course these low-energy constants are not all independent as they are related by Lorentz invariance. In principle one could simply perform this matching at any given order, but this procedure certainly leaves a lot to be desired.

The problem can be circumvented if one rearranges the non-relativistic theory in such a way that the prefactor on the left-hand side of Eq. (1.8) vanishes. This is achieved by introducing a new field $\Phi(x) = (2W)^{-1/2}\phi(x)$, where $W = \sqrt{M^2 - \Delta}$, leading to a non-local modified Lagrangian of the very compact form,

$$\mathcal{L} = 2\Phi^\dagger W(i\partial_t - W)\Phi + C_0(\Phi^\dagger)^2\Phi^2 + \ldots \ . \tag{1.12}$$

The ellipsis stands for four-particle interactions of higher order in ϵ. For the two-point function based on this modified Lagrangian we obtain

$$i\langle 0|\phi(x)\phi^\dagger(y)|0\rangle = \int \frac{d^4p}{(2\pi)^4} \frac{e^{-ip(x-y)}}{2w(\mathbf{p})(w(\mathbf{p}) - p_0 - i\epsilon)} \ . \tag{1.13}$$

This propagator has some interesting features that explain to what extent the theory is still non-relativistic. If we split up the relativistic propagator according to

$$\frac{1}{M^2 - p^2 - i\epsilon} = \underbrace{\frac{1}{2w(\mathbf{p})(w(\mathbf{p}) - p_0 - i\epsilon)}}_{\text{non-relativistic}} + \underbrace{\frac{1}{2w(\mathbf{p})(w(\mathbf{p}) + p_0 - i\epsilon)}}_{\text{anti-particle}} \ , \tag{1.14}$$

we observe that the non-relativistic part describes the propagation of the particle, while it does not account for the anti-particle. In that sense the number of heavy particles in the theory is conserved: no particle–anti-particle pairs can be created or annihilated,[#3] and no additional inelastic thresholds complicate the analytic structure of the amplitude. This concludes our discussion of the construction of the modified non-relativistic effective field theory framework. Part I of thesis deals with the application of the theory to the decay $\eta \to 3\pi$.

1.2 Non-perturbative methods – Dispersion relations

Effective field theories such as chiral perturbation theory and the modified non-relativistic effective field theories reach their limitations as soon as strong final-state interactions at large energies (as compared to the scale) are involved. In the case of ChPT this scale is given by the appearance of the first resonances, e.g. the $\sigma(500)$ and the $\rho(770)$ in pion–pion scattering. We already discussed that contributions of these resonances are subsumed in low-energy constants

[#3] To be precise, we refer to the creation and annihilation of particle–anti-particle pairs heavier than pions ($K\bar{K}$, $\eta\bar{\eta}, \ldots$). We allow, however, for inelastic charge exchange in the two-pion final-state when taking into account isospin breaking in $\eta \to 3\pi$.

of the theory, but they are not dynamically included: any process containing these resonances in the physical regime cannot be described by either of the above effective field theories. Such processes involve the decays of the lowest lying (ω, ϕ, ...) vector mesons, where the ρ resonance is sufficiently close to (in case of the ω) or even part of the physical region, so that effective field theory approaches are doomed to failure. One has to conceive methods that go beyond a perturbative expansion in small energies – non-perturbative methods of which we will introduce dispersion relations in this section. We follow Ref. [35] and further treatment and references on the subject may be found there.

1.2.1 Analyticity and unitarity

To study the subject of dispersion relations we shall consider a specific process, the analytic structure of which we wish to investigate in the following. We shall focus on the elastic scattering of two spinless particles of the same mass,

$$1(p_1)2(p_2) \to 3(p_3)4(p_4) \ . \tag{1.15}$$

In the latter stages of this work we will analyze the decay of one particle into three final-state products. This process is related to the above by analytic continuation, but at the same time entails a more complicated analytic structure. It is therefore more instructive to start with this rather simple case. The transition from an initial state $|n\rangle$ to a final state $|m\rangle$ is described by the so-called *S-matrix*,

$$\langle m|S|n\rangle \ . \tag{1.16}$$

Since the probability of the system ending up in some other state must be unity, the S-matrix necessarily fulfills the condition,

$$S^\dagger S = S S^\dagger = \mathbb{1} \ , \tag{1.17}$$

thus S is unitary. For our specific process the transition matrix element is given by

$$\langle p_3, p_4|S|p_1, p_2\rangle \ . \tag{1.18}$$

It is most convenient to express matrix elements and amplitudes in terms of the Lorentz-invariant *Mandelstam variables*,

$$s = (p_1 + p_2)^2 \ , \quad t = (p_1 - p_3)^2 \ , \quad u = (p_1 - p_4)^2 \ , \tag{1.19}$$

which due to momentum conservation and the mass shell relation for each particle fulfill

$$s + t + u = \sum_{i=1}^{4} M_i^2 = 4M^2 \ . \tag{1.20}$$

Separating the trivial part and thus isolating the interesting piece that is due to interactions, we can rewrite the S-matrix as

$$S = \mathbb{1} + iT \ , \tag{1.21}$$

which substituted into the unitarity relation Eq. (1.17) leads to

$$T - T^\dagger = iT^\dagger T = iTT^\dagger \ . \tag{1.22}$$

Finally we extract the transition amplitude $\mathcal{M}$ from the T-matrix, which is related by a momentum conserving δ-function

$$\langle p_3, p_4|T|p_1, p_2\rangle = (2\pi)^4\delta(p_1 + p_2 - p_3 - p_4)\mathcal{M}(s,t,u) \ . \tag{1.23}$$

In the case of two-particle scattering $\mathcal{M}(s,t,u)$ in principle depends only on two of the Mandelstam variables due to Eq. (1.20). We will thus also use $\mathcal{M}(s,t)$ always implying that Eq. (1.20) is enforced. In the following we study the implications of unitarity on the analytic structure of $\mathcal{M}$. First of all we note that thresholds generate branch cuts of the amplitude [36] in the complex s-plane starting at $s > 4M^2$, so-called *right-hand* cuts, with additional cuts starting at the respective multi-particle thresholds, $s = 9M^2$, $s = 16M^2$, and so forth. We will concentrate on elastic processes exclusively in this section, so only the cut at $s = 4M^2$ is relevant in the following. It is of course convention to use the positive real axis for the cut: its only purpose is to remove ambiguities by selecting a single sheet of the Riemann surface, and thus to arrive at single-valued functions. So long as we do not cross any of the branch cuts we are by definition located on the *physical sheet*. As soon as we cross a branch cut, we land on unphysical sheets.

For time-invariant interactions, that is for processes in which $\langle m|S|n\rangle = \langle n|S|m\rangle$, we find upon invoking the unitarity relation in the form of Eq. (1.22),

$$\begin{aligned} 2\mathrm{Im}\,\langle p_3p_4|\mathcal{M}|p_1p_2\rangle = \int \frac{d^4k_1}{(2\pi)^4}\frac{d^4k_2}{(2\pi)^4}(2\pi)\delta(k_1^2 - M^2)(2\pi)\delta(k_2^2 - M^2) \\ \times (2\pi)^4\delta^{(4)}(p_1 + p_2 - k_1 - k_2)\langle p_3p_4|\mathcal{M}|k_1k_2\rangle\langle p_1p_2|\mathcal{M}|k_1k_2\rangle^* + \dots \ , \end{aligned} \tag{1.24}$$

where the ellipsis stands for intermediate states of allowed physical processes beyond the two-particle threshold. We note that in general $\langle m|S|n\rangle \neq \langle n|S|m\rangle$ and the imaginary part has to be replaced by the discontinuity across the cut. This issue will be discussed at a later stage. For now we observe that unitarity implies that whenever a physical process is allowed as an intermediate state it will generate a singularity in the scattering amplitude. This is part of the statement of maximal analyticity that the amplitude possesses no singularities other than those dictated by unitarity and crossing symmetry. In the following we will study how crossing symmetry influences the analytic structure.

For that we first observe that the physical region of $\mathcal{M}(s,t)$ for the process $1,2 \to 3,4$ is constrained in the Mandelstam plane,

$$s \geq 4M^2 \ , \quad t \leq 0 \ , \quad u \leq 0 \ , \tag{1.25}$$

which is easily seen when resorting to the center-of-mass frame, in which

$$\begin{aligned} s &= 4(M^2 + q^2) \ , \\ t &= -2q^2(1 - \cos\theta) \ , \\ u &= -2q^2(1 - \cos\theta) \ , \end{aligned} \tag{1.26}$$

where $q^2 = s/4 - M^2$ is the center-of-mass momentum squared, $\cos\theta$ the center-of-mass scattering angle, and obviously $q^2 > 0$. If one analytically continues $\mathcal{M}(s,t)$ to the region where

$$t \geq 4M^2 \ , \quad s \leq 0 \ , \quad u \leq 0 \ , \tag{1.27}$$

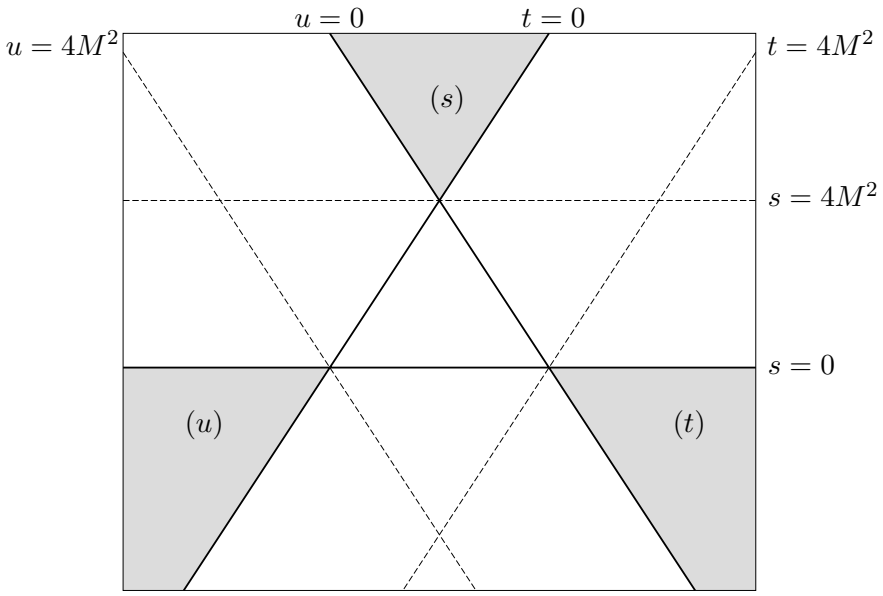

Figure 1.3: The Mandelstam plane for elastic two-particle scattering with equal masses M. The dashed lines denote the threshold of the respective channel.

one instead describes the physical region for $1, \bar{3} \to \bar{2}, 4$, which is related to the above by crossing symmetry. The same exercise for the analytic continuation to

$$u \geq 4M^2 \ , \quad s \leq 0 \ , \quad t \leq 0 \ , \tag{1.28}$$

yields the scattering amplitude for the process $1, \bar{4} \to \bar{2}, 3$. In other words the analytic structure of the decay amplitude in different physical regions is related through crossing symmetry: we can use the *same* function $\mathcal{M}(s,t)$ to describe these channels as long as we perform the correct analytic continuation. This principle will be of fundamental importance later on when we construct dispersion relations for three-body decays. The analytic continuation itself is a little more involved in that case, but the principle is the same. A visualization of the physical regions may be found in Fig. 1.3.

Crossing symmetry also implies the existence of an additional singularity in the s-channel itself. To be specific let us consider a fixed value of t, say $t_0 = 0$. Then the branch cut at the two-particle threshold in the u-channel generates a *left-hand* cut in the s-channel through Eq. (1.20) starting at

$$s = -t_0 - u_{\text{thr}} + 4M^2 = -t_0 \ . \tag{1.29}$$

The complex s-plane thus has two cuts, one starting at $s = -t_0$ and running along the negative real axis up to infinity, and one starting $s = 4M^2$ running along the positive real axis to infinity. Again, the real axis is chosen by convention: only the branch points themselves are fixed and in principle the cut can be distorted arbitrarily without changing the function $\mathcal{M}(s, t_0)$ – so long as one does not hit another singularity. Perturbation theory implies that the physical amplitude is given by approaching the right-hand branch cut from above,[#4]

$$\mathcal{M}_{\text{physical}} = \lim_{\epsilon \to 0+} \mathcal{M}(s + i\epsilon, t_0) \ . \tag{1.30}$$

[#4]This is equivalent to bestowing a small negative imaginary part on the mass in the Feynman propagator, see Ref. [35]

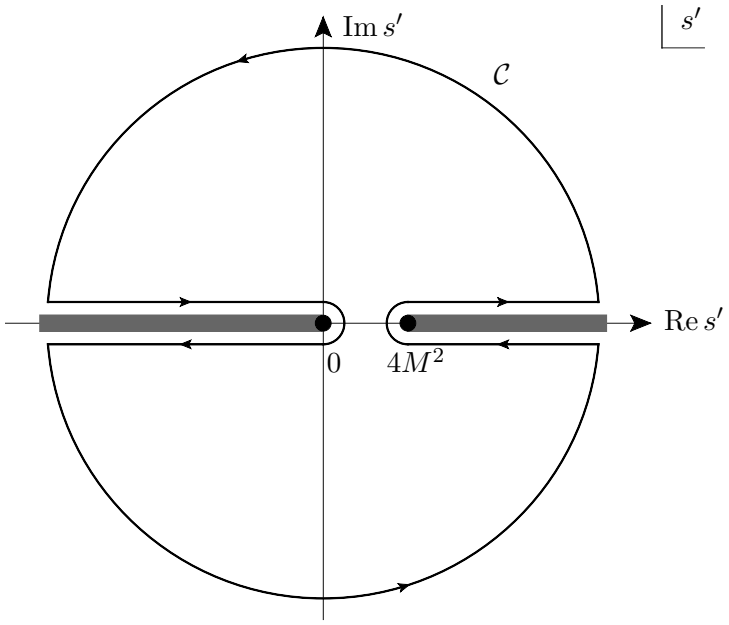

Figure 1.4: Integration contour $\mathcal{C}$ for Cauchy's theorem as in Eq. (1.31) (with $t_0 = 0$) and cut structure of the complex s-plane.

Up to this point we have a fairly good idea of the analytic structure of the function $\mathcal{M}(s, t_0)$, but to what end? To address this question we invoke Cauchy's theorem,

$$\mathcal{M}(s, t_0) = \frac{1}{2\pi i} \int_{\mathcal{C}} ds' \frac{\mathcal{M}(s', t_0)}{s' - s} \ , \tag{1.31}$$

where the integration contour $\mathcal{C}$ is shown in the complex s-plane in Fig. 1.4. Provided that $\mathcal{M}(s, t_0)$ falls off sufficiently fast as $|s'| \to \infty$, the contribution of the outer half-circles to the integral vanishes and we are left with

$$\mathcal{M}(s, t_0) = \frac{1}{2\pi i} \int_{-\infty}^{-t_0} ds' \frac{\mathrm{disc}\, \mathcal{M}(s', t_0)}{s' - s} + \frac{1}{2\pi i} \int_{4M^2}^{\infty} ds' \frac{\mathrm{disc}\, \mathcal{M}(s', t_0)}{s' - s} \ , \tag{1.32}$$

where the discontinuities across the left- and right-hand cut respectively are defined as

$$\mathrm{disc}\, \mathcal{M}(s, t_0) = \lim_{\epsilon \to 0} \Big[\mathcal{M}(s + i\epsilon, t_0) - \mathcal{M}(s - i\epsilon, t_0) \Big] \ . \tag{1.33}$$

As long as $\langle m|S|n\rangle = \langle n|S|m\rangle$ the discontinuity can be expressed in terms of the imaginary part as $\mathrm{disc}\, \mathcal{M}(s, t_0) = 2i \mathrm{Im}\, \mathcal{M}(s, t_0)$. In general, however, the discontinuity is complex as is the case in three-body decays. Using $s' + t_0 + u' = 4M^2$, we can reexpress Eq. (1.32) according to

$$\mathcal{M}(s, t_0) = \frac{1}{2\pi i} \int_{4M^2}^{\infty} ds' \Big\{ \frac{1}{s' - s} + \frac{1}{s' - u} \Big\} \mathrm{disc}\, \mathcal{M}(s', t_0) \ . \tag{1.34}$$

This equation is a so-called fixed-t *dispersion relation* and a very powerful tool at that: once the singularity structure of a particular process is known the full amplitude can be determined on the grounds of unitarity and crossing symmetry. Dispersion relations have found numerous application in scattering processes: currently the most precise determinations of $\pi\pi$ scattering

phase shifts are performed using so-called Roy equations. These are derived from fixed-t dispersion relations using partial-wave expansions of the scattering amplitudes, see Refs. [37–41]. A very elaborate treatment of pion–nucleon scattering with Roy-Steiner equations (respecting the spin structure of the nucleon) as well as a dispersive calculation of the scalar form factor of the nucleon may be found in Refs. [42, 43].

Our discussion so far had a rather serious caveat. We assumed $\mathcal{M}(s,t_0)$ to drop off sufficiently fast as $|s|\to\infty$. However, this need not be (and in most relevant examples is not) the case. Let us instead assume that the amplitude behaves as

$$|\mathcal{M}(s,t_0)| \propto |s|^{N-1} \ . \tag{1.35}$$

as $s\to\infty$. In this case the integral equation (1.34) does not converge. This can easily be remedied: the function

$$\frac{\mathcal{M}(s,t_0)}{(s-s_1)\dots(s-s_N)} \ , \tag{1.36}$$

has the desired behavior and tends to zero as $|s|\to\infty$. The new dispersion relation then takes the form,

$$\begin{aligned}\mathcal{M}(s,t_0) = P(s) + \frac{(s-s_1)\dots(s-s_N)}{2\pi i}\int_{4M^2}^{\infty} ds'\Big\{&\frac{1}{(s'-s_1)\dots(s'-s_N)(s'-s)}\\ &+\frac{1}{(s'-u_1)\dots(s'-u_N)(s'-u)}\Big\}\operatorname{disc}\mathcal{M}(s',t_0) \ ,\end{aligned} \tag{1.37}$$

where u_i is determined by $s_i+t_0+u_i=4M^2$ and $P(s)$ is a polynomial of degree $N-1$. The unknown N coefficients are called *subtraction constants* and have to be fixed independently. In the case of $\pi\pi$ scattering for example this is done by matching the low-energy representation to ChPT (see Ref. [44]). We will discuss our matching procedures for the distinct processes at the appropriate stages of our analyses. In general we will determine the maximal number of necessary subtractions from the Froissart–Martin bound [45, 46], that states that the total cross section does not grow faster than $\log^2 s$ as $s\to\infty$.

In this section we introduced dispersion relations with a somewhat artificial example. Part II of this thesis is dedicated to the discussion of rather complicated "real-life" processes in hadronic three-body decays and transition form factors. There is, however, a rather simple example with a physical application: the pion vector form factor. We will revisit it quite frequently throughout the second part of this work, especially when discussing the transition form factors $\omega/\phi\to\pi^0\gamma^*$, so that it is as instructive as it is convenient to treat it in some detail at this stage, as we shall do in the following.

1.2.2 A simple application: the pion vector form factor

We consider the process of two pions converting into a photon. The matrix element for this process is given by

$$\langle\pi^+(p)\pi^-(q)|J_\mu(0)|0\rangle = i(p_\mu-q_\mu)F_\pi^V(s) \ , \tag{1.38}$$

where J_μ is the electromagnetic current and the scalar function $F_\pi^V(s)$ is known as the pion vector form factor. This process is particularly simple from a dispersive point-of-view, since it does not contain a left-hand cut: there are no physically allowed crossed-channel processes.

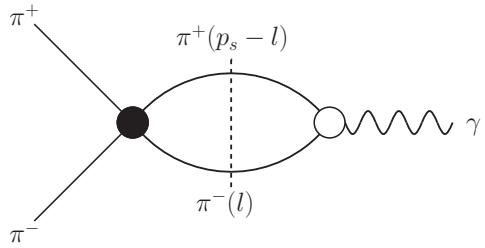

Figure 1.5: Diagram for the pion vector form factor. The black circle denotes the $\pi\pi$ scattering amplitude, the white circle the pion vector form factor describing the $\pi^+\pi^- \to \gamma$ transition.

To set up the dispersion relations as outlined in the previous section, we need to calculate the discontinuity of the form factor. To that end we assume that the form factor is dominated by $\pi\pi$ intermediate states as shown in Fig 1.5. The discontinuity of this diagram is given as [47][#5]

$$(p-q)_\mu \text{disc}\, F_\pi^V(s) = \frac{i}{2}\int \frac{d^4l}{(2\pi)^4}(2\pi)\delta(l^2 - M_\pi^2)(2\pi)\delta((p_s-l)^2 - M_\pi^2)\mathcal{T}_I(s,z_l)(p_s-2l)_\mu F_\pi^V(s)\ , \tag{1.39}$$

where $\mathcal{T}^I(s,z)$ denotes the $\pi\pi$ scattering amplitude of isospin I in terms of s and the center-of-mass scattering angle $\cos\theta_l = z_l$, $p_s = p+q$ with $p_s^2 = s$, and M_π is the pion mass. After carrying out the momentum integration, we obtain

$$(p-q)_\mu \text{disc}\, F_\pi^V(s) = \frac{i}{64\pi^2}\sigma_\pi(s) F_\pi^V(s)\int d\Omega_l \mathcal{T}_I^*(s,z_l)(p_s-2l)_\mu\ , \tag{1.40}$$

where we defined $\sigma_\pi(s) = \sqrt{1-4M_\pi^2/s}$ and the integral measure $d\Omega_l$ is the solid angle of the $\pi\pi$ subsystem. One can easily show (for example by evaluation in the center-of-mass system) that the integral can be rewritten as

$$\int d\Omega_l \mathcal{T}_I^*(s,z_l)(p_s-2l)_\mu = 2\pi(p-q)_\mu \int_{-1}^{1} dz_l\, z_l\, \mathcal{T}_I^*(s,z_l)\ . \tag{1.41}$$

Using the partial-wave expansion of the $\pi\pi$ scattering amplitude,

$$\mathcal{T}_I(s,z) = 32\pi \sum_{\ell=0}^{\infty}(2\ell+1)t_\ell^I(s)P_\ell(z)\ , \tag{1.42}$$

where $t_\ell^I(s)$ is the amplitude of the ℓ-th partial wave with isospin I and P_l are the Legendre polynomials, along with the orthogonality condition,

$$(2\ell+1)\int_{-1}^{1} dz P_\ell(z)P_{\ell'}(z) = 2\delta_{\ell\ell'}\ , \tag{1.43}$$

we find that only the $\ell = 1$ partial-wave is projected out. Due to Bose symmetry only isospin $I = 1$ contributes. We have

$$\text{disc}\, F_\pi^V(s) = 2i\sigma_\pi(s)F_\pi^V(s)t_1^{1*}(s)\theta(s-4M_\pi^2)\ , \tag{1.44}$$

[#5]The factor 1/2 is often incorporated in the definition of the isospin amplitude $\mathcal{T}_I(s)$. We choose to retain it explicitly in the following.

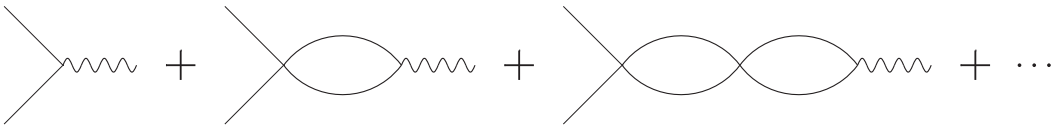

Figure 1.6: Iteration of bubble diagrams for the vector form factor.

and finally, after reparametrizing the partial-wave amplitude via the phase shift,

$$t_1^1(s) = \frac{1}{\sigma_\pi(s)} \sin\delta_1^1(s) e^{i\delta_1^1(s)} \ , \tag{1.45}$$

we arrive at the final result for the discontinuity of the form factor,

$$\text{disc}\, F_\pi^V(s) = 2iF_\pi^V(s) \sin\delta_1^1(s) e^{-i\delta_1^1(s)} \theta(s-4M_\pi^2) \ . \tag{1.46}$$

The above is the manifestation of Watson's final-state theorem [48] that states that the phase of the form factor below inelastic thresholds is given by the two-particle scattering phase shift, $\delta_{F_\pi^V}(s) = \delta_1^1(s)$. We can construct an analytical solution for Eq. (1.46): first consider a special solution $\Omega_1^1(s)$ that is free of zeros (otherwise the zeros can be subsumed in a polynomial). We obtain the general solution for $F_\pi^V(s)$ by multiplying with a real polynomial $P(s)$,

$$F_\pi^V(s) = P(s)\Omega_1^1(s) \ . \tag{1.47}$$

Noting that the special solution to Eq. (1.46) has to fulfill

$$\Omega_1^1(s-i\epsilon) = \Omega_1^1(s+i\epsilon) e^{-2i\delta_1^1(s)} \ , \tag{1.48}$$

we find upon taking the logarithm that

$$\text{disc}\, \log\Omega_1^1(s) = 2i\delta_1^1(s) \ , \tag{1.49}$$

which can be cast into a dispersion relation

$$\log\Omega_1^1(s) = \frac{1}{2\pi i} \int_{4M_\pi^2}^\infty ds' \frac{\text{disc}\, \log\Omega_1^1(s')}{s'-s} \ . \tag{1.50}$$

Adjusting the normalization in such a way that $\Omega_1^1(0) = 1$, we arive at the final result,

$$\Omega_1^1(s) = \exp\Big\{ \frac{s}{\pi} \int_{4M_\pi^2}^\infty ds' \frac{\delta_1^1(s')}{s'(s'-s)} \Big\} \ . \tag{1.51}$$

The above solution for the form factor integral equation is known as the Omnès function [49] (see also Ref. [50]). One can think of it as an iteration of bubble diagrams as visualized in Fig. 1.6. The Omnès function is entirely determined by the input for the P-wave phase shift of $\pi\pi$ scattering, on which we will comment more elaborately at a later stage. We reiterate that the solution we derived here is valid for elastic scattering. Inelastic channels modify the unitarity relation (1.46), see Refs. [51–53]. Nevertheless, Eq. (1.51) is of fundamental importance: it has been used to constrain the contribution of hadronic vacuum polarization to $g-2$ of the muon [52,53] and is an essential input for the Roy-Steiner analysis of πN scattering [42, 43]. We will make ample use of it in our analyses of three-body decays and transition form factors.

Part I

Perturbative methods: Non-relativistic effective field theory

Chapter 2

Rescattering effects in $\eta \to 3\pi$ decays[#1]

2.1 Introduction

The decay $\eta \to 3\pi$ has been the center of attention in many theoretical and experimental works over the recent decades. The considerable interest is due to the fact that the decay can only occur via isospin-breaking operators and is therefore sensitive to the up- and down-quark mass difference. Indeed, the $\eta \to 3\pi$ transition amplitude is inversely proportional to the quark mass double ratio $\mathcal{Q}^2$,

$$\frac{1}{\mathcal{Q}^2} = \frac{m_d^2 - m_u^2}{m_s^2 - \hat{m}^2} \ , \qquad \hat{m} = \frac{1}{2}(m_u + m_d) \ , \tag{2.1}$$

and thus the decay provides an excellent testing ground for the breaking of chiral symmetry.

Despite valiant efforts it seemed difficult to bring theoretical description and experimental results in agreement. First attempts that relied on an electromagnetic transition [55, 56] were unsuccessful in explaining the decay. SU(3) current algebra techniques in combination with the partially conserved axial-vector current hypothesis [57,58] were generalized to SU(3) chiral perturbation theory (ChPT) and initiated systematic improvements to the decay rate. While the one- and two-loop corrections to the decay were sizable [59,60], a consistent implementation of electromagnetic contributions only lead to small effects [61, 62]. Despite these theoretical improvements the Dalitz plot expansion, especially of the neutral decay, remained an unsolved puzzle. The slope α vanishes at leading order, while at next-to-leading order ($\mathcal{O}(p^4)$, one loop) it disagrees in sign with experimental findings [63–71]. The same holds for the next-to-next-to-leading order ($\mathcal{O}(p^6)$, two loops) calculation [60]. The error on the final result is rather large, so that it allows for a negative slope parameter. However, this error is not based on the uncertainties due to the low-energy constants at $\mathcal{O}(p^6)$, which are estimated by resonance saturation, but results solely from the authors' fitting procedure.

It has been argued that $\pi\pi$ final-state interactions are the dominant force behind the sizable corrections [72, 73], motivating several dispersive analyses [74–78] (see also Ref. [79]), which were able to give a more robust prediction of the slope parameter. Among the shortcomings of these dispersion relation techniques and the next-to-next-to-leading-order calculation is the

[#1] The contents of this Chapter have been published in [54].

treatment of higher-order isospin-breaking effects due to electromagnetism, as for example the mass difference between charged and neutral pions. It is not yet clear how to incorporate these effects.

An analysis of $\eta \to 3\pi$ in the framework of unitarized chiral perturbation theory has been conducted in Ref. [80], producing remarkable agreement with experiment. In particular, the experimental value of the slope parameter in the neutral decay channel can be accommodated. However, since this approach is based on an elaborate fitting procedure, wherein the U(3) expansion parameters are determined from several hadronic η and η' decay channels, among those $\eta \to 3\pi$, we do not consider this value for the slope parameter an unbiased *prediction*. Finally, a study of $\eta \to 3\pi$ in the framework of resummed ChPT is currently work in progress [81].

In this chapter we attempt to bridge the gap between the ChPT prediction and the dispersive analysis using the modified non-relativistic effective field theory framework. While this framework does not allow for a fundamental prediction of physical observables, it is ideally suited to study the dynamics of the final-state interactions. At two-loop accuracy and with the correct empirical $\pi\pi$ scattering parameters, we ought to have a reasonable approximation to the full dispersive resummation of rescattering effects at hand, so when matching to ChPT at $\mathcal{O}(p^4)$, we can hope to find a transparent interpretation of the dispersive results obtained in a similar fashion [74]. Additionally, the non-relativistic framework provides access to investigating the effects of isospin-breaking corrections.

This chapter is organized as follows. In Section 2.2 we begin with a general discussion of the properties of the $\eta \to 3\pi$ decay and a short description of the Dalitz plot expansion and the conventions used throughout this chapter. An introduction to the non-relativistic framework, its power counting, the matching procedure, and numerical input is given in Section 2.3. Sections 2.4 and 2.5 comprise the analytic and numerical results in the isospin limit and with isospin breaking included. In Section 2.6 we study final-state interaction effects on an isospin relation between the charged and the neutral decay channel. In Section 2.7 finally, we briefly comment on the $\eta \to 3\pi$ partial widths and their ratio, before summarizing our findings in Section 2.8. Several details of the calculation and more laborious formulae are relegated to the appendices.

2.2 Dalitz plot expansion of the decay amplitude

In the following we consider the charged and neutral decay modes

$$\begin{aligned} \eta(P_\eta) \to \pi^+(p_1)\pi^-(p_2)\pi^0(p_3)\ , \qquad & s_1+s_2+s_3 = 3s_c = M_\eta^2 + 2M_\pi^2 + M_{\pi^0}^2\ , \\ & Q_c = M_\eta - 2M_\pi - M_{\pi^0}\ , \\ \eta(P_\eta) \to \pi^0(p_1)\pi^0(p_2)\pi^0(p_3)\ , \qquad & s_1+s_2+s_3 = 3s_n = M_\eta^2 + 3M_{\pi^0}^2\ , \\ & Q_n = M_\eta - 3M_{\pi^0}\ , \end{aligned} \tag{2.2}$$

where the kinematical variables are defined as $s_i = (P_\eta - p_i)^2$ with $p_i^2 = M_i^2$, $i = 1,2,3$, and $Q_{n/c}$ is the excess energy of the respective channel.[#1] We will use the notation $M_\pi \doteq M_{\pi^\pm}$ throughout.

[#1] For convenience with respect to the non-relativistic effective field theory, we use a different notation from what is usually found in the literature. The transition can be made setting $s_1 = t$, $s_2 = u$, $s_3 = s$.

In experimental analyses of these decays, the squared absolute value of the amplitude is conventionally expanded as a polynomial around the center of the Dalitz plot in terms of symmetrized coordinates. For the charged decay channel one uses

$$x = \sqrt{3}\frac{E_2 - E_1}{Q_c} = \frac{s_1 - s_2}{\sqrt{3}R_c} \ , \qquad y = \frac{3E_3}{Q_c} - 1 = \frac{s_n - s_3}{R_c} + \delta \ , \tag{2.3}$$

where $E_i = p_i^0 - M_i$ is the kinetic energy of i-th particle in the η rest frame, and we used the definitions

$$p_i^0 = \frac{M_\eta^2 + M_i^2 - s_i}{2M_\eta} \ , \qquad R_{c/n} = \frac{2}{3}M_\eta Q_{c/n} \ , \qquad \delta = \frac{Q_n}{Q_c} - 1 \ . \tag{2.4}$$

For the neutral channel one defines

$$z = \frac{2}{3}\sum_{i=1}^{3}\Big(\frac{3E_i}{Q_n} - 1\Big)^2 = \frac{2}{3}\sum_{i=1}^{3}\frac{(s_i - s_n)^2}{R_n^2} = x_n^2 + y_n^2 \ ,$$
$$x_n = \sqrt{z}\cos(\phi) \ , \quad y_n = \sqrt{z}\sin(\phi) \ , \tag{2.5}$$

where we have introduced polar coordinates (z, ϕ) in the center of the Dalitz plot. These definitions of x_n and y_n agree with x and y only for $M_\pi = M_{\pi^0}$. In current experimental analyses data is then fitted to the *Dalitz plot* distribution, which is of the form (assuming charge conjugation invariance)

$$|\mathcal{M}_c(x,y)|^2 = |\mathcal{N}_c|^2\big\{1 + ay + by^2 + dx^2 + fy^3 + gx^2y + \dots\big\} \ ,$$
$$|\mathcal{M}_n(z)|^2 = |\mathcal{N}_n|^2\big\{1 + 2\alpha z + 2\beta z^{3/2}\sin(3\phi) + 2\gamma z^2 + \dots\big\} \ , \tag{2.6}$$

where a, b, d, f, g and α, β, γ are the Dalitz plot parameters and $\mathcal{N}_c$, $\mathcal{N}_n$ are the normalizations of the charged and the neutral decay, respectively. We note that of the higher-order parameters beyond quadratic order in x and y, only f has been measured so far (by the KLOE collaboration [82] and in Ref. [83]). However, with the advent of very high statistics measurements for $\eta \to 3\pi^0$ e.g. at MAMI [84], a determination of β and γ might not be beyond the realm of possibility.

We wish to comment on the validity of the polynomial expansion Eq. (2.6) in particular for the neutral decay channel. The boundary of the Dalitz plot for $\eta \to 3\pi^0$ is shown in Fig. 2.1. The dotted lines denote the three symmetry axes, the dotted circle depicts the beginning of the rapid decrease of pure phase space for radii $\sqrt{z} > \sqrt{0.756}$. It is important to note that the cusps due to $\pi^+\pi^- \to \pi^0\pi^0$ final state rescattering occur at $s_i = 4M_\pi^2$ and not at a single z value; the smallest and the largest values of z crossing the cusp lines ($z = 0.598$ and $z = 0.882$, respectively) are indicated at the corresponding arrows. Therefore the polynomial representation for the neutral Dalitz plot distribution (2.6) is only valid for $z < 0.598$, i.e. inside the dashed circle.

Table 2.1 summarizes the latest experimental determinations and theoretical predictions for α. In the following we propose an explanation for the disagreement between the ChPT result and experimental data. Our findings substantiate the dispersive result [74], and we are confident that it leads to a better understanding of the nature of the final-state interactions.

It is worthwhile at this point to quote the ChPT decay amplitudes at leading order p^2 and up to next-to-leading order in the isospin-breaking parameters $m_d - m_u$ and e^2. For the

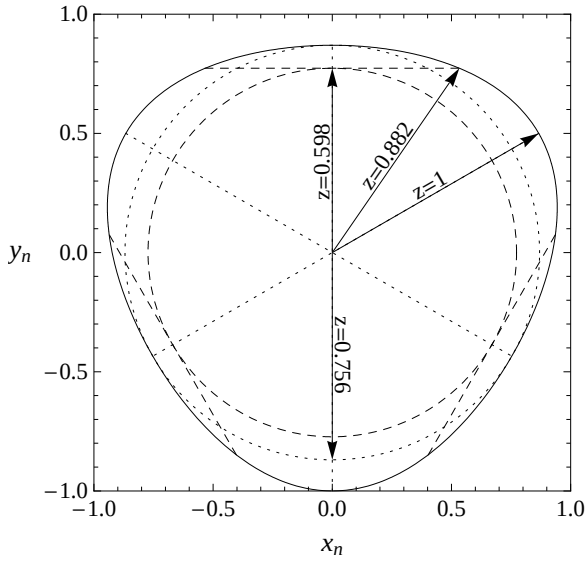

Figure 2.1: Boundary of the $\eta \to 3\pi^0$ Dalitz plot. Dotted: symmetry axes and biggest enclosed circle. Dashed: cusps at $s_i = 4M_\pi^2$ and corresponding circle. Arrows: indicating specific z values (see text for details).

charged and neutral decay, respectively, they read [62] (we use the Condon–Shortley phase convention throughout)

$$\begin{aligned} \mathcal{M}_c^{\mathrm{LO}}(s_1, s_2, s_3) &= \frac{B_0(m_d - m_u)}{3\sqrt{3}F_\pi^2}\left\{1 + \frac{3(s_3 - s_n)}{M_\eta^2 - M_{\pi^0}^2}\right\} , \\ \mathcal{M}_n^{\mathrm{LO}}(s_1, s_2, s_3) &= -\frac{B_0(m_d - m_u)}{\sqrt{3}F_\pi^2} , \end{aligned} \tag{2.7}$$

where $F_\pi = 92.2$ MeV is the pion decay constant, and B_0 is linked to the quark condensate in the (SU(3)) chiral limit in the standard manner. Equation (2.7) shows the isospin-violating nature of the decay, as both leading-order amplitudes are explicitly of order $m_d - m_u$. At that order in isospin breaking, the $\eta \to 3\pi$ amplitudes fulfill the well-known $\Delta I = 1$ relation

$$\mathcal{M}_n(s_1, s_2, s_3) = -\mathcal{M}_c(s_1, s_2, s_3) - \mathcal{M}_c(s_2, s_3, s_1) - \mathcal{M}_c(s_3, s_1, s_2) , \tag{2.8}$$

which can be easily checked in Eq. (2.7). This relation even holds in general at leading order in the isospin-breaking parameters, i.e. also for terms of $\mathcal{O}(e^2)$ [61], and is only violated at $\mathcal{O}((m_d - m_u)e^2)$ [62]. In the following, we will often adopt a loose way of talking and speak about the *isospin limit* for the charged and neutral $\eta \to 3\pi$ amplitudes; this only refers to the approximation in which the relation Eq. (2.8) holds, in particular $M_{\pi^0} = M_\pi$, and *not* to the limit $m_u = m_d$, where the decay $\eta \to 3\pi$ is (almost) forbidden.

Note furthermore that all contributions involving $\Delta_\pi = M_\pi^2 - M_{\pi^0}^2 = \mathcal{O}(e^2)$ in the charged decay amplitude have been absorbed by writing Eq. (2.7) in terms of s_n. This motivates an expansion of the decay amplitudes of *both* channels around the point $s_3 = s_n$, $s_1 = s_2$: we anticipate that, defined this way, higher-order isospin-breaking corrections to the $\Delta I = 1$ rule for the normalization of the amplitude are going to be of chiral order p^4, without contributions from the tree-level amplitudes Eq. (2.7), and therefore small. This "center" of the Dalitz plot

Theory	α
ChPT $\mathcal{O}(p^4)$ [59]	$+0.013$
ChPT $\mathcal{O}(p^6)$ [60]	$+0.013 \pm 0.032$
Dispersive [74]	$-0.007 \ldots -0.014$
Experiment	α
Crystal Ball@BNL [63]	-0.031 ± 0.004
Crystal Barrel@LEAR [64]	-0.052 ± 0.020
GAMS-2000 [65]	-0.022 ± 0.023
KLOE [66]	$-0.0301 \pm 0.0035^{+0.0022}_{-0.0035}$
MAMI-B [67]	$-0.032 \pm 0.002 \pm 0.002$
MAMI-C [68]	-0.032 ± 0.003
SND [69]	$-0.010 \pm 0.021 \pm 0.010$
WASA@CELSIUS [70]	$-0.026 \pm 0.010 \pm 0.010$
WASA@COSY [71]	$-0.027 \pm 0.008 \pm 0.005$

Table 2.1: Theoretical predictions and experimental findings on the slope parameter α.

then corresponds to $s_1 = s_2 = s_3 = s_n$ and $x_n = y_n = z = 0$ in the neutral channel, but to $s_1 = s_2 = s_n + \Delta_\pi$, $s_3 = s_n$ or $x = 0$ and $y = \delta \neq 0$ in the charged case. The charged and neutral decay amplitudes then take the form

$$\begin{aligned}
\mathcal{M}_c(s_1,s_2,s_3) &= \tilde{\mathcal{N}}_c\Big\{1 + \tilde{a}(s_3-s_n) + \tilde{b}(s_3-s_n)^2 + \tilde{d}(s_1-s_2)^2 + \tilde{f}(s_3-s_n)^3 \\
&\quad + \tilde{g}(s_1-s_2)^2(s_3-s_n) + \ldots\Big\} \\
&= \mathcal{N}_c\Big\{1 + \bar{a}y + \bar{b}y^2 + \bar{d}x^2 + \bar{f}y^3 + \bar{g}x^2y + \ldots + \mathcal{O}\big((R_n - R_c)^2\big)\Big\}\,, \\
\mathcal{M}_n(s_1,s_2,s_3) &= \mathcal{N}_n\Big\{1 + \tilde{\alpha}\big[(s_1-s_n)^2 + (s_2-s_n)^2 + (s_3-s_n)^2\big] \\
&\quad + \tilde{\beta}\big[(s_1-s_n)^3 + (s_2-s_n)^3 + (s_3-s_n)^3\big] \\
&\quad + \tilde{\gamma}\big[(s_1-s_n)^4 + (s_2-s_n)^4 + (s_3-s_n)^4\big] + \ldots\Big\} \\
&= \mathcal{N}_n\Big\{1 + \bar{\alpha}z + \bar{\beta}z^{3/2}\sin(3\phi) + \bar{\gamma}z^2 + \ldots\Big\}\,. \qquad (2.9)
\end{aligned}$$

The relations between the expansion parameters up to first order in isospin breaking are found to be

$$\begin{aligned}
&\mathcal{N}_c = \bar{\mathcal{N}}_c \times \tilde{\mathcal{N}}_c\,, \qquad \bar{\mathcal{N}}_c = 1 + \tilde{a}(R_n - R_c)\,, \\
&\bar{a} = -R_c\frac{\tilde{a} + 2(R_n - R_c)\tilde{b}}{\bar{\mathcal{N}}_c}\,, \quad \bar{b} = R_c^2\frac{\tilde{b} + 3(R_n - R_c)\tilde{f}}{\bar{\mathcal{N}}_c}\,, \quad \bar{d} = 3R_c^2\frac{\tilde{d} + \tilde{g}(R_n - R_c)}{\bar{\mathcal{N}}_c}\,, \\
&\bar{f} = -\frac{R_c^3\tilde{f}}{\bar{\mathcal{N}}_c}\,, \quad \bar{g} = -\frac{3R_c^3\tilde{g}}{\bar{\mathcal{N}}_c}\,, \quad \bar{\alpha} = \frac{3}{2}R_n^2\tilde{\alpha}\,, \quad \bar{\beta} = \frac{3}{4}R_n^3\tilde{\beta}\,, \quad \bar{\gamma} = \frac{9}{8}R_n^4\tilde{\gamma}\,. \qquad (2.10)
\end{aligned}$$

The expansion in powers of $R_n - R_c \simeq 3.35 \times 10^{-3}$ GeV^2 hinges on the fact that we have considered isospin breaking corrections in the definition of y (in the isospin limit, $R_n = R_c$,

we reproduce the results derived in Ref. [60]). The relations to the Dalitz plot parameters of the squared value of the respective amplitudes Eq. (2.6) are then easily shown to be

$$\begin{aligned} &a = 2\,\mathrm{Re}(\bar{a})\ , && b = |\bar{a}|^2 + 2\,\mathrm{Re}(\bar{b})\ , && d = 2\,\mathrm{Re}(\bar{d})\ , && f = 2\,\mathrm{Re}(\bar{a}\bar{b}^* + \bar{f})\ , \\ &g = 2\,\mathrm{Re}(\bar{a}\bar{d}^* + \bar{g})\ , && \alpha = \mathrm{Re}(\bar{\alpha})\ , && \beta = \mathrm{Re}(\bar{\beta})\ , && \gamma = \mathrm{Re}(\bar{\gamma})\ . \end{aligned} \tag{2.11}$$

The $\Delta I = 1$ rule Eq. (2.8) gives rise to relations between Dalitz plot parameters and normalizations of the neutral and the charged decay amplitude, namely

$$\mathcal{N}_n = -3\tilde{\mathcal{N}}_c\ , \qquad \tilde{\alpha} = \frac{1}{3}(\tilde{b} + 3\tilde{d})\ . \tag{2.12}$$

2.3 Modified non-relativistic effective field theory and $\eta \to 3\pi$

An analysis of $\eta \to 3\pi$ within the non-relativistic framework is useful for the following reasons. While the non-relativistic amplitude is perturbative, just as the chiral amplitude, it allows for a more accurate implementation of $\pi\pi$ interactions due to the inclusion of phenomenological threshold parameters as determined from Roy equations. Non-perturbative treatments, as for example dispersive analyses, are expected to yield yet more precise results. Compared to such numerically very involved studies, however, the NREFT calculation leads to a very transparent analytic representation. Moreover, it allows for the direct implementation of isospin breaking in particular in all kinematic effects, which is much more involved in ChPT and still in its infancy in dispersive analyses [85]. In that context it is useful to narrow down the precise definition of the term "non-relativistic" as it is used in our work.

Our representation of the decay amplitude is only non-relativistic in the sense that inelastic thresholds outside the physical region are subsumed into point-like effective coupling constants. Inside the physical region, however, we arrive at a fully covariant expression with the correct non-analytic low-energy behavior. The number of low-energy Dalitz plot couplings to be included in the Lagrangian at tree-level is modeled after the traditional (experimental) Dalitz plot expansion, which seems to yield a rather good description of the experimental data in the center of the Dalitz plot. We note again, see Section 2.2, that the *full* Dalitz plot is not accurately described by a polynomial expansion, since such a representation neglects non-analytic effects, such as cusps at the opening of the charged pion threshold (see also Refs. [26, 28, 62]).

In fact, the non-relativistic approach to $\eta \to 3\pi$ is not entirely new. In Ref. [28] the authors performed a fit to experimental data in an attempt to investigate the cusp effect in $\eta \to 3\pi^0$ generated at the opening of the charged pion threshold. The scope of our work is entirely different. We focus specifically on an analysis of the Dalitz plot parameters based on numerical input parameters derived from ChPT. For that endeavor the amplitudes are calculated to yet-higher accuracy in order to ensure the incorporation of the most prominent effects generated by the final-state interactions. In the following section we briefly report how the modified non-relativistic framework is applied to $\eta \to 3\pi$.

2.3.1 Power counting (1): specifics for $\eta \to 3\pi$

Let us review the power counting based on what we have observed in Section 1.1.1. We use the formal parameter ϵ and count as before

- pion 3-momenta in the η rest frame as $\mathcal{O}(\epsilon)$,

- kinetic energies $T_i = p_i^0 - M_i$ as $\mathcal{O}(\epsilon^2)$,
- masses of the particles involved as $\mathcal{O}(1)$, but now isospin breaking effects such as $\Delta_\pi = M_\pi^2 - M_{\pi^0}^2$ are counted as $\mathcal{O}(\epsilon^2)$,
- and the excess energy $Q_n = M_\eta - 3M_{\pi^0}$ and $Q_c = M_\eta - 2M_\pi - M_{\pi^0}$ as $\mathcal{O}(\epsilon^2)$.

Loop corrections in the perturbative series involve $\pi\pi$ rescattering at not-too-high energies, which can be related to the effective range expansion of the $\pi\pi$ amplitude. Since these effective range parameters are phenomenologically small, we use them as an additional power counting parameter, referred to generically as $a_{\pi\pi}$. We thus have a correlated expansion in $a_{\pi\pi}$ and ϵ and can uniquely assign powers to our loop expansion (see also Refs. [25–27, 33]).

2.3.2 Non-relativistic Lagragian and tree-level amplitudes

In this section we provide the non-relativistic Lagrangian that is required for the calculations performed in this work. These results have previously been reported in Ref. [26]. The full Lagrangian for the process is composed of a direct $\eta \to 3\pi$ part and $\pi\pi$ final-state interactions. We start off by displaying the $\eta \to 3\pi$ Lagrangian,

$$\begin{aligned}\mathcal{L}_\eta = {} & 2\eta^\dagger W_\eta (i\partial_t - W_\eta)\eta + L_0\big(K^\dagger \Phi_0\Phi_+\Phi_- + h.c.\big) \\ & + L_1\big(\eta^\dagger (W_0 - M_{\pi^0})\Phi_0\Phi_+\Phi_- + h.c.\big) + L_2\big(\eta^\dagger (W_0 - M_{\pi^0})\Phi_0\Phi_+\Phi_- + h.c.\big) \\ & + L_3\big(\eta^\dagger \Phi_0 (W_\pm^2\Phi_+\Phi_- + \Phi_+ W_\pm^2\Phi_- - 2W_\pm\Phi_+ W_\pm\Phi_-) + h.c.\big) \\ & + \frac{1}{6}\big(\eta^\dagger\Phi_0^3 + h.c.\big) + \frac{1}{2}K_1\big(\eta^\dagger\Phi_0^2(W_0 - M_{\pi^0})^2\Phi_0 + h.c.\big) + \dots \ , \end{aligned} \tag{2.13}$$

where $W_i = \sqrt{M_i^2 - \Delta}$ and $\eta, \Phi_\pm, \Phi_0$ denote the non-relativistic fields of the η particle, the charged, and the neutral pion, respectively. The Lagrangian in Eq. (2.13) is an expansion valid up to $\mathcal{O}(\epsilon^4)$ in the counting scheme. It gives rise to the tree-level amplitudes

$$\begin{aligned}\mathcal{M}_n^{\text{tree}}(s_1,s_2,s_3) &= K_0 + K_1\Big[(p_1^0 - M_{\pi^0})^2 + (p_2^0 - M_{\pi^0})^2 + (p_3^0 - M_{\pi^0})^2\Big] + \mathcal{O}(\epsilon^6) \ , \\ \mathcal{M}_c^{\text{tree}}(s_1,s_2,s_3) &= L_0 + L_1(p_3^0 - M_{\pi^0}) + L_2(p_3^0 - M_{\pi^0})^2 + L_3(p_1^0 - p_2^0)^2 + \mathcal{O}(\epsilon^6) \ , \end{aligned} \tag{2.14}$$

where the low-energy couplings K_i, L_i are of $\mathcal{O}(1)$ and are related to the traditional Dalitz plot, see Section 2.3.4. The isospin relation Eq. (2.8) translates into

$$K_0 = -(3L_0 + L_1 Q_n - L_3 Q_n^2) \ , \qquad K_1 = -(L_2 + 3L_3) \ . \tag{2.15}$$

The number of constants included here corresponds to expanding the Dalitz plot up to quadratic order; we briefly comment on the possible inclusion of cubic terms at tree level in Section 2.4.2. We remark that the number of four independent tree-level couplings (in the isospin limit) chosen here equals the number of subtraction constants in several of the dispersive analyses [75, 76] (compare Refs. [77, 78], though).

Similarly, the Lagrangian for $\pi\pi$ finals-state interactions can be determined. We consider the following final-state processes (i) ($\pi^a\pi^b \to \pi^c\pi^d$): (00) (00; 00), (+0) (+0; +0), (x) (+−; 00), and (+−) (+−; +−). The Lagrangian can be displayed as

$$\mathcal{L}_{\pi\pi} = 2\sum_\pm \Phi_\pm^\dagger W_\pm\big(i\partial_t - W_\pm\big)\Phi_\pm + 2\Phi_0^\dagger W_0(i\partial_t - W_0)\Phi_0 + \sum_{i=(00),\dots,(+-)} \mathcal{L}_i \ , \tag{2.16}$$

and upon introducing the notations

$$
\begin{aligned}
&(\Phi_n)_\mu = (\mathcal{P}_n)_\mu \Phi_n \ , \qquad (\Phi_n)_{\mu\nu} = (\mathcal{P}_n)_\mu (\mathcal{P}_n)_\nu \Phi_n \ , \qquad (\mathcal{P}_n)_\mu = (W_n, -i\nabla) \ , \\
&(\Phi_n^\dagger)_\mu = (\mathcal{P}_n^\dagger)_\mu \Phi_n^\dagger \ , \qquad (\Phi_n^\dagger)_{\mu\nu} = (\mathcal{P}_n^\dagger)_\mu (\mathcal{P}_n^\dagger)_\nu \Phi_n^\dagger \ , \qquad (\mathcal{P}_n^\dagger)_\mu = (W_n, i\nabla) \ ,
\end{aligned} \tag{2.17}
$$

for $n = a,\ b,\ c,\ d$, one finds

$$
\begin{aligned}
\mathcal{L}_i &= x_i C_i \Big\{ \Phi_c^\dagger \Phi_d^\dagger \Phi_a \Phi_b + h.c. \Big\} \\
&+ x_i D_i \Big\{ (\Phi_c^\dagger)_\mu (\Phi_d^\dagger)^\mu \Phi_a \Phi_b + \Phi_c^\dagger \Phi_d^\dagger (\Phi_a)_\mu (\Phi_b)^\mu - h_i \Phi_c^\dagger \Phi_d^\dagger \Phi_a \Phi_b + h.c. \Big\} \\
&+ \frac{u_i E_i}{2} \Big\{ \big(\Phi_c^\dagger (\Phi_d^\dagger)^\mu - (\Phi_c^\dagger)^\mu \Phi_d^\dagger \big) \big((\Phi_a)_\mu \Phi_b \big) - \Phi_a (\Phi_b)_\mu \big) + h.c. \Big\} \\
&+ x_i F_i \Big\{ (\Phi_c^\dagger)_{\mu\nu} (\Phi_d^\dagger)^{\mu\nu} \Phi_a \Phi_b + \Phi_c^\dagger \Phi_d^\dagger (\Phi_a)_{\mu\nu} (\Phi_b)^{\mu\nu} \\
&\quad + 2 (\Phi_c^\dagger)_\mu (\Phi_d^\dagger)^\mu (\Phi_a)_\nu (\Phi_b)^\nu + h_i^2 \Phi_c^\dagger \Phi_d^\dagger \Phi_a \Phi_b \\
&\quad - 2 h_i \big((\Phi_c^\dagger)_\mu (\Phi_d^\dagger)^\mu \Phi_a \Phi_b + \Phi_c^\dagger \Phi_d^\dagger (\Phi_a)_\mu (\Phi_b)^\mu \big) + h.c. \Big\} + \dots \ ,
\end{aligned} \tag{2.18}
$$

where $h_i = s_i^{\rm thr} - \frac{1}{2}(M_a^2 + M_b^2 + M_c^2 + M_d^2)$, and $s_i^{\rm thr}$ denotes the threshold of the pertinent channel, $s_{00}^{\rm thr} = 4M_{\pi^0}^2$, $s_{+0}^{\rm thr} = (M_{\pi^0} + M_\pi)^2$, $s_x^{\rm thr} = 4M_\pi^2$, $s_{+-}^{\rm thr} = 4M_\pi^2$. The combinatorial factors are given as $x_{00} = 1/4$, $x_{+0} = x_x = x_{+-} = 1$, $u_{00} = u_x = 0$, $u_{+0} = u_{+-} = 1$. The expansion is valid up-to-and-including $\mathcal{O}(\epsilon^4)$ in the S wave and $\mathcal{O}(\epsilon^2)$ in the P and D waves. From Eq. (2.18) we can derive the threshold expansion of the amplitudes up to $\mathcal{O}(a_{\pi\pi}^2 \epsilon^2)$ in the respective channels as

$$
\begin{aligned}
{\rm Re}\, T_{NR}^{00} &= 2C_{00} + 2D_{00}(s - s_{00}^{\rm thr}) + 2F_{00}(s - s_{00}^{\rm thr})^2 + 4C_x^2 J_{+-}(s) + \dots \ , \\
{\rm Re}\, T_{NR}^{x} &= 2C_x + 2D_x(s - s_x^{\rm thr}) + 2F_x(s - s_x^{\rm thr})^2 + \dots \ , \\
{\rm Re}\, T_{NR}^{+0} &= 2C_{+0} + 2D_{+0}(s - s_{+0}^{\rm thr}) + 2F_{+0}(s - s_{+0}^{\rm thr})^2 - E_{+0}(t-u) + \dots \ , \\
{\rm Re}\, T_{NR}^{+-} &= 2C_{+-} + 2D_{+-}(s - s_{+-}^{\rm thr}) + 2F_{+-}(s - s_{+-}^{\rm thr})^2 - E_{+-}(t-u) + \dots \ .
\end{aligned} \tag{2.19}
$$

The one-loop function of the non-relativistic theory,

$$
J_{+-}(s) = \frac{i}{16\pi} \sqrt{1 - \frac{4M_\pi^2}{s}} \ , \tag{2.20}
$$

is responsible for a cusp structure in the (00)-channel (see Refs. [25,86] and Appendix A.1 for further details). The low-energy couplings are matched to the effective range expansion in the following section.

2.3.3 Matching (1): $\pi\pi$ scattering

We want to make more sense of the low-energy couplings introduced in the previous section. To determine the matching relations for the low-energy constants of $\pi\pi$ scattering, we resort to the effective range expansion of the $\pi\pi \to \pi\pi$ scattering amplitude, which is conventionally decomposed into partial waves according to

$$
\mathcal{T}_I(s,t) = 32\pi \sum_\ell (2l+1) t_\ell^I(s) P_\ell(z) \ , \tag{2.21}
$$

where $t_\ell^I(s)$ is the partial wave amplitude of angular momentum ℓ and isospin I, $P_\ell(z)$ are the Legendre polynomials, and $z = \cos\theta$ is the cosine of the scattering angle in the center-of-mass system. Close to threshold the partial wave amplitude can be expanded in terms of the center-of-mass momentum $q^2 \doteq q^2(s) = (s - 4M_\pi^2)/4$, leading to

$$\mathrm{Re}\, t_\ell^I(s) = q^{2l}\{a_\ell^I + b_\ell^I q^2 + c_\ell^I q^4 + \mathcal{O}(q^6)\} \ , \tag{2.22}$$

where a_ℓ^I is the scattering length, b_ℓ^I is the effective range, and c_ℓ^I is the (leading) shape parameter. In the following we use the simplified notation a_I, b_I, c_I, as only S- and P-waves will be considered. In the language of NREFT power counting the previous equation is an expansion in orders of ϵ, since $q^2 \propto \epsilon^2$. The effective range expansion is thus naturally related to the non-relativistic $\pi\pi$ scattering amplitude in Eq. (2.19), and we can read off the matching relations for the low-energy couplings, shown here for simplicity in the isospin limit:

$$\begin{aligned}
C_{00} &= \frac{16\pi}{3}(a_0 + 2a_2) \ , & D_{00} &= \frac{4\pi}{3}(b_0 + 2b_2) \ , & F_{00} &= \frac{\pi}{3}(c_0 + 2c_2) \ , & \\
C_x &= \frac{16\pi}{3}(-a_0 + a_2) \ , & D_x &= \frac{4\pi}{3}(-b_0 + b_2) \ , & F_x &= \frac{\pi}{3}(-c_0 + c_2) \ , & \\
C_{+0} &= 8\pi a_2 \ , & D_{+0} &= 2\pi b_2 \ , & F_{+0} &= \frac{\pi}{2}c_2 \ , & E_{+0} &= 12\pi a_1 \ , \\
C_{+-} &= \frac{8\pi}{3}(2a_0 + a_2) \ , & D_{+-} &= \frac{2\pi}{3}(2b_0 + b_2) \ , & F_{+-} &= \frac{\pi}{6}(2c_0 + c_2) \ , & E_{+-} &= 12\pi a_1 \ .
\end{aligned} \tag{2.23}$$

Isospin-breaking corrections to these matching relations are discussed in Appendix A.2.1. Note that Eq. (2.23) is only valid up to $\mathcal{O}(a_{\pi\pi}^2)$, i.e. $\pi\pi$ scattering to one loop, or $\eta \to 3\pi$ to two loops. At higher loop orders, the low-energy couplings D_i and F_i are renormalized, which we will briefly discuss in the context of higher-loop resummation at the end of Section 2.4.1.

We will use two sets of phenomenological values for the $\pi\pi$ effective range parameters, the combined Roy equation plus ChPT analysis of Refs. [37, 44] (henceforth denoted by ACGL) and a combination of forward dispersion relations and Roy equations [40] (KPY). The central or "best" values for S- and P-wave scattering lengths and effective ranges as obtained in those two analyses are quoted in Table 2.2. The determination of the shape parameters is a little more delicate. We use the respective parameterizations of the phase shifts given in Refs. [37,40] and calculate the scattering amplitude according to

$$\mathrm{Re}\, t_0^I(q^2) = \left(1 + \frac{M_\pi^2}{q^2}\right)^{1/2} \frac{\tan\delta_I}{1 + \tan^2\delta_I} \ , \qquad I = 0,\, 2 \ . \tag{2.24}$$

Since the shape parameters are numerically very small in comparison to effective ranges and scattering lengths, they are rather sensitive to the method by which they are determined. For example, one receives rather different results when extracting the shape parameter from a strict threshold expansion of the amplitude, or from a fit over a certain low-energy range, minimizing the χ^2-function

$$\chi^2(c_I) = \left(\mathrm{Re}\, t_0^I(q^2) - a_I - b_I q^2 - c_I q^4\right)^2 \ , \tag{2.25}$$

in a range from the threshold $4M_\pi^2$ up to the expansion point s_n. Furthermore, the inclusion of an additional term $d_I q^6$ causes significant deviations in the $I = 0$ channel, since this term and the leading shape parameter are of comparable size. We decide to use the central values

	ACGL	KPY
a_0	0.220	0.223
a_2	−0.0444	−0.0444
$b_0 \times M_\pi^2$	0.276	0.290
$b_2 \times M_\pi^2$	−0.0803	−0.081
$c_0 \times 10^2 M_\pi^4$	−0.19	0.04
$c_2 \times 10^2 M_\pi^4$	1.33	0.68
$a_1 \times 10 M_\pi^2$	0.379	0.381
$b_1 \times 10^2 M_\pi^4$	0.567	0.512

Table 2.2: Input values for the scattering lengths a_I, effective ranges b_I, and shape parameters c_I as determined from the two parameterizations ACGL [37, 44] and KPY [40] (see text for discussion).

obtained from the minimization of Eq. (2.25) as the most reasonable approximation to the true partial wave. The numerical results for $c_{0,2}$ thus obtained are also given in Table 2.2. In the following, we use the variation between the central values of the two parameterizations [37, 40] as a means to estimate the uncertainty due to $\pi\pi$ rescattering.

2.3.4 Matching (2): $\eta \to 3\pi$

We compare Eqs. (2.9) and (2.14) to derive the matching relation between the low-energy couplings of the $\eta \to 3\pi$ tree amplitude and the traditional Dalitz plot parameterization, namely

$$\begin{aligned} K_0 &= \tilde{\mathcal{N}}_n^{\text{tree}} \left(1 - 3\tilde{\alpha}^{\text{tree}} R_n^2\right) , & K_1 &= 4\tilde{\mathcal{N}}_n^{\text{tree}} M_\eta^2 \tilde{\alpha}^{\text{tree}}, \\ L_0 &= \tilde{\mathcal{N}}_c^{\text{tree}} (1 + \tilde{a}^{\text{tree}} R_n + \tilde{b}^{\text{tree}} R_n^2) , & L_1 &= -2\tilde{\mathcal{N}}_c^{\text{tree}} M_\eta (\tilde{a}^{\text{tree}} + 2\tilde{b}^{\text{tree}} R_n) , \\ L_2 &= 4\tilde{\mathcal{N}}_c^{\text{tree}} M_\eta^2 \tilde{b}^{\text{tree}} , & L_3 &= 4\tilde{\mathcal{N}}_c^{\text{tree}} M_\eta^2 \tilde{d}^{\text{tree}} , \end{aligned} \tag{2.26}$$

where the superscript "tree" denotes tree-level input parameters. Note that Eq. (2.26) fulfills the isospin relation Eq. (2.15) as long as Eq. (2.12) is satisfied. To extract the Dalitz plot parameters in the non-relativistic framework, we have to fix the numerical input for the tree-level low-energy couplings for the $\eta \to 3\pi$ amplitude. We determine the low-energy couplings of the Dalitz plot in Eq. (2.26) by matching the non-relativistic framework to the one-loop ChPT amplitude [59] at the center of the Dalitz plot. Following Ref. [62], we evaluate the chiral $\eta \to 3\pi$ amplitude using *neutral* masses everywhere.

We remark that the upcoming [76] (and previous [75]) dispersive analyses use the Adler zero of the $\eta \to \pi^+\pi^-\pi^0$ amplitude as the matching point, compare Eq. (2.7). It is protected by SU(2) symmetry and therefore not prone to large strange-quark-mass corrections. The chiral series is thus expected to converge rather quickly, which makes the Adler zero a natural choice. The fact that it lies outside the physical region at roughly $s_A \approx \frac{4}{3} M_\pi^2$, however, renders matching the non-relativistic framework to the chiral amplitude at this point ill-fated: the expansion in terms of ϵ does not necessarily converge there, and we therefore have to resort to matching inside the Dalitz plot.

For the matching procedure we tune the rescattering parameters in the non-relativistic amplitude in such a way as to mimic the chiral amplitude. In essence this means that the scattering lengths and effective ranges are fixed at their current algebra values (this corresponds to the insertion of $\mathcal{O}(p^2)$ vertices in the chiral expansion). Explicitly, we have

$$\begin{aligned} a_0^{\mathrm{CA}} &= \frac{7M_\pi^2}{32\pi F_\pi^2} , & a_2^{\mathrm{CA}} &= -\frac{M_\pi^2}{16\pi F_\pi^2} , & a_1^{\mathrm{CA}} &= \frac{1}{24\pi F_\pi^2} , \\ b_0^{\mathrm{CA}} &= \frac{1}{4\pi F_\pi^2} , & b_2^{\mathrm{CA}} &= -\frac{1}{8\pi F_\pi^2} . \end{aligned} \tag{2.27}$$

We proceed analogously with the $\eta \to 3\pi$ couplings that enter the non-relativistic amplitude at one-loop level and derive from Eq. (2.7)

$$\tilde{\mathcal{N}}_c^{\mathrm{LO}} = -\frac{(M_\eta^2 - M_\pi^2)(M_\pi^2 + 3M_\eta^2)}{16\mathcal{Q}^2\sqrt{3}F_\pi^2 M_\pi^2} , \qquad \tilde{a}^{\mathrm{LO}} = \frac{3}{M_\eta^2 - M_\pi^2} . \tag{2.28}$$

For our numerical analysis we will use the value for $\mathcal{Q}$ dictated by Dashen's theorem, $\mathcal{Q}_D = 24.2$. Note that the specific choice does not hold any ramifications for our main statements, since it merely enters in the normalization, which drops out in the Dalitz plot parameters.

The above matching procedure is consistent as it ensures that the imaginary parts are exclusively generated by $\pi\pi$ final-state interactions. Residual effects from the chiral pion loops are purely real and absorbed in the low-energy couplings. We use matching to $\mathcal{O}(p^4)$ and not to $\mathcal{O}(p^6)$ for practical reasons: the above matching procedure is simpler and our results can be used to compare with and interpret the dispersive analyses directly. A high-precision determination of the Dalitz plot parameters would likely require matching to $\mathcal{O}(p^6)$, but for that purpose the low-energy constants showing up at $\mathcal{O}(p^6)$ may not be known with sufficient accuracy. Numerically we obtain from matching to the ChPT amplitude at $\mathcal{O}(p^4)$ (using the chiral SU(3) low-energy constant[#2] $L_3^{\mathrm{r}} = -3.5 \times 10^{-3}$ [19])

$$\begin{aligned} \tilde{\mathcal{N}}_c^{\mathrm{tree}} &= -0.158 , & \tilde{a}^{\mathrm{tree}} &= 13.428\ \mathrm{GeV}^{-2} , \\ \tilde{b}^{\mathrm{tree}} &= -7.291\ \mathrm{GeV}^{-4} , & \tilde{d}^{\mathrm{tree}} &= 5.189\ \mathrm{GeV}^{-4} . \end{aligned} \tag{2.29}$$

The particle masses used throughout this analysis are given by the current particle data group values [87], i.e. $M_\pi = 139.57$ MeV, $M_{\pi^0} = 134.98$ MeV, and $M_\eta = 547.86$ MeV.

2.3.5 Power counting (2): loops and $\eta \to 3\pi$

The power counting scheme discussed in Section 2.3.1 gives rise to a natural decomposition of the NREFT amplitude. This can be seen as follows. The modified non-relativistic propagator counts as $\mathcal{O}(\epsilon^{-2})$ (see e.g. Ref. [25]), the loop integration measure (with one energy and three momentum integration variables) as ϵ^5, therefore any loop integral with two-body rescattering contributes at $\mathcal{O}(\epsilon)$. Moreover, such a loop always involves a $\pi\pi$ rescattering vertex and is thus of $\mathcal{O}(a_{\pi\pi})$. The decomposition of the full $\eta \to 3\pi$ amplitude according to its loop-structure,

$$\mathcal{M}_{n/c}(s_1, s_2, s_3) = \mathcal{M}_{n/c}^{\text{tree}}(s_1, s_2, s_3) + \mathcal{M}_{n/c}^{\text{1-loop}}(s_1, s_2, s_3) + \mathcal{M}_{n/c}^{\text{2-loop}}(s_1, s_2, s_3) + \dots , \tag{2.30}$$

[#2] The effects of varying L_3^{r} within its error were checked to be tiny compared to other uncertainties. We therefore only use the central value.

is thus an expansion in powers of $a_{\pi\pi}\epsilon$. There is an interesting simplification of Eq. (2.30) close to the center of the Dalitz plot ($s_1 \approx s_2$, $s_3 \approx s_n$) above all two-pion thresholds. The contribution of the one-loop function is purely imaginary as can be seen from Eq. (2.20). At the same time the two-loop bubble diagram, which is the product of two one-loop functions, is purely real and it can be shown that the imaginary part of the non-trivial two-loop function does not contribute at this order (see Appendix A.1 and Refs. [25, 26]). Symbolically we can write both amplitudes in terms of the power counting parameter $a_{\pi\pi}$,

$$\mathcal{M} = \mathcal{M}_{\text{tree}} + i\mathcal{M}_{\text{1-loop}}a_{\pi\pi} + \mathcal{M}_{\text{2-loop}}a_{\pi\pi}^2 + \mathcal{O}(ia_{\pi\pi}^3\epsilon^3, ia_{\pi\pi}^2\epsilon^4) \ , \tag{2.31}$$

where the $\mathcal{O}(ia_{\pi\pi}^2\epsilon^4)$ term stems from the three-particle cut at two-loop order, which is numerically small as discussed in Appendix A.4 and therefore neglected. By taking the absolute value squared we obtain

$$|\mathcal{M}|^2 = \mathcal{M}_{\text{tree}}^2 + (\mathcal{M}_{\text{1-loop}}^2 + \mathcal{M}_{\text{tree}} \times \mathcal{M}_{\text{2-loop}})a_{\pi\pi}^2 + \mathcal{O}(a_{\pi\pi}^4\epsilon^4, a_{\pi\pi}^3\epsilon^5) \ . \tag{2.32}$$

We therefore expect one- and two-loop effects to be of the same size at the center of the Dalitz plot, as only the two-loop contributions can interfere with the dominant tree terms there, and thus to impact the Dalitz plot parameters about equally.

The heightened importance of rescattering effects in Dalitz plot parameters is further substantiated by another observation. Consider the generic one-loop function of $\pi\pi$ rescattering in the non-relativistic theory expanded about the center of the Dalitz plot ($s = s_n$, we neglect isospin-breaking effects in the following discussion, so that $M_{\pi^0} = M_\pi$):

$$\begin{aligned} J(s) &= \frac{i\sqrt{1-\frac{4M_\pi^2}{s_n}}}{16\pi}\Big(1 + \frac{6M_\pi^2}{s_n}\frac{s-s_n}{M_\eta^2 - 9M_\pi^2} - \frac{18M_\pi^2(s_n - 3M_\pi^2)}{s_n^2}\Big(\frac{s-s_n}{M_\eta^2-9M_\pi^2}\Big)^2 + \dots\Big) \\ &= \mathcal{O}(\epsilon) \ , \end{aligned} \tag{2.33}$$

since $s - s_n = \mathcal{O}(\epsilon^2)$ and $M_\eta - 3M_\pi = \mathcal{O}(\epsilon^2)$. The same holds true for the two-loop functions. This implies that contributions to higher-order Dalitz plot parameters from the loop functions are enhanced non-analytically in $M_\eta - 3M_\pi$. We conclude from Eq. (2.32)

$$\mathcal{M}_{\text{1-loop}}^2 + \mathcal{M}_{\text{tree}} \times \mathcal{M}_{\text{2-loop}} = \mathcal{O}(\epsilon^2) \ , \tag{2.34}$$

which has substantial consequences for the slope parameter α of the neutral decay channel. We can parametrize the slope parameter according to

$$\alpha = \alpha_0 + \alpha_2 a_{\pi\pi}^2 + \mathcal{O}(a_{\pi\pi}^4) \ . \tag{2.35}$$

From relations Eq. (2.26) we find $\tilde{\alpha}^{\text{tree}} = \mathcal{O}(1)$ and consequently the slope parameter at tree-level is of order $\alpha_0 \propto Q_n^2\tilde{\alpha}^{\text{tree}} = \mathcal{O}(\epsilon^4)$, whereas rescattering effects enter the slope parameter at $\mathcal{O}(a_{\pi\pi}^2\epsilon^2)$. This obviously implies that rescattering effects become increasingly more important for higher-order Dalitz plot parameters. On the other hand, they are far less significant (as we will confirm numerically below) for the normalization of the amplitude, for which we expect higher-order quark-mass renormalization effects to be more important.

The full NREFT representation beyond tree level with isospin breaking included is given in Appendix A.3. It comprises the loop graph topologies, displayed in Fig. 2.2 (see also Appendix A.1 for a detailed discussion), and is fully consistent in terms of non-relativistic

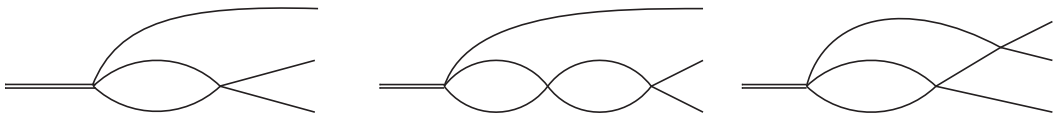

Figure 2.2: The Feynman graph topologies at one and two loops contributing to the decay $\eta \to 3\pi$ in NREFT. The double line denotes the η particle, the single lines stand for pions (of arbitrary charges).

power counting up-to-and-including $\mathcal{O}(a_{\pi\pi}^2\epsilon^4)$, i.e. the vertices of the two-loop graphs are included at $\mathcal{O}(\epsilon^2)$. Phenomenologically, one finds that the expansions of the $\eta \to 3\pi$ and $\pi\pi \to \pi\pi$ polynomials in powers of ϵ^2 only converge well starting from next-to-next-to-leading order, i.e. the $\mathcal{O}(\epsilon^2)$ terms (the linear slope in $\eta \to \pi^+\pi^-\pi^0$ and the $\pi\pi$ effective ranges) are not really suppressed compared to the leading (constant) terms. This observation is readily understood resorting to chiral perturbation theory: due to the Goldstone nature of the pions, the constant terms are chirally suppressed by powers of M_π^2 and the leading $\mathcal{O}(p^2)$ amplitudes are linear in energy s. In other words, the $\mathcal{O}(\epsilon^2)$ contributions are "suppressed" versus the constant ones by factors of s/M_π^2, and only starting from $\mathcal{O}(\epsilon^4)$, the relative suppression is s/Λ_χ^2 with $\Lambda_\chi \approx 1$ GeV. The chiral two-loop or $\mathcal{O}(p^6)$ calculation [60] contains all the leading $\mathcal{O}(p^2)$ vertices and therefore the linear $\eta \to 3\pi$ slope as well as effective ranges for the $\pi\pi$ interaction (although not quite the phenomenologically accurate ones). In order to guarantee that our NREFT representation of the decay amplitude is at least as accurate as the chiral two-loop one, we include all combinations of linear energy dependencies in the three vertices of the two-loop diagrams. Thus, our amplitude also contains terms that are of $\mathcal{O}(a_{\pi\pi}^2\epsilon^6)$ and $\mathcal{O}(a_{\pi\pi}^2\epsilon^8)$, and due to the enhancement discussed above, the numerically most important ones appearing at those orders. The representation of the "double bubbles" (see also Fig. 2.2) is even strictly complete up to $\mathcal{O}(a_{\pi\pi}^2\epsilon^6)$, as P-wave contributions only start at $\mathcal{O}(a_{\pi\pi}^2\epsilon^8)$. Furthermore, we have added shape parameter terms in the "double bubbles" and in the outer vertex of the irreducible two-loop graph, where the addition of these terms is trivial.

2.4 The isospin limit

We first give an analytic and numerical treatment of the amplitude in the isospin limit, which we *define* as $M_{\pi^0} = M_\pi$ and using Eq. (2.15). This already includes the gross features of our total analysis. However, in the isospin limit, we can give relatively simple closed analytic expressions for all parts of the amplitudes up to two loops.

2.4.1 Structure of the amplitude

The non-relativistic decay amplitude (for the charged channel) can be split into parts consisting of tree and final-state contributions

$$\mathcal{M}_c(s_1,s_2,s_3) = \mathcal{M}_c^{\text{tree}}(s_1,s_2,s_3) + \mathcal{M}_c^{\text{fsi}}(s_1,s_2,s_3)\ , \tag{2.36}$$

where the tree amplitude is given by

$$\mathcal{M}_c^{\text{tree}}(s_1,s_2,s_3) = \tilde{\mathcal{N}}_c^{\text{tree}}\Big\{1 + \tilde{a}^{\text{tree}}(s_3-s_n) + \tilde{b}^{\text{tree}}(s_3-s_n)^2 + \tilde{d}^{\text{tree}}(s_1-s_2)^2\Big\}\ , \tag{2.37}$$

and the rescattering contributions of the amplitude can be decomposed up to $\mathcal{O}(p^8)$ according to the isospin structure of the final-state pions [75, 88, 89] (see also Section 3.3),

$$\begin{aligned}\mathcal{M}_c^{\text{fsi}}(s_1,s_2,s_3) = \mathcal{M}_0(s_3) + (s_3-s_1)\mathcal{M}_1(s_2) + (s_3-s_2)\mathcal{M}_1(s_1) \\ +\mathcal{M}_2(s_1) + \mathcal{M}_2(s_2) - \frac{2}{3}\mathcal{M}_2(s_3)\ ,\end{aligned} \tag{2.38}$$

where the index $I = 0, 1, 2$ of the function $M_I(s_i)$ denotes the total isospin of the respective kinematic channel. At $\mathcal{O}(a_{\pi\pi}^2\epsilon^4)$ (for details see Section 2.3.5) the isospin amplitudes are given as

$$\begin{aligned}
\mathcal{M}_0(s) &= \frac{5}{3}\Big\{\ell_0(s)J(s)\Big(1+16\pi a_0(s)J(s)\Big) \\
&\quad + \frac{32\pi}{3}\Bigg[\Big(\ell_0'(s)a_0(\tilde{s}) + 2\ell_2'(s)a_2(\tilde{s})\Big)F^{(0)}(s) + \Bigg(\frac{2L_1}{M_\eta}\Big(\frac{2}{5}a_0(\tilde{s}) - a_2(\tilde{s})\Big) - \ell_0'(s)b_0 \\
&\quad - 2\ell_2'(s)b_2\Bigg)\frac{M_\eta \mathbf{Q}^2}{2Q^0}F^{(1)}(s) - 2L_1\Big(\frac{2}{5}b_0 - b_2\Big)\frac{M_\eta\mathbf{Q}^4}{4{Q^0}^2}F^{(2)}(s)\Bigg]\Big\}16\pi a_0(s)\ , \\
\mathcal{M}_1(s) &= \Bigg\{-\frac{q^2\ell_1(s)}{M_\eta}J(s) + \frac{80\pi s}{M_\eta Q^0}\Bigg[\Big(\ell_0'(s)a_0(\tilde{s}) - \ell_2'(s)a_2(\tilde{s})\Big)\big(F^{(0)}(s) - 2F^{(1)}(s)\big) \\
&\quad + \Bigg(\frac{L_1}{M_\eta}\Big(\frac{4}{5}a_0(\tilde{s}) + a_2(\tilde{s})\Big) - \ell_0'(s)b_0 + \ell_2'(s)b_2\Bigg)\frac{M_\eta\mathbf{Q}^2}{2Q^0}\big(F^{(1)}(s) - 2F^{(2)}(s)\big) \\
&\quad - L_1\Big(\frac{4}{5}b_0 + b_2\Big)\frac{M_\eta\mathbf{Q}^4}{4{Q^0}^2}\big(F^{(2)}(s) - 2F^{(3)}(s)\big)\Bigg]\Bigg\}4\pi a_1(s)\ , \\
\mathcal{M}_2(s) &= \Bigg\{\ell_2(s)J(s)\big(1+16\pi a_2(s)J(s)\big) \\
&\quad + \frac{16\pi}{3}\Bigg[\Big(5\ell_0'(s)a_0(\tilde{s}) + \ell_2'(s)a_2(\tilde{s})\Big)F^{(0)}(s) + \Bigg(\frac{4L_1}{M_\eta}\Big(a_0(\tilde{s}) - \frac{a_2(\tilde{s})}{4}\Big) - 5\ell_0'(s)b_0 \\
&\quad - \ell_2'(s)b_2\Bigg)\frac{M_\eta\mathbf{Q}^2}{2Q^0}F^{(1)}(s) - 4L_1\Big(b_0 - \frac{b_2}{4}\Big)\frac{M_\eta\mathbf{Q}^4}{4{Q^0}^2}F^{(2)}(s)\Bigg]\Bigg\}16\pi a_2(s)\ ,
\end{aligned} \tag{2.39}$$

where the various polynomials are given by

$$\begin{aligned}
&\ell_0(s) = \frac{3}{5}\ell(s) + \frac{2}{5}\ell_2(s)\ , \quad \ell(s) = L_0 + L_1\left(p^0 - M_\pi\right) + L_2\left(p^0 - M_\pi\right)^2 + L_3\frac{4\mathbf{Q}^2}{3s}\,q^2\ , \\
&\ell_2(s) = L_0 + L_1\Big(\frac{Q^0}{2} - M_\pi\Big) + L_2\Bigg[\Big(\frac{Q^0}{2} - M_\pi\Big)^2 + \frac{\mathbf{Q}^2}{3s}\,q^2\Bigg] + L_3\Bigg[\Big(\frac{Q^0}{2} - p^0\Big)^2 + \frac{\mathbf{Q}^2}{3s}\,q^2\Bigg]\ , \\
&\ell_1(s) = L_1 + 2L_2\Big(\frac{Q^0}{2} - M_\pi\Big) + 2L_3\Big(p^0 - \frac{Q^0}{2}\Big)\ , \quad \ell_0'(s) = \frac{3}{5}\ell'(s) + \frac{2}{5}\ell_2'(s)\ , \\
&\ell'(s) = L_0 + L_1\Big(\frac{s}{2Q^0} - M_\pi\Big)\ , \quad \ell_2'(s) = L_0 + L_1\Big(\frac{M_\eta}{2} - M_\pi - \frac{s}{4Q^0}\Big)\ , \\
&a_I(s) = a_I + b_I q^2 + c_I q^4\ ,
\end{aligned} \tag{2.40}$$

and we use the kinematic variables

$$p^0 = \frac{M_\eta^2 + M_\pi^2 - s}{2M_\eta}\ , \quad Q^0 = \frac{M_\eta^2 - M_\pi^2 + s}{2M_\eta}\ , \quad \mathbf{Q}^2 = \frac{\lambda(M_\eta^2, M_\pi^2, s)}{4M_\eta^2}\ ,$$

$$\tilde{s} = 2M_\pi^2 - s + \frac{M_\eta}{Q^0}\left(s + 2\mathbf{Q}^2\right) \ , \tag{2.41}$$

with the Källén function $\lambda(x,y,z) = x^2 + y^2 + z^2 - 2(xy + xz + yz)$. Note that the shape parameter terms $\propto c_I$ are to be omitted in $a_I(\tilde{s})$; we also neglect them in the $I = 1$ partial wave. We use the shorthand expressions $J(s) \doteq J_{+-}(s)$ and $F^{(n)}(s) \doteq F_+^{(n)}(M_\pi, M_\pi, M_\pi, M_\pi, s)$ (in the isospin limit), where for the exact form of the two-loop functions we refer to Appendix A.3. We can now write the Dalitz plot parameters in terms of the isospin amplitudes, namely for the charged channel

$$\begin{aligned}
\mathcal{N}_c &= \tilde{\mathcal{N}}_c^{\text{tree}} + \mathcal{M}_0(s_n) + \frac{4}{3}\mathcal{M}_2(s_n) \ , \\
\bar{a} &= -\frac{R_c}{\mathcal{N}_c}\Big(\tilde{\mathcal{N}}_c^{\text{tree}}\tilde{a}^{\text{tree}} + \mathcal{M}_0^{(1)}(s_n) + 3\mathcal{M}_1(s_n) - \frac{5}{3}\mathcal{M}_2^{(1)}(s_n)\Big) \ , \\
\bar{b} &= \frac{R_c^2}{\mathcal{N}_c}\Big(\tilde{\mathcal{N}}_c^{\text{tree}}\tilde{b}^{\text{tree}} + \frac{1}{2}\mathcal{M}_0^{(2)}(s_n) - \frac{3}{2}\mathcal{M}_1^{(1)}(s_n) - \frac{1}{12}\mathcal{M}_2^{(2)}(s_n)\Big) \ , \\
\bar{d} &= \frac{3R_c^2}{\mathcal{N}_c}\Big(\tilde{\mathcal{N}}_c^{\text{tree}}\tilde{d}^{\text{tree}} + \frac{1}{2}\mathcal{M}_1^{(1)}(s_n) + \frac{1}{4}\mathcal{M}_2^{(2)}(s_n)\Big) \ , \\
\bar{f} &= -\frac{R_c^3}{\mathcal{N}_c}\Big(\frac{1}{6}\mathcal{M}_0^{(3)}(s_n) + \frac{3}{8}\mathcal{M}_1^{(2)}(s_n) - \frac{11}{72}\mathcal{M}_2^{(3)}(s_n)\Big) \ , \\
\bar{g} &= -\frac{3R_c^3}{8\mathcal{N}_c}\Big(\mathcal{M}_1^{(2)}(s_n) - \mathcal{M}_2^{(3)}(s_n)\Big) \ ,
\end{aligned} \tag{2.42}$$

and for the neutral channel

$$\begin{aligned}
\bar{\alpha} &= \frac{R_n^2}{4\mathcal{N}_c}\Big(2\tilde{\mathcal{N}}_c^{\text{tree}}\big(\tilde{b}^{\text{tree}} + 3\tilde{d}^{\text{tree}}\big) + \mathcal{M}_0^{(2)}(s_n) + \frac{4}{3}\mathcal{M}_2^{(2)}(s_n)\Big) \ , \\
\bar{\beta} &= \frac{R_n^3}{24\mathcal{N}_c}\Big(\mathcal{M}_0^{(3)}(s_n) + \frac{4}{3}\mathcal{M}_2^{(3)}(s_n)\Big) \ , \\
\bar{\gamma} &= \frac{R_n^4}{64\mathcal{N}_c}\Big(\mathcal{M}_0^{(4)}(s_n) + \frac{4}{3}\mathcal{M}_2^{(4)}(s_n)\Big) \ ,
\end{aligned} \tag{2.43}$$

where $\mathcal{M}_I^{(n)}(s_n)$ denotes the n-th derivative of the function $\mathcal{M}_I(s)$, evaluated at the center of the Dalitz plot. Note that $\bar{d}$ and $\bar{g}$ do not receive contributions from the isospin $I = 0$ amplitude.

Despite working in the limit of evaluating all amplitudes for the *charged* pion mass, we employ the physical values for R_c and R_n in Eqs. (2.42), (2.43). These prefactors stem from the conversion of $\tilde{a}$, $\tilde{\alpha}$ etc. into $\bar{a}$, $\bar{\alpha}$ etc., see Eq. (2.10), and are just due to a normalization choice in the definition of the Dalitz plot variables x and y; we therefore decide to present our results including this "trivial" isospin-breaking effect already at this stage. Note that due to $(M_\eta - 3M_{\pi^0})/(M_\eta - 3M_\pi) \approx 1.11$ and $(M_\eta - 2M_\pi - M_{\pi^0})/(M_\eta - 3M_\pi) \approx 1.04$, the effects of using these normalization factors in the isospin limit are large, most so for the neutral channel, where α for instance is affected by a shift of 22%.

In our numerical analysis we will observe that among the two-loop contributions those of the non-trivial two-loop graphs, see Fig. 2.2 (right), are in general strongly suppressed. This can be traced back to the isospin properties of these pieces: for those Dalitz plot parameters to which the $I = 0$ partial wave can contribute, it usually dominates. For those graphs

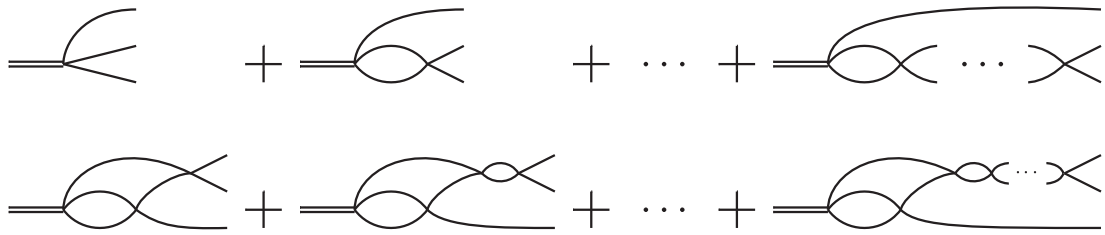

Figure 2.3: Diagrammatic expression of the resummed amplitudes. Above: the bubble chain. Below: resummed external vertex of the non-trivial two-loop graph. The line style is as in Fig. 2.2.

that only describe rescattering in one channel and can be written as simple products of one-loop functions, see Fig. 2.2 (middle), the $I = 0$ isospin amplitude receives contributions proportional to second powers of a_0, b_0, etc., whereas the "inner" vertex in the non-trivial two-loop contributions has parts of $I = 0$ and $I = 2$ (P-waves vanish due to symmetry reasons in the isospin limit) that tend to partially cancel each other.

In an attempt to estimate (partial) higher-order corrections, we therefore expect to find a good approximation to the full result by iterating the bubble diagrams and the exterior two-particle rescattering of the non-trivial two-loop function as depicted diagrammatically in Fig. 2.3. In the aforementioned representation the unitarized amplitudes are easily determined to be

$$\begin{aligned}
\mathcal{M}_0^{\mathrm{u}}(s) &= \frac{\mathcal{M}_0(s) - \frac{5}{3}\ell_0(s)\big(16\pi a_0(s)J(s)\big)^2}{1 - 16\pi a_0(s)J(s)} \,, \\
\mathcal{M}_1^{\mathrm{u}}(s) &= \frac{\mathcal{M}_1(s)}{1 - 16\pi a_1(s)q^2J(s)} \,, \\
\mathcal{M}_2^{\mathrm{u}}(s) &= \frac{\mathcal{M}_2(s) - \ell_2(s)\big(16\pi a_2(s)J(s)\big)^2}{1 - 16\pi a_2(s)J(s)} \,.
\end{aligned} \tag{2.44}$$

The inclusion of iterated diagrams requires modified matching relations for the effective range parameters. This becomes obvious when considering the expansion of the iterated bubble sum of $\pi\pi$ scattering of isospin $I = 0, 2$ at the $\pi\pi$ threshold:

$$\mathrm{Re}\Big[\frac{a_I(s)}{1 - 16\pi a_I(s)J(s)}\Big] = a_I + \Big(b_I - \frac{a_I^3}{M_\pi^2}\Big)q^2 + \Big(c_I + \frac{a_I^3 + a_I^5 - 3a_I^2 b_I M_\pi^2}{M_\pi^4}\Big)q^4 + \mathcal{O}(q^6) \,. \tag{2.45}$$

One immediately sees that the effective range picks up a contribution from two-loop diagrams, the shape parameter from two- and four-loop diagrams. To account for this shift, the above expression has to be compared with the effective range expansion of the $\pi\pi$ amplitude (for $l = 0$),

$$\mathrm{Re}\, t_0^I(q^2) = a_I + b_I q^2 + c_I q^4 + \mathcal{O}(q^6) \,, \qquad I = 0, 2 \,, \tag{2.46}$$

from which one reads off the following renormalization prescriptions:

$$a_I^{\mathrm{ren}} = a_I \,, \qquad b_I^{\mathrm{ren}} = b_I + \frac{a_I^3}{M_\pi^2} \,, \qquad c_I^{\mathrm{ren}} = c_I - \frac{a_I^3 - 2a_I^5 - 3a_I^2 b_I M_\pi^2}{M_\pi^4} \,. \tag{2.47}$$

	charged channel					
	$\lvert\mathcal{N}_c\rvert^2$	a	b	d	f	g
tree	0.0310	−1.306	0.393	0.071	0.022	−0.046
one-loop	0.0338	−1.450	0.580	0.085	−0.026	−0.078
two-loop*	0.0289	−1.288	0.334	0.093	0.078	−0.076
full two-loop	0.0287	−1.290	0.379	0.056	0.071	−0.045
unitarized	0.0284	−1.268	0.342	0.053	0.101	−0.042
	neutral channel					
	$\lvert\mathcal{N}_n\rvert^2$	α	β	γ		
tree	0.279	0.0107	0	0.0001		
one-loop	0.304	0.0227	0.0005	0.0000		
two-loop*	0.260	−0.0209	−0.0027	0.0007		
full two-loop	0.258	−0.0192	−0.0036	0.0009		
unitarized	0.255	−0.0249	−0.0043	0.0013		

Table 2.3: Results for the charged and neutral Dalitz plot parameters in the isospin limit. We show tree, one-loop, two-loop neglecting the irreducible two-loop graphs (marked "two-loop*"), and full two-loop results calculated as described in the text, plus the result employing the unitarized amplitudes according to Eq. (2.44).

The $a_I^{\rm ren}$, $b_I^{\rm ren}$, $c_I^{\rm ren}$ are now to be inserted into the matching relations for the coupling constants C_i, D_i, F_i. The renormalization prescriptions have pretty remarkable effects in the isospin $I = 0$ channel, where the shape parameter is shifted from $-0.002 M_\pi^{-4}$ to $+0.030 M_\pi^{-4}$ (for the ACGL parameter set). We note that the P-wave effective range b_1 does not pick up an additional contribution due to the $q^2(s)$ prefactor. Corrections in the P-wave channel start at $\mathcal{O}(\epsilon^8)$, that is the higher-order shape parameter d_1.

2.4.2 Numerical results

We begin our numerical analysis of the various $\eta \to 3\pi$ Dalitz plot parameters by investigating how the tree-level values are modified at one- and two-loop order, and finally beyond two loops (via the estimate through the unitarized amplitudes in Eq. (2.44)). This part of the analysis is based solely on the ACGL parameters for the $\pi\pi$ final-state interaction; the qualitative conclusions are identical for the KPY parameterization. We keep the $\eta \to 3\pi$ tree level parameters fixed as obtained by matching to ChPT at $\mathcal{O}(p^4)$ throughout, see Section 2.3.4. Our results are summarized in Table 2.3. In particular, we observe the following:

1. Individual loop corrections to the Dalitz plot parameters are sizable; their relative importance grows with increasing order (in ϵ) of the parameters concerned, as suggested a priori by power-counting arguments (see Section 2.3.5).

2. One- and two-loop contributions are in general of the same size, as indeed expected, with a tendency to cancel to varying extent due to contributions of opposite sign. This

again substantiates the power-counting arguments of the NREFT framework, which is particularly interesting in the case of α: while at one loop we see a sizable positive shift added to the already positive tree-level result, the two-loop correction overwhelms both, leading to a negative total. We therefore find the correct sign for α, as opposed to the ChPT result. At two loops our result is in fairly good agreement with the dispersive one from Ref. [74].

3. There are large contributions from derivative couplings at two-loop order. This is seen when considering the amplitude expanded only up to $\mathcal{O}(a_{\pi\pi}\epsilon^5, a_{\pi\pi}^2\epsilon^2)$ (cf. Ref. [26]), at which order only constant vertices are implemented at two loops. In this approximation, we find numerically e.g. $\alpha = +0.033$. Once the effective range corrections in the $I = 0$ two-loop bubble are added, α receives a shift to -0.017. This observation explains why the authors of Ref. [28] obtain a positive sign for α when matching to ChPT at tree-level: no derivative couplings at two-loop level are included in that work. With respect to this omission, matching to ChPT at tree-level plays a minor role in the deviation from our result.

4. By comparing the two-loop contributions with and without the parts due to the irreducible two-loop graphs, see Fig. 2.2 (right), we see that at least in those parameters that receive contributions from the $I = 0$ amplitude the irreducible two-loop graphs only give a very small contribution. As detailed before, this can be traced back to the isospin structure of the different amplitudes. Specifically α is a case in point: the simple "bubble sum" type two-loop graphs shift it by about -0.044, while the irreducible graphs only add $+0.002$.

5. Our estimate of higher-order effects via simple two-channel unitarization shows that those are significantly smaller than the (individual) one- and two-loop effects, although not negligible throughout. Due to the smallness of the irreducible two-loop graphs, we expect to catch the major part of the higher-order corrections in this way.

In order to study the dependence of our results on the precise input for $\pi\pi$ scattering, we next compare the values obtained for the various charged and neutral Dalitz plot parameters, at two loops and unitarized, for the ACGL and the KPY parameter sets in Table 2.4. In most cases, the variation with different $\pi\pi$ input is a bit smaller than the difference due to the higher-order estimates, although not by much. As our final result in the last column of Table 2.4, we determine central values and (symmetric) errors in such a way as to cover all four values for each parameter.

Our finding for the $\eta \to 3\pi^0$ slope parameter, $\alpha = -0.024 \pm 0.005$, is considerably closer to the current experimental average $\alpha = -0.0317 \pm 0.0016$ [87] than previous theoretical approaches. Note again that the theoretical prediction for α is lowered (in absolute value) by about 22% if the charged pion mass is used in the definition of z. We predict the (yet unmeasured) higher-order Dalitz plot parameters β and γ in the neutral channel to be different from zero, but very small. In particular, neglecting a term $\propto \gamma z^2$ in an experimental extraction of α based on the radial distribution $d\Gamma/dz$ alone (in which a term $\propto \beta$ cancels for $z < 0.756$, compare Fig. 2.1) should affect α by less than the value of γ, hence still below the current uncertainty, although not by much given the precision of the most recent experimental determinations.

As we will see below, there are sizable isospin-breaking shifts in the charged Dalitz plot parameters. We therefore defer a detailed comparison to experimental values to Section 2.5.

	ACGL 2-loop	ACGL unit.	KPY 2-loop	KPY unit.	average
$\lvert\mathcal{N}_c\rvert^2$	0.0287	0.0284	0.0285	0.0282	0.0284 ± 0.0002
a	-1.290	-1.268	-1.291	-1.267	-1.279 ± 0.012
b	0.379	0.342	0.382	0.340	0.361 ± 0.021
d	0.056	0.053	0.052	0.050	0.053 ± 0.003
f	0.071	0.101	0.073	0.107	0.089 ± 0.018
g	-0.045	-0.042	-0.043	-0.041	-0.043 ± 0.002
α	-0.0192	-0.0249	-0.0227	-0.0291	-0.0242 ± 0.0049
β	-0.0036	-0.0043	-0.0043	-0.0051	-0.0043 ± 0.0007
γ	0.0009	0.0013	0.0013	0.0017	0.0013 ± 0.0004

Table 2.4: Results for charged and neutral Dalitz plot parameters in the isospin limit with different input on $\pi\pi$ scattering parameters from Refs. [37] and [40]; see Section 2.3.3. Shown are the results both for two loops and for the unitarized amplitudes. $|\mathcal{N}_n|^2 = 9|\mathcal{N}_c|^2$ is not shown separately.

We only wish to make a remark on the cubic parameters f and g here. Apart from the fact that a large contribution to these is given by $2\mathrm{Re}(\bar{a}\bar{b}^*)$ and $2\mathrm{Re}(\bar{a}\bar{d}^*)$, respectively, the remainders (or $\bar{f}$, $\bar{g}$) are given entirely in terms of loop contributions. If we, in addition, allow for cubic tree level terms $\bar{f}^{\mathrm{tree}}$ and $\bar{g}^{\mathrm{tree}}$ and match the latter to ChPT at $\mathcal{O}(p^4)$, the total results receive shifts of -0.002 and -0.011 hence very and relatively small effects, respectively. Although chiral $\mathcal{O}(p^6)$ corrections might modify these numbers significantly, we still regard them as indications that the dominance of loop contributions (as suggested by ϵ power counting) holds here.

2.4.3 Comparison to α in ChPT at two loops

While dispersive analyses find values for α similar to ours [74], a serious puzzle is the question why the calculation of this quantity in ChPT to two loops [60] does not arrive at least at a negative value for α "naturally", i.e. as the central value (disregarding the large error bar due to the estimated fit uncertainty). After all, in addition to potentially significant chiral SU(3) renormalization effects of what would be subsumed in the tree-level couplings of the NREFT representation, ChPT at $\mathcal{O}(p^6)$ also includes all the pion two-loop graphs shown to be important here.

It turns out that this failure of the chiral two-loop calculation can partly be understood within our framework, investigating rescattering effects only, but of course neglecting the $\mathcal{O}(p^6)$ modified tree-level couplings. In order to mimic the chiral expansion, we note that in an $\mathcal{O}(p^6)$ calculation, the $\pi\pi$ vertices inside two-loop graphs are only included to their current-algebra (or $\mathcal{O}(p^2)$) accuracy, see Eq. (2.27), while inside the one-loop diagrams, $\pi\pi$ rescattering is taken care of up to $\mathcal{O}(p^4)$. By inserting the respective values for the $\pi\pi$ threshold parameters in our amplitude, we find

$$\alpha_{\mathrm{ChPT}} = -0.0011 \ , \tag{2.48}$$

hence a value close to zero. We attribute the remaining difference to the central result for α in Ref. [60] to different tree-level couplings as determined in that paper. As we found

that precisely the two-loop effects turn α negative, dominated by the $I = 0$ amplitude, we conclude that a large part of the discrepancy between ChPT at $\mathcal{O}(p^6)$ and our result (or the one from dispersion relations) is due to the significantly weaker $\pi\pi$ rescattering (compare e.g. $a_0^{\rm CA} \approx 0.16$ vs. $a_0 = 0.220$ from Ref. [37], which enters the two-loop effects squared). The precise choice of the set of rescattering parameters therefore has a large effect on the result for α (and, slightly less dramatically so, on other Dalitz plot parameters). The inclusion of improved values for the effective ranges and shape parameters produces a large shift of the chiral result towards the experimental value.

In a very condensed manner, we can therefore point to one specific diagram, Fig. 2.2 (middle), which accounts for roughly half of the discrepancy between the central value of the chiral prediction at $\mathcal{O}(p^6)$ and the experimental value for α. More specifically, the discrepancy is caused by contributions of the diagrammatic topology of this kind. Since (at least) next-to-leading order contributions to the $\pi\pi$ vertices are required, one needs to include these diagrams up to $\mathcal{O}(p^8)$ and higher in strict chiral power counting. To substantiate this claim and ensure that it is not an artifact of the non-relativistic framework, we replace the non-relativistic two-point function $J(s)$, Eq. (2.20), by its relativistic counterpart $\bar{J}_{\pi\pi}(s)$, which differs from the former by its real part (given explicitly in Eq. (A.63)). Doing so requires a different matching procedure to account for the (otherwise absent) mass renormalization effects on the various coupling constants thus induced; we will not spell out this exercise in detail. The main conclusion, however, is fully consistent with our findings above: the "double bubble" graphs alone shift α by -0.042 (to be compared with -0.044, see Table 2.3); calculating them with current algebra values for the $\pi\pi$ threshold parameters reduces this effect by nearly a factor of two, which corresponds to the discrepancy between Eq. (2.48) and the value obtained in NREFT.

One might argue that a parameter as subtle as α could also be subject to other very sizable $\mathcal{O}(p^6)$ corrections; in particular, contributions from chiral low-energy constants appear for the first time at that order. For a superficial impression of these effects, we investigate precisely the $\mathcal{O}(p^6)$ polynomial in the amplitude calculated in Ref. [60]. One easily finds the following combination of low-energy constants contributing to α:

$$\alpha_{\rm LEC}^{(6)} = \frac{12R_n^2}{F_\pi^4}\big(C_5^r + C_8^r + 3C_9^r + C_{10}^r - 2C_{12}^r + 2C_{22}^r + 3C_{24}^r + C_{25}^r\big) \ . \tag{2.49}$$

The couplings C_i^r are estimated in Ref. [60] using resonance saturation. Vector contributions cancel in Eq. (2.49), as they must, with no P-waves appearing in the neutral decay channel. Using the scalar resonance estimates given in Ref. [60], we arrive at the very simple and compact expression

$$\alpha_{\rm LEC}^{(6)} = \frac{12R_n^2 c_d c_m}{F_\pi^2 M_S^4} \approx 0.005 \ , \tag{2.50}$$

where $c_m = 0.042$ GeV, $c_d = 0.032$ GeV, and $M_S = 0.98$ GeV. There are serious doubts about the reliability of the resonance saturation hypothesis in the scalar sector [90]; indeed one might argue that the masses of even heavier scalar states ought to be used in Eq. (2.50), further suppressing their contribution to α. We nevertheless confirm that contributions from the ChPT low-energy polynomial at $\mathcal{O}(p^6)$ are rather small; in particular they have a positive sign, so they cannot serve as an alternative explanation to arrive at a negative α. We also emphasize that the above is only a very rough estimate of the expected size of the effects and does not by any means replace a consistent matching procedure.

2.5 Isospin breaking in $\eta \to 3\pi$

In this section we discuss higher-order isospin-breaking contributions to the decay $\eta \to 3\pi$. We concentrate on the following four contributions:

1. Isospin breaking in $\eta \to \pi^+\pi^-\pi^0$ due to $Q_n \neq Q_c$. There are significant corrections to the charged Dalitz plot parameters due to the terms $\propto (R_n - R_c)$ in Eq. (2.10), which stem from the subtleties in the definition of the center of the Dalitz plot discussed in Section 2.2.

2. Other isospin corrections due to the difference between the charged and the neutral pion mass. These in particular concern the incorporation of the correct thresholds inside the loop contributions, which is necessary for a description of the boundary regions of the Dalitz plot, among them the cusp effect in $\eta \to 3\pi^0$. The representation of the amplitude in the non-relativistic framework allows us to work in the particle (and not in the isospin) basis, and thus we can incorporate mass effects in a straightforward fashion.

3. Isospin-breaking corrections to the $\pi\pi$ rescattering parameters. We use the phenomenological values for the scattering lengths and effective ranges, which have been determined in the isospin limit [37, 40], and calculate corrections to each channel from the one-loop SU(2) $\pi\pi$-scattering amplitudes with electromagnetic corrections included.

4. Next-to-leading-order isospin-breaking effects in the $\eta \to 3\pi$ tree level couplings, calculated in one-loop ChPT, which modify Eqs. (2.12).

The representation of the NREFT amplitude to two loops with fully general masses and coupling constants, allowing for all of these isospin-breaking effects, is given in Appendix A.3.1. Furthermore Appendix A.3.2 shows the generalization of the unitarization prescription given in Eq. (2.44) for the case of isospin violation. In our numerical evaluation we will add these contributions cumulatively to the results of Section 2.4.

In this context we should comment on radiative (real- and virtual-photon) corrections to these decays. In order to be able to sensibly discuss a Dalitz plot expansion of the squared amplitudes in question, we assume that the universal radiative corrections (Gamow–Sommerfeld factor, bremsstrahlung contributions etc.), as discussed in the framework of NREFT in Ref. [27], have already been subtracted from the experimental data when determining Dalitz plot parameters. In order to extract the corrections of point 4 above from the calculation in Ref. [62], these subtracted contributions have to be matched correctly, as detailed in Appendix A.2.2. The non-universal or "internal" radiative corrections that play an important role in the analysis of the cusp effect in $K \to 3\pi$ [27, 91] do not have a similarly enhanced effect in the center of the Dalitz plot. From the point of view of chiral power counting of isospin-breaking corrections, these constitute higher-order effects than those considered consistently in Ref. [62] (as they only appear at two loops); furthermore, in $\eta \to \pi^+\pi^-\pi^0$, even diagrams beyond those calculated in Ref. [27] would have to be included. We have checked, though, that the effect of photon exchange inside the charged-pion loops on the $\eta \to 3\pi^0$ Dalitz plot expansion is small, even on the scale of the other small isospin-breaking effects discussed below.

The by far largest isospin-breaking effects on the Dalitz plot parameters, beyond the use of the correct overall normalization factors of Q_n and Q_c in the definitions of the kinematic variables that was already incorporated in the previous sections, are the kinematic effects due

	$Q_c \neq Q_n$	masses	$\pi\pi$	$\eta \to 3\pi^0$
$\lvert\mathcal{N}_c\rvert^2$	0.0310 ± 0.0003	0.0309 ± 0.0003	0.0310 ± 0.0003	0.0310 ± 0.0003
a	-1.218 ± 0.013	-1.214 ± 0.013	-1.214 ± 0.014	-1.213 ± 0.014
b	0.314 ± 0.023	0.310 ± 0.023	0.308 ± 0.023	0.308 ± 0.023
d	0.051 ± 0.003	0.051 ± 0.003	0.050 ± 0.003	0.050 ± 0.003
f	0.084 ± 0.019	0.082 ± 0.018	0.083 ± 0.019	0.083 ± 0.019
g	-0.039 ± 0.002	-0.039 ± 0.002	-0.039 ± 0.002	-0.039 ± 0.002
$\lvert\mathcal{N}_n\rvert^2$	0.256 ± 0.002	0.256 ± 0.002	0.255 ± 0.002	0.252 ± 0.008
α	-0.0242 ± 0.0049	-0.0241 ± 0.0049	-0.0247 ± 0.0048	-0.0246 ± 0.0049
β	-0.0043 ± 0.0007	-0.0043 ± 0.0008	-0.0042 ± 0.0007	-0.0042 ± 0.0007
γ	0.0013 ± 0.0004	0.0012 ± 0.0004	0.0013 ± 0.0004	0.0013 ± 0.0004

Table 2.5: Central results for the charged and neutral Dalitz plot parameters with isospin breaking in kinematic relations, masses in loop functions, $\pi\pi$ threshold parameters, and $\eta \to 3\pi^0$ tree level couplings (see text for details).

to the fact that for the decay $\eta \to \pi^+\pi^-\pi^0$ the position defined by $x = y = 0$ does not coincide with $s_1 = s_2 = s_3$ when $M_\pi \neq M_{\pi^0}$. Using the correct prescriptions given in Eq. (2.10), we find the results listed in the left column of Table 2.5. The corrections are very sizable: our analysis shows that a is reduced (in magnitude) by 5%, b by even 14%. These kinematic effects constitute the bulk of the isospin breaking corrections to the charged parameters.

The modifications that arise from using physical pion masses in the loop functions and derivative couplings are very small in the expansion around the center of the Dalitz plot, see Table 2.5 (second column). The charged parameters are typically reduced in magnitude on the level of about 1%; α is shifted by $+0.0001$ only, an order of magnitude below the uncertainty due to different $\pi\pi$ parametrizations. The importance of pion-mass effects in loops only becomes really visible when studying the full Dalitz plot distribution also at its boundaries (see Refs. [28, 62]).

The next column in Table 2.5 shows the effect of isospin-breaking corrections in the $\pi\pi$ threshold parameters. For this purpose, we have calculated the electromagnetic contributions to the matching relations up-to-and-including $\mathcal{O}(e^2p^2)$ in the chiral expansion for S- and P-wave scattering lengths and S-wave effective ranges, using the results for the one-loop $\pi\pi$ scattering amplitudes in the presence of virtual photons of Refs. [92, 93]. The necessary matching procedure is described in detail in Appendix A.2.1. The modifications in the Dalitz plot parameters are largest for α, where a 3% effect is observed. The contributions to the remaining parameters stay well below or around 1%. In all cases the shifts are dominated by isospin-breaking corrections in the S-wave scattering lengths and thereby the $\mathcal{O}(e^2)$ chiral corrections, as expected by power counting.

Finally, we want to investigate the effects of isospin breaking on the relations in Eq. (2.12), i.e. next-to-leading order isospin breaking in the $\eta \to 3\pi$ tree level couplings. These can be extracted from the chiral one-loop calculation of the $\eta \to 3\pi$ decay amplitudes to $\mathcal{O}(e^2(m_d - m_u))$ in Ref. [62]. We write the corrections in the form

$$\mathcal{N}_n = -3\tilde{\mathcal{N}}_c + \Delta_{\tilde{\mathcal{N}}} \,, \qquad \tilde{\alpha} = \frac{1}{3}(\tilde{b} + 3\tilde{d}) + \Delta_{\tilde{\alpha}} \,, \tag{2.51}$$

Theory	a	b	d
ChPT $\mathcal{O}(p^4)$	-1.34 ± 0.04	0.434 ± 0.018	0.077 ± 0.008
ChPT $\mathcal{O}(p^6)$	-1.271 ± 0.075	0.394 ± 0.102	0.055 ± 0.057
Dispersive	-1.16	$0.24 \ldots 0.26$	$0.09 \ldots 0.10$
$\mathcal{O}(p^4)$+NREFT	-1.213 ± 0.014	0.308 ± 0.023	0.050 ± 0.003
Experiment	a	b	d
KLOE [82]	$-1.090 \pm 0.005^{+0.008}_{-0.019}$	$0.124 \pm 0.006 \pm 0.010$	$0.057 \pm 0.006^{+0.007}_{-0.016}$
Adlarson [83]	$-1.076 \pm 0.025^{+0}_{-0.032}$	$0.157 \pm 0.030^{+0.082}_{-0.032}$	0.139 ± 0.028
Crystal Barrel [94]	-1.22 ± 0.07	0.22 ± 0.11	0.06 ± 0.04 (input)
Layter *et al.* [95]	-1.08 ± 0.014	0.034 ± 0.027	0.046 ± 0.031
Gormley *et al.* [95]	-1.17 ± 0.02	0.21 ± 0.03	0.06 ± 0.04

Table 2.6: Results for the charged Dalitz plot parameters in comparison with various theoretical and experimental determinations (the next-to-leading-order errors are only due to L_3^{r}). Not that for b we combined the two asymmetric errors given in Ref. [83] according to the formalism named "Model 1" in Ref. [96]. This also skews the central value.

where $\Delta_{\tilde{\mathcal{N}}} = \mathcal{O}(e^2(m_d - m_u))$ and $\Delta_{\tilde{\alpha}} = \mathcal{O}(e^2)$. Note that no corrections of $\mathcal{O}((m_d - m_u)^2)$ (in $\Delta_{\tilde{\mathcal{N}}}$) and $\mathcal{O}(m_d - m_u)$ (in $\Delta_{\tilde{\alpha}}$) occur, respectively. The analytic results of the expansion and further details are given in Appendix A.2.2. With the numerical input for various low-energy constants chosen as in Ref. [62], we find that the corrections to the isospin relations are very small,

$$\frac{\Delta_{\tilde{\mathcal{N}}}}{\mathcal{N}_n} = (-0.7 \pm 1.5)\% \,, \qquad \Delta_{\tilde{\alpha}} = 0.035 \pm 0.003 \text{ GeV}^{-4} \,. \tag{2.52}$$

The numerical analysis shows that the corrections to α are below 1% and thus very small, even for isospin breaking corrections. It is interesting to note that the modification induced by $\Delta_{\tilde{\alpha}}$ is largely counterbalanced by the modification due to $\Delta_{\tilde{\mathcal{N}}}$. Even though the modifications Eq. (2.51) only affect the $\eta \to 3\pi^0$ tree-level couplings, these in principle also enter the charged channel via (inelastic) rescattering effects, however these shifts are too small to register. The corresponding values, which also constitute our final results, are collected in the final column of Table 2.5.

After analyzing the isospin-breaking contributions we can now compare our final results for the charged Dalitz plot parameters with several other theoretical determinations and experimental findings in Table 2.6.

We receive mixed results for the different Dalitz plot parameters. d is generally in fairly good agreement with experiment with the exception of the result given by Adlarson, which is off by about a factor of 2.5 from other theoretical and experimental determinations. a shows deviations of about 10% to the results from Layter and Adlarson and most notably from the precision measurement of the KLOE collaboration, which – due to the relatively small errors – exceeds even very generous confidence levels. Our result is more or less compatible with the $\mathcal{O}(p^6)$ ChPT result. The dispersive calculation is somewhat closer to experiment, but no error range is given for us to compare with. The situation is even worse with b, where the

Input	1	$\bar{a}^{\text{tree}}$	$\bar{b}^{\text{tree}}$	$\bar{d}^{\text{tree}}$
$\mathcal{N}/\tilde{\mathcal{N}}_c$	$0.9119 + 0.2954i$	$0.0028 + 0.0005i$	$-0.0097 + 0.0174i$	$-0.0156 + 0.0643i$
$\bar{a}$	$0.0202 - 0.4228i$	$1.0092 - 0.1902i$	$-0.0393 - 0.0182i$	$-0.0200 - 0.0378i$
$\bar{b}$	$-0.0421 - 0.0166i$	$0.0152 - 0.1205i$	$1.0106 - 0.0834i$	$-0.0069 + 0.0079i$
$\bar{d}$	$-0.0182 + 0.0127i$	$-0.0156 - 0.0483i$	$0.0091 - 0.0079i$	$0.9782 - 0.3583i$
$\bar{f}$	$-0.0009 - 0.0118i$	$-0.0327 + 0.0011i$	$0.0331 - 0.2371i$	$-0.0214 - 0.1175i$
$\bar{g}$	$0.0041 - 0.0027i$	$-0.0031 + 0.0074i$	$-0.0022 - 0.0115i$	$-0.0330 - 0.0783i$
$\bar{\alpha}$	$-0.0345 - 0.0028i$	$-0.0004 - 0.0964i$	$0.5823 - 0.0522i$	$0.5548 - 0.2001i$
$\bar{\beta}$	$0.0015 + 0.0028i$	$0.0090 + 0.0018i$	$-0.0108 + 0.0688i$	$-0.0036 + 0.0119i$
$\bar{\gamma}$	$-0.0010 - 0.0064i$	$-0.0008 - 0.0016i$	$-0.0216 - 0.0016i$	$-0.0075 + 0.0099i$

Table 2.7: Parameterization of Dalitz plot parameters in terms of tree input parameters.

deviation between our result and measurements from KLOE and Adlarson is rather alarming. The dispersive analysis indicates that even higher-order effects might be somewhat important in the determination of a and b, however it cannot account for the discrepancy we find for b. A main source of uncertainty that we have not addressed so far is the tree-level input, which could receive rather large contributions from matching to the chiral amplitude at $\mathcal{O}(p^6)$. It is possible that the deviation in a can be accounted for by such a matching prescription. There is no indication, however, that this is also the case for b. This issue is put under tense scrutiny in the next section. The results obtained in that discussion question to some extent the consistency between the charged and neutral Dalitz plot measurements. — Our result for the cubic parameter, $f = 0.083 \pm 0.019$, is reasonably compatible with the KLOE determination, $f = 0.14 \pm 0.01 \pm 0.02$ [82], and the result from Adlarson, $f = 0.109 \pm 0.064^{+0.022}_{-0.102}$ [83].

2.6 Relating charged and neutral Dalitz plot parameters

2.6.1 Isospin limit $Q_n = Q_c$

Up to this point we have only discussed uncertainties due to the effective range parameterization in the final-state interactions. A by far greater source of uncertainty is the tree-level input to our calculation, i.e. the matching to the ChPT one-loop amplitude, which we deem responsible for most of the remaining deviation from the experimental results. At higher orders (chiral $\mathcal{O}(p^6)$), these tree parameters will receive chiral SU(3) corrections, or renormalizations of $\mathcal{O}(m_s)$, which certainly are potentially large. In order to document our findings beyond the matching to the chiral one-loop amplitude, we provide a direct parameterization of the various Dalitz plot parameters in terms of these input (tree) parameters. For this purpose, we first revert back to the case $Q_n = Q_c$ as expressions become much simpler in this limit. Table 2.7 shows the coefficients of the respective input parameters. The entries are to be understood as follows: e.g., the second line means that the value for $\bar{a}$ including final-state interactions is determined by the tree input according to

$$\begin{aligned}\bar{a} = {} & 0.0202 - 0.4228i + (1.0092 - 0.1902i)\bar{a}^{\text{tree}} \\ & - (0.0393 + 0.0182i)\bar{b}^{\text{tree}} - (0.0200 + 0.0378i)\bar{d}^{\text{tree}} \ . \end{aligned} \tag{2.53}$$

All numerical coefficients are determined by $\pi\pi$ scattering alone. They are again averaged from the four different results (two loops plus unitarized, with ACGL and KPY parameters used as input) as in Table 2.4. The error range of Dalitz plot parameters calculated with this parameterization may be taken from the last column of Table 2.4. Furthermore, we only show the relations linear in the tree parameters (that is, no terms of quadratic etc. order), which are the by far dominant contributions.

As we will now show, Table 2.7 can be used to construct an explicit relation between charged and neutral channel Dalitz plot parameters. From Eq. (2.12) one can derive the following relation (again, we only consider $R_n \neq R_c$ or $Q_n \neq Q_c$ in the overall normalization for the moment):

$$\alpha = \frac{Q_n^2}{4Q_c^2}\big(d + b - |\bar{a}|^2\big) \;, \tag{2.54}$$

and consequently (cf. Ref. [60])

$$\alpha = \frac{Q_n^2}{4Q_c^2}\Big(d + b - \frac{a^2}{4}\Big) - \frac{Q_n^2}{4Q_c^2}\big(\mathrm{Im}(\bar{a})\big)^2 \leq \frac{Q_n^2}{4Q_c^2}\Big(d + b - \frac{a^2}{4}\Big) \;, \tag{2.55}$$

which turns into an equality only for $\mathrm{Im}(\bar{a}) = 0$. The obvious question arises: as $\mathrm{Im}(\bar{a})$ is generated by final-state interactions but in turn depends on the Dalitz plot parameters, can we quantify the *equality* in Eq. (2.55) in such a way that we obtain a testable consistency relation between the experimental observables α, a, b, and d, *independent* of any (potentially insufficiently accurate) ChPT input? The answer is yes – precisely by using the information contained in Table 2.7. We consider Eq. (2.53) and first note that, to very good accuracy, the contributions from $\bar{b}^{\mathrm{tree}}$ and $\bar{d}^{\mathrm{tree}}$ can be neglected: with these parameters matched as previously, we have $\bar{a}^{\mathrm{tree}} \approx -0.656$, $\bar{b}^{\mathrm{tree}} \approx -0.017$, $\bar{d}^{\mathrm{tree}} \approx 0.037$, which is sufficient to demonstrate that $\bar{b}^{\mathrm{tree}}$ and $\bar{d}^{\mathrm{tree}}$ are suppressed compared to $\bar{a}^{\mathrm{tree}}$ by at least one order of magnitude, irrespective of potential higher-order corrections. (The neglected terms are retained explicitly in the following Section 2.6.2, compare Eq. (2.62), which fully justifies their omission.) So via $\bar{a}^{\mathrm{tree}}$ in Eq. (2.53), $\mathrm{Im}(\bar{a})$ can be solved for $\mathrm{Re}(\bar{a}) = a/2$, and we find

$$\alpha = \frac{Q_n^2}{4Q_c^2}\Big(b + d - \frac{a^2}{4}\Big) - \zeta_1(1 + \zeta_2 a)^2 \;, \quad \zeta_1 = 0.050 \pm 0.005 \;, \quad \zeta_2 = 0.225 \pm 0.003 \;. \tag{2.56}$$

We wish to emphasize once more that the values for $\zeta_{1/2}$ depend solely on $\pi\pi$ rescattering effects and are independent on any chiral one-loop input. The most precise determinations of the charged Dalitz plot parameters come from the KLOE experiment [82], see Table 2.6. Inserting their numbers for a, b, and d into Eq. (2.56), we find

$$\alpha_{\mathrm{KLOE,NREFT}} = -0.062 \pm 0.003(\mathrm{stat})^{+0.004}_{-0.006}(\mathrm{syst}) \pm 0.003(\pi\pi) \;, \tag{2.57}$$

where the statistical and systematic errors are calculated from the respective uncertainties and their correlations in Ref. [82], and the last error is the uncertainty inherent in our assessment of final-state interactions in Eq. (2.56). This result disagrees rather strongly with the world average of $\alpha = -0.0317 \pm 0.0016$ [87] as well as KLOE's own direct experimental finding $\alpha = -0.0301 \pm 0.0035^{+0.0022}_{-0.0035}$ [66].

This observation seems to be at odds with a result presented in Ref. [82], where a separate fit has been performed using an alternative parameterization [97], which incorporates final-state $\pi\pi$ rescattering based on a strict $\Delta I = 1$ rule and allows to extract α therefrom. The

result of that alternative fit is

$$\alpha_{\Delta I=1,\text{exp}} = -0.038 \pm 0.003(\text{stat})^{+0.012}_{-0.008}(\text{syst}) \ , \tag{2.58}$$

and thus seems to be in very reasonable agreement with the direct determination of α. However, the parameterization from Ref. [97] is based on chiral one-loop phases or imaginary parts, hence leading-order rescattering with $\mathcal{O}(p^2)$ $\pi\pi$ vertices. If we reduce our rescattering formalism to that order (and also set $Q_n = Q_c$), we find for the coefficients in Eq. (2.56) $\zeta_1 = 0.021$, $\zeta_2 = 0.188$ instead, and as a result

$$\alpha_{\Delta I=1,\text{NREFT}} = -0.042 \pm 0.002(\text{stat})^{+0.003}_{-0.005}(\text{syst}) \ , \tag{2.59}$$

in satisfactory agreement with Eq. (2.58) within errors (which stem from the Dalitz plot input exclusively). We therefore understand why the rescattering formalism employed in Ref. [97] leads to a seemingly consistent result for α; however, the large impact of higher orders in the effective range parameters renders this procedure unreliable. Employing a more precise parameterization for $\pi\pi$ final-state interactions, responsible for the imaginary parts necessary for the relations Eqs. (2.55) and (2.56), shows that there seems to be a significant tension between the available experimental results of the KLOE collaboration for charged and neutral Dalitz plot parameters.

One can perform the same exercise with the data from Ref. [83]. We note that both this measurement and the KLOE measurement are in agreement concerning the parameters a and b, yet disagree rather strongly concerning the parameter d. With these parameters we obtain

$$\alpha_{\text{Adlarson,NREFT}} = -0.027 \pm 0.012(\text{stat})^{+0.023}_{-0.008}(\text{syst}) \pm 0.003(\pi\pi) \ . \tag{2.60}$$

While the errors on this determination are rather large, we find very good agreement between this set for charged Dalitz plot parameters and the central value for α. Interestingly, the large value of d allows this parameter set to be consistent with our analysis. However, the systematic errors on a, b, and d might still be somewhat larger than pointed out [98]. In the following we will study isospin breaking corrections on the above relations.

2.6.2 Isospin-breaking corrections due to $Q_n \neq Q_c$

We now study isospin-breaking corrections to the above relations due to kinematic effects stemming from $Q_n \neq Q_c$. Following the results of Section 2.5, all other effects are certainly included in the uncertainties. If we denote the charged Dalitz plot parameters as calculated in Section 2.4 by a_{iso}, b_{iso}, and so forth, the "real" ones a, b, ... as deduced from Eq. (2.10) are related to the former according to

$$\begin{aligned} a_{\text{iso}} &= a + \delta\left(2b - a^2\right) + \mathcal{O}(\delta^2) \ , \\ b_{\text{iso}} &= b + \delta\left(3f - ab\right) + \mathcal{O}(\delta^2) \ , \\ d_{\text{iso}} &= d + \delta\left(g - ad\right) + \mathcal{O}(\delta^2) \ , \end{aligned} \tag{2.61}$$

where $\delta = Q_n/Q_c - 1 \approx 0.069$, and only f and g do not receive corrections as long as we disregard Dalitz plot parameters of $\mathcal{O}(\epsilon^8)$. The corrections $\propto \delta$ produce large shifts (as discussed in Section 2.5), so that one may wonder whether the relation Eq. (2.56) between charged and neutral Dalitz plot parameters may also receive large corrections. To investigate this, we have to amend Eq. (2.56) in two respects:

1. incorporate the isospin-breaking shifts due to Eq. (2.61) in the terms $b + d - a^2/4$;
2. improve the parameterization of $\mathrm{Im}(\bar{a})$ to include $\mathcal{O}(\epsilon^4)$ effects (proportional to b, d, and a^2 neglected before) in order to consistently incorporate the shifts due to Eq. (2.61) in the contribution to α stemming from the imaginary part of $\bar{a}$.

Although significantly more complicated in result, the manipulations are much the same as before, relying on Table 2.7. The improved result is of the form

$$\begin{aligned}\alpha = \frac{Q_n^2}{4Q_c^2}\Bigg\{ & b + d - \frac{a^2}{4} - \delta\left[2a\Big(b - \frac{a^2}{4} + \frac{d}{2}\Big) - 3f - g\right]\Bigg\} \\ & - \zeta_1\Big[1 + \zeta_2 a + \big(\zeta_3 - \delta\zeta_2\big)a^2 + \big(\zeta_4 + 2\delta\zeta_2\big)b + \zeta_5 d\Big]^2 \ , \qquad \zeta_1 = 0.050 \pm 0.005 \ , \\ \zeta_2 = 0.223 \pm 0.003 \ , \quad & \zeta_3 = -0.008 \pm 0.001 \ , \quad \zeta_4 = 0.030 \pm 0.004 \ , \quad \zeta_5 = 0.051 \pm 0.001 \ .\end{aligned} \tag{2.62}$$

It turns out that the more refined description of $\mathrm{Im}(\bar{a})$ in Eq. (2.62) and therefore the complicated piece in the relation between charged and neutral Dalitz plot parameters changes the result only minimally: it shifts α by a mere $+0.001$. The term $\propto \delta$ in the first line of Eq. (2.62) is a bit more difficult to evaluate, as it involves large cancellations between the various contributions. This becomes evident, when analyzing the dependence of that term on the specific value for f. Varying f from the experimental result to our determination alone shifts the contribution of the δ-term from $+0.002$ to -0.002.

For our final result we resort to the KLOE and Adlarson parameters again and use correlated errors, except for g, where there is neither a measurement nor a determination of its correlation coefficients to be found in the literature. We simply choose to vary it independently between zero and the result of our calculation in Table 2.5. However, despite these generous variations, the total effect of these additional contributions proportional to δ is still so small that it hardly shows in the overall uncertainty. Our final result for the KLOE measurement is

$$\alpha_{\mathrm{KLOE,NREFT}} = -0.059 \pm 0.003(\mathrm{stat})^{+0.004}_{-0.006}(\mathrm{syst}) \pm 0.003(\pi\pi) \ , \tag{2.63}$$

while for the Adlarson analysis we find

$$\alpha_{\mathrm{Adlarson,NREFT}} = -0.023 \pm 0.014(\mathrm{stat})^{+0.027}_{-0.009}(\mathrm{syst}) \pm 0.003(\pi\pi) \ . \tag{2.64}$$

The overall correction to Eq. (2.57) turns out to be small and we are still left with a significant disagreement between charged and neutral channel for the KLOE measurement, whereas we find reasonable agreement within admittedly large errors for the Adlarson measurement. Comparing the charged Dalitz plot parameters entering Eq. (2.56), we see that the main disagreement is due to the parameter b, which is strongly over-predicted in our analysis: we find $b = 0.308 \pm 0.023$ to be compared with $b_{\mathrm{KLOE}} = 0.124 \pm 0.006 \pm 0.010$. Interestingly enough we find the same disagreement with the central parameter of the Adlarson measurement, $b_{\mathrm{Adlarson}} = 0.157 \pm 0.030^{+0.082}_{-0.032}$, but here the effect is counterbalanced by a very large $d_{\mathrm{Adlarson}} = 0.139 \pm 0.028$, so that overall this result is consistent with our treatment of final-state interactions. Notice also that the large errors in Eq. (2.64) stem from b and not from d. Of course, the NREFT results are consistent within themselves: inserting our values for a, b, d into the relation Eq. (2.56) reproduces our result for α. We also mention that there is some non-negligible variation between the KLOE and Adlarson results for the charged Dalitz

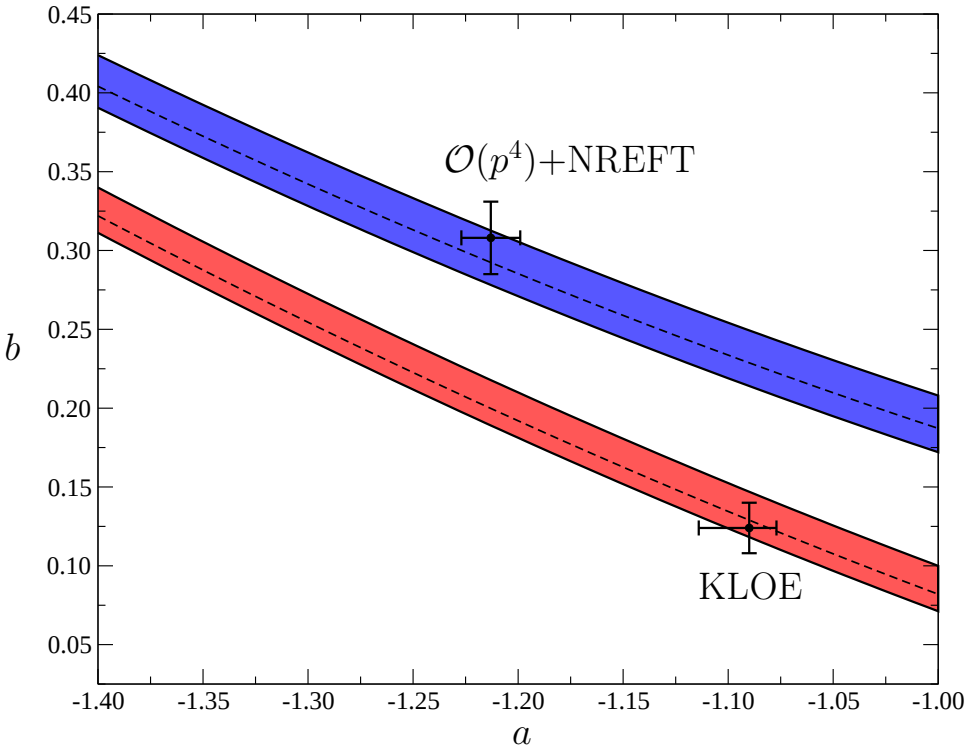

Figure 2.4: Allowed range for charged Dalitz plot parameters a and b with fixed α and d. Blue curve: allowed range according to Eq. (2.56). Red curve: allowed range using $\zeta_1 = 0$.

plot parameters and several older, less precise measurements [94, 95, 99]; a re-measurement of these quantities by some of the modern high-precision experiments would therefore be very welcome.

The relation between α and the charged Dalitz plot parameters is further illustrated in Fig. 2.4. Due to the smallness of the higher-order corrections in Eq. (2.62), it suffices to use the simplified representation Eq. (2.56). As $\alpha = -0.0317 \pm 0.0016$ is experimentally agreed upon to very high precision, and as our result for d agrees well with the KLOE determination $d = 0.057 \pm 0.006^{+0.007}_{-0.016}$, we may take these two experimental results for granted, such that Eq. (2.56) provides a relation between a and b. This constraint in the $a-b$ plane is shown in Fig. 2.4. The blue curve shows the allowed range for b as a function of a according to Eq. (2.56), whereas the red curve shows the same relation for $\zeta_1 = 0$, i.e. fully neglecting the imaginary part of the amplitude, or $\mathrm{Im}(\bar{a}) = 0$. While the NREFT prediction for a and b falls nicely into the allowed band (the agreement here looks even better than in the direct comparison to α as the band also reflects the experimental error in d), the KLOE determination of both is consistent with a vanishing imaginary part. In our framework these latter values cannot be brought into agreement with a consistent implementation of final-state interactions.

Comparing our calculation to the dispersion-theoretical analysis of Ref. [76], there are indications that the discrepancy we find may be slightly over-predicted: in the terminology of the iterative solution determined there, our two-loop calculation cannot be expected to be better than the second iteration of the dispersive amplitude. Ref. [76] shows that while the real part of the amplitude has converged to the final result almost perfectly, there are still non-negligible corrections in the imaginary part beyond that, i.e. in terms of our represen-

tation at (irreducible) three loops and higher. Whether those corrections in the imaginary part that precisely constitute the additional terms in the relations Eqs. (2.56), (2.62) are sufficient to reduce the apparent discrepancy between charged and neutral Dalitz plot parameter measurements remains to be seen.

2.7 Partial widths and the ratio r

In this work, we have concentrated almost exclusively on the energy dependence of the two $\eta \to 3\pi$ Dalitz plot distributions, mainly as encoded in the Dalitz plot parameters. It is rather obvious in particular from Table 2.3 that the overall *normalization* of the amplitudes is not improved in our formalism compared to what we match our parameters to, here ChPT at $\mathcal{O}(p^4)$; indeed, the overall rates are even slightly smaller. To be specific, evaluating the partial widths of the neutral decay according to

$$\begin{aligned}\Gamma(\eta \to 3\pi^0) &= \frac{1}{(2\pi)^3}\frac{1}{32M_\eta^3}\int_{4M_{\pi^0}^2}^{(M_\eta - M_{\pi^0})^2} ds_3 \int_{s_1^-(s)}^{s_1^+(s)} ds_1 |\mathcal{M}_N(s_1,s_2,s_3)|^2 \ , \\ s_1^\pm(s) &= \frac{1}{2}\Big\{3s_n - s_3 \pm \frac{1}{s_3}\lambda^{1/2}(M_\eta, M_{\pi^0}, s_3)\lambda^{1/2}(M_{\pi^0}^2, M_{\pi^0}^2, s_3)\Big\} \ , \end{aligned} \tag{2.65}$$

and of the charged decay according to

$$\begin{aligned}\Gamma(\eta \to \pi^+\pi^-\pi^0) &= \frac{1}{(2\pi)^3}\frac{1}{32M_\eta^3}\int_{4M_{\pi}^2}^{(M_\eta - M_{\pi^0})^2} ds_3 \int_{s_1^-(s)}^{s_1^+(s)} ds_1 |\mathcal{M}_C(s_1,s_2,s_3)|^2 \ , \\ s_1^\pm(s) &= \frac{1}{2}\Big\{3s_c - s_3 \pm \frac{1}{s_3}\lambda^{1/2}(M_\eta, M_{\pi^0}, s_3)\lambda^{1/2}(M_{\pi}^2, M_{\pi}^2, s_3)\Big\} \ , \end{aligned} \tag{2.66}$$

where we integrate the amplitude squared over the physical region of the Dalitz plot including all isospin-breaking effects (corresponding to the last column of Table 2.5), we find

$$\begin{aligned}\Gamma(\eta \to 3\pi^0) &= \big[201 \pm 3(\pi\pi) \pm 6(\Delta_{\tilde{N}})\big]\,\text{eV} \ , \\ \Gamma(\eta \to \pi^+\pi^-\pi^0) &= \big[144 \pm 2(\pi\pi)\big]\,\text{eV} \ . \end{aligned} \tag{2.67}$$

Several remarks are in order here. First, as we have pointed out earlier, for our normalization we use $\mathcal{Q} = 24.2$ as given by means of Dashen's theorem, which leads to a very small width. Changing the value to $\mathcal{Q} = 22.3$ [76], say, immediately increases the widths by nearly 40%. Second, Ref. [60] finds that next-to-next-to-leading order chiral corrections increase the width by nearly 70%, thus bringing it a lot closer to the experimental value of about $\Gamma(\eta \to \pi^+\pi^-\pi^0) \approx (296 \pm 16)\,\text{eV}$ [87]. We wish to emphasize once more that this failure to reproduce the chiral enhancements in the width in the non-relativistic framework does not invalidate our predictions for the Dalitz plot parameters: the power counting argument of Section 2.3.5 explains why we catch the important rescattering effects in particular for the higher-order energy dependence, but not in the overall normalization. The $\eta \to 3\pi$ tree-level coupling constants that receive sizable quark-mass renormalization effects nicely factor out of the complete (tree plus loop) amplitudes and play no role in the calculation of the Dalitz plot parameters. As a third remark, the errors shown in Eq. (2.67) do not at all reflect these uncertainties from our matching procedure, but purely the one due to $\pi\pi$ final-state interactions (determined as in the previous sections), and in the case of $\Gamma(\eta \to 3\pi^0)$ due to the uncertainty in $\Delta_{\tilde{N}}$, see Eq. (2.51).

Despite all the above-mentioned deficits in a calculation of the decay widths, the ratio of neutral-to-charged partial widths r should be predicted much more reliably, as the normalization of the amplitude (in the isospin limit) drops out. In particular, here we may expect a somewhat heightened importance of isospin-breaking corrections [62]. We find

$$r = \frac{\Gamma(\eta \to 3\pi^0)}{\Gamma(\eta \to \pi^+\pi^-\pi^0)} = 1.40 \pm 0.01(\pi\pi) \pm 0.04(\Delta_{\tilde{\mathcal{N}}}) \ , \tag{2.68}$$

in agreement with the experimental finding $r = 1.43 \pm 0.02$ [87]. We note that the dependence on $\pi\pi$ rescattering in Eq. (2.68) is very small, our error is dominated by the 1.5% uncertainty in $\Delta_{\tilde{\mathcal{N}}}$. Equation (2.68) is extremely accurately reproduced by just integrating the phenomenological Dalitz plot distribution, with our values for the Dalitz plot parameters from Table 2.5 (last column) instead of the exact amplitudes: obviously r is affected by cusps in the neutral channel or yet-higher-order Dalitz plot parameters at or below the permille level. We can therefore easily derive the dependence of r on the parameters a, b, d, ..., making use of the relation of α to these in Eq. (2.55) and neglecting pieces that affect r at the permille level (e.g. the terms $\propto \beta$, γ in the neutral rate), and find

$$r = 1.485 \left(1 - 0.029\, a - 0.061\, a^2 + 0.024\, b + 0.032\, d + 0.008\, f - 0.014\, g\right) \left(1 + \frac{2\Delta_{\tilde{\mathcal{N}}}}{\mathcal{N}_n}\right) \ . \tag{2.69}$$

Errors on this result are to be taken from Eq. (2.68). The various numerical coefficients are given by $\pi\pi$ phase shifts and phase space integration only. This demonstrates to very good approximation that r does not depend on the normalization and thus possibly sizable quark mass renormalization effects.

2.8 Summary and conclusion

In this article we have analyzed rescattering effects in $\eta \to 3\pi$ decays by means of the modified non-relativistic effective field theory framework. The main findings of our investigation can be summarized as follows:

1. NREFT provides a simple and transparent representation of the amplitude to two loops, including higher-order isospin breaking. In order to estimate higher-order loop effects we have furthermore applied a simplified unitarization prescription. The amplitude thus obtained is – at the very least – fully competitive with the chiral expansion at next-to-next-to-leading order. The coupling constants involved have been matched to phenomenological $\pi\pi$ scattering threshold parameters and, in the case of the $\eta \to 3\pi$ tree-level couplings, to ChPT at $\mathcal{O}(p^4)$.

2. One- and two-loop contributions to the Dalitz plot parameters are in general of the same size, an observation which is predicted by non-relativistic power counting arguments. Irreducible two-loop graphs are generally suppressed, while derivative couplings at two-loop level are essential to find the correct sign for the $\eta \to 3\pi^0$ slope parameter α. Higher-order effects beyond two loops were shown to be relatively small, but not negligible.

3. While our results for the Dalitz plot parameters are in qualitative agreement with previous dispersive results, we can provide an explanation for the apparent failure of two-loop ChPT to reproduce α: the treatment of $\pi\pi$ final-state interactions is still not sufficiently

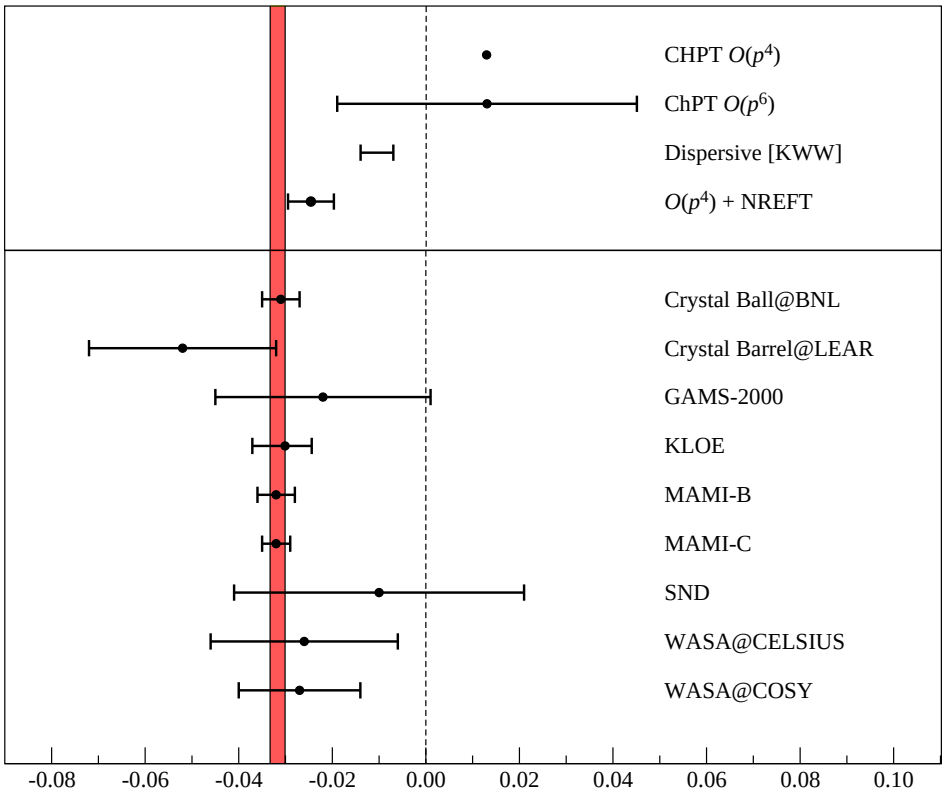

Figure 2.5: Comparison of values for the slope parameter α. Top: theoretical predictions. Bottom: experimental determinations. The red shaded area is the particle data group average [87].

accurate at that order. We can identify one specific diagram, the double rescattering graph with $\pi\pi$ vertices beyond leading order, as being responsible for at least half of the discrepancy between the $\mathcal{O}(p^6)$ prediction for α and the experimental value. These effects are of chiral order p^8 and higher, but included in the NREFT two-loop representation.

4. Apart from normalization effects and subtleties in the definition of the center of the Dalitz plot in the charged decay channel, higher-order isospin-breaking corrections on the Dalitz plot parameters are very small.

5. Our final result for neutral Dalitz slope parameter,

$$\alpha = -0.025 \pm 0.005 \ , \tag{2.70}$$

is compared in Fig. 2.5 to several other determinations. It is considerably closer to the experimental world average $\alpha = -0.0317 \pm 0.0016$ [87] than previous theoretical approaches. Notice though that Eq. (2.70) does not take uncertainties stemming from matching to ChPT at $\mathcal{O}(p^4)$ into account, which we expect to be non-negligible.

6. Our results for the charged Dalitz plot parameters show somewhat larger deviations from the currently most accurate measurement by the KLOE collaboration. By relating

charged and neutral decay channel via the $\Delta I = 1$ rule we find indications for a significant tension between the Dalitz plot parameters of both channels, which is solely due to final-state interactions. A re-measurement of the charged Dalitz plot parameters by high-precision experiments [100, 101], or even preferably access to improved full Dalitz plot distributions, is thus highly desirable.

7. While the partial widths calculated in our framework do not improve upon the chiral one-loop prediction we match to (due to the absence of further quark-mass renormalization effects not captured in our framework), we can give a value for the ratio of neutral-to-charged partial widths unaffected by this deficit, $r = 1.40 \pm 0.04$, where the error is dominated by isospin-breaking effects.

Possible future improvements on the theoretical approach include matching to $\mathcal{O}(p^6)$ ChPT in order to constrain the tree-level Dalitz plot couplings more tightly. Furthermore, it will be extremely useful to match the non-relativistic representation to the upcoming dispersive analysis [76] in order to obtain a reliable description of the whole physical Dalitz plot: in this way one can include elastic $\pi\pi$ rescattering to all orders, and at the same time implement in particular non-analytic effects (cusps) at or near the boundaries of the Dalitz plot due to isospin-breaking up to next-to-next-to-leading order. This combination should then also provide the best-possible representation of the decay amplitude for a precision extraction of the quark mass ratio $\mathcal{Q}$.

Part II

Non-perturbative methods: Dispersion relations

Chapter 3

Dispersive analysis of $\eta' \to \eta\pi\pi$ decays

3.1 Introduction

The treatment of hadronic three-body decays using a dispersion relation approach is a classic subject. Already in the 1960s Khuri and Treiman developed a framework in the context of $K \to 3\pi$ decays [102]. One of its main virtues is the fact that final-state interactions among the three pions are fully taken into account, in contrast to perturbative, field-theory-based approaches; the constraints coming from analyticity and unitarity are respected exactly to all orders. This becomes the more important, the higher the mass of the decaying particle, hence the higher the possible energies of the two-pion subsystems within the Dalitz plot. But even for decays of relatively "low-energy" like $\eta \to 3\pi$, where final-state interactions strongly perturb the spectrum, such approaches are worthwhile, see Refs. [75–77, 103]. In the following Chapter we present the application of these techniques to the decay $\eta' \to \eta\pi\pi$.

The decay $\eta' \to \eta\pi\pi$ has received considerable interest in past years for several reasons. Due to the $\mathrm{U}(1)_A$ anomaly the η' is not a Goldstone boson and therefore "standard" chiral perturbation theory based on the breakdown of $\mathrm{SU}(3)\times\mathrm{SU}(3)$ chiral symmetry fails to adequately describe processes involving the η'. In the large-N_C limit the axial anomaly vanishes and gives rise to a $\mathrm{U}(3)_L\times\mathrm{U}(3)_R$ symmetry, so that a simultaneous expansion in small momenta, small quark masses and large-N_C gives rise to a power counting scheme that in principle allows one to describe interactions of the pseudoscalar nonet (π, K, η, η'). However, the question whether this framework dubbed large-N_C chiral perturbation theory [104, 105] is actually well-established remains under discussion, mainly due to the large η' mass. This is in principle an issue that can be addressed by a study of $\eta' \to \eta\pi\pi$. So far there are indications that a large-N_C ChPT treatment alone is not sufficient to describe the decay, as final-state interactions play a rather important role, see Refs. [105, 106].

Perhaps most importantly at present, the $\eta' \to \eta\pi\pi$ decay channel is believed to allow potentially clean access to constrain $\pi\eta$ scattering: the η' mass is sufficiently small so that the channel is not polluted by non-virtual intermediate states other than the rather well-constrained $\pi\pi$ scattering. In the past claims were made that $a_0(980) \to \pi\eta$ even dominates the decay [107–109]. These claims are based on effective Lagrangian models with the explicit inclusion of a scalar nonet incorporating the $a_0(980)$, $f_0(980)$ and σ resonances. These claims were further supported by Refs. [110, 111]: a chiral unitary approach shows large corrections

in the $\pi\eta$ channel and there is a dominant low-energy constant in the $U(3)$ ChPT calculation that is saturated mostly by the $a_0(980)$. The $\pi\eta$ P wave, however was found to be strongly suppressed [29, 80, 112].

The $\eta' \to \eta\pi^0\pi^0$ decay channel is expected to show a cusp effect at the charged-pion threshold [29] that in principle can be used to further constrain $\pi\pi$ scattering lengths. So far this phenomenon has not been observed, but at the same time this particular decay channel has not yet been measured with sufficient accuracy: the most recent measurement with the GAMS-4π spectrometer did not have sufficient statistics to resolve this subtle effect [113].

The extraction of $\pi\eta$ scattering parameters such as the scattering length and the effective range parameter is a more complicated subject compared to $\pi\pi$ scattering. There is no one-loop cusp effect as in the $\pi\pi$ channel, since the $\pi\eta$ threshold sits on the border of the physical region and not inside. The hope of extracting scattering parameters from a two-loop cusp is shattered likewise: there is rather subtle cancellation of this effect at threshold (see Refs. [114, 115] for an elaborate discussion).

Measurements of the Dalitz plot of the charged channel have been performed by BES-III [116] and the VES collaboration [117], while earlier measurements at rather low statistics have been reported in Refs. [118, 119]. The more recent measurements seem to disagree considerably with regard to the values of the Dalitz plot parameters, and also in comparison with the GAMS-4π measurement the picture remains inconsistent.

This Chapter is devised as follows. We will start by discussing some kinematics and the ensuing analytic structure of $\eta' \to \eta\pi\pi$ in Section 3.2 before deriving dispersion relations for the decay in Section 3.3. In Section 3.4 we will discuss the solution strategy to the numerical problem of solving these integral equations. Finally we will discuss some numerical results in Section 3.5.

3.2 Kinematics and analytic structure

We define the kinematic variables of the $\eta' \to \eta\pi\pi$ decay in the usual fashion,

$$\eta'(P_{\eta'}) \to \eta(p_3)\pi^i(p_1)\pi^j(p_2) \ , \tag{3.1}$$

where $(i,j) = (0,0)$ or $(i,j) = (+,-)$ respectively[#1] and the label $k = 3$ is assigned to the "odd" particle, in this case the η. We define the Mandelstam variables for the three-particle decay processes according to

$$s = (P_{\eta'} - p_3)^2 \ , \quad t = (P_{\eta'} - p_1)^2 \ , \quad u = (P_{\eta'} - p_2)^2 \ , \tag{3.2}$$

which fulfill the relation

$$s + t + u = M_{\eta'}^2 + M_\eta^2 + 2M_\pi^2 \doteq 3s_{\eta'} \ . \tag{3.3}$$

The process is invariant under exchange of the pions, that is under $t \leftrightarrow u$. In the center-of-mass system of particles 1 and 2 (the pions) we find the following relations,

$$t(s, \cos\theta_s) = \frac{1}{2}(3s_{\eta'} - s + \kappa_{\pi\pi}(s)\cos\theta_s) \ ,$$

[#1] We consider $(i,j) = (+,-)$ in the following. $(i,j) = (0,0)$ differs from that only when taking isospin breaking effects into account, which we will not.

$$u(s,\cos\theta_s) = \frac{1}{2}(3s_{\eta'} - s - \kappa_{\pi\pi}(s)\cos\theta_s) \ , \tag{3.4}$$

where $\cos\theta_s$ is the scattering angle in the center-of-mass system,

$$\cos\theta_s = \frac{t-u}{\kappa_{\pi\pi}(s)} \ , \quad \kappa_{\pi\pi}(s) = \frac{\lambda(M_\pi^2, M_\pi^2, s)^{1/2}\lambda(M_{\eta'}^2, M_\eta^2, s)^{1/2}}{s} \ , \tag{3.5}$$

and $\lambda(x,y,z) = x^2+y^2+z^2-2(xy+xz+yz)$ is the Källén function as defined in the previous chapter. The same exercise can be performed in the $\pi\eta$ system, where the relations are slightly complicated by the π–η mass difference. In the center-of-mass system of particles 2 and 3 we find

$$\begin{aligned} s(t,\cos\theta_t) &= \frac{1}{2}\Big(3s_{\eta'} - t - \frac{\Delta_{\eta'\pi}\Delta_{\eta\pi}}{t} - \kappa_{\pi\eta}(t)\cos\theta_t\Big) \ , \\ u(t,\cos\theta_t) &= \frac{1}{2}\Big(3s_{\eta'} - t + \frac{\Delta_{\eta'\pi}\Delta_{\eta\pi}}{t} + \kappa_{\pi\eta}(t)\cos\theta_t\Big) \ , \end{aligned} \tag{3.6}$$

where we used $\Delta_{ij} = M_i^2 - M_j^2$, and

$$\cos\theta_t = \frac{t(u-s) - \Delta_{\eta'\pi}\Delta_{\eta\pi}}{t\,\kappa_{\pi\eta}(t)} \ , \quad \kappa_{\pi\eta}(t) = \frac{\lambda(M_\eta^2, M_\pi^2, t)^{1/2}\lambda(M_{\eta'}^2, M_\pi^2, t)^{1/2}}{t} \ , \tag{3.7}$$

and finally in the center-of-mass system of particles 1 and 3 we have the analogous relations,

$$\begin{aligned} s(u,\cos\theta_u) &= \frac{1}{2}\Big(3s_{\eta'} - u - \frac{\Delta_{\eta'\pi}\Delta_{\eta\pi}}{u} + \kappa_{\pi\eta}(u)\cos\theta_u\Big) \ , \\ t(u,\cos\theta_u) &= \frac{1}{2}\Big(3s_{\eta'} - u + \frac{\Delta_{\eta'\pi}\Delta_{\eta\pi}}{u} - \kappa_{\pi\eta}(u)\cos\theta_u\Big) \ , \end{aligned} \tag{3.8}$$

with

$$\cos\theta_u = \frac{u(s-t) + \Delta_{\eta'\pi}\Delta_{\eta\pi}}{u\,\kappa_{\pi\eta}(u)} \ . \tag{3.9}$$

In Fig. 3.1 we show the Mandelstam plane, which is significantly altered when compared to $\pi\pi$ scattering as discussed in Chapter 1. The fact that the η' is heavy enough to decay into an η and two pions gives rise to a newly allowed physical region in the center of the Mandelstam plane. It is bounded by [120]

$$G(t, s, M_\eta^2, M_\pi^2, M_{\eta'}^2, M_\pi^2) \leq 0 \ , \tag{3.10}$$

where

$$\begin{aligned} G(x,y,z,u,v,w) = {} & x^2y + xy^2 + z^2u + zu^2 + v^2w + vw^2 + xzw + xuv + yzv + yuw \\ & - xy(z+u+v+w) - zu(x+y+v+w) - vw(x+y+z+u) \ . \end{aligned} \tag{3.11}$$

The physical region of the decay in the s-, t-, and u-channel is bounded by

$$\begin{aligned} s &= [4M_\pi^2, (M_{\eta'} - M_\eta)^2] \ , \\ t &= [(M_\eta + M_\pi)^2, (M_{\eta'} - M_\pi)^2] \ , \\ u &= [(M_\eta + M_\pi)^2, (M_{\eta'} - M_\pi)^2] \ . \end{aligned} \tag{3.12}$$

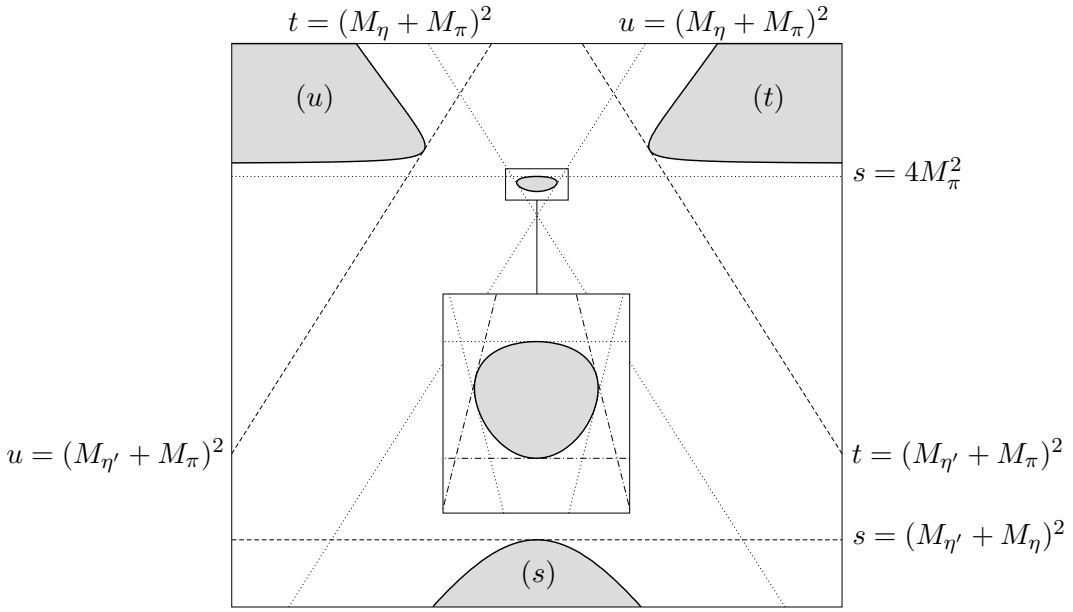

Figure 3.1: The Mandelstam plane for $\eta'\eta \to \pi\pi$ and its crossed channels $\eta'\pi \to \eta\pi$ including the decay process $\eta' \to \eta\pi\pi$. The inset shows a magnification of the decay region. Dashed lines denote the thresholds of the corresponding scattering channels, dotted lines denote the thresholds of the scattering subsystems of the decay, and dashed-dotted lines (in the inset only) denote the end of the physical region for each channel s, t, and u of the decay, which corresponds to the scattering pseudothresholds.

In contrast to previous works [74,75] we thus have to deal with two different thresholds, $4M_\pi^2$ in the s-channel and $(M_\eta+M_\pi)^2$ in the t- and u-channel. In the following we will set up dispersion relations for the decay process. The idea behind our approach is rather simple: we derive a set of integral equations for the *elastic* scattering processes $\eta'\eta \to \pi\pi$ and $\pi\eta' \to \pi\eta$: in this kinematic regime the procedure is straightforward and was already described in Section 1.2.1. The dispersion relation for the decay channel is then obtained by analytic continuation of the scattering processes to the decay region. This will be done in the following section.

Since we only consider the elastic scattering processes one may worry about potentially large effects arising from the finite with of the η', with the largest decay channel other than $\eta\pi\pi$ being an intermediate $\rho^0\gamma$ state. However, we have shown in Ref. [29], that such a contribution leads to a very small correction of the imaginary part of the complex wave-function renormalization, which can moreover be absorbed in an overall phase. In Chapter 4 we briefly discuss a partial incorporation of inelasticity effects in the $\pi\pi$ scattering amplitude. These will turn out to be extremely small, which is why we will not discuss them in the case at hand.

3.3 Dispersion relations for $\eta' \to \eta\pi\pi$

We will begin our discussion of dispersion relations for $\eta' \to \eta\pi\pi$ by deriving a decomposition of the amplitude as functions of only one variable. This form will prove to be very convenient in the derivation of the integral equations and their numerical solution at a later stage.

3.3.1 Decomposition of the amplitude

The decomposition that we derive in the following was first shown in the context of $\pi\pi$ scattering in Ref. [88] and subsequently generalized in Ref. [121]. Let us assume that the amplitude for the scattering processes is given in terms of Mandelstam variables, $\mathcal{M}(s,t,u)$, analogously to Section 1.2.1. The amplitude has an s-channel unitarity cut starting at $s_0 = 4M_\pi^2$, the t- and u-channel cuts start at $t_0 = u_0 = (M_\eta + M_\pi)^2$. The latter appear as left-hand cuts in the s-channel. We can write down a dispersion relation for the amplitude for a fixed value of t,

$$\mathcal{M}(s,t,u) = P^t_{n-1}(s,t,u) + \frac{s^n}{2\pi i}\int_{s_0}^{\infty} ds' \frac{\operatorname{disc}\mathcal{M}(s',t,u(s'))}{s'^n(s'-s)} + \frac{u^n}{2\pi i}\int_{u_0}^{\infty} du' \frac{\operatorname{disc}\mathcal{M}(s(u'),t,u')}{u'^n(u'-u)} \ , \tag{3.13}$$

where we used

$$\begin{aligned} s(u') &= 3s_{\eta'} - t - u' = s + u - u' \ , \\ u(s') &= 3s_{\eta'} - t - s' = s + u - s' \ , \end{aligned} \tag{3.14}$$

and $P^t_{n-1}(s,t,u)$ is a subtraction polynomial of order n. Its coefficients depend on t and because of Eq. (3.3) it can be written in the form

$$P^t_{n-1}(s,t,u) = p_0(t) + p_1(t)(s-u) + \dots \ . \tag{3.15}$$

We now introduce a cutoff Λ^2 to the dispersion integrals, which is chosen such that $\Lambda^2 \gg s,u$, and we can expand

$$\frac{1}{s'-s} = \frac{1}{s'} + \frac{s}{s'^2} + \dots \ . \tag{3.16}$$

The remainder of the dispersion integral then becomes

$$\frac{s^n}{2\pi i}\int_{\Lambda^2}^{\infty} ds' \frac{\operatorname{disc}\mathcal{M}(s',t,u(s'))}{s'^n(s'-s)} = s^n I(t) + \mathcal{O}(s^{n+1}) \ . \tag{3.17}$$

The u'-integral can be treated analogously. Terms of higher order in s and u are suppressed due to the low-energy restriction of the system and will therefore be discarded[#2]: the additional terms of order s^n and u^n can be absorbed by incorporating an additional term in the subtraction polynomial. In principle one has to choose the subtraction polynomial such that the discarded terms are sufficiently small. We find

$$\mathcal{M}(s,t,u) = P^t_{n}(s,t,u) + \frac{s^n}{2\pi i}\int_{s_0}^{\Lambda^2} ds' \frac{\operatorname{disc}\mathcal{M}(s',t,u(s'))}{s'^n(s'-s)} + \frac{u^n}{2\pi i}\int_{u_0}^{\Lambda^2} du' \frac{\operatorname{disc}\mathcal{M}(s(u'),t,u')}{u'^n(u'-u)} \ , \tag{3.18}$$

where we neglect terms of $\mathcal{O}(s^n,u^n)$. We now perform a partial-wave expansion of the s- and u-channel of the amplitude,

$$\begin{aligned} \mathcal{M}(s,t,u) &= m_0(s) + m_{l\geq 2}(s,t,u) \ , \\ \mathcal{M}(s,t,u) &= n_0(u) + n_1(u)\cos\theta_u + n_{l\geq 2}(s,t,u) \ , \end{aligned} \tag{3.19}$$

with the definition of the scattering angle $\cos\theta_u$ as above. Note that the $\pi\pi$ scattering channel is purely isospin $I = 0$, so only even partial waves can contribute. We truncate the partial

[#2] In a chiral perturbation theory framework these terms are of $\mathcal{O}(p^{2n+2})$.

wave expansion at $\ell = 1$: it has been shown in Ref. [29] that already the $\pi\eta$ P wave produces a negligible effect and the process is entirely dominated by S waves. We note that the above truncation of the series means that we assume partial waves of $\ell \geq 2$ to be *real*: only their discontinuities are neglected. In Section B.4 we have performed an estimate of the effects of such an approximation in the case of $\omega \to 3\pi$ and found that they are indeed tiny.

Inserting the partial-wave expansion into the dispersion integrals and using the above definition for $\cos\theta_u$ we thus find

$$\begin{aligned}\mathcal{M}(s,t,u) = P_n^t(s,t,u) &+ \frac{s^n}{2\pi i}\int_{s_0}^{\Lambda^2} ds' \frac{\operatorname{disc} m_0(s')}{s'^n(s'-s)} + \frac{u^n}{2\pi i}\int_{u_0}^{\Lambda^2} du' \frac{\operatorname{disc} n_0(u')}{u'^n(u'-u)} \\ &+ \frac{u^n}{2\pi i}\int_{u_0}^{\Lambda^2} du' \frac{(u'(u-u'+s-t)+\Delta_{\eta'\pi}\Delta_{\eta\pi})\operatorname{disc} n_1(u')}{u'^{n+1}\kappa_{\pi\eta}(u')(u'-u)} \,, \end{aligned} \tag{3.20}$$

where the integral over the $\pi\eta$ P wave can be simplified according to

$$\begin{aligned}&\frac{u^n}{2\pi i}\int_{u_0}^{\Lambda^2} du' \frac{(u'(u-u'+s-t)+\Delta_{\eta'\pi}\Delta_{\eta\pi})\operatorname{disc} n_1(u')}{u'^{n+1}\kappa_{\pi\eta}(u')(u'-u)} \\ &\quad= \frac{u^n}{2\pi i}\int_{u_0}^{\Lambda^2} du' \frac{\operatorname{disc} n_1(u')}{u'^n\kappa_{\pi\eta}(u')} + (s-t)\frac{u^n}{2\pi i}\int_{u_0}^{\Lambda^2} du' \frac{\operatorname{disc} n_1(u')}{u'^n\kappa_{\pi\eta}(u')(u'-u)} \\ &\qquad+ \Delta_{\eta'\pi}\Delta_{\eta\pi}\frac{u^n}{2\pi i}\int_{u_0}^{\Lambda^2} du' \frac{\operatorname{disc} n_1(u')}{u'^{n+1}\kappa_{\pi\eta}(u')(u'-u)} \,. \end{aligned} \tag{3.21}$$

The first integral is a polynomial in u and can be absorbed in $P_n^t(s,t,u)$ as well as a piece proportional to u^{n-1} that arises from adding and subtracting u' in the last integral of Eq. (3.21). We are left with

$$\begin{aligned}\mathcal{M}(s,t,u) = P_n^t(s,t,u) &+ \frac{s^n}{2\pi i}\int_{s_0}^{\Lambda^2} ds' \frac{\operatorname{disc} m_0(s')}{s'^n(s'-s)} + \frac{u^n}{2\pi i}\int_{u_0}^{\Lambda^2} du' \frac{\operatorname{disc} n_0(u')}{u'^n(u'-u)} \\ &+ \Big[u(s-t)+\Delta_{\eta'\pi}\Delta_{\eta\pi}\Big]\frac{u^{n-1}}{2\pi i}\int_{u_0}^{\Lambda^2} du' \frac{\operatorname{disc} n_1(u')}{u'^n\kappa_{\pi\eta}(u')(u'-u)} \,. \end{aligned} \tag{3.22}$$

The same exercise can be performed at fixed u and yields

$$\begin{aligned}\mathcal{M}(s,t,u) = P_n^u(s,t,u) &+ \frac{s^n}{2\pi i}\int_{s_0}^{\Lambda^2} ds' \frac{\operatorname{disc} m_0(s')}{s'^n(s'-s)} + \frac{t^n}{2\pi i}\int_{t_0}^{\Lambda^2} dt' \frac{\operatorname{disc} n_0(t')}{t'^n(t'-t)} \\ &+ \Big[t(s-u)+\Delta_{\eta'\pi}\Delta_{\eta\pi}\Big]\frac{t^{n-1}}{2\pi i}\int_{t_0}^{\Lambda^2} dt' \frac{\operatorname{disc} n_1(t')}{t'^n\kappa_{\pi\eta}(t')(t'-t)} \,. \end{aligned} \tag{3.23}$$

Comparing Eqs. (3.22) and (3.23) we observe that the term containing s-channel $\pi\pi$ scattering is the same in both cases. Moreover at fixed t the latter two integrals of Eq. (3.23) can be absorbed in $P_n^t(s,t,u)$ and vice versa for fixed u. We can thus write down a symmetrized dispersion relation,

$$\begin{aligned}\mathcal{M}(s,t,u) = P_n(s,t,u) &+ \frac{s^n}{2\pi i}\int_{s_0}^{\Lambda^2} ds' \frac{\operatorname{disc} m_0(s')}{s'^n(s'-s)} \\ &+ \frac{u^n}{2\pi i}\int_{u_0}^{\Lambda^2} du' \frac{\operatorname{disc} n_0(u')}{u'^n(u'-u)} + \frac{t^n}{2\pi i}\int_{t_0}^{\Lambda^2} dt' \frac{\operatorname{disc} n_0(t')}{t'^n(t'-t)} \end{aligned}$$

$$+\Big[u(s-t)+\Delta_{\eta'\pi}\Delta_{\eta\pi}\Big]\frac{u^{n-1}}{2\pi i}\int_{u_0}^{\Lambda^2}du'\frac{\mathrm{disc}\,n_1(u')}{u'^n\kappa_{\pi\eta}(u')(u'-u)}$$
$$+\Big[t(s-u)+\Delta_{\eta'\pi}\Delta_{\eta\pi}\Big]\frac{t^{n-1}}{2\pi i}\int_{t_0}^{\Lambda^2}dt'\frac{\mathrm{disc}\,n_1(t')}{t'^n\kappa_{\pi\eta}(t')(t'-t)}\ . \qquad (3.24)$$

In summary the $\eta' \to \eta\pi\pi$ decay amplitude can be decomposed according to

$$\mathcal{M}(s,t,u) = \mathcal{M}_0(s) + \mathcal{M}_0^{\pi\eta}(t) + \{(s-u)t + \Delta_{\eta'\pi}\Delta_{\eta\pi}\}\mathcal{M}_1^{\pi\eta}(t) + (t \leftrightarrow u)\ , \qquad (3.25)$$

where $\mathcal{M}_0(s), \mathcal{M}_{0,1}^{\pi\eta}(t)$ are functions of one variable that only possess a right-hand cut. Note again that the above relation is predicated on neglecting discontinuities of $\ell \geq 2$ partial waves.

3.3.2 Unitarity implications for the final-state scattering amplitudes

In this subsection we will briefly discuss the final-state scattering amplitudes that are involved in $\eta' \to \eta\pi\pi$, namely $\pi\pi \to \pi\pi$ and $\pi\eta \to \pi\eta$. We define the amplitude of the $\pi\pi$ intermediate states (assuming isospin conservation) according to

$${}_I\langle\pi^i(p_1)\pi^j(p_2)|\mathcal{T}_{\pi\pi}|\pi^k(p_3)\pi^l(p_4)\rangle_I = \mathcal{T}_I^{ij,kl}(s,\theta_s)\ , \qquad (3.26)$$

where the label I denotes the total isospin of the $\pi\pi$ scattering amplitude, s denotes the center-of-mass energy squared of the $\pi\pi$ pair and θ_s is the center-of-mass scattering angle between the initial and the final state. The pion eigenstates in isospin basis are related to the eigenstates in the particle basis according

$$|\pi^\pm\rangle = \frac{1}{\sqrt{2}}(|\pi^1\rangle \pm i|\pi^2\rangle\ , \qquad |\pi^0\rangle = |\pi^3\rangle\ . \qquad (3.27)$$

We can define projection operators for the pion pairs,

$$|\pi^k\pi^l\rangle_I = \mathcal{P}_I^{kl,ij}|\pi^i\pi^j\rangle\ , \qquad (3.28)$$

which take the form [122]

$$\mathcal{P}_0^{kl,ij} = \frac{1}{3}\delta^{ij}\delta^{kl}\ ,$$
$$\mathcal{P}_1^{kl,ij} = \frac{1}{2}(\delta^{ik}\delta^{jl} - \delta^{il}\delta^{kj})\ ,$$
$$\mathcal{P}_2^{kl,ij} = \frac{1}{2}(\delta^{ik}\delta^{jl} + \delta^{il}\delta^{kj}) - \frac{1}{3}\delta^{ij}\delta^{kl}\ . \qquad (3.29)$$

These hermitian operators fulfill $\mathcal{P}_I^{kl,ab}\mathcal{P}_J^{ab,ij} = \delta_{IJ}\mathcal{P}_I^{ij,kl}$, and can be used to write the $\pi\pi$ amplitude as

$$\mathcal{T}_{\pi\pi}^{ij,kl}(s,\theta_s) = \mathcal{P}_0^{ij,kl}\mathcal{T}_0(s,\theta_s) + \mathcal{P}_1^{ij,kl}\mathcal{T}_1(s,\theta_s) + \mathcal{P}_2^{ij,kl}\mathcal{T}_2(s,\theta_s)\ , \qquad (3.30)$$

where the $\mathcal{T}_I$ are the respective isospin amplitudes.

The unitarity relation Eq. (1.24) for $\pi\pi$ scattering after carrying out the integration over the zero component translates to

$$\mathrm{Im}\,\mathcal{T}_{\pi\pi}^{ij,kl}(s,\theta_s) = \frac{1}{4(2\pi)^2}\sum_{a,b}\int\frac{d^3k_1 d^3k_2}{2k_1^0 2k_2^0}\delta^4(p_1+p_2-k_1-k_2)\mathcal{T}_{\pi\pi}^{ij,ab}(s,\theta_s')\mathcal{T}_{\pi\pi}^{*ab,kl}(s,\theta_s'')\ , \qquad (3.31)$$

where the sum runs over all possible $\pi\pi$ intermediate states and we have accounted for a symmetry factor of 1/2. θ_s' denotes the center-of-mass scattering angle between the initial and intermediate state and θ_s'' the center-of-mass scattering angle between the intermediate and final state. Inserting Eq. (3.30) on the left- and right-hand side of Eq. (3.31) we arrive at (suppressing for the moment the arguments of the functions $\mathcal{T}_I$)

$$\mathcal{P}_0^{ij,kl}\mathrm{Im}\,\mathcal{T}_0 + \mathcal{P}_1^{ij,kl}\mathrm{Im}\,\mathcal{T}_1 + \mathcal{P}_2^{ij,kl}\mathrm{Im}\,\mathcal{T}_2 = \frac{1}{64\pi^2}\int \frac{d^3k_1 d^3k_2}{k_1^0 k_2^0}\delta^4(p_1+p_2-k_1-k_2) \times \left(\mathcal{P}_0^{ij,kl}\mathcal{T}_0\mathcal{T}_0^* + \mathcal{P}_1^{ij,kl}\mathcal{T}_1\mathcal{T}_1^* + \mathcal{P}_2^{ij,kl}\mathcal{T}_2\mathcal{T}_2^*\right) , \tag{3.32}$$

from which we can project out the partial-wave amplitudes to obtain

$$\mathrm{Im}\,\mathcal{T}_I(s,\theta_s) = \frac{1}{64\pi^2}\int \frac{d^3k_1 d^3k_2}{k_1^0 k_2^0}\delta^4(p_1+p_2-k_1-k_2)\mathcal{T}_I(s,\theta_s')\mathcal{T}_I^*(s,\theta_s'') \ . \tag{3.33}$$

Performing the momentum integration yields

$$\mathrm{Im}\,\mathcal{T}_I(s,\theta_s) = \frac{1}{128\pi^2}\sqrt{1-\frac{4M_\pi^2}{s}}\int d\Omega_s'\mathcal{T}_I(s,\theta_s')\mathcal{T}_I^*(s,\theta_s'') \ , \tag{3.34}$$

where the integration runs over the solid angle Ω_s' between initial and intermediate state pions. We now insert the previously defined partial-wave expansion of the $\pi\pi \to \pi\pi$ scattering amplitude,

$$\mathcal{T}_I(s,t) = 32\pi\sum_\ell (2l+1)t_\ell^I(s)P_\ell(z) \ , \tag{3.35}$$

and use[#3]

$$\int d\Omega' P_\ell(\cos\theta_s')P_{l'}(\cos\theta_s'') = \frac{4\pi}{2l+1}\delta_{ll'}P_\ell(\cos\theta_s) \ , \tag{3.36}$$

to arrive at a unitarity relation for the partial-wave amplitude,

$$\mathrm{Im}\,t_\ell^I(s) = \sqrt{1-\frac{4M_\pi^2}{s}}t_\ell^I(s)t_\ell^{I*}(s) \ . \tag{3.37}$$

which suggests the representation

$$t_\ell^I(s) = \frac{1}{\sqrt{1-4M_\pi^2/s}}e^{i\delta_\ell^I(s)}\sin\delta_\ell^I(s) \ , \tag{3.38}$$

where $\delta_\ell^I(s)$ is the $\pi\pi$ scattering phase shift with angular momentum ℓ and isospin I. Consequently, if we restrict ourselves to include only S and P waves we find for the isospin amplitudes

$$\mathcal{T}_0(s,\theta_s) = \frac{32\pi}{\sqrt{1-4M_\pi^2/s}}e^{i\delta_0^0(s)}\sin\delta_0^0(s) \ ,$$
$$\mathcal{T}_1(s,\theta_s) = \frac{96\pi\cos\theta_s}{\sqrt{1-4M_\pi^2/s}}e^{i\delta_1^1(s)}\sin\delta_1^1(s) \ ,$$

[#3] This relation can easily be proven using the addition theorem for spherical functions $P_\ell(\cos\theta'') = \frac{4\pi}{2l+1}\sum_{m=-l}^{l}Y_{lm}(\theta,\phi)Y_{lm}^*(\theta',\phi')$ for angles that fulfill $\cos\theta'' = \cos\theta\cos\theta' + \sin\theta\sin\theta'\cos(\phi-\phi')$.

$$\mathcal{T}_2(s,\theta_s) = \frac{32\pi}{\sqrt{1-4M_\pi^2/s}} e^{i\delta_0^2(s)} \sin\delta_0^2(s) \ . \tag{3.39}$$

Isospin conservation of the decay constrains the total isospin of the final-state pions to $I = 0$, so the latter two equations are only shown for educational purposes. From now on we will label the phase-shift by its angular momentum, $\delta_0^0 \doteq \delta_0$

The $\pi\eta$ scattering amplitude can be treated in a completely analogous fashion. We define

$$\langle \pi^i(p_1)\eta(p_2)|\mathcal{T}_{\pi\eta}|\pi^k(p_3)\eta(p_4)\rangle = \mathcal{T}_{\pi\eta}^{ik}(t,\theta_t) \ , \tag{3.40}$$

where the $\pi\eta$ pair always has total isospin $I = 1$ (the pion has isospin one and the η' has isospin zero), which is the only isospin channel that has to be taken into account. We can thus define

$$\mathcal{T}_{\pi\eta}^{ik}(t,\theta_t) = \delta^{ik}\mathcal{T}_{\pi\eta}(t,\theta_t) \ . \tag{3.41}$$

Using the unitarity relation in exactly the same way as before we can derive a representation for the $\pi\eta$ amplitude,

$$\mathcal{T}_{\pi\eta}(t,\theta_t) = \frac{8\pi}{\sqrt{\frac{\lambda(t,M_\eta^2,M_\pi^2)}{4t^2}}} \Big(\sin\delta_0^{\pi\eta}(t) e^{i\delta_0^{\pi\eta}(t)} + 3\cos\theta_t \sin\delta_1^{\pi\eta}(t) e^{i\delta_1^{\pi\eta}(t)} \Big) \ , \tag{3.42}$$

where $\delta_\ell^{\pi\eta}$ is $\pi\eta$ phase shift of angular momentum ℓ. Equipped with these representations of the scattering amplitude we can now set out to derive dispersion relations for $\eta' \to \eta\pi\pi$.

3.3.3 Integral equations for $\eta' \to \eta\pi\pi$

The unitarity condition for the decay of the η' to a generic three-body final state n can be written as[#4]

$$\operatorname{disc}\mathcal{M}_n = i\sum_{n'}(2\pi)^4\delta^{(4)}(p_n - p_{n'})\mathcal{T}_{n'n}^*\mathcal{M}_{n'} \ , \tag{3.43}$$

where $\mathcal{M}_{n'}$ denotes the $\eta' \to n'$ decay amplitude and $\mathcal{T}_{n'n}$ describes the $n' \to n$ transition, while the sum over n' runs over all possible intermediate $\pi\pi$ and $\pi\eta$ states. The integration over the intermediate state momenta is implied in this short-hand notation. In the nomenclature of the previous section the decay process $\eta' \to \eta\pi\pi$ can be described by the amplitude

$$\langle \pi^i(p_1)\pi^j(p_2)\eta(p_3)|\mathcal{M}|\eta'(P_{\eta'})\rangle = \mathcal{M}^{ij}(s,t,u) = \delta^{ij}\mathcal{M}(s,t,u) \ . \tag{3.44}$$

where $\mathcal{M}(s,t,u)$ can be decomposed according to Eq. (3.25). Plugged into Eq. (3.43) this leads to

$$\begin{aligned}\operatorname{disc}\mathcal{M}^{ij}(s,t,u) = \frac{i}{(2\pi)^2}\Bigg\{ &\frac{1}{2}\sum_{a,b=1}^{3}\int \frac{d^3k_a d^3k_b}{2k_a^0 2k_b^0}\delta^4(k_a+k_b-p_1-p_2)\mathcal{T}_{\pi\pi}^{*ab,ij}(s,\theta_s'')\mathcal{M}^{ab}(s,t',u') \\ &+\sum_{a=1}^{3}\int \frac{d^3k_a d^3k_\eta}{2k_a^0 2k_\eta^0}\delta^4(k_a+k_\eta-p_2-p_3)\mathcal{T}_{\pi\eta}^{*ai}(t,\theta_t'')\mathcal{M}^{aj}(s',t,u')\end{aligned}$$

[#4] In the following relations that involve the discontinuity are always thought to contain an implicit θ-function that denotes the opening of the respective threshold, i.e. $\theta(s-4M_\pi^2)$ for the $\pi\pi$ channel and $\theta(t-(M_\eta+M_\pi)^2)$ for the $\pi\eta$ channel.

$$+\sum_{a=1}^{3}\int \frac{d^3k_a d^3k_\eta}{2k_a^0 2k_\eta^0}\delta^4(k_a+k_\eta-p_1-p_3)\mathcal{T}^{*ai}_{\pi\eta}(u,\theta''_u)\mathcal{M}^{aj}(s',t',u)\Big\}\ , \tag{3.45}$$

where $k_{a,b}$ denotes the momentum of the intermediate pion states and k_η is the momentum of the intermediate η. Evaluating the sum and carrying out the phase-space integration, we obtain

$$\begin{aligned}\operatorname{disc}\mathcal{M}(s,t,u) = \frac{i}{2\pi}\Big\{&\frac{1}{32\pi}\sqrt{1-\frac{4M_\pi^2}{s}}\int d\Omega'_s\,\mathcal{T}_0^*(s,\theta''_s)\mathcal{M}(s,t',u')\\ &+\frac{1}{8\pi}\sqrt{\frac{\lambda(t,M_\eta^2,M_\pi^2)}{4t^2}}\int d\Omega'_t\,\mathcal{T}^*_{\pi\eta}(t,\theta''_t)\mathcal{M}(s',t,u')\\ &+\frac{1}{8\pi}\sqrt{\frac{\lambda(u,M_\eta^2,M_\pi^2)}{4u^2}}\int d\Omega'_u\,\mathcal{T}^*_{\pi\eta}(u,\theta''_u)\mathcal{M}(s',t',u)\Big\}\ ,\end{aligned} \tag{3.46}$$

where $d\Omega'_{s,t,u}$ denotes the solid-angle integration measure between the initial and intermediate state of the respective s-,t-,u-channel subsystem. Using the representations for the partial-wave amplitudes Eq. (3.39) and Eq. (3.42), we find

$$\begin{aligned}\operatorname{disc}\mathcal{M}(s,t,u) =\frac{i}{2\pi}\Big\{&\int d\Omega'_s e^{-i\delta_0(s)}\sin\delta_0(s)\mathcal{M}(s,t',u')\\ &+\int d\Omega'_t\Big(\sin\delta_0^{\pi\eta}(t)e^{-i\delta_0^{\pi\eta}(t)}+3\cos\theta''_t\sin\delta_1^{\pi\eta}(t)e^{-i\delta_1^{\pi\eta}(t)}\Big)\mathcal{M}(s',t,u')\\ &+\int d\Omega'_u\Big(\sin\delta_0^{\pi\eta}(u)e^{-i\delta_0^{\pi\eta}(u)}+3\cos\theta''_u\sin\delta_1^{\pi\eta}(u)e^{-i\delta_1^{\pi\eta}(u)}\Big)\mathcal{M}(s',t',u)\Big\}\ .\end{aligned} \tag{3.47}$$

Finally, we can insert the decomposition of the decay amplitude Eq. (3.25) on the left- and right-hand side of Eq. (3.47) and find unitarity relations for each partial-wave:

$$\begin{aligned}\operatorname{disc}\mathcal{M}_0(s) &= 2i\big\{\mathcal{M}_0(s)+\hat{\mathcal{M}}_0(s)\big\}\sin\delta_0(s)e^{-i\delta_0(s)}\ ,\\ \operatorname{disc}\mathcal{M}_0^{\pi\eta}(t) &= 2i\big\{\mathcal{M}_0^{\pi\eta}(t)+\hat{\mathcal{M}}_0^{\pi\eta}(t)\big\}\sin\delta_0^{\pi\eta}(t)e^{-i\delta_0^{\pi\eta}(t)}\ ,\\ \operatorname{disc}\mathcal{M}_1^{\pi\eta}(t) &= 2i\big\{\mathcal{M}_1^{\pi\eta}(t)+\hat{\mathcal{M}}_1^{\pi\eta}(t)\big\}\sin\delta_1^{\pi\eta}(t)e^{-i\delta_1^{\pi\eta}(t)}\ ,\end{aligned} \tag{3.48}$$

while analogous equations for the u-channel can be obtained by exchanging $t\leftrightarrow u$. The *inhomogeneities* $\hat{\mathcal{M}}_I^{(\pi\eta)}$ are given as (suppressing for a moment the pertinent arguments of the various functions for simplicity)

$$\begin{aligned}\hat{\mathcal{M}}_0 &= 2\langle\mathcal{M}_0^{\pi\eta}\rangle+\frac{1}{2}\big[3(s-s_0)(3s_0-s)+2\Delta_{\eta'\pi}\Delta_{\eta\pi}\big]\langle\mathcal{M}_1^{\pi\eta}\rangle+\frac{1}{2}\langle z_s^2\mathcal{M}_1^{\pi\eta}\rangle\ ,\\ \hat{\mathcal{M}}_0^{\pi\eta} &= \langle\mathcal{M}_0\rangle^- + \langle\mathcal{M}_0^{\pi\eta}\rangle^+ + \frac{1}{4}\Big[3(s_{\eta'}-t)(3s_{\eta'}-t)+2\Delta_{\eta'\pi}\Delta_{\eta\pi}\Big(1-\frac{\Delta_{\eta'\pi}\Delta_{\eta\pi}}{2t^2}\Big)\Big]\langle\mathcal{M}_1^{\pi\eta}\rangle^+\\ &\quad-\frac{\kappa_{\pi\eta}}{2}\Big[t+\frac{\Delta_{\eta'\pi}\Delta_{\eta\pi}}{t}\Big]\langle z_t\mathcal{M}_1^{\pi\eta}\rangle^+ + \frac{\kappa_{\pi\eta}^2}{4}\langle z_t^2\mathcal{M}_1^{\pi\eta}\rangle^+\ ,\\ \hat{\mathcal{M}}_1^{\pi\eta} &= \frac{3}{t\kappa_{\pi\eta}}\Big\{\langle z_t\mathcal{M}_0\rangle^- + \langle z_t\mathcal{M}_0^{\pi\eta}\rangle^+\end{aligned}$$

$$+\frac{1}{4}\Big[3(s_{\eta'}-t)(3s_{\eta'}-t)+2\Delta_{\eta'\pi}\Delta_{\eta\pi}\Big(1-\frac{\Delta_{\eta'\pi}\Delta_{\eta\pi}}{2t^2}\Big)\Big]\langle z_t\mathcal{M}_1^{\pi\eta}\rangle^+$$
$$-\frac{\kappa_{\pi\eta}}{2}\Big[t+\frac{\Delta_{\eta'\pi}\Delta_{\eta\pi}}{t}\Big]\langle z_t^2\mathcal{M}_1^{\pi\eta}\rangle^+ + \frac{\kappa_{\pi\eta}^2}{4}\langle z_t^3\mathcal{M}_1^{\pi\eta}\rangle^+\Big\}\,, \tag{3.49}$$

where we defined the short-hand notation,

$$\langle z^n f\rangle^{(\pm)} = \frac{1}{2}\int_{-1}^{1} dz\, z^n f\Big(\frac{3s_{\eta'}-s+z\kappa_i(s)(\pm\Delta_{\eta'\pi}\Delta_{\eta\pi}/s)}{2}\Big)\,, \tag{3.50}$$

with $i=\pi\pi,\pi\eta$ chosen appropriately for the specific channels. Harmless as Eq. (3.49) may look it requires a significant amount of work to perform the correct analytic continuation of these relations, a topic that will be discussed extensively in Section 3.4. For now we will work towards a solution of the unitarity relations, which we discuss generically for

$$\operatorname{disc}\mathcal{M}(s) = 2i(\mathcal{M}(s)+\hat{\mathcal{M}}(s))\sin\delta(s)e^{-i\delta(s)}\,. \tag{3.51}$$

We have already seen the solution of the *homogeneous* version of this equation, i.e. where $\hat{\mathcal{M}}(s)=0$, in Section 1.2.2: it is precisely the Omnès function. The solution of the inhomogeneous equation can be found resorting to variation of parameters: we make the ansatz that the full solution is given as $\mathcal{M}(s)=m(s)\Omega(s)$, where $m(s)$ is the function we have to vary. We first rewrite Eq. (3.51) as

$$\mathcal{M}(s+i\epsilon)e^{-2i\delta(s)} - \mathcal{M}(s-i\epsilon) = 2i\hat{\mathcal{M}}(s)\sin\delta(s)e^{-i\delta(s)}\,. \tag{3.52}$$

Inserting the variation ansatz and using $\Omega(s\pm i\epsilon)=|\Omega(s)|e^{\pm i\delta(s)}$, we find

$$(m(s+i\epsilon)-m(s-i\epsilon))|\Omega(s)|e^{-i\delta(s)} = 2i\hat{\mathcal{M}}(s)\sin\delta(s)e^{-i\delta(s)}\,, \tag{3.53}$$

from which we deduce a relation for the discontinuity of $m(s)$,

$$\operatorname{disc} m(s) = \frac{2i\sin\delta(s)\hat{\mathcal{M}}(s)}{|\Omega(s)|}\,. \tag{3.54}$$

We can now write down a dispersion relation for the function $m(s)$, namely

$$m(s) = P(s) + \frac{s^n}{\pi}\int_{s_0}^{\infty}\frac{ds'}{s'^n}\frac{\sin\delta(s')\hat{\mathcal{M}}(s')}{|\Omega(s')|(s'-s)}\,, \tag{3.55}$$

where s_0 is the threshold of the pertinent channel and $P(s)$ is a subtraction polynomial of order $n-1$. We thus obtain the desired integral equations that solve Eq. (3.48),

$$\mathcal{M}_0(s) = \Omega_0(s)\Big\{P_0(s)+\frac{s^n}{\pi}\int_{s_0}^{\infty}\frac{ds'}{s'^n}\frac{\hat{\mathcal{M}}_0(s')\sin\delta_0(s')}{|\Omega_0(s')|(s'-s)}\Big\}\,,$$
$$\mathcal{M}_0^{\pi\eta}(t) = \Omega_0^{\pi\eta}(t)\Big\{P_0^{\pi\eta}(t)+\frac{t^n}{\pi}\int_{t_0}^{\infty}\frac{dt'}{t'^n}\frac{\hat{\mathcal{M}}_0^{\pi\eta}(t')\sin\delta_0^{\pi\eta}(t')}{|\Omega_0^{\pi\eta}(t')|(t'-t)}\Big\}\,,$$
$$\mathcal{M}_1^{\pi\eta}(t) = \Omega_1^{\pi\eta}(t)\Big\{P_1^{\pi\eta}(t)+\frac{t^n}{\pi}\int_{t_0}^{\infty}\frac{dt'}{t'^n}\frac{\hat{\mathcal{M}}_1^{\pi\eta}(t')\sin\delta_1^{\pi\eta}(t')}{|\Omega_1^{\pi\eta}(t')|(t'-t)}\Big\}\,. \tag{3.56}$$

The order n of the subtraction polynomials in the dispersion relations are determined such that the dispersion integral is convergent. However, we can always "oversubtract" a dispersion integral at the expense of having to fix the additional subtraction constants and possible ramifications for the high-energy behavior of our amplitude.[#5] To study the convergence behavior of the integrand we have to make assumptions about the asymptotic behavior of the phase shifts. We let

$$\delta_0(s) \to 2\pi \ , \quad \delta_0^{\pi\eta}(t) \to \pi \ , \quad \delta_1^{\pi\eta}(t) \to 0 \ , \tag{3.57}$$

as $s \to \infty$ and $t \to \infty$. We wish to briefly comment on the asymptotic behavior of the isospin-zero $\pi\pi$ phase shift $\delta_0(s)$. A fully consistent description would require the solution of a coupled-channel problem with $\pi\pi$ and $K\bar{K}$ intermediate states. If one reduces the system to an effective one-channel problem two scenarios of the phase motion at the $f_0(980)$ resonance are conceivable depending on how strongly the system couples to strangeness [123,124]: large strangeness production manifests itself as a peak at the position of the $f_0(980)$ in the corresponding Omnès function and thus the phase shift is increased by about π while running through the resonance (this scenario is realized in the $\pi\pi$ scattering phase shift). If the coupling to the channel with strangeness is weak, the corresponding Omnès function has a dip at the resonance position and the corresponding phase shift decreases (this is realized in the phase of the scalar form factor of the pion). The decision to choose the first scenario in our analysis is motivated by two observations. On the one hand the resonance Lagrangian of $\eta' \to \eta\pi\pi$ strongly couples to the $f_0(980)$ [105], on the other hand one can show using the large-N_C ChPT Lagrangian (see e.g. Ref. [105]) that the coupling to the $\eta' \to \eta K\bar{K}$-channel is sizable, suggesting large strangeness production.

Let us assume that the asymptotic behavior of the phase sets in at $s = \Lambda_\Omega^2$, so that $\delta(s) = k\pi$ for $s \geq \Lambda_\Omega^2$. Then using the integral representation of the Omnès function as derived in Section 1.2.2, we find

$$\begin{aligned}
\Omega(s) &= \exp\Big\{\frac{s}{\pi}\int_{s_0}^{\infty} ds' \frac{\delta(s')}{s'(s'-s)}\Big\} \\
&= \exp\Big\{\frac{s}{\pi}\int_{s_0}^{\Lambda_\Omega^2} ds' \frac{\delta(s')}{s'(s'-s)} + \frac{s}{\pi}\int_{\Lambda_\Omega^2}^{\infty} ds' \frac{\delta(s')}{s'(s'-s)}\Big\} \\
&\propto \Big(\frac{\Lambda_\Omega^2}{\Lambda_\Omega^2 - s}\Big)^k \quad \text{for} \quad s \to \infty \ ,
\end{aligned} \tag{3.58}$$

where we used that the first term in the second line is constant as $s \to \infty$. Note that for $\Omega_1^1(s)$ this asymptotic behavior concurs with the $1/s$ behavior of the pion vector form factor ($\delta_1(s) \to \pi$) that is found in perturbative QCD, see Ref. [125].

Additionally the Froissart–Martin [45,46] bound constrains the asymptotic behavior of the amplitude according to

$$\mathcal{M}_0(s) = \mathcal{O}(s) \ , \quad \mathcal{M}_0^{\pi\eta}(t) = \mathcal{O}(t) \ , \quad \mathcal{M}_1^{\pi\eta}(t) = \mathcal{O}(t^{-1}) \ , \tag{3.59}$$

which allows the following choice for the subtraction polynomials,

$$P_0(s) = \alpha_0^{\pi\pi} + \beta_0^{\pi\pi} s + \gamma_0^{\pi\pi} s^2 + \delta_0^{\pi\pi} s^3 \ ,$$

[#5] Each additional subtraction constant contributes an additional power of s to the asymptotic behavior of the amplitude if the corresponding sum-rule for the subtraction constant is not fulfilled exactly. This can lead to a violation of the Froissart-Martin bound.

$$P_0^{\pi\eta}(t) = \alpha_0^{\pi\eta} + \beta_0^{\pi\eta} t + \gamma_0^{\pi\eta} t^2 \ ,$$
$$P_1^{\pi\eta}(t) = 0 \ . \tag{3.60}$$

The subtraction constants thus defined are correlated since the decomposition Eq. (3.25) is not unique. In Appendix B.1 we show that it remains invariant under the transformation

$$\mathcal{M}_0(s) \to \mathcal{M}_0(s) + c_1 + c_2(s - s_{\eta'}) \ ,$$
$$\mathcal{M}_0^{\pi\eta}(t) \to \mathcal{M}_0^{\pi\eta}(t) - \frac{1}{2}c_1 + c_2(t - s_{\eta'}) \ . \tag{3.61}$$

This brings us to the final form of the integral equations,

$$\mathcal{M}_0(s) = \Omega_0(s)\left\{\alpha_0^{\pi\pi} + \beta_0^{\pi\pi} s + \gamma_0^{\pi\pi} s^2 + \delta_0^{\pi\pi} s^3 + \frac{s^4}{\pi}\int\limits_{s_0}^{\infty} \frac{ds'}{s'^4} \frac{\hat{\mathcal{M}}_0(s')\sin\delta_0(s')}{|\Omega_0(s')|(s'-s)}\right\} \ ,$$

$$\mathcal{M}_0^{\pi\eta}(t) = \Omega_0^{\pi\eta}(t)\left\{\gamma_0^{\pi\eta} t^2 + \frac{t^3}{\pi}\int\limits_{t_0}^{\infty} \frac{dt'}{t'^3} \frac{\hat{\mathcal{M}}_0^{\pi\eta}(t')\sin\delta_0^{\pi\eta}(t')}{|\Omega_0^{\pi\eta}(t')|(t'-t)}\right\} \ ,$$

$$\mathcal{M}_1^{\pi\eta}(t) = \frac{\Omega_1^{\pi\eta}(t)}{\pi}\int\limits_{t_0}^{\infty} dt' \frac{\hat{\mathcal{M}}_1^{\pi\eta}(t')\sin\delta_1^{\pi\eta}(t')}{|\Omega_1^{\pi\eta}(t')|(t'-t)}\Bigg\} \ . \tag{3.62}$$

The amplitude $\mathcal{M}(s,t,u)$ based on the above integral equations is diagrammatically visualized in Fig. 3.2. Of course such a visualization has to be taken with a grain of salt: we are performing an iterative solution of these equations so there are no well-defined diagrams for tree level, one-loop level, and so forth.

The numerical evaluation of these integral equations is very involved and is discussed in some detail in Section 3.4. We note that in these calculations we shall neglect the $\ell = 1$ $\pi\eta$ partial wave: the P wave in a chiral framework is strongly suppressed with respect to the S wave of $\pi\pi$ and $\pi\eta$ scattering, see for example Ref. [29]. In fact, the $\pi\eta$ P wave has exotic quantum numbers and only starts at $\mathcal{O}(p^8)$ (three loops) in a chiral counting scheme. It is therefore justified to set $\delta_1^{\pi\eta} = 0$, and therefore $\mathcal{M}_1^{\pi\eta}(t) = 0$. We also note that in the following we will use a dispersion integral with three subtractions for the isospin-zero $\pi\pi$ amplitude, so that the system of integral equations is summarily given as

$$\mathcal{M}_0(s) = \Omega_0(s)\left\{\alpha_0^{\pi\pi} + \beta_0^{\pi\pi} s + \gamma_0^{\pi\pi} s^2 + \frac{s^3}{\pi}\int\limits_{s_0}^{\infty} \frac{ds'}{s'^3} \frac{\hat{\mathcal{M}}_0(s')\sin\delta_0(s')}{|\Omega_0(s')|(s'-s)}\right\} \ ,$$

$$\mathcal{M}_0^{\pi\eta}(t) = \Omega_0^{\pi\eta}(t)\left\{\gamma_0^{\pi\eta} t^2 + \frac{t^3}{\pi}\int\limits_{t_0}^{\infty} \frac{dt'}{t'^3} \frac{\hat{\mathcal{M}}_0^{\pi\eta}(t')\sin\delta_0^{\pi\eta}(t')}{|\Omega_0^{\pi\eta}(t')|(t'-t)}\right\} \ . \tag{3.63}$$

In that case the fourth subtraction constant is given by a sum rule,

$$\delta_0^{\pi\pi} = \frac{1}{\pi}\int_{s_0}^{\infty} \frac{ds'}{s'^4} \frac{\hat{\mathcal{M}}_0(s')\sin\delta_0(s')}{|\Omega_0(s')|} \ . \tag{3.64}$$

The reason for introducing this subtraction constant was the assumed high-energy behavior of the integrand of the dispersion integral. It turns out, however, that the integrand is still convergent due to the fact that $\sin\delta_0(s') \to 0$ sufficiently fast. The sum rule (3.64) thus converges as well and the use of Eq. (3.63) is justified.

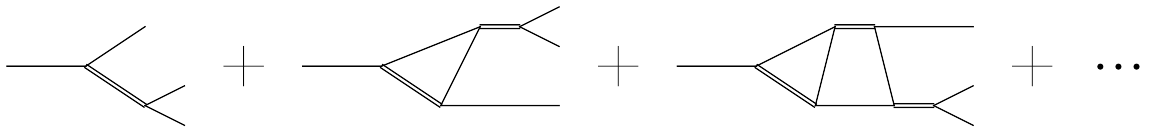

Figure 3.2: Diagrammatic representation of $\mathcal{M}(s,t,u)$ based on the integral equations (3.62). The double lines denote $\pi\pi$ and $\pi\eta$ bubble sums.

3.3.4 Analytic continuation of the inhomogeneities

Before going into the details we wish to recapitulate our general strategy of treating a three-body decay. Let us assume for a moment that we only have particles of the same mass, i.e. $M_{\eta'} = M_\eta = M_\pi$, and the η' cannot decay. Then assuming we disregard all considerations involving isospin the above equations describe a system of $\pi\pi \to \pi\pi$ scattering and the integration in Eq. (3.49) is straightforward: the z integration does not interfere with any of the two-particle thresholds. Assuming isospin conservation[#6] the same still holds if we now set $M_{\eta'} = M_\eta \neq M_\pi$. We then have a coupled system of $\eta\eta \to \pi\pi$ and $\eta\pi \to \eta\pi$ scattering, where the channels s, t, and u are related by crossing symmetry, and the situation can still be treated as described in Section 1.2.1. The evaluation of Eq. (3.49) is still straightforward. If, however, we now allow for $M_{\eta'} > M_\eta + 2M_\pi$, so that the decay $\eta' \to \eta\pi\pi$ becomes possible, the integration contours can hit the two-particle cuts and a new analytic structure develops: a three-particle cut. The strategy now is to start off in the respective scattering regions and perform an analytic continuation to the decay region by distorting the integration contours in such a way as to avoid the two-particle cuts. For more information in the case of $\eta \to 3\pi$ see Refs. [74, 75, 103, 122].

We begin with a study of $\hat{\mathcal{M}}_0(s)$ since the situation is slightly more clear in this case: the integration over the $\pi\eta$ amplitude exclusively involves the center-of-mass angle of the t-channel. It is instructive to restore the arguments of the amplitudes in Eq. (3.49) by performing a change of the integration variable according to

$$z'_s = \frac{1}{\kappa_{\pi\pi}(s)}(2t' - 3s_{\eta'} + s) \ , \tag{3.65}$$

which, neglecting the $\pi\eta$ P wave, leads to

$$\hat{\mathcal{M}}_0(s) = \frac{2}{\kappa_{\pi\pi}(s)} \int_{\mathcal{C}'_t} dt' \mathcal{M}_0^{\pi\eta}(t') \ ,$$

where $\mathcal{C}'_t$ is the integration contour in the complex t'-plane with endpoints $t_-(s)$ and $t_+(s)$, where

$$t_\pm(s) = \frac{1}{2}(3s_{\eta'} - s \pm \kappa_{\pi\pi}(s)) \ . \tag{3.66}$$

For $M_{\eta'} = M_\eta = M_\pi$ the function $\kappa_{\pi\pi}(s)$ and thus the endpoints are purely real. Hence, the integration contour lies on the real axis just above the cut and never crosses it. For physical masses the real and imaginary part of the endpoints as a function of s are shown in Fig. 3.3. It is convenient to define the function

$$\tilde{\kappa}_{\pi\pi}(s) = \frac{\sqrt{|\lambda(M_\pi^2, M_\pi^2, s)\lambda(M_{\eta'}^2, M_\eta^2, s)|}}{s} \ . \tag{3.67}$$

[#6] Simply to keep the η from decaying into 3 pions.

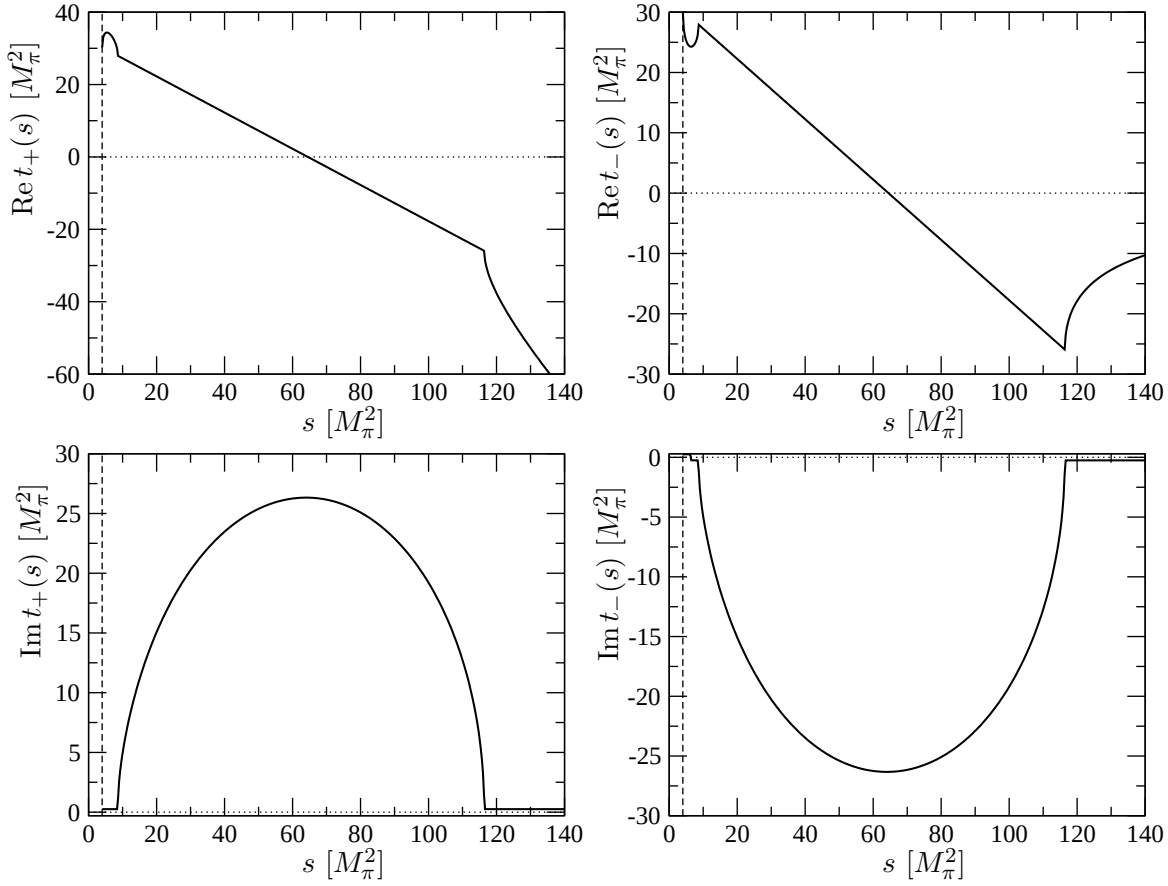

Figure 3.3: Real and imaginary part of the endpoints $t_\pm(s)$ of the integration contour of $\hat{M}_0(s)$. The dashed vertical line denotes the threshold $s = 4M_\pi^2$.

There are basically four sections for specific values of s that we have to distinguish to find the correct analytic continuation of the integration endpoints, which are visualized in Fig. 3.4 (see also the analogous treatment in Ref. [74]):

I) $4M_\pi^2 < s < s_{\rm II} = M_\pi(M_{\eta'}^2 - M_\eta^2)/(M_\eta + M_\pi)$: s lies in the physical decay region and $\kappa_{\pi\pi}(s)$ is purely real. Analogously to the respective $\pi\pi$ scattering process the integration contour just above the elastic threshold is well-defined: it runs infinitesimally above the cut from $t_-(s)$ to $t_+(s)$,

$$t_+(s) = \frac{1}{2}\big(3s_{\eta'} - s + \tilde{\kappa}_{\pi\pi}(s)\big) + i\epsilon \ ,$$
$$t_-(s) = \frac{1}{2}\big(3s_{\eta'} - s - \tilde{\kappa}_{\pi\pi}(s)\big) + i\epsilon \ . \tag{3.68}$$

II) $s_{\rm II} < s < a_s = (M_{\eta'} - M_\eta)^2$: since s is still below the end of the physical decay region, i.e. below the $\eta'\eta$ pseudo-threshold, $\kappa_{\pi\pi}(s)$ is still purely real. However, at the point $s_{\rm II}$ the lower endpoint of the integration contour, $t_-(s)$, approaches the beginning of the cut generated by the $\pi\eta$ threshold and turns around smoothly to the region below the cut. From there the endpoint travels on infinitesimally below the real axis until s reaches the

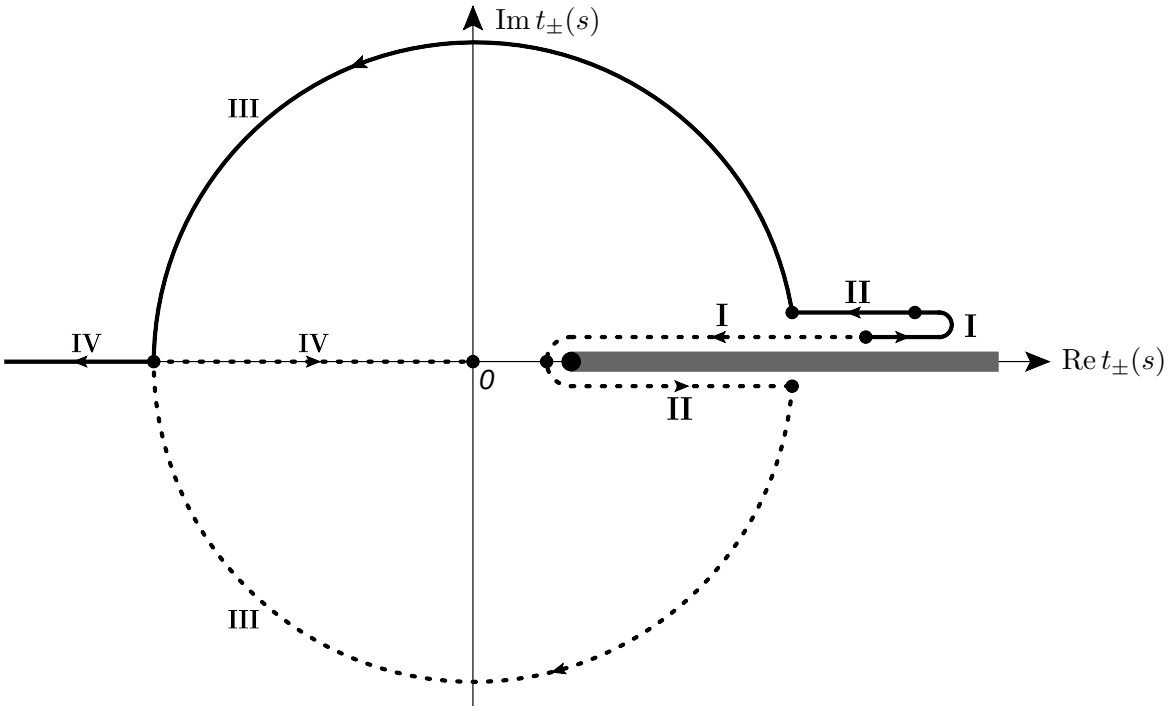

Figure 3.4: Trajectories of the integration endpoints $t_\pm(s)$ in the complex t-plane. The shaded gray line denotes the cut starting at $t = (M_\eta + M_\pi)^2$. Further details may be found in the text.

end of the physical region. The upper endpoint stays above the cut at all times. The prescription for the correct analytic continuation is

$$t_+(s) = \frac{1}{2}\big(3s_{\eta'} - s + \tilde{\kappa}_{\pi\pi}(s)\big) + i\epsilon \ ,$$
$$t_-(s) = \frac{1}{2}\big(3s_{\eta'} - s - \tilde{\kappa}_{\pi\pi}(s)\big) - i\epsilon \ . \tag{3.69}$$

III) $a_s < s < b_s = (M_{\eta'} + M_\eta)^2$: s has now entered the unphysical region above the pseudo-threshold. At this point $\kappa_{\pi\pi}(s)$ is purely imaginary and the endpoints become complex. The trajectory of $t_-(s)$ is continued smoothly into the lower half of the complex t-plane, while $t_+(s)$ turns into the upper half. Both trajectories follow opposing arced paths until they coincide for $s = (M_{\eta'} + M_\eta)^2$. The correct prescription is

$$t_+(s) = \frac{1}{2}\big(3s_{\eta'} - s + i\tilde{\kappa}_{\pi\pi}(s)\big) \ ,$$
$$t_-(s) = \frac{1}{2}\big(3s_{\eta'} - s - i\tilde{\kappa}_{\pi\pi}(s)\big) \ . \tag{3.70}$$

It turns out that parametrizing the integration contour for the numerical implementation by exactly the above prescription is the most efficient and least time consuming way to proceed. A more elaborate discussion of the numerical implementation may be found in Section 3.4.

IV) $b_s < s$: for values of s above the $\eta'\eta$ threshold $\kappa_{\pi\pi}(s)$ is purely real. The correct analytic continuation is to let $t_-(s) \to 0$ and $t_+(s) \to -\infty$ for $s \to \infty$,

$$t_+(s) = \frac{1}{2}\big(3s_{\eta'} - s - \tilde{\kappa}_{\pi\pi}(s)\big) \ ,$$
$$t_-(s) = \frac{1}{2}\big(3s_{\eta'} - s + \tilde{\kappa}_{\pi\pi}(s)\big) \ . \tag{3.71}$$

We wish to emphasize the importance of the point II). Let us assume that $M_{\eta'} < M_\eta + 2M_\pi$, then we have $s_{\rm II} < 4M_\pi^2$, and at no point does the integration contour interfere with the $\pi\eta$ cut in the complex t-plane. Thus for $M_{\eta'} > M_\eta + 2M_\pi$ a novel complex analytic structure with respect to the elastic scattering process is generated: it is precisely a three-particle cut. We will resume the discussion on the analytic structure in the context of $V \to 3\pi$ and also study some direct consequences for the partial-wave amplitude in Section 4.6. An analogous treatment can be performed for $\hat{\mathcal{M}}_0^{\pi\eta}(t)$. The details of that discussion are relegated to Appendix B.2.

We have now established the complete system of integral equations to describe $\eta' \to \eta\pi\pi$. In the following section we will devote some time to explaining the numerical methods that we use to solve these integral equations.

3.4 Solution strategy and numerical methods

In this section we discuss the numerical treatment of the integral equations (3.62). Due to the peculiar structure of the integration path as outlined in the previous section and the singular nature of the integrand of the dispersion integrals this is not a straightforward procedure. The solution of the integral equation is obtained by an iteration procedure: we start with arbitrary functions $\mathcal{M}_0$ and $\mathcal{M}_0^{\pi\eta}$, which we choose to be the respective Omnès functions. The final result is of course independent of the particular choice of these starting points. Then we calculate the inhomogeneities $\hat{\mathcal{M}}_0$ and $\hat{\mathcal{M}}_0^{\pi\eta}$, and insert these into the dispersion integrals (3.62). This procedure is repeated until sufficient convergence with respect to the input functions is reached. The integral equations have a remarkable property that greatly reduces the numerical cost of the calculations: they are linear in the subtraction constants.[#7] Thus we can write

$$\mathcal{M}(s,t,u) = \alpha_0^{\pi\pi}\mathcal{M}_{\alpha_0^{\pi\pi}}(s,t,u) + \beta_0^{\pi\pi}\mathcal{M}_{\beta_0^{\pi\pi}}(s,t,u) + \gamma_0^{\pi\pi}\mathcal{M}_{\gamma_0^{\pi\pi}}(s,t,u) + \gamma_0^{\pi\eta}\mathcal{M}_{\gamma_0^{\pi\eta}}(s,t,u) \ , \tag{3.72}$$

where we defined

$$\mathcal{M}_{\alpha_0^{\pi\pi}}(s,t,u) = \mathcal{M}(s,t,u)\Big|_{\alpha_0^{\pi\pi}=1,\beta_0^{\pi\pi}=\gamma_0^{\pi\pi}=\gamma_0^{\pi\eta}=0} \ , \tag{3.73}$$

and analogously for the remaining *basis functions*. Notice that due to the linearity of the above equation we may use one of the subtraction constants as an overall normalization, for which we choose $\alpha_0^{\pi\pi}$. In the following we will thus refer to rescaled subtraction constants,

$$\beta_0^{\pi\pi} \to \alpha_0^{\pi\pi}\beta_0^{\pi\pi} \ , \qquad \gamma_0^{\pi\pi} \to \alpha_0^{\pi\pi}\gamma_0^{\pi\pi} \ , \qquad \gamma_0^{\pi\eta} \to \alpha_0^{\pi\pi}\gamma_0^{\pi\eta} \ , \tag{3.74}$$

exclusively. Each of the basis functions fulfills the decomposition Eq. (3.25), and we can perform the iteration procedure separately for each of them while fixing the subtraction constants after the iteration.

[#7] We are grateful to Gilberto Colangelo, Stefan Lanz, and Heiri Leutwyler for pointing this out to us.

To further speed up the iteration procedure all non-trivial functions, i.e. all functions that require a numerical integration, are first defined on a discrete one-dimensional array and then interpolated. Away from the kinematic threshold we use cubic splines for the interpolation, while close to kinematic singularities (that includes thresholds and pseudothresholds) we increase the number of grid points using sampling functions of the type,

$$f_n(x) = \frac{\log(1+nx)}{\log(n+1)} \,, \tag{3.75}$$

where n is an integer chosen such that the desired number of grid points is located close to the threshold. We then fit the proper threshold (square-root or cubic square-root) behavior. The numerical solution is implemented in `C++`, making use of the following GNU Scientific Library (GSL) routines:

- `gsl_integration_qag`: simple adaptive Gauss–Kronrod algorithm used for numerical integrations,
- `gsl_spline`: cubic spline algorithm used for interpolations,
- `gsl_multimin`: minimization algorithm used for fits.

We start the discussion with the calculation of the Omnès function, after which we will describe how to evaluate the inhomogeneities. We will conclude with a treatment of the dispersion integrals. The methods presented in the following have partly been covered in Refs. [103,122], however, there are also some fundamental differences in the approach that we use to speed up the iteration process and improve the accuracy of the final results.

3.4.1 The Omnès function

Let us consider the Omnès function for values of s above and below the cut,[#8]

$$\Omega(s \pm i\epsilon) = \exp\left\{ \frac{s}{\pi} \int_{s_0}^{\infty} ds' \frac{\delta(s')}{s'(s'-s\pm i\epsilon)} \right\} . \tag{3.76}$$

If $s > s_0$ the integrand has a singularity in the integration region at $s' = s$. This can be treated by resorting to the Sokhotsky–Plemelj formula,

$$\Omega(s \pm i\epsilon) = \exp\left\{ \pm i\delta(s) + \frac{s}{\pi} \mathcal{P} \int_{s_0}^{\infty} \frac{\delta(s')}{s'(s'-s)} \right\} , \tag{3.77}$$

where $\mathcal{P}$ denotes the Cauchy principal value. We add and subtract $\delta(s)$ in the integrand of the principal value integral, which leads to

$$\Omega(s \pm i\epsilon) = \exp\left\{ \pm i\delta(s) + \frac{s}{\pi} \left[\delta(s) \mathcal{P} \int_{s_0}^{\infty} ds' \frac{1}{s'(s'-s)} + \mathcal{P} \int_{s_0}^{\infty} ds' \frac{\delta(s')-\delta(s)}{s'(s'-s)} \right] \right\} . \tag{3.78}$$

The first integral on the right-hand side of the equation can be integrated analytically,

$$\mathcal{P} \int_{s_0}^{\infty} ds' \frac{1}{s'(s'-s)} = \lim_{\epsilon\to 0} \left\{ \int_{s_0}^{s-\epsilon} ds' \frac{1}{s'(s'-s)} + \int_{s+\epsilon}^{\infty} ds' \frac{1}{s'(s'-s)} \right\} = \frac{1}{s} \log\left(\frac{s_0}{s-s_0} \right) , \tag{3.79}$$

[#8] We are suppressing angular momentum indices and just consider a generic channel. The following observations are the same in both cases.

whereas the second integral,

$$\mathcal{P}\int_{s_0}^{\infty} ds' \frac{\delta(s')-\delta(s)}{s'(s'-s)} \ , \tag{3.80}$$

has a finite integrand and can be treated numerically. We still have to give a description of how to treat the upper end of the integration intervals: of course the $\pi\pi$ and $\pi\eta$ phase shifts are not known to arbitrarily high energies. Unless noted otherwise we have used the following method: beyond a certain cutoff Λ_δ^2 the phase is smoothly guided to its asymptotic value, Eq. (3.57), according to the prescription (this approach is modeled after the one found in Ref. [126]),

$$\delta(s) = n\pi - \frac{a_\delta}{b_\delta + (s/\Lambda_\delta^2)^{3/2}} \qquad \text{for } s > \Lambda_\delta^2 \ , \tag{3.81}$$

where a_δ and b_δ are chosen such that $\delta(s)$ and its first derivative are continuous at $s = \Lambda_\delta^2$,

$$a_\delta = \frac{3(n\pi - \delta(\Lambda_\delta^2))^2}{2\Lambda_\delta^2 \delta'(\Lambda_\delta^2)} \ , \qquad b_\delta = -1 + \frac{3(n\pi - \delta(\Lambda_\delta^2))}{2\Lambda_\delta^2 \delta'(\Lambda_\delta^2)} \ . \tag{3.82}$$

The remainder of the Omnès function can now be integrated analytically. The final expression is rather lengthy, which is why we refrain from showing it here.

If $s < s_0$ or s complex we use Eq. (3.76) directly for the numerical implementation up until $s' = \Lambda_\delta^2$. Beyond that point the integral can be performed analytically. For $s = s_0$ we simply use

$$\Omega(s_0) \doteq \frac{\Omega(s_0-\epsilon) + \Omega(s_0+\epsilon)}{2} \ , \tag{3.83}$$

where ϵ is a numerical parameter that has to be chosen sufficiently small.

3.4.2 The inhomogeneities

We have to calculate the inhomogeneities along the integration contour outlined in Section 3.3.4. Again we only discuss the $\pi\pi$ inhomogeneity – the $\pi\eta$ case can be treated completely analogously. Let us consider

$$\hat{\mathcal{M}}_0(s) = \frac{2}{\kappa_{\pi\pi}(s)} \int_{\mathcal{C}_t'} dt' \mathcal{M}_0^{\pi\eta}(t') \ ,$$

with $\mathcal{C}_t'$ as defined previously. We will discuss the numerical implementation of the integration contours for the separate regions I) – IV) step by step:

I) $s_0 < s < s_{\rm II}$: in this segment the integration is straightforward. Since both endpoints lie above the cut we can simply integrate along a straight line,

$$\hat{\mathcal{M}}_0(s) = \frac{2}{\kappa_{\pi\pi}(s)} \int_{t_-(s)}^{t_+(s)} dt' \mathcal{M}_0^{\pi\eta}(t') \ . \tag{3.84}$$

II) $s_{\rm II} < s < a_s$: we start the integration along a line below the cut from $t_-(s)$ to just below the threshold $t_0 - \epsilon$. The integration along the imaginary axis cancels and the final path proceeds along a straight line from $t_0 - \epsilon$ to $t_+(s)$ just above the real axis,

$$\hat{\mathcal{M}}_0(s) = \frac{2}{\kappa_{\pi\pi}(s)} \left\{ \int_{t_-(s)}^{t_0-\epsilon} dt' \mathcal{M}_0^{\pi\eta}(t'-i\epsilon) + \int_{t_0-\epsilon}^{t_+(s)} dt' \mathcal{M}_0^{\pi\eta}(t'+i\epsilon) \right\} \ . \tag{3.85}$$

III) $a_s < s < b_s$: as we have stated before it turns out that the most efficient way to implement this integration path is to parametrize it by the trajectories of the endpoints.[#9] We integrate along a line from $t_-(s)$ to $t_-(b_s) = t_+(b_s)$ and on to $t_+(s)$. The only drawback of this procedure is that one picks up singularities at the endpoints $t_\pm(b_s)$ and $t_\pm(a_s)$. This can be easily remedied, however, by splitting up the integration path further and performing a change of the integration variables:

- $(a_s + b_s)/2 < s < b_s$: performing the substitution

$$y_b(t') = \sqrt{\frac{(M_{\eta'} + M_\eta) + \sqrt{t'}}{2}} - \sqrt{\frac{(M_{\eta'} + M_\eta) - \sqrt{t'}}{2}} \,, \tag{3.86}$$

the integration can be rewritten as

$$\hat{\mathcal{M}}_0(s) = \frac{2}{\kappa_{\pi\pi}(s)} \left\{ \int_{y_b^-(s)}^{y_b^-(b)} dy_b \frac{dt'}{dy_b} \mathcal{M}_0^{\pi\eta}\big(t'(y_b)\big) + \int_{y_b^+(b)}^{y_b^+(s)} dy_b \frac{dt'}{dy_b} \mathcal{M}_0^{\pi\eta}\big(t'(y_b)\big) \right\} , \tag{3.87}$$

where we introduced the short-hand notation $y_i^\pm(s) = y_i(t_\pm(s))$ with $i = a, b$.

- $a_s < s < (a_s + b_s)/2$: with the additional substitution,

$$y_a(t') = \sqrt{\frac{\sqrt{t'} + (M_{\eta'} - M_\eta)}{2}} - \sqrt{\frac{\sqrt{t'} - (M_{\eta'} - M_\eta)}{2}} \,, \tag{3.88}$$

the integral becomes

$$\begin{aligned} \hat{\mathcal{M}}_0(s) = \frac{2}{\kappa_{\pi\pi}(s)} \Bigg\{ & \int_{y_a^-(s)}^{y_a^-(\frac{a+b}{2})} dy_b \frac{dt'}{dy_a} \mathcal{M}_0^{\pi\eta}\big(t'(y_a)\big) + \int_{y_b^-(\frac{a+b}{2})}^{y_b^-(b)} dy_b \frac{dt'}{dy_b} \mathcal{M}_0^{\pi\eta}\big(t'(y_b)\big) \\ & + \int_{y_b^+(b)}^{y_b^+(\frac{a+b}{2})} dy_b \frac{dt'}{dy_b} \mathcal{M}_0^{\pi\eta}\big(t'(y_b)\big) + \int_{y_a^-(\frac{a+b}{2})}^{y_a^+(s)} dy_a \frac{dt'}{dy_a} \mathcal{M}_0^{\pi\eta}\big(t'(y_a)\big) \Bigg\} . \end{aligned} \tag{3.89}$$

With the above description the singularities are pushed out of the integration intervals.

IV) $b_s < s$: in this segment we may again use a simple straight line running from $t_-(s)$ to $t_+(s)$ as an integration contour,

$$\hat{\mathcal{M}}_0(s) = \frac{2}{\kappa_{\pi\pi}(s)} \int_{t_-(s)}^{t_+(s)} dt' \mathcal{M}_0^{\pi\eta}(t') \,. \tag{3.90}$$

A visualization of each region is displayed in Fig. 3.5.

[#9] This is markedly different from the procedure used in Refs. [122], where the function is interpolated on a two-dimensional grid. For the same accuracy one needs the squared amount of grid points.

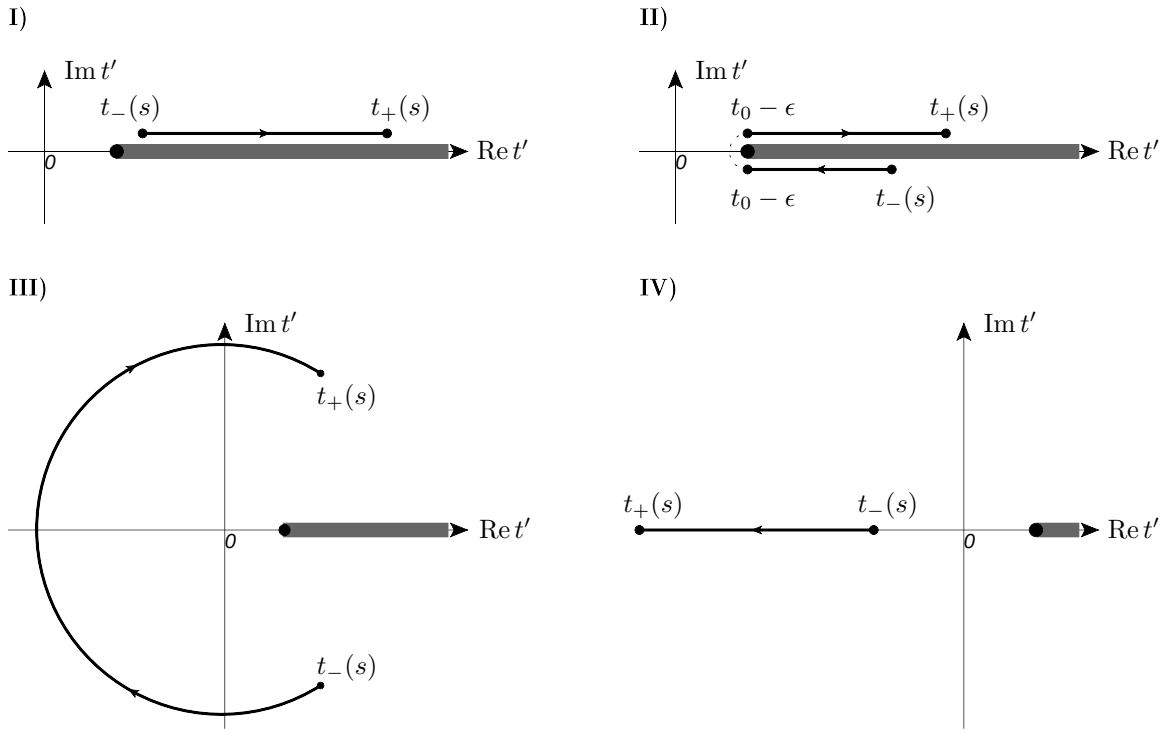

Figure 3.5: Real and imaginary part of the integration contour used in the numerical implementation. The black curve denotes the integration contour, the gray line the threshold cut.

3.4.3 The dispersion integral

In this section we will discuss the numerical treatment of the dispersion integrals given in Eq. (3.62). It behooves us to study a slightly more general case (for $P \to ijk$),

$$\mathcal{I}(s) = \int_{s_0}^{\infty} ds' \frac{\sin\delta(s')\tilde{\mathcal{M}}(s')}{\kappa(s')^{2n+1}|\Omega(s')|s'^m(s'-s)} \,, \tag{3.91}$$

where $\tilde{\mathcal{M}}(s) = \kappa(s)^{2n+1}\hat{\mathcal{M}}(s)$, and we represent $\kappa(s)$ in the form,

$$\kappa(s) = \sqrt{\frac{\lambda(s, M_i^2, M_j^2)}{s^2}}\sqrt{a-s}\sqrt{b-s} \,, \tag{3.92}$$

so that $s_0 = (M_i + M_j)^2$, $a = (M_P - M_k)^2$ and $b = (M_P + M_k)^2$. In the case at hand we have $n = 0$ and $m = 3$, however, in our later studies of $\omega/\phi \to 3\pi$ decays, we will come across P-wave final states, where $n = 1$.

It is obvious that the roots s_0, a and b of the function $\kappa(s)$ in the integration interval complicate the numerical integration. Of these s_0 is the least problematic since the inhomogeneity as well as the phase shift $\sin\delta(s)$ vanish with the leading threshold behavior. There is no contribution to the integral. Likewise the point $s' = b$ does not present a problem: the inhomogeneity vanishes again as can be seen from Fig. 3.4, and the integrand is finite. Numerically, we tackle this by evaluating the integrand at several points around $s' = b$, fit a polynomial to these points and interpolate the exact value.

From Fig. 3.4 we observe that the inhomogeneity of the S wave does not vanish at $s' = a$, so that the integrand diverges as $(a-s')^{-1/2}$. For the P wave one can show that the inhomogeneity vanishes as $(a - s')$ so that the singular behavior is still $(a - s')^{-1/2}$. The singularity is integrable, but provides a challenge for the numerical implementation. We will discuss the procedure step by step making ample use of the functions

$$\mathcal{G}(s) = \frac{\sin\delta(s)\tilde{\mathcal{M}}(s)}{s^m\Big(\sqrt{\frac{\lambda(s,M_i^2,M_j^2)}{s^2}}\sqrt{b-s}\Big)^{2n+1}|\Omega(s)|}\,, \qquad \mathcal{H}(s) = \frac{\sin\delta(s)\tilde{\mathcal{M}}(s)}{\kappa(s)^{2n+1}|\Omega(s)|}\,. \tag{3.93}$$

In the following only the case $n = 0$ is considered, whereas the case $n = 1$ is relegated to Appendix B.3. We need to study several possibilities for values of s.

- $s_0 < s < b$: in this case s lies in the integration interval, and the most convenient way to proceed is to split the interval according to

$$\int_{s_0}^{\Lambda^2} = \int_{s_0}^{p} + \int_{p}^{b} + \int_{b}^{\Lambda^2}\,, \tag{3.94}$$

  where we introduced the integral cutoff Λ^2 and the variable $p = (a + s)/2$. Note that for $s < a$ we have $p < a$ and for $s > a$ we find $p > a$, which suggests to further break down separate cases of s:

  - $s < a$: in this case we need to take care of the singularity $s' = s$ in the integration interval from s_0 to p, and of $s' = a$ in the interval from p to b. This can by achieved by splitting up the integral according to

$$\begin{aligned}\mathcal{I}(s) = &\int_{s_0}^{p} ds' \frac{\mathcal{H}(s') - \mathcal{H}(s)}{s'^m(s'-s)} + \mathcal{H}(s)\mathcal{R}(s,s_0,p) \\ &+ \int_{p}^{b} ds' \frac{\mathcal{G}(s') - \mathcal{G}(a)}{(a-s')^{1/2}(s'-s)} + \mathcal{G}(a)\mathcal{Q}(s,a,p,b) + \int_{b}^{\Lambda^2} ds' \frac{\mathcal{G}(s')}{(a-s')^{1/2}(s'-s)}\,,\end{aligned} \tag{3.95}$$

    where we have added and subtracted $\mathcal{H}(s)$ and $\mathcal{G}(a)$ in the respective integrals and defined

$$\mathcal{R}(s,x,y) = \int_x^y \frac{ds'}{s'^m(s'-s)} = \frac{i\pi}{s^m} + \frac{1}{s^m}\log\frac{1-s/y}{s/x-1} + \sum_{n=1}^{m-1}\frac{s^{n-m}}{n}(y^{-n} - x^{-n})\,, \tag{3.96}$$

    for all $m \in \mathbb{N}$, and

$$\begin{aligned}\mathcal{Q}(s,a,x,y) &= \int_x^y \frac{ds'}{(a-s')^{1/2}(s'-s)} \\ &= \frac{2}{\sqrt{s-a}}\Big(\arctan\frac{i\sqrt{y-a}}{\sqrt{s-a}} - \arctan\frac{\sqrt{a-x}}{\sqrt{s-a}}\Big)\,.\end{aligned} \tag{3.97}$$

    The remaining integrals in the first and second line of Eq. (3.95) can be solved numerically. However, the situation, especially for the first integral in the second line, is rather delicate since one has to calculate a ratio of zeros. We found that the best way to proceed is to expand $\mathcal{G}(s')$ around a,

$$\mathcal{G}(s') \simeq \mathcal{G}(a) + g_0(a-s')^{1/2} + g_1(a-s') + g_2(a-s')^{3/2} + \dots\,, \tag{3.98}$$

and fit the coefficients g_0, g_1, g_2 in a small region around a. The integrand at the point a itself is then determined by interpolation, using

$$\frac{\mathcal{G}(s') - \mathcal{G}(a)}{(a-s')^{1/2}} \simeq g_0 + g_1(a-s')^{1/2} + g_2(a-s') + \dots \ . \tag{3.99}$$

Thus we guarantee that the integrand is finite at all times.

– $s > a$: This case is much like the above with the exception that now the singularity $s' = s$ lies in the integration interval from p to b, and $s' = a$ in the interval s_0 to p. We have

$$\begin{aligned}\mathcal{I}(s) = &\int_{s_0}^{p} ds' \frac{\mathcal{G}(s') - \mathcal{G}(a)}{(a-s')^{1/2}(s'-s)} + \mathcal{G}(a)\mathcal{Q}(s,a,s_0,p) \\ &+ \int_{p}^{b} ds' \frac{\mathcal{H}(s') - \mathcal{H}(s)}{s'^m(s'-s)} + \mathcal{H}(s)\mathcal{R}(s,p,b) + \int_{b}^{\Lambda^2} ds' \frac{\mathcal{G}(s')}{(a-s')^{1/2}(s'-s)} \ .\end{aligned} \tag{3.100}$$

- $s > b$: s is still part of the integration interval, but in this case the singularity is located in the integration interval from b to Λ^2, we do not need to split up the lower integration interval and can simply write

$$\begin{aligned}\mathcal{I}(s) = &\int_{s_0}^{b} ds' \frac{\mathcal{G}(s') - \mathcal{G}(a)}{(a-s')^{1/2}(s'-s)} + \mathcal{G}(a)\mathcal{Q}(s,a,s_0,b) \\ &+ \int_{b}^{\Lambda^2} ds' \frac{\mathcal{H}(s') - \mathcal{H}(s)}{s'^m(s'-s)} + \mathcal{H}(s)\mathcal{R}(s,b,\Lambda^2) \ .\end{aligned} \tag{3.101}$$

- $s < s_0$ and s complex: s does not lie in the integration interval, so that we only have to amend the singularity at $s' = a$, thus

$$\mathcal{I}(s) = \int_{s_0}^{\Lambda^2} ds' \frac{\mathcal{G}(s') - \mathcal{G}(a)}{(a-s')^{1/2}(s'-s)} + \mathcal{G}(a)\mathcal{Q}(s,a,s_0,\Lambda^2) \ . \tag{3.102}$$

3.5 Numerical results

In this section we present some numerical results based on the methods presented before. These analyses are more of qualitative than of quantitative nature. We therefore refrain from an elaborate error discussion. We begin by specifying the input that we use to perform our analysis, then briefly discuss the convergence behavior of the iteration procedure, and expose our calculations to experimental findings by comparing to recent Dalitz plot measurements.

3.5.1 Numerical input

Before starting the iteration procedure to determine the basis functions we need to fix the scattering phase shifts that enter the Omnès functions and dispersion integrals. We then discuss our input for the subtraction constants. We resort to two methods: first, we determine the subtraction constants based on matching to extensions of Chiral Perturbation Theory. We choose next-to-leading order Large-N_C Chiral Perturbation theory and Resonance Chiral Theory (RChT) for that purpose, both of which are taken from the analysis outlined in

Ref. [105]. Second, we will generate data samples from two recent measurements of the Dalitz plot parameterization by the BES-III [116] and the VES [117] collaborations. We perform fits to these data samples in Section 3.5.4 and compare with the Large-N_C and RChT amplitudes. Throughout this analysis we use experimentally determined values for the particle masses [87], namely $M_{\eta'} = 957.78$ MeV, $M_\pi = 139.57$ MeV, and $M_\eta = 547.86$ MeV.

Phase shifts

For $\pi\pi$ scattering we resort to the results of a very sophisticated dispersive analysis with Roy equations [39, 41]. It suffices to only take one of these parameterizations into account: both analyses agree rather well considering the accuracy that we are aiming at and the uncertainty will be entirely dominated by the $\pi\eta$ phase shift. We choose to use the parameterization from Ref. [39] for the qualitative analysis that we are aiming for at this stage. In our later analysis of $\omega/\phi \to 3\pi$, we have to make a more careful assessment of these uncertainties, and we shall discuss the issue in a little more detail then. The phase shift is continued beyond the range of validity of the Roy equations according to the prescription Eq. (3.81). In Fig. 3.6 we display the phase shift and the resulting Omnès function calculated with the methods described in Section 3.4.1. We observe that the phase shift is dominated by the broad structure of the σ for energies between the threshold and about 0.9 GeV, after which the $f_0(980)$ resonance and the opening of the $K\bar{K}$ threshold leave the strongest imprint on the phase motion.

Next to the subtraction constants the largest uncertainties that we have to deal with in our analysis are generated by the $\pi\eta$ scattering phase shift. The $\pi\eta$ threshold parameters are not well-constrained by chiral symmetry [29, 127] (see also an extensive treatment in generalized ChPT in Ref. [128]), and there is currently no dispersive analysis extending beyond the low-energy regime. As was pointed out before, one of the motivations to study $\eta' \to \eta\pi\pi$ is to actually obtain some information about $\pi\eta$ scattering. However, we need the phase shifts as an input to solve the integral equations, so we devise the following procedure: on the one hand we will use a $\pi\eta$ scattering phase shift extracted from a unitarized tree-level ChPT amplitude with coupled channels $\pi\eta$ and $K\bar{K}$ using parameters as described in Ref. [129] (see Refs. [123, 124, 130, 131] and references therein for some additional information on coupled-channel unitarized ChPT). In such a scenario the $a_0(980)$ resonance is generated dynamically. On the other hand we will parametrize the phase shift by a simple Breit–Wigner function[#10] with energy-dependent width and resonance parameters of the $a_0(980)$ taken from [87],

$$\delta_0^{\pi\eta}(t) = \arctan\left\{ \frac{\lambda(t, M_\eta^2, M_\pi^2)^{1/2}}{\lambda(M_{a_0}^2, M_\eta^2, M_\pi^2)^{1/2}} \frac{\Gamma_{a_0} M_{a_0}^3}{t(M_{a_0}^2 - t)} \right\} \theta(t - (M_\eta + M_\pi)^2) \ , \tag{3.103}$$

where $M_{a_0} = 984.7$ MeV, and $\Gamma_{a_0} \simeq 75$ MeV. (The width is known to lie between 50 MeV and 100 MeV. We simply chose to take the central value.) In Fig. 3.7 we display the two $\pi\eta$ phase shifts along with the corresponding Omnès function. Obviously, the phase shift is dominated by the $a_0(980)$ resonance. We also observe that the Breit–Wigner phase shift is significantly larger than the unitarized phase shift in the physical decay region.

[#10] If one strove for a precision analysis of $\eta' \to \eta\pi\pi$, one should resort to a more sophisticated parametrization of the $a_0(980)$ that describes the behavior of the $\pi\eta$ phase shift at the $K\bar{K}$ threshold more realistically. Such a parametrization is for example given by a Flatté-like distribution, see Ref. [132] and references therein. At the accuracy level of our analysis the Breit–Wigner distribution is sufficient.

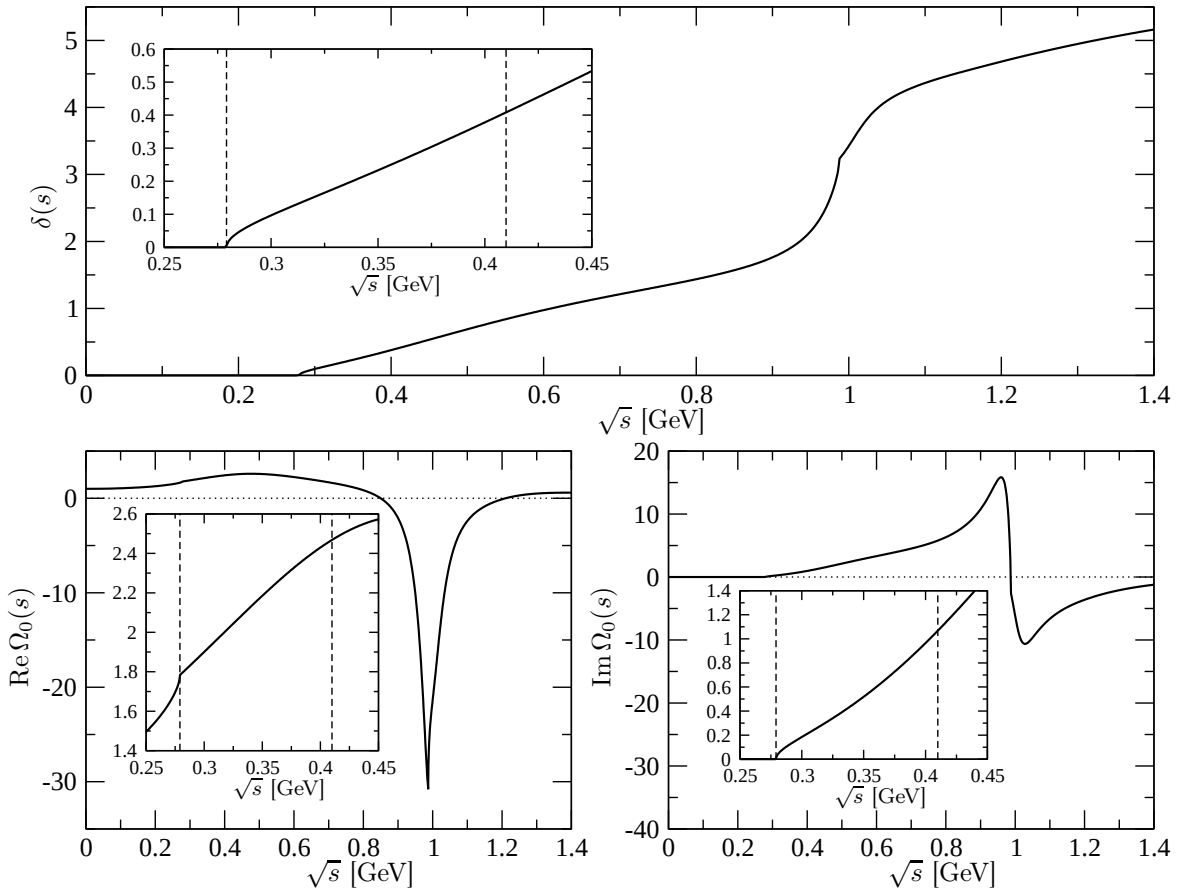

Figure 3.6: The isospin-zero $\pi\pi$ phase shift, $\delta_0(s)$ (top panel) along with the real (bottom left panel) and imaginary (bottom right panel) part of the corresponding Omnès function, $\Omega_0(s)$. The insets show a magnification of the physical region of the decay $\eta' \to \eta\pi\pi$, where the dashed vertical lines denote the threshold $s = 4M_\pi^2$ and the end of the physical region $(M_{\eta'} - M_\eta)^2$, respectively.

Matching to large-N_C ChPT and RChT

Large-N_C Chiral Perturbation Theory allows the explicit inclusion of the η' meson in an effective-Lagrangian framework. It is founded on the notion that as $N_C \to \infty$ the $\mathrm{U}(1)_A$ anomaly and thus the chiral-limit mass of the η' vanishes: the η' becomes a Goldstone boson as the $\mathrm{U}(3)_L \times \mathrm{U}(3)_R$ symmetry is spontaneously broken down to $U(3)_V$ [18,104,105]. At leading order (LO) it is easily shown that the $\eta' \to \eta\pi\pi$ amplitude is given as [57,105,108,133–137]

$$\mathcal{M}_{\mathrm{LO}}^{\mathrm{ChPT}}(s,t,u) = \frac{M_\pi^2}{6F^2}\Big[2\sqrt{2}\cos(2\theta_P) - \sin(2\theta_P)\Big] \,, \tag{3.104}$$

where θ_P is the $\eta - \eta'$ mixing angle, which relates the octet and singlet states to the physical η, η' states at leading order,

$$\begin{pmatrix}\eta_8\\ \eta_0\end{pmatrix} = \begin{pmatrix}\cos\theta_P & \sin\theta_P\\ -\sin\theta_P & \cos\theta_P\end{pmatrix}\begin{pmatrix}\eta\\ \eta'\end{pmatrix} \,, \tag{3.105}$$

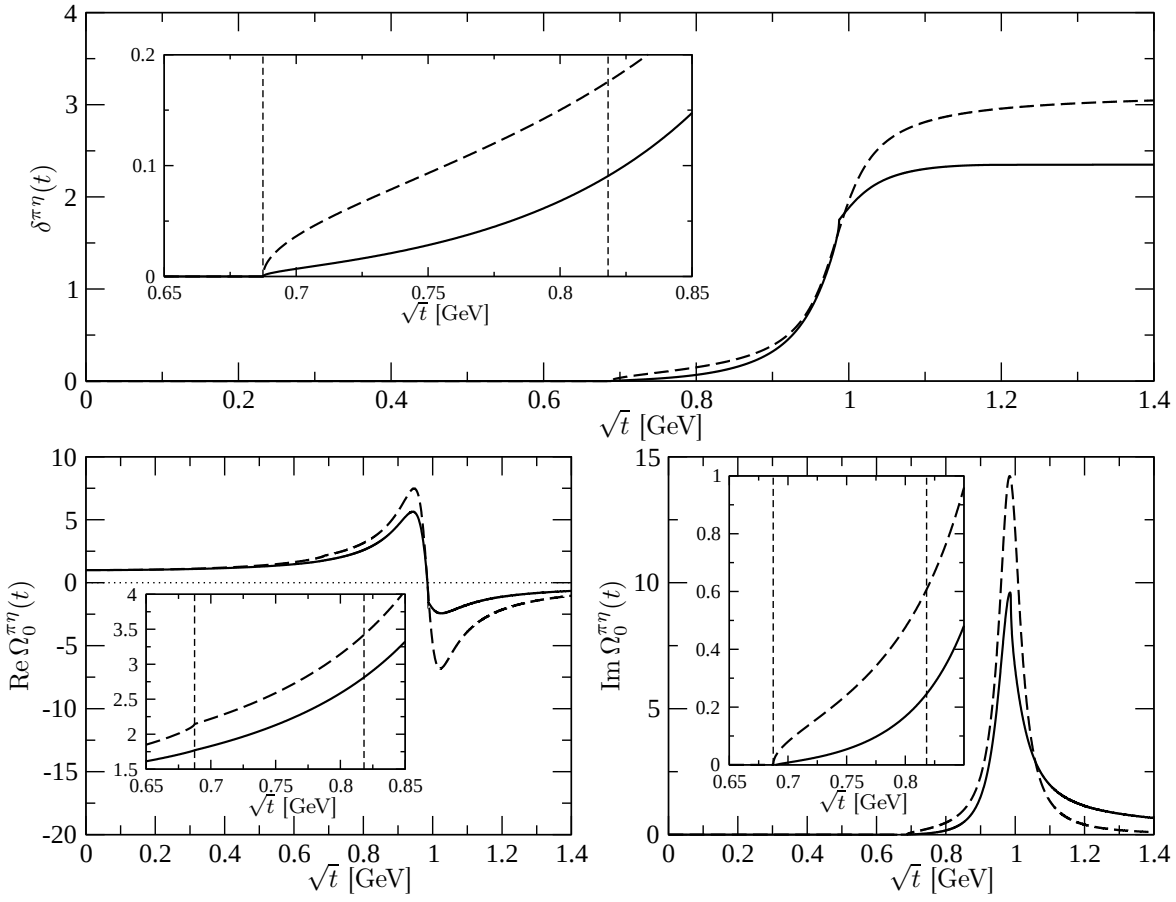

Figure 3.7: The isospin-zero $\pi\eta$ phase shift, $\delta_0^{\pi\eta}(t)$ (top panel) along with the real (bottom left panel) and imaginary (bottom right panel) part of the corresponding Omnès function, $\Omega_0^{\pi\eta}(t)$. The solid curve represents the phase shift calculated with unitarized ChPT, whereas the dashed curve is parametrized by a Breit–Wigner function, see the text for details. The insets show a magnification of the respective functions in the physical region of the decay $\eta' \to \eta\pi\pi$, where the dashed vertical lines denote the threshold $t = (M_\eta + M_\pi)^2$ and the end of the physical region $(M_{\eta'} - M_\pi)^2$.

and $F = F_\pi$ (at leading order) is the pion decay constant. At next-to-leading order (NLO) loop contributions are still suppressed in the large-N_C counting, and the full amplitude can be derived from the NLO Lagrangian [105],

$$\begin{aligned}\mathcal{M}_{\mathrm{NLO}}^{\mathrm{ChPT}}(s,t,u) = \frac{c_{qq}}{F^2}\Big[\frac{M_\pi^2}{2} + \frac{2(3L_2+L_3)}{F_\pi^2}(s^2+t^2+u^2-M_{\eta'}^4-M_\eta^4-2M_\pi^4) \\ - \frac{2L_5}{F_\pi^2}(M_{\eta'}^2+M_\eta^2+2M_\pi^2)M_\pi^2 + \frac{24L_8}{F_\pi^2}M_\pi^4 + \frac{2}{3}\Lambda_2 M_\pi^2\Big] + \frac{c_{sq}}{F^2}\frac{\sqrt{2}}{3}\Lambda_2 M_\pi^2\ ,\end{aligned} \tag{3.106}$$

where in our numerical analysis we use the values from Ref. [138] for the low-energy constants (see also Refs. [139, 140]; again we do not think it sensible to perform an error analysis on

these parameters at this stage),

$$(3L_2 + L_3) = 0.6 \times 10^{-3} \ , \quad L_5 = 1.4 \times 10^{-3} \ , \quad L_8 = 0.9 \times 10^{-3} \ , \tag{3.107}$$

and

$$\begin{aligned} c_{qq} &= -\frac{F^2}{3F_8^2 F_0^2 \cos^2(\theta_8 - \theta_0)} \Big[2F_8^2 \sin(2\theta_8) - F_0^2 \sin(2\theta_0) - 2\sqrt{2} F_8 F_0 \cos(\theta_8 + \theta_0) \Big] \ , \\ c_{sq} &= -\frac{F^2}{3F_8^2 F_0^2 \cos^2(\theta_8 - \theta_0)} \Big[\sqrt{2} F_8^2 \sin(2\theta_8) + \sqrt{2} F_0^2 \sin(2\theta_0) + F_8 F_0 \cos(\theta_8 + \theta_0) \Big] \ , \end{aligned} \tag{3.108}$$

and we use $F_8 = 1.28 F_\pi$, $F_0 = 1.25 F_\pi$, $\theta_8 = -20^\circ$, $\theta_0 = -4^\circ$, and $\Lambda_2 = 0.4$. Note that at next-to-leading order the $\eta - \eta'$ mixing scenario (3.105) necessarily has to be generalized to involve the *two* mixing angles θ_0 and θ_8 [141, 142]. The next-to-leading order large-N_C amplitude does not involve any rescattering. Thus to match the dispersive representation to Eq. (3.106), we go to the limit of no rescattering, i.e. $\delta_0, \delta_0^{\pi\eta} \to 0$, and thus $\Omega_0, \Omega_0^{\pi\eta} \to 1$ and $\hat{\mathcal{M}}_0, \hat{\mathcal{M}}_0^{\pi\eta} \to 0$. Comparing both representations we find

$$\alpha_0^{\pi\pi} = -12.4 \ , \qquad \beta_0^{\pi\pi} = 0 \ , \qquad \gamma_0^{\pi\pi} = \gamma_0^{\pi\eta} = -1.13 \ \text{GeV}^{-4} \ , \tag{3.109}$$

for the subtraction constants. $\alpha_0^{\pi\pi}$ is an overall normalization constant and not really relevant for Dalitz plot studies. We note that the subtraction constants $\gamma_0^{\pi\pi}, \gamma_0^{\pi\eta}$ are saturated up to 95% by the term $-1/(M_{\eta'}^4 - M_\eta^4)$, i.e. where $M_\pi = 0$.

In the so-called soft-pion limit, where the momenta and masses of the pions go to zero, we find that the amplitude in Eq. (3.106) has zeros at

$$s = 0 \ , \qquad t^2 + u^2 = M_{\eta'}^4 + M_\eta^4 \ , \qquad t + u = M_{\eta'}^2 + M_\eta^2 \ . \tag{3.110}$$

These relations give rise to two *Adler zeros* (see also [106, 143, 144]) at

$$t_1 = M_{\eta'}^2 \ , \ u_1 = M_\eta^2 \ ; \qquad t_2 = M_\eta^2 \ , \ u_2 = M_{\eta'}^2 \ . \tag{3.111}$$

These Adler zeros are protected by SU(2)×SU(2) symmetry. This is immediately clear by inspection of Eq. (3.106): the corrections to these zeros are of $\mathcal{O}(M_\pi^2)$. However, claims have been made in the past that the $a_0(980)$ resonance removes the Adler zero based on the explicit inclusion of a scalar resonance propagator [107]. We will study this issue within our more elaborate framework that fulfills all the requirements of analyticity and unitarity.

Our second matching procedure makes use of Resonance Chiral Theory, which describes the interactions between Goldstone bosons and resonances explicitly [145–148]. RChT finds its most prominent application in the estimate of low-energy constants by means of resonance saturation. It can, however, also be used to directly derive the $\eta' \to \eta\pi\pi$ decay amplitude from the RChT Lagrangian [105]:

$$\begin{aligned} \mathcal{M}^{\text{RChT}}(s,t,u) = & \frac{c_{qq}}{F^2} \Bigg\{ \frac{M_\pi^2}{2} + \frac{1}{F_\pi^2} \frac{(c_d(s - M_{\eta'}^2 - M_\eta^2) + 2c_m M_\pi^2)(c_d(s - 2M_\pi^2) + 2c_m M_\pi^2)}{M_S^2 - s} \\ & + \frac{1}{F_\pi^2} \frac{(c_d(t - M_{\eta'}^2 - M_\pi^2) + 2c_m M_\pi^2)(c_d(t - M_\eta - M_\pi^2) + 2c_m M_\pi^2)}{M_S^2 - t} \\ & + \frac{1}{F_\pi^2} \frac{(c_d(u - M_{\eta'}^2 - M_\pi^2) + 2c_m M_\pi^2)(c_d(t - M_\eta - M_\pi^2) + 2c_m M_\pi^2)}{M_S^2 - u} \Bigg\} \ , \end{aligned} \tag{3.112}$$

where c_d and c_m describe the coupling between the scalar resonances and the Goldstone bosons, and $M_S = 0.980$ GeV is the mass of the scalar multiplet. We will use $c_d \simeq 0.028$ GeV and the theoretical constraint $4c_d c_m = F^2$ [105]. Again, even if the uncertainty in the coupling constants is rather large (although all estimates fulfill the theoretical constraint rather well), this uncertainty is still dominated by the different $\pi\eta$ phase-shift variants in our dispersive analysis. In the limit of large scalar masses, that is $s, t, u \ll M_S^2$ the low-energy expansion of the amplitude (3.112) agrees with Eq. (3.106) for [105]

$$3L_2 + L_3 = c_d^2/2M_S^2 \ , \quad L_5 = c_d c_m/M_S^2 \ , \quad L_8 = c_m^2/2M_S^2 \ , \quad \Lambda_{1,2} = 0 \ . \tag{3.113}$$

To properly match the above expression to the dispersive amplitude it is useful to slightly reshuffle Eq. (3.112). The amplitude can be recast into the following form:

$$\mathcal{M}^{\mathrm{RChT}}(s,t,u) = \frac{c_{qq}}{F^2}\left\{ \frac{M_\pi^2}{2} + \frac{a_{\pi\pi} + b\,s + c_d^2 s^2}{F_\pi^2(M_S^2 - s)} + \frac{a_{\pi\eta} + b\,t + c_d^2 t^2}{F_\pi^2(M_S^2 - t)} + \frac{a_{\pi\eta} + b\,u + c_d^2 u^2}{F_\pi^2(M_S^2 - u)} \right\} , \tag{3.114}$$

where we defined

$$\begin{aligned} a_{\pi\pi} &= 2M_\pi^2(M_{\eta'}^2 + M_\eta^2)c_d^2 - 6M_\pi^2 s_{\eta'} c_d c_m + 4M_\pi^4 c_m^2 \ , \quad b = -3s_{\eta'}c_d^2 + 4M_\pi^2 c_m c_d \ , \\ a_{\pi\eta} &= (M_{\eta'}^2 + M_\pi^2)(M_\eta^2 + M_\pi^2)c_d^2 - 6M_\pi^2 s_{\eta'} c_d c_m + 4M_\pi^4 c_m^2 \ . \end{aligned} \tag{3.115}$$

Using Eq. (3.3) one finds

$$\begin{aligned} \mathcal{M}^{\mathrm{RChT}}(s,t,u) = \frac{c_{qq}}{F^2}\Bigg\{ & \frac{M_S^2}{M_S^2 - s}\Bigg[\frac{a_{\pi\pi}M_S^2 + 2a_{\pi\eta}M_S^2 + 3(a_{\pi\eta} + b\,M_S^2)s_{\eta'}}{F_\pi^2 M_S^4} + \frac{M_\pi^2}{2} \\ & - \left(\frac{3a_{\pi\eta}M_S^2 + 3(a_{\pi\eta} + b\,M_S^2)s_{\eta'}}{F_\pi^2 M_S^6} + \frac{M_\pi^2}{2M_S^2} \right) s + \frac{a_{\pi\eta} + b\,M_S^2 + M_S^4 c_d^2}{F_\pi^2 M_S^6} s^2 \Bigg] \\ & + \left(\frac{M_S^2}{M_S^2 - t} t^2 + \frac{M_S^2}{M_S^2 - u} u^2 \right) \frac{a_{\pi\eta} + b\,M_S^2 + c_d M_S^4}{F_\pi^2 M_S^6} \Bigg\} \ . \end{aligned} \tag{3.116}$$

To correctly perform the matching to the dispersive amplitude we assume that the $f_0(980)$ and $a_0(980)$ resonances reduce to narrow pole terms with mass M_S at large N_C.[#11] It was shown in a unitarized ChPT calculation at $\mathcal{O}(p^6)$ that the mass of the σ resonance grows with N_C. However, there are indications of a subleading $q\bar{q}$ component, which dominates for $N_C > 8$ and stabilizes the σ mass at around 1 GeV [150]. This motivates a slightly more realistic large-N_C limit for the Omnès function (as opposed to simply letting the phase shifts go to zero as before),

$$\lim_{N_C \to \infty} \Omega_0^{(\pi\eta)}(s) = \frac{M_S^2}{M_S^2 - s} \ . \tag{3.117}$$

We can then easily match the RChT amplitude (3.116) to the dispersive one, and find

$$\alpha_0^{\pi\pi} = -6.48 \ , \qquad \beta_0^{\pi\pi} = -0.67 \ \mathrm{GeV}^{-2} \ , \qquad \gamma_0^{\pi\pi} = \gamma_0^{\pi\eta} = -0.15 \ \mathrm{GeV}^{-4} \ . \tag{3.118}$$

for the subtraction constants. Again, $\alpha_0^{\pi\pi}$ is used as an overall normalization.

[#11] Strictly speaking this only holds for $q\bar{q}$ meson states. However, the nature of the scalar resonances is a heavily debated topic and beyond the scope of this work. We point to Ref. [149] and references therein for more information on the relation between the large-N_C limit and the nature of the scalar resonances.

	BES-III [116]	VES [117]
a	$-0.047 \pm 0.011 \pm 0.003$	$-0.127 \pm 0.016 \pm 0.008$
b	$-0.069 \pm 0.019 \pm 0.009$	$-0.106 \pm 0.028 \pm 0.014$
c	$+0.019 \pm 0.011 \pm 0.003$	$+0.015 \pm 0.011 \pm 0.014$
d	$-0.073 \pm 0.012 \pm 0.003$	$-0.082 \pm 0.017 \pm 0.008$
# events	$43\,826 \pm 211$	$\simeq 9612$
# x bins	26	8
# y bins	22	8

Table 3.1: Dalitz plot measurements by the BES-III and VES collaborations. The first error on the Dalitz plot parameters is always statistical, the second systematical. We have estimated the number of $\eta' \to \eta\pi\pi$ events for the VES collaboration from the total number of η' events and the branching ratio $\mathcal{B}(\eta' \to \eta\pi\pi) = 44.5 \pm 1.4\%$ [87].

Sampling of experimental Dalitz plots

The experimental analysis of the Dalitz plot of $\eta' \to \eta\pi\pi$ is analogous to what is conventionally done in $\eta \to 3\pi$, and what has been discussed in Section 2.2: one defines symmetrized coordinates x and y according to

$$x = \frac{\sqrt{3}(t-u)}{2M_{\eta'}Q_{\eta'}} , \qquad y = \frac{(M_\eta + 2M_\pi)[(M_{\eta'} - M_\eta)^2 - s]}{M_\pi M_{\eta'} Q_{\eta'}} - 1 . \tag{3.119}$$

The squared amplitude of the decay is then expanded in terms of these variables,

$$|\mathcal{M}(x,y)|^2 = |\mathcal{N}|^2 \{1 + ay + by^2 + cx + dx^2 + \dots\} , \tag{3.120}$$

and the parameters a, b, c, d are fitted to experimental data. Note that a non-zero value for the parameter c would indicate C violation, so that in principle $\eta' \to \eta\pi\pi$ would allow one to study these effects that are not included in the Standard Model. However, there is no indication of a non-zero c up to this point. In the following we consider only two recent measurements of the charged final state $\eta' \to \eta\pi^+\pi^-$. These determinations of the Dalitz plot parameters by the BES-III [116] and the VES [117] collaboration currently feature the highest statistics. In Table 3.1 we have summarized some details and results of the two experiments.

For our analysis we have generated data samples from the Dalitz plot distributions as measured by the two groups. Our procedure is as follows [151]: to emulate the experimental measurement as closely as possible we choose the same binning as in the experiment. We then randomly draw values x_S and y_S within the allowed bin ranges, and accept these values on the condition that the center of the bin they belong to lies within the Dalitz plot, i.e. fulfills the condition in Eq. (3.10).[#12] The remaining events are submitted to an accept/reject-type sampling: first we calculate the maximum value $N_{\max}$ of $|\mathcal{M}(x,y)|^2$ across the allowed bin range. Then we determine $|\mathcal{M}(x_S, y_S)|^2$ and accept the event as a realization of $|\mathcal{M}(x,y)|^2$

[#12] The choice of the bin center being part of the Dalitz plot is somewhat arbitrary, however it guarantees that the bins of accepted events are distributed symmetrically across the Dalitz plot.

if $N_{\max} u \leq |\mathcal{M}(x_S, y_S)|^2$, where u is drawn from the uniform distribution $U(0,1)$. In this manner we fill the Dalitz plot region until the number of accepted events corresponds to the total number of experimentally measured events.

In Fig. 3.8 we display the Dalitz plot distributions that we have obtained for both experiments. To check our results we have refitted the parameterization (3.120) to the synthesized data sets. We get the following results for the fit parameters and the correlation matrix of the BES-III measurement at $\chi^2/\text{ndof} = 1.05$ and normalization $|\mathcal{N}|^2 = 105 \pm 1$:

$$\begin{array}{l} \\ a = -0.041 \pm 0.009 \\ b = -0.073 \pm 0.017 \\ c = +0.012 \pm 0.007 \\ d = -0.071 \pm 0.011 \end{array} \begin{array}{c} \begin{array}{cccc} a & b & c & d \end{array} \\ \begin{pmatrix} 1.000 & -0.403 & -0.006 & -0.224 \\ & 1.000 & 0.008 & 0.279 \\ & & 1.000 & 0.015 \\ & & & 1.000 \end{pmatrix} \end{array}, \tag{3.121}$$

which agrees with the fit parameters of Ref. [116] within the uncertainty. Note that we have only taken statistical errors into account. Also the correlation matrix is in good agreement with the reference values. The above errors tend to be slightly too small, but overall the quality of the above data sample serves the purpose of our endeavor to perform a qualitative analysis. Refitting the VES parameters we obtain equally good results at $\chi^2/\text{ndof} = 0.92$ and $|\mathcal{N}|^2 = 208 \pm 4$,

$$\begin{array}{l} \\ a = -0.135 \pm 0.009 \\ b = -0.103 \pm 0.019 \\ c = +0.004 \pm 0.014 \\ d = -0.089 \pm 0.023 \end{array} \begin{array}{c} \begin{array}{cccc} a & b & c & d \end{array} \\ \begin{pmatrix} 1.000 & -0.473 & -0.000 & -0.253 \\ & 1.000 & 0.013 & 0.327 \\ & & 1.000 & 0.018 \\ & & & 1.000 \end{pmatrix} \end{array}, \tag{3.122}$$

which again agree within statistical uncertainties. We notice that the two data sets do not agree on the parameter a within a one σ uncertainty, and it would desirable if this experimental disagreement could be resolved by future measurements. A U(3) coupled-channel approach to $\eta' \to \eta\pi\pi$ predicts a to be consistent with the VES measurement [80, 112]. However, the VES data set was part of a global fit of the low-energy constants in that analysis.

3.5.2 Convergence of the iteration procedure

Based on the numerical input that we fixed in the previous section we are now in the position to study the convergence behavior of the amplitude during the iteration procedure. We only display the case where the $\pi\eta$ phase shift is given by a Breit–Wigner function, while for the phase shift deduced from unitarized ChPT one observes very similar results. For illustration we show successive iteration steps of the s- and t-dependent functions that arise from the decomposition

$$\mathcal{M}_{\alpha_0^{\pi\pi}}(s,t,u) = \mathcal{M}_{\alpha_0^{\pi\pi}}(s) + \mathcal{M}^{\pi\eta}_{\alpha_0^{\pi\pi}}(t) + \mathcal{M}^{\pi\eta}_{\alpha_0^{\pi\pi}}(u) \tag{3.123}$$

in Fig. 3.9. The starting point of the iteration of $\mathcal{M}_{\alpha_0^{\pi\pi}}(s)$ is simply the Omnès function. We have left out the "first" iteration step, since it is identical to the Omnès function represented by the gray curve in Fig. 3.9. This is due to the fact that $\hat{\mathcal{M}}_{\alpha_0^{\pi\pi}}(s)$ only depends on the angular average of $\mathcal{M}^{\pi\eta}_{\alpha_0^{\pi\pi}}(t)$, which is identical to zero before the iteration. For the real and imaginary part of both functions we observe rapid convergence with the first iteration step

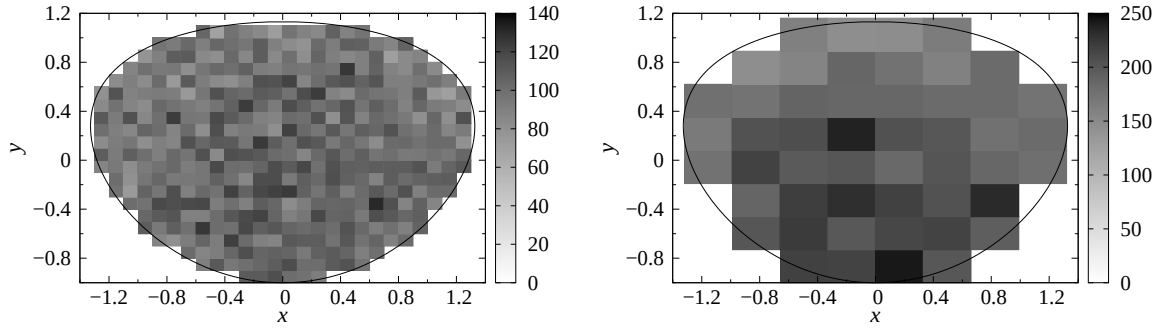

Figure 3.8: Dalitz plot samples for $\eta' \to \eta\pi\pi$ from the experimental Dalitz plot distribution in Tab. 3.1 for the BES-III (left panel) and the VES (right panel) experiment.

being all but indistinguishable from the final result. Still, the final result differs noticeably from the "zeroth" iteration step, pointing at rather large crossed-channel rescattering effects. We observe that the $f_0(980)$ peak is slightly enhanced by the rescattering effects and shifted towards lower energies.

3.5.3 Large-N_C ChPT and RChT matching and comparison to experiment

In this section we compare the dispersive analyses with the subtraction constants given in Eqs. (3.109) and (3.118) to experimental data. To illustrate the dependence on the variables x and y, respectively, we display the integrated decay spectra along each direction divided by phase space and normalized to one for $x = 0$, resp. $y = 0$, in Fig. 3.10.

At first sight these results do not seem very encouraging. While the large-N_C calculation predicts Dalitz plot parameters that do not differ too much from the experimental findings, at least not by orders of magnitude, the same cannot be said for the dispersive solution with subtraction constants matched to large-N_C: it predicts a much larger slope and curvature, especially for $y < 0$. Indeed, the dispersive representation yields Dalitz plot parameters that are off by more than an order of magnitude, see Tab. 3.2. This strongly contradicts comments in Refs. [80,112] that crossed-channel rescattering effects are negligible. Even if the error band that is generated by varying $\delta_{\pi\eta}(t)$ between a Breit–Wigner phase and the coupled-channel unitarized ChPT solution is very large, the data points of the BES-III and VES experiments cannot be accommodated. The situation improves when the subtraction constants of the dispersive solution are fixed from RChT. The Dalitz plot parameters are then compatible with those predicted in large-N_C ChPT, but compared to experiment the predicted slope is still larger by more than a factor of 3 (depending on which experimental measurement is used for comparison). The scale chosen for the diagram suppresses the size of the deviations somewhat, but they are clearly observed in the Dalitz Plot parameters listed in Tab. 3.2. On the other hand the x^2 dependence is nicely reproduced.

For the case where the subtraction constants are fixed by large-N_C ChPT at NLO it appears that the matching procedure itself is at fault for the deviations. Notice that we match the subtraction constants to the large-N_C ChPT calculation at *tree-level* despite being

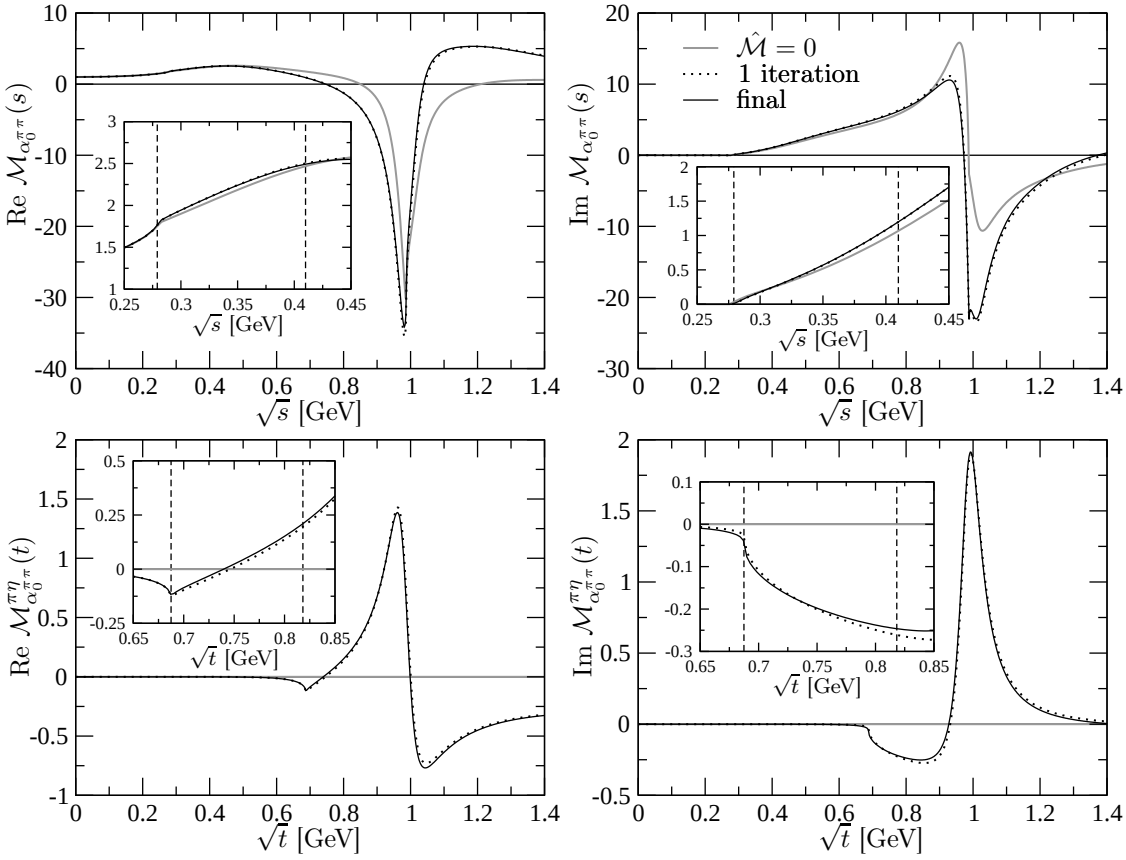

Figure 3.9: Successive iteration steps of real (left panel) and imaginary (right panel) part of the amplitude $\mathcal{M}_{\alpha_0^{\pi\pi}}(s)$ (top) and $\mathcal{M}^{\pi\eta}_{\alpha_0^{\pi\pi}}(t)$ (bottom) for $\eta' \to \eta\pi\pi$. The insets focus on the physical region, which is denoted by the vertical dashed lines.

next-to-leading order (loop corrections only enter at next-to-next-to-leading order in the large-N_C formalism). We cannot completely rule out that matching to next-to-next-to-leading order has potentially large effects on the subtraction constants $\gamma_0^{\pi\pi}, \gamma_0^{\pi\eta}$. A fit to experimental data predicts these parameters to be an order of magnitude smaller, see Section 3.5.4. However, such an explanation is not entirely satisfactory, since a lot of fine-tuning would be involved in reducing the values of the subtraction constants. One might reason that the low-energy constants L_i that enter the large-N_C calculation pose a problem: some of these are saturated by resonances, which in our framework are incorporated in the Omnès functions and are thus double-counted. However, as we stated before low-energy constants contribute only about 5% to the size of $\gamma_0^{\pi\pi}, \gamma_0^{\pi\eta}$.

Pertaining to the above it is also possible that the way in which we performed the matching procedure is too naive: we took the limit of the phase shifts $\delta_0(s)$ and $\delta_0^{\pi\eta}(t)$ going to zero to represent the case without final-state interactions, and expect the iteration procedure to perturbatively imprint the effects of rescattering on the amplitude. Such a simplified point of view, however, might not be viable. Indeed, it turns out that one of the largest contributions to the amplitude stems from the basis function $\mathcal{M}_{\gamma_0^{\pi\eta}}(s)$ that in a perturbative picture one would expect to be small.

The latter point is to some extent supported by inspection of the dispersive amplitude

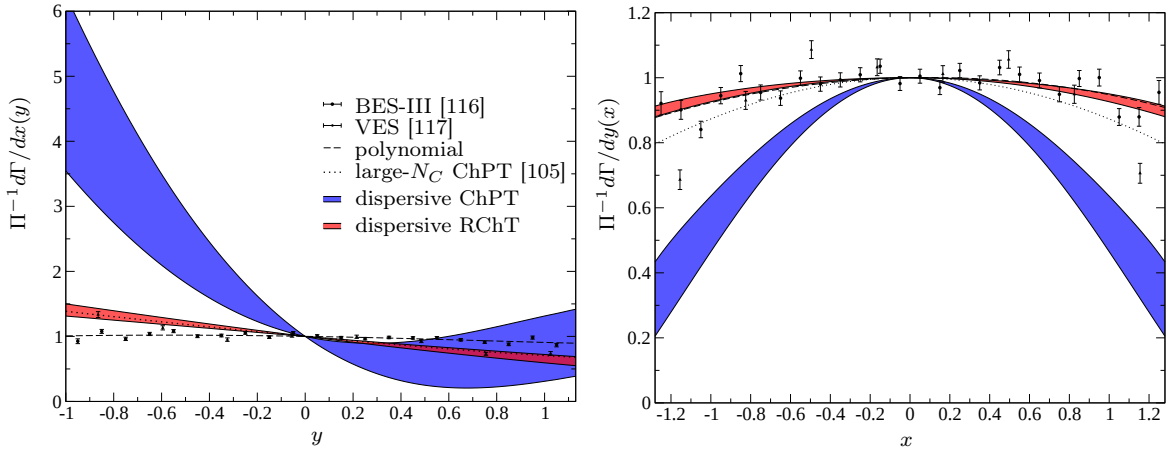

Figure 3.10: Decay spectrum integrated over the variable x, divided by phase space and normalized to one at $y = 0$ (left panel) and analogously for $x \leftrightarrow y$ (right panel). We show the sampled data sets for the BES-III [116] and the VES [117] parameterization. The dashed curve represents the Dalitz plot parameterization using the BES-III central values, the dotted curve denotes the large-N_C ChPT result at next-to-leading order, the blue shaded curve is the dispersive solution with subtraction constants matched to large-N_C ChPT, and finally the red shaded curve stems from matching to RChT (see text). The error bands reflect the uncertainties ensued by the variation between the two $\pi\eta$ phase-shift parameterizations.

with subtraction constants matched to RChT. Here the higher-order subtraction constants $\gamma_0^{\pi\pi}, \gamma_0^{\pi\eta}$ are smaller by an order of magnitude and the corresponding basis functions are more strongly suppressed: some of the rescattering effects are already accounted for in the resonance propagators in the RChT scheme. Unfortunately, Resonance Chiral Theory provides a much less systematic framework than large-N_C Chiral Perturbation Theory, so it is difficult to envision how to further improve the approach beyond what was presented here. One might be tempted to fit the constant c_d in order to get a deeper insight into these resonance couplings and compare with findings from other approaches (the $a_0(980)$ decay width [152], resonance saturation of low-energy constants [145], $I = 1/2, 3/2$ $K\pi$ S-wave scattering [153], and so forth). We have observed, though, that by varying c_d towards the lower end of the parameter range, which is still compatible with the extractions mentioned above, the deviations become much larger, even to the extent of exceeding what we observe for the large-N_C ChPT matching. Towards the upper end of the allowed range (and even beyond) the variations are barely visible from what is shown here rendering an attempt to fit c_d as the lone parameter futile.

3.5.4 Fitting the dispersive representation to data

In this section we choose to fit the subtraction constants to data. Of course we lose all predictability in this case. Nevertheless, we can deliver a representation of the amplitude that fulfills the strong constraints of analyticity and unitarity. This is essential if one should endeavor to perform a dispersive analysis of $\eta' \to 3\pi$.[#13] For such a treatment a polynomial

[#13]Notice that the decay $\eta' \to 3\pi$ can proceed via $\eta' \to \eta\pi\pi$ and isospin breaking rescattering $\eta\pi \to \pi\pi$ (which can be extracted from analytic continuation of the dispersive amplitude $\eta \to 3\pi$ [154]) and direct isospin breaking $\eta' \to 3\pi$.

	large-N_C [105]	dispersive ChPT	RChT [105]	dispersive RChT
a	-0.303	$-1.03 \ldots -2.87$	-0.119	$-0.30 \ldots -0.46$
b	$+0.001$	$+1.41 \ldots +2.25$	$+0.001$	$+0.02 \ldots +0.05$
d	-0.089	$-0.36 \ldots -0.52$	-0.056	$-0.05 \ldots -0.07$

Table 3.2: Dalitz plot parameters obtained from fitting the polynomial expansion (3.120) to the dispersive amplitude with the subtraction constants matched to large-N_C ChPT and RChT compared to the Dalitz plot parameters predicted by large-N_C ChPT at next-to-leading order and RChT. The error range of the dispersive analysis stems from varying between the two different parameterizations of the $\pi\eta$ phase shift, which is the dominant uncertainty. There is no fit value for c, since our representation is necessarily symmetric in x, and $c = 0$. The values shown here are to be compared with Tab. 3.1.

parameterization is certainly not sufficient.

In Fig. 3.11 we display the results of our fits to the data sets sampled from the BES-III and the VES parameterization respectively. The fit parameters and corresponding χ^2/ndof are shown in Table 3.3. Note that we use *real* fit parameters: in principle the subtraction constants can have imaginary parts due to the complex discontinuity (3.48). However, since the phase space of $\eta' \to \eta\pi\pi$ is small the subtraction constants are likewise expected to have a very small imaginary part to the extent that – given the precision of the data sets – their effect is entirely negligible (this is not the case for processes involving the decay of heavier mesons). Across the board the fits proceed well and the χ^2/ndof is close to one for each fit. The polynomial Dalitz plot parameterization is well-reproduced: in the y-direction the dispersive integral is virtually indistinguishable, whereas in the x-direction the small asymmetry due to the c-dependent term is seen as a main distinction. The fit quality should not be surprising since we are fitting a data set that is well-described by a three-parameter polynomial with a dispersive amplitude with likewise three free parameters (note that $\alpha_0^{\pi\pi}$ is merely an overall normalization). It is, however, interesting to observe a large variation of the allowed parameter range, especially for $\beta_0^{\pi\pi}$ and $\gamma_0^{\pi\pi}$. This is readily explained by the correlation matrix, which we show for illustration for the first column in Table 3.3 (the results for the other correlation matrices are similar),

$$\begin{array}{rc} & \begin{array}{cccc} \alpha_0^{\pi\pi} & \beta_0^{\pi\pi} & \gamma_0^{\pi\pi} & \gamma_0^{\pi\eta} \end{array} \\ \begin{array}{r} \alpha_0^{\pi\pi} = 13.0 \pm 0.9 \\ \beta_0^{\pi\pi} = -4.62 \pm 0.31 \\ \gamma_0^{\pi\pi} = -4.84 \pm 1.57 \\ \gamma_0^{\pi\eta} = -0.21 \pm 0.02 \end{array} & \begin{pmatrix} 1.000 & -0.500 & 0.240 & -0.749 \\ & 1.000 & -0.959 & -0.194 \\ & & 1.000 & 0.452 \\ & & & 1.000 \end{pmatrix} . \end{array} \tag{3.124}$$

The parameters $\beta_0^{\pi\pi}$ and $\gamma_0^{\pi\pi}$ are thus strongly anti-correlated. The fit to the VES data set is overconstrained due to the very low-statistics so that both parameters can be varied in a large range and still reproduce data relatively well.

In Fig. 3.12 we study the development of the Adler zeros in the dispersive amplitude after performing the fit. We stated before that these are supposedly protected by SU(2)×SU(2) symmetry. We take the first correction to the relation (3.110) into account and study the Adler zeros at $s^2 = 2M_\pi^4$, instead of $s = 0$. We observe an interesting phenomenon: the real

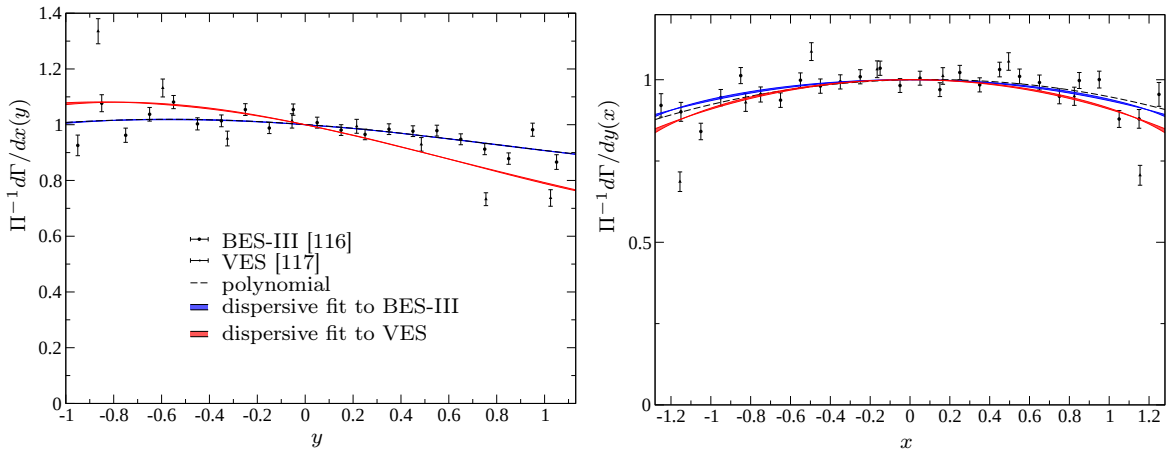

Figure 3.11: Decay spectrum integrated over the variable x, divided by phase space and normalized to one at $y = 0$ (left panel) and analogously for $x \leftrightarrow y$ (right panel). We show the sampled data sets for the BES-III [116] and the VES [117] parameterization. The blue shaded curve represents the dispersive results with subtraction constants fitted to the BES-III data set, while the red shaded curve denotes the VES-fitted data set. The dashed line represents the polynomial representation with parameters fitted to the BES-III data set.

part of the amplitude falls off from $x = 0$ to higher $|x|$ until it reaches the vicinity of the $a_0(980)$ resonance and sees a strong increase up to the peak position at $|x| \simeq 5.7$. For the BES-III data sample the influence of the $a_0(980)$ resonance is sufficient to remove the Adler zeros from the amplitude, which supports the argument of Ref. [107]. The same statement cannot be made for the VES data sample, where the real part of the amplitude crosses zero before the influence of the $a_0(980)$ is felt. Moreover, the zeros lie in the vicinity of those of the large-N_C amplitude. The current experimental situation does not allow for a definite conclusion on whether the low-energy theorem is violated in $\eta' \to \eta\pi\pi$ or not.

The above results have rather daunting consequences as far as the extraction of $\pi\eta$ scattering phase shifts and threshold parameters is concerned: the subtraction constants completely absorb any kind of dependence on the specific shape of the $\pi\eta$ phase shift. This is also in agreement with the findings of Ref. [29]. Also the strong violation of the low-energy theo-

$\delta_0^{\pi\eta}$	unitarized	Breit–Wigner	unitarized	Breit–Wigner
	BES-III		VES	
χ^2/ndof	1.06	1.06	0.89	0.90
$\alpha_0^{\pi\pi}$	13.0 ± 0.9	10.1 ± 0.6	18.3 ± 2.7	12.8 ± 1.6
$\beta_0^{\pi\pi}$	-4.6 ± 0.3	-3.1 ± 0.5	-3.7 ± 0.7	-1.0 ± 1.2
$\gamma_0^{\pi\pi}$	-4.8 ± 1.6	-0.3 ± 2.4	0.5 ± 3.2	-9.7 ± 5.9
$\gamma_0^{\pi\eta}$	-0.21 ± 0.02	-0.28 ± 0.03	-0.29 ± 0.04	-0.40 ± 0.07

Table 3.3: Fit results for the subtraction constants for both the BES-III and the VES data sample for the unitarized coupled-channel and Breit–Wigner $\pi\eta$ phase shift $\delta_0^{\pi\eta}(t)$.

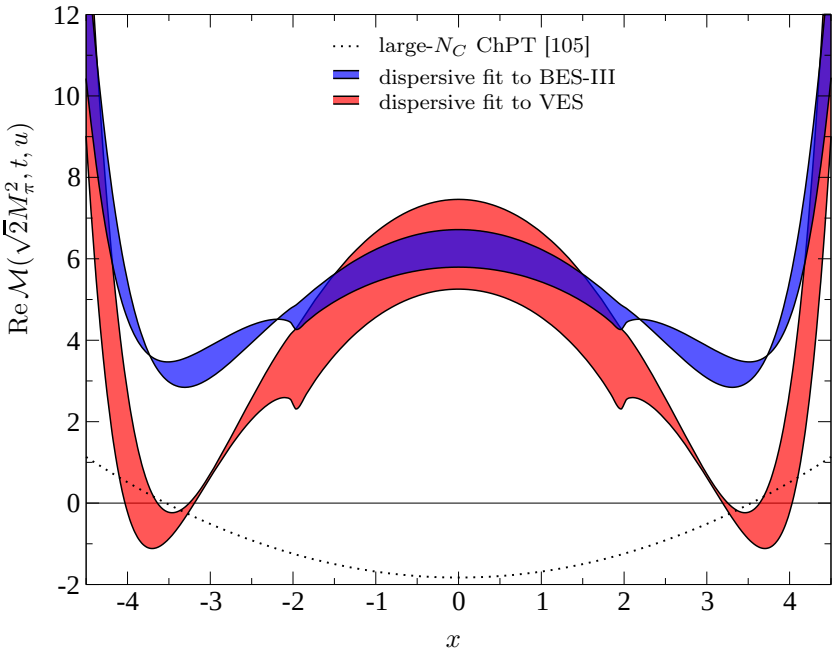

Figure 3.12: Real part of the amplitude at $s^2 = 2M_\pi^4$. along the line $t - u$. We show the large-N_C ChPT result (dotted line), and the fit of the dispersive representation to the BES-III (blue curve) and VES (red curve) data sets.

rem (3.110) casts some doubt on matching to large-N_C ChPT as the theory is built on the approximate fulfillment of low-energy theorems. Unless the subtraction constants can be fixed by some means despite fitting to data the extraction of information on $\pi\eta$ scattering remains elusive.

3.6 Summary and conclusion

In this Chapter we have presented a dispersive analysis of the decay $\eta' \to \eta\pi\pi$. We have derived a set of integral equations on the grounds of unitarity for the corresponding scattering process and performed an analytic continuation to the physical region of the three-particle decay. The ensuing analytic structure, most notably the generation of three-particle cuts, is in full agreement with our findings in the previous chapter, where we treated these effects in a perturbative framework.

The integral equations depend on $\pi\pi$ and $\pi\eta$ scattering phase shifts as well as a set of subtraction constants. The phase shift of $\pi\pi$ scattering is strongly constrained by chiral symmetry and Roy equations in contrast to $\pi\eta$ scattering, which constitutes the dominant uncertainty aside from the subtraction constants. In our numerical analysis we devised two separate methods to fix the latter: on the one hand we matched them to the low-energy theories of large-N_C ChPT and RChT, and on the other we fitted them to data sets. These data sets have been sampled from experimentally measured polynomial Dalitz plot parameterizations.

Matching to large-N_C ChPT we found large deviations from the polynomial parameterization rendering this approach unfit to be used in an attempt to extract information on $\pi\eta$ scattering. The deviations are smaller when matching to RChT, however, they are still siz-

able and the framework does not allow for systematic improvements. Fitting the subtraction constants to data showed good agreement with experiment, but the limited accuracy of the data samples allowed for a wide parameter range. Any effects stemming from differences in the $\pi\eta$ phase shifts were absorbed in the subtraction constants. The fitted parameterization could in principle be used as input for a dispersive analysis of $\eta' \to 3\pi$.

At the very least the results of this Chapter emphasize the importance of understanding the interplay between the low- and high-energy regime, as evidenced by the matching of the subtraction constants. It is a bit of a stretch to call the method presented here a "precision analysis" up to this point. In the following Chapter we apply the same method to a decay process that only involves one subtraction constant. Thus the dynamics of the decay are completely determined by rescattering effects so that it presents a strong testing ground for the theory.

Chapter 4

Dispersive analysis of $\omega \to 3\pi$ and $\phi \to 3\pi$ decays[#1]

4.1 Introduction

In this Chapter we apply the previously introduced dispersion theory methods to a simpler but certainly not less interesting system: the three-pion decay of the lightest isoscalar vector mesons $\omega/\phi \to 3\pi$. The system is simpler since we only have to take pion–pion final states into account. Moreover, due to Bose symmetry the pions can only interact in partial waves of odd angular momenta. We will find that under such constraints only P-wave interactions are relevant.

On the other hand this decay channel serves to expose the advantages of a dispersion relation approach to a greater extent than $\eta' \to \eta\pi\pi$. The mass of the decaying particle and thus the allowed energy of the two-pion subsystem is sufficiently large so that the influence of the ρ resonance is already strongly felt in the case of the ω or even observed in the the form of resonance bands inside the Dalitz plot in the case of the ϕ. Even though decays like $K \to 3\pi$ or $\eta \to 3\pi$ have successfully been analyzed in perturbative settings such as chiral perturbation theory [59, 60] or even non-relativistic effective field theories as discussed in Chapter 2 and Refs. [25, 33], it is obvious that these break down at the resonance scale. Dispersion relations allow us to connect both, the low-energy region and the resonance region, on the grounds of analyticity. From that vantage point the study of $\omega/\phi \to 3\pi$ may also be seen as exploratory for the decays of heavier mesons.

In recent years, there has been a flourish of attempts to treat the physics of vector mesons in effective-field-theory approaches [156–163], motivated by their prominent nature in hadronic physics involving virtual photons, their relatively low masses among the various meson resonances, and their strong coupling to the light pseudoscalars. However, when it comes to the three-pion decays of ω and ϕ, descriptions in terms of vector-meson dominance and improved tree-level models (mostly incorporating a finite width of the intermediate ρ resonances) [161, 164–166] (see also Ref. [167] for earlier references), which do not fully respect analyticity and unitarity constraints, still seem to be state of the art.[#2]

[#1] The contents of this Chapter have been published in [155].

[#2] It needs to be pointed out, though, that Lagrangian-based approaches often have the advantage of relating various different processes to each other; such symmetry constraints most of the time have nothing to do with analyticity and unitarity, and hence can at best be imposed *a posteriori* in dispersive studies.

In this respect, we consider this an ideal time to take up dispersive studies of these decays once more, even though these have been performed in the past [168]. High-precision phase-shift analyses of pion–pion scattering are now available [37, 39, 41] and can be employed as input for decay studies. On the experimental side, high-statistics Dalitz plot investigations have either been performed ($\phi \to 3\pi$ [169,170]), or are planned or ongoing ($\omega \to 3\pi$ [101,171,172]). Furthermore, the $\omega/\phi \to 3\pi$ partial-wave will prove to be an essential ingredient in a dispersive analysis of the $V \to \pi^0\gamma^*$ transition form factor that is presented in Chapter 5.

The outline of this chapter is as follows. We introduce the necessary basics on kinematics and partial-wave decomposition in Section 4.2, and describe the formalism for a dispersion-theoretical description of the decays $\omega/\phi \to 3\pi$ in Section 4.3. First numerical results of our solutions are discussed in Section 4.4, before we compare in detail to the experimental Dalitz plot studies for $\phi \to 3\pi$ and predict Dalitz plot parameters for $\omega \to 3\pi$ in Section 4.5. As a further application, we calculate the contribution of $\omega\pi$ intermediate states to the inelasticity in the pion–pion P partial wave in Section 4.7. We conclude in Section 4.8. Several aspects that lie somewhat outside the main line of argument are relegated to the Appendices, where we discuss higher partial waves (Appendix B.4) as well as possible contributions from heavier resonances (Appendix B.5), and derive a generalization of the Omnès representation taking into account inelasticities (Appendix B.6).

4.2 Kinematics and partial-wave decomposition

We consider the three-pion decay of the lightest isoscalar vector mesons,

$$V(p_V) \to \pi^+(p_+)\pi^-(p_-)\pi^0(p_0) \;, \qquad V = \omega/\phi \;, \tag{4.1}$$

where the particle momenta are conventionally related to the Mandelstam variables by $s = (p_V - p_0)^2$, $t = (p_V - p_+)^2$, $u = (p_V - p_-)^2$, with

$$3s_0 \doteq s + t + u = M_V^2 + 3\,M_\pi^2 \;. \tag{4.2}$$

Here and in the following we restrict ourselves to the isospin limit, $M_{\pi^0} = M_{\pi^\pm} \doteq M_\pi$, unless explicitly stated otherwise.

Since $V \to 3\pi$ is of odd intrinsic parity, the amplitude can be decomposed as

$$\mathcal{M}(s,t,u) = i\epsilon_{\mu\nu\alpha\beta} n^\mu p_+^\nu p_-^\alpha p_0^\beta \mathcal{F}(s,t,u) \;, \tag{4.3}$$

where $\epsilon_{\mu\nu\alpha\beta}$ is the totally antisymmetric Levi-Civita tensor, n^μ is the polarization vector of the decaying vector particle, and $\mathcal{F}(s,t,u)$ is a scalar function. The absolute value squared of the amplitude reads

$$\begin{aligned} |\mathcal{M}(s,t,u)|^2 &= \epsilon_{\mu\nu\alpha\beta}\epsilon^{\mu}{}_{\bar\nu\bar\alpha\bar\beta} p_+^\nu p_-^\alpha p_0^\beta p_+^{\bar\nu} p_-^{\bar\alpha} p_0^{\bar\beta} |\mathcal{F}(s,t,u)|^2 \\ &= \frac{1}{4}\Big[s\,t\,u - M_\pi^2\big(M_V^2 - M_\pi^2\big)^2\Big]|\mathcal{F}(s,t,u)|^2 \\ &= \frac{s}{16}\kappa^2(s)\sin^2\theta_s |\mathcal{F}(s,t,u)|^2 \;, \end{aligned} \tag{4.4}$$

where averaging over all possible polarization states of the vector particle in the first line leads to $\sum_{\text{pol.}} n^{\bar\mu} n^\mu = -g^{\mu\bar\mu}$, θ_s is the center-of-mass scattering angle in the s-channel, $\cos\theta_s = (t-u)/\kappa(s)$, and

$$\kappa(s) = \sigma_\pi(s)\lambda^{1/2}(M_V^2, M_\pi^2, s) \;, \tag{4.5}$$

with the Källén function $\lambda(x,y,z) = x^2+y^2+z^2-2(xy+xz+yz)$ as defined in the previous chapters, and $\sigma_\pi(s) = \sqrt{1-4M_\pi^2/s}$.

Due to Bose symmetry only partial waves of odd angular momentum can contribute to the amplitude. Accordingly, the partial-wave decomposition of the scalar part of the amplitude reads [173]

$$\mathcal{F}(s,t,u) = \sum_{\ell \text{ odd}} f_\ell(s) P_\ell'(z_s) \ , \tag{4.6}$$

where $z_s = \cos\theta_s$, $P_\ell'(z_s)$ is the differentiated Legendre polynomial, and one can project onto the partial-wave amplitude $f_\ell(s)$ with the prescription

$$f_\ell(s) = \frac{1}{2}\int_{-1}^{1} dz_s \big[P_{\ell-1}(z_s) - P_{\ell+1}(z_s)\big]\, \mathcal{F}(s,t,u) \ . \tag{4.7}$$

For the dominant $\ell = 1$ partial wave we have

$$f_1(s) = \frac{3}{4}\int_{-1}^{1} dz_s \big(1-z_s^2\big)\, \mathcal{F}(s,t,u) \ . \tag{4.8}$$

In our analysis we neglect discontinuities of F- and higher partial waves (see the corresponding discussion in Appendix B.4), so that $\mathcal{F}(s,t,u)$ can be decomposed in a fully analogous fashion to what has been done in Section 3.3.1 in terms of functions of a single variable as

$$\mathcal{F}(s,t,u) = \mathcal{F}(s) + \mathcal{F}(t) + \mathcal{F}(u) \ , \tag{4.9}$$

where $\mathcal{F}(s)$ only has a right-hand cut. Again, the dispersion relations that we will derive in the following will be given in terms of these single-variable functions $\mathcal{F}(s)$. Equation (4.9) represents a symmetrized partial-wave expansion, its generalized form allowing for F-wave discontinuities is shown in Appendix B.4, Eq. (B.32).

We will also make use of the partial-wave expansion of the $\pi\pi \to \pi\pi$ scattering amplitude that has been previously defined and that we repeat for convenience,

$$\mathcal{T}_I(s,t,u) = 32\pi \sum_{\ell=0}^{\infty} (2\ell+1) t_\ell^I(s) P_\ell(z) \ , \tag{4.10}$$

where t_ℓ^I is the partial-wave amplitude of isospin I and angular momentum ℓ and can be expressed in terms of the phase shift δ_ℓ^I according to

$$t_\ell^I(s) = \frac{e^{2i\delta_\ell^I(s)} - 1}{2i\sigma_\pi(s)} \ . \tag{4.11}$$

4.3 Dispersion relations for $\omega/\phi \to 3\pi$ decays

In this section we discuss how to apply the framework that has been developed in great detail in the previous section to $V \to 3\pi$ decays. We reiterate that the advantage of using dispersion relations to account for final-state interactions in three-body decays is the incorporation of three-particle cuts, a substantial analytic ingredient that is left out in isobaric models, like vector-meson dominance models [161,164]. Again, the strategy is to set up a set of dispersion relations for the corresponding *scattering* process, i.e. $V\pi \to \pi\pi$, with $M_V < 3M_\pi$ and $s >$

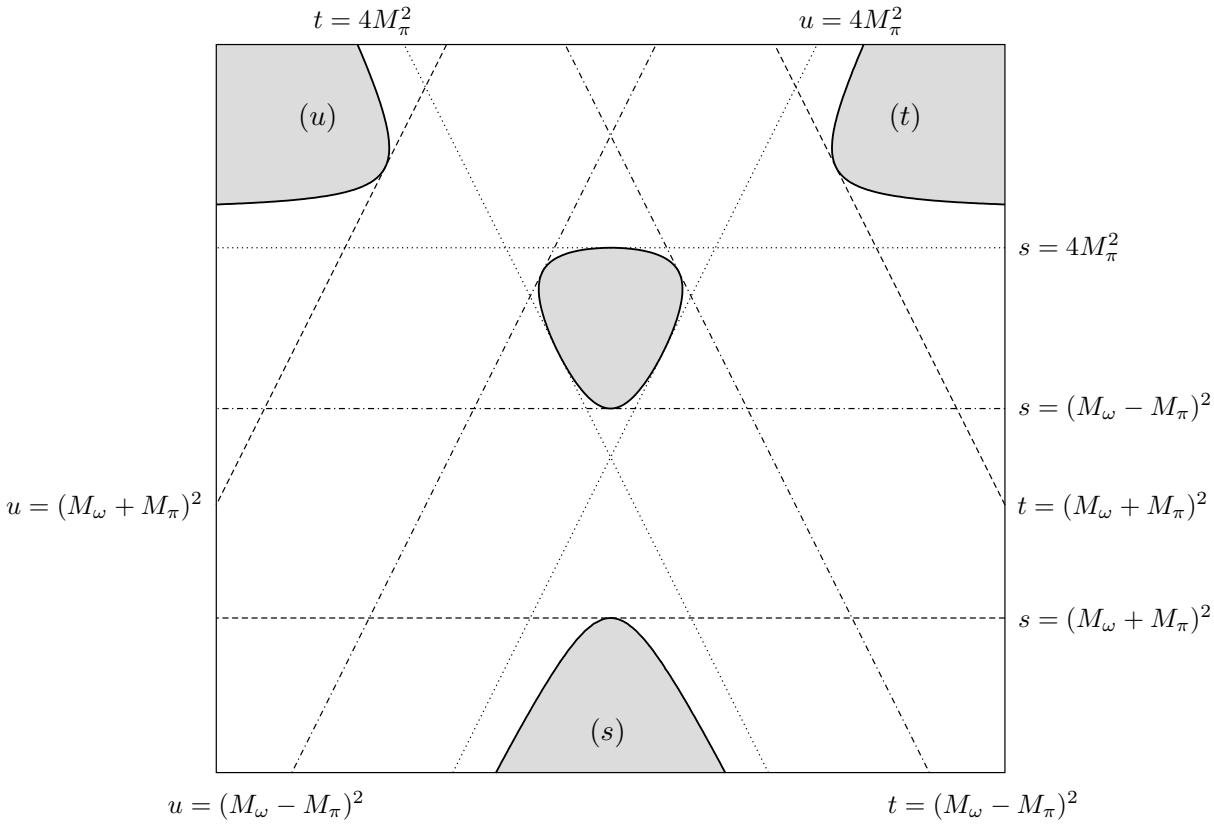

Figure 4.1: The Mandelstam plane for $\omega\pi \to \pi\pi$ with all crossed channels including the decay process $\omega \to 3\pi$. Dashed lines denote the thresholds of the corresponding scattering channels, dotted lines denote the thresholds of the scattering subsystems of the decay channel, and dashed-dotted lines the end of the physical decay region for each channel.

$(M_V + M_\pi)^2$, and analytically continue the resulting expressions to the physical realm of the *decay* process, $M_V > 3M_\pi$ and $4M_\pi^2 \leq s \leq (M_V - M_\pi)^2$, see also Fig. 4.1 for an illustration of the physical regions that we connect through analytic continuation.

We reiterate that we essentially only consider *elastic* unitarity in the following (see Section 4.4.4 for an attempt to partially account for inelasticity effects in the pion–pion P partial wave). One might suspect that the dominant decay $\phi \to K\bar{K}$ with subsequent inelastic rescattering $K\bar{K} \to 3\pi$, see Fig. 4.2, may have a substantial impact on the Dalitz plot distribution for $\phi \to 3\pi$. This is not the case for the following reason: the $K\bar{K}$ intermediate state occurs at a fixed total energy of $(p_K + p_{\bar{K}})^2 = M_\phi^2$, where the rescattering $K\bar{K} \to 3\pi$ will be entirely dominated by the (very narrow) ϕ resonance. The diagram therefore factorizes, and the whole effect of the $K\bar{K}$ intermediate state can be absorbed into a complex wave-function renormalization constant for the ϕ field, which amounts to an unobservable overall (constant) phase of the amplitude. The Dalitz plot distribution of $\phi \to 3\pi$ remains therefore entirely unaffected.

Note finally that in the sense of a dispersion-theory analysis, there is no $\rho\pi$ two-body intermediate state contributing to the ϕ decay in a similar fashion as $K\bar{K}$ depicted in Fig. 4.2: $\rho\pi$ is no distinct state from 3π, the effect conventionally encoded that way shows up in our analysis as the resonant two-body $\pi\pi$ P-wave interaction. From the point of view of dispersion theory, there is no meaningful way to differentiate between $\rho\pi$ and 3π final states in ϕ decays.

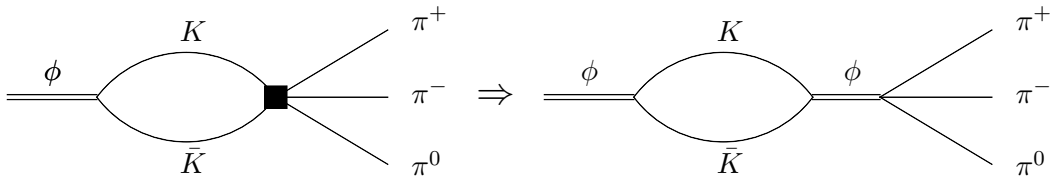

Figure 4.2: Contribution of $K\bar{K}$ intermediate states to $\phi \to 3\pi$. The general rescattering $K\bar{K} \to \pi^+\pi^-\pi^0$, denoted by the black square in the left diagram, is entirely dominated by the ϕ resonance for $(p_K + p_{\bar{K}})^2 = M_\phi^2$, see the right diagram.

4.3.1 Unitarity relation

In the following, we relate the discontinuity of the $V\pi \to \pi\pi$ s-channel partial-wave amplitude to the amplitude itself and the $\pi\pi$ P-wave phase shift. Similar considerations for t- and u-channel proceed completely analogously, and will not be discussed separately. In the elastic approximation with only pion–pion intermediate states one has for the discontinuity of the diagram in Fig. 4.3 [47]

$$\operatorname{disc}\mathcal{M}(s,z_s) = \frac{i}{2}\int\frac{d^4l}{(2\pi)^4}\mathcal{M}(s,z_s')\mathcal{T}_1^*(s,z_s'')(2\pi)\delta\big(l^2-M_\pi^2\big)\,(2\pi)\delta\big((q-l)^2-M_\pi^2\big)\;, \quad (4.12)$$

where $q = p_+ + p_-$, $z_s = \cos\theta_s$, $z_s' = \cos\theta_s'$, and $z_s'' = \cos\theta_s''$, where θ_s denotes the center-of-mass scattering angle between the initial- and final-state momenta, θ_s' between initial and intermediate state, and θ_s'' between intermediate and final state.

We insert Eq. (4.3) on both sides of Eq. (4.12) and find

$$\epsilon_{\mu\nu\alpha\beta}n^\mu p_+^\nu p_-^\alpha p_0^\beta \operatorname{disc}\mathcal{F}(s,z_s) = \frac{i}{2}\int\frac{d^4l}{(2\pi)^4}\epsilon_{\mu\nu\alpha\beta}n^\mu p_+^\nu p_-^\alpha l^\beta \mathcal{F}(s,z_s')\mathcal{T}_1^*(s,z_s'') \times (2\pi)\delta\big(l^2-M_\pi^2\big)\,(2\pi)\delta\big((q-l)^2-M_\pi^2\big)\;. \quad (4.13)$$

We obviously need to find a way to treat the l_β term before we are able to carry out the momentum integration. To that end we note that the scattering process has three independent Lorentz structures, namely the momenta p_+, p_-, p_0. The remaining momentum p_V is related to the former by total momentum conservation. We therefore rewrite the integration according to

$$\int d^4l\, l^\beta(\ldots) = p_+^\beta\mathcal{I}_+ + p_-^\beta\mathcal{I}_- + p_0^\beta\mathcal{I}_0\;, \quad (4.14)$$

and determine the integrals $\mathcal{I}_{+,-,0}$ by solving the system of linear equations that emerges after contraction with $p_{+\beta}$, $p_{-\beta}$, and $p_{0\beta}$. Due to the antisymmetry of the Levi-Cevita tensor, only the term proportional to p_0 survives and upon elimination of the δ-functions, we may write

$$\operatorname{disc}\mathcal{F}(s,z_s) = \frac{i\sigma_\pi(s)}{64\pi^2}\int_{-1}^{1}dz_s'\int_0^{2\pi}d\phi_s'\frac{z_s''-z_sz_s'}{1-z_s^2}\mathcal{F}(s,z_s')\mathcal{T}_1^*(s,z_s'')\;, \quad (4.15)$$

where $z_s'' = z_sz_s' + \sqrt{1-z_s^2}\sqrt{1-z_s'^2}\cos\phi_s'$. Finally, we can use the partial-wave expansion for the amplitudes $\mathcal{F}$ and $\mathcal{T}_1$ given in Eqs. (4.6) and (4.10), and project out the $\ell = 1$ partial wave to arrive at the Watson-like unitarity relation,

$$\operatorname{disc} f_1(s) = 2i\, f_1(s)\theta(s-4M_\pi^2)\sin\delta(s)e^{-i\delta(s)}\;, \quad (4.16)$$

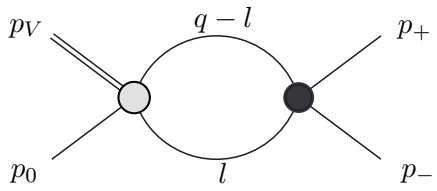

Figure 4.3: Diagram of the $V\pi \to \pi\pi$ s-channel scattering amplitude. The double line denotes the vector meson, all single lines refer to pions. The gray circle corresponds to the $V\pi \to \pi\pi$ amplitude $\mathcal{M}(s, z_s'')$, the black one to the $\pi\pi \to \pi\pi$ amplitude $\mathcal{T}^1(s, z_s')$ (of isospin $I = 1$). To calculate the amplitude one cuts through the intermediate pion propagators with momenta l and $q - l$.

where $\delta(s) \doteq \delta_1^1(s)$ is the $\pi\pi$ P-wave phase shift. Noting that $\operatorname{disc} f_1(s) = \operatorname{disc} \mathcal{F}(s)$, the previous expression can be recast into

$$\operatorname{disc} \mathcal{F}(s) = 2i \left(\mathcal{F}(s) + \hat{\mathcal{F}}(s)\right)\theta(s - 4M_\pi^2) \sin\delta(s) e^{-i\delta(s)} \ , \tag{4.17}$$

where $\hat{\mathcal{F}}(s)$ is the inhomogeneity of the integral equation that we have encountered before and is given by angular averages over $\mathcal{F}$ according to

$$\begin{aligned} \hat{\mathcal{F}}(s) &= 3\langle (1 - z^2)\mathcal{F}\rangle(s) \ , \\ \langle z^n f\rangle(s) &= \frac{1}{2}\int_{-1}^{1} dz\, z^n f\Big(\tfrac{1}{2}(3s_0 - s + z\kappa(s))\Big) \ . \end{aligned} \tag{4.18}$$

$\hat{\mathcal{F}}(s)$ contains the left-hand-cut contribution to the partial wave $f_1(s)$. The previous expressions are well-defined in the scattering regime. We have observed that special care has to be taken in the decay region due to the non-trivial behavior of the function $\kappa(s)$, that imposes a complex analytic structure on the angular integration. This is entirely analogous to what we have outlined in great detail in Section 3.3.4. In the following we will discuss the solution to these integral equations.

4.3.2 Homogeneous equation and the charged pion radius

We already discussed the solution for the simplified case of $\hat{\mathcal{F}}(s) = 0$: in this case we have precisely the unitarity relation of the vector form factor that was discussed in Section 1.2.2, and its solution was given by the Omnès function,

$$\Omega(s) = \exp\left\{\frac{s}{\pi}\int_{4M_\pi^2}^{\infty} ds' \frac{\delta(s')}{s'(s' - s)}\right\} \ . \tag{4.19}$$

At this point we would like to pick up the discussion of the asymptotic behavior of the Omnès function, that we have already touched upon in Section 3.3.3. As mentioned before it is constrained by the asymptotic behavior of the phase shift: for $\delta(s) \to k\pi$ as $s \to \infty$ one finds $\Omega(s) \to s^{-k}$. We shall assume $k = 1$ for the asymptotic behavior of the P wave, which guarantees the high-energy fall-off for the form factor $\propto 1/s$ as suggested by perturbative QCD (up to logarithmic corrections) exactly if $P(s)$ is a constant, and hence due to gauge invariance, $P(s) = 1$.

Pertaining to this issue the behavior of the $\pi\pi$ phase shift is not known to arbitrarily high energies. We devise a slightly different method than what was presented in the previous chapter: in our numerical calculations we use a phenomenological parameterization of the phase shift up to a certain energy $s = \Lambda_\Omega^2$, beyond which it is set to a constant. At the accuracy at which we are working this constant does not have to be π exactly. This is dicussed in some detail Ref. [174], and can also be deduced from our error discussion in Section 4.4.4.

One possibility to suppress the high-energy behavior of the phase shift in the Omnès function that we have not discussed so far is to resort to a twice-subtracted dispersion integral, as opposed to the once-subtracted version used in Eq. (4.19) (cf. e.g. Ref. [175]). Due to the identification $F_\pi^V(s) = \Omega(s)$, the additional subtraction constant can be related to the charge radius of the pion,

$$\Omega(s) = \exp\left\{\frac{1}{6}\langle r^2\rangle_\pi^V\, s + \frac{s^2}{\pi}\int_{4M_\pi^2}^\infty ds' \frac{\delta(s')}{s'^2(s'-s)}\right\} . \tag{4.20}$$

Comparing to Eq. (4.19), we can then express the charge radius in terms of a sum rule,

$$\langle r^2\rangle_\pi^V = \frac{6}{\pi}\int_{4M_\pi^2}^\infty ds' \frac{\delta(s')}{s'^2} . \tag{4.21}$$

To take advantage of the suppression of high energies in the oversubtracted dispersion integral, one may make use of an independent phenomenological determination of the charge radius. This allows us to reparametrize our lack of knowledge of the behavior of the amplitude at large s as a polynomial, which should be a decent approximation at the energies we are working at. In Section 4.4.4 we discuss the numerical effects of using the two different versions of the Omnès function. We want to emphasize that, as a matter of principle, using a radius different from the sum-rule value Eq. (4.21) is inconsistent: it leads to a wrong (exponential) high-energy behavior. In practice, however, and for the (small) deviations in the charge radius we consider, the effects of this error are not visible within the physical region of the decays under consideration.

4.3.3 Integral equation and solution strategy

Using the same methods as described in Section 3.3.3 we find the integral equation that solves Eq. (4.17), namely

$$\mathcal{F}(s) = \Omega(s)\left\{a + \frac{s}{\pi}\int_{4M_\pi^2}^\infty \frac{ds'}{s'}\frac{\sin\delta(s')\hat{\mathcal{F}}(s')}{|\Omega(s')|(s'-s)}\right\} , \tag{4.22}$$

where a is a subtraction constant. The order of the subtraction polynomial is limited by the asymptotic behavior of the integrand. The Froissart bound [45] constrains the behavior of the amplitude for large s, $\mathcal{M}(s,t,u) < Cs\log^2(s)$ for some constant C, and consequently $\hat{\mathcal{F}}(s) < C's^{-1/2}\log^2(s)$ for $s \to \infty$ (and another constant C'). Along with the asymptotic behavior of the Omnès function it is obvious that the integral remains finite. Since $\hat{\mathcal{F}}$ is linear in $\mathcal{F}$ we again simplify Eq. (4.22) from the point of view of the numerical implementation:

$$\begin{aligned}
&\mathcal{F}(s) = a\mathcal{F}_a(s) , \quad \hat{\mathcal{F}}(s) = a\hat{\mathcal{F}}_a(s) , \\
&\mathcal{F}_a(s) = \Omega(s)\left\{1 + \frac{s}{\pi}\int_{4M_\pi^2}^\infty \frac{ds'}{s'}\frac{\sin\delta(s')\hat{\mathcal{F}}_a(s')}{|\Omega(s')|(s'-s)}\right\} .
\end{aligned} \tag{4.23}$$

Our results will be pure predictions aside from an overall normalization constant that can be fixed after the iteration process. For lack of a better theoretical method to fix the normalization, we fit to the experimentally determined partial decay width unless explicitly stated otherwise.

The integral equation (4.23) can now be solved by the same iterative numerical procedure that was outlined before: we start from an arbitrary input function $\mathcal{F}(s)$ and calculate the inhomogeneity $\hat{\mathcal{F}}(s)$ from Eq. (4.18), which in turn is used as an input for the calculation of an updated $\mathcal{F}(s)$ by means of Eq. (4.23). The process is repeated until the solution converges to a fixed point with sufficient accuracy. We will use $\mathcal{F}(s) = \Omega(s)$ as our starting point: as the $\pi\pi$ P wave is dominated by the ρ resonance at low energies, this closely corresponds to an isobaric description of the decay, and the modification of $\mathcal{F}(s)$ in the iteration procedure, the difference between starting and fixed point, allows us to quantify crossed-channel effects generated by the iteration in a plausible way.

4.3.4 Oversubtraction

The integral in the solution of the dispersion relation for $V \to 3\pi$ decays, Eq. (4.23), is guaranteed to converge, given our assumptions on the high-energy behavior of amplitudes and phases. This solution has the maximal degree of predictability, as it only depends on one single real parameter, the subtraction constant a that merely represents the overall normalization of the amplitude (the phase of which is of course unobservable); the complete Dalitz plot distribution is then a prediction.

We will discuss various sources of the theoretical errors in this representation, most of which are in one way or the other associated with the high-energy behavior, in Section 4.4.4. It is obvious, though, that while our high-energy constraints on the amplitudes, including e.g. the assumed smooth continuation of the scattering phase, present a plausible and internally consistent procedure to interpolate between the very well-constrained low-energy part and the asymptotic behavior as suggested by the Froissart bound, we certainly neglect various details in the description of an intermediate-energy range, in particular inelastic contributions. The hope (which, eventually, has to be checked phenomenologically) is that inside the dispersive integrals, this intermediate-energy range does not influence the low-energy description of the decay amplitudes too much. However, similar to what we explained for the Omnès function, in order to suppress the influence of inelastic contributions even further, we can alternatively subtract the dispersive solution once more than strictly necessary, at the expense of introducing another subtraction constant (see also Appendix B.1):

$$\mathcal{F}(s) = \Omega(s)\left\{a + b's + \frac{s^2}{\pi}\int_{4M_\pi^2}^{\infty} \frac{ds'}{s'^2} \frac{\sin\delta(s')\hat{\mathcal{F}}(s')}{|\Omega(s')|(s'-s)}\right\} . \tag{4.24}$$

This is equivalent to Eq. (4.22) if b' obeys the sum rule

$$b' = \frac{1}{\pi}\int_{4M_\pi^2}^{\infty} \frac{ds'}{s'^2} \frac{\sin\delta(s')\hat{\mathcal{F}}(s')}{|\Omega(s')|} . \tag{4.25}$$

Because of the special analytic structure of $\hat{\mathcal{F}}(s)$, which is due to three-particle cuts in the decay amplitude as discussed in Section 3.3 and briefly revisited in Section 4.6, the subtraction constant b' is complex. If one allows it to take values different from the sum rule in order to give the dispersive representation more freedom in a fit to experimental data, it therefore

represents two new *real* parameters, modulus and phase of b'. Again, as in the discussion for the Omnès function, such a b' different from its sum-rule value is in principle inconsistent and leads to a high-energy behavior violating the Froissart bound. We will, however, again find that these violations do not manifest themselves in practice in the energy range considered here.

The linearity of Eq. (4.24) in the subtraction constants a and b' also massively simplifies the numerical solution strategy in this case. The full solution can be constructed as the linear combination

$$\mathcal{F}(s) = a\big[\mathcal{F}'_a(s) + b\mathcal{F}_b(s)\big] \ , \tag{4.26}$$

where $b = b'/a$, in terms of the basis solutions found from

$$\begin{aligned}
\mathcal{F}'_a(s) &= \Omega(s)\left\{1 + \frac{s^2}{\pi}\int_{4M_\pi^2}^{\infty}\frac{ds'}{s'^2}\frac{\sin\delta(s')\hat{\mathcal{F}}'_a(s')}{|\Omega(s')|(s'-s)}\right\} \ , \\
\mathcal{F}_b(s) &= \Omega(s)\left\{s + \frac{s^2}{\pi}\int_{4M_\pi^2}^{\infty}\frac{ds'}{s'^2}\frac{\sin\delta(s')\hat{\mathcal{F}}_b(s')}{|\Omega(s')|(s'-s)}\right\} \ .
\end{aligned} \tag{4.27}$$

$\mathcal{F}'_a(s)$ and $\mathcal{F}_b(s)$ can therefore be calculated by the iterative procedure explained above, *before* adjusting the subtraction constants in a fit to experimental data.

4.4 Numerical results

In this section we show the numerical results from solving Eq. (4.23). We start off by discussing the numerical input in Section 4.4.1 before showing the convergence behavior for both $\omega \to 3\pi$ and $\phi \to 3\pi$ in the iteration procedure in Section 4.4.2. In Section 4.4.3 Dalitz plot distributions are presented along with a study of crossed-channel rescattering effects, followed by a discussion on how these effects hold up against the expected errors of our analysis in Section 4.4.4. The comparison to experiment follows in Section 4.5.

4.4.1 Numerical input

The integral equation Eq. (4.23) is fully determined except for the $\pi\pi$ input and the subtraction constant. This input is subject to uncertainties, the discussion of which we defer to Section 4.4.4. Instead, we only give a central set of parameters used in the following. It was already pointed out that we use the partial decay width to fix the subtraction constant (that serves as the overall normalization of the amplitude), namely [87]

$$\Gamma_{\omega\to3\pi} = 7.56\,\text{MeV} \ , \qquad \Gamma_{\phi\to3\pi} = 0.65\,\text{MeV} \ . \tag{4.28}$$

It should be noted that we do not consider errors on the partial decay widths, since the uncertainties thus generated are by far superseded by the error sources discussed in Ref. [174] and briefly in Section 4.4.4. Furthermore, the masses involved are given by $M_\omega = 782.65\,\text{MeV}$, $M_\phi = 1019.46\,\text{MeV}$, and $M_\pi = 139.57\,\text{MeV}$. We use the $\pi\pi$ P-wave phase shift based on an ongoing Roy-equation analysis [39] (first aspects of which have recently been published [38]). There are other parameterizations of the P-wave phase shift of comparable accuracy available, see for example Ref. [41]. We will briefly discuss the influence of the difference between the two in our error discussion.

Λ_Ω	1.3 GeV
Λ	2.0 GeV
# subtractions in $\Omega(s)$	one
phase-shift param.	Ref. [39]
inelasticities	none

Table 4.1: Input to the analysis, see text for explanations.

There are other error sources that relate to the upper limit of the dispersion integrals in Eqs. (4.19) and (4.23). Our procedure in the Omnès integral is as follows: the phase shift derived from the Roy-equation analysis is strictly known up to the validity limit of the Roy equations of $\sqrt{s} = 1.15\,\text{GeV}$. We use the somewhat extended phenomenological parameterization of Ref. [39] up to $\Lambda_\Omega = 1.3\,\text{GeV}$, set the phase to a constant beyond that point, and calculate the Omnès integral analytically. The upper limit of the dispersion integral in Eq. (4.23) has less physical significance, it is rather an indicator how well one sums up the remainder of the integral. In our analysis the integral is cut off at $\Lambda = 2\,\text{GeV}$. We emphasize that this does not mean that we know the physics of $\pi\pi$ interactions up to that point, but it certainly is a better approximation to the integrand than setting it to zero beyond the validity range of the Roy equations.

We have also considered methods to include elastic resonances between 1.3 and 2.0 GeV ($\rho'(1450)$ and $\rho''(1700)$), as well as inelasticities e.g. from 4π intermediate states. Furthermore we have estimated the possible contribution of a ρ_3-dominated $\pi\pi$ F wave. The corrections stemming from these contributions are tiny and also deferred to the error discussion and the Appendices. Our input parameters are summarized in Table 4.1.

4.4.2 Convergence behavior of the amplitude

Since the physical regime of the decay is considerably larger than in the case of $\eta' \to \eta\pi\pi$, it is illustrative to briefly study the convergence behavior also in this case. This may also serve as an indicator on how fast the iteration converges for decay processes with even heavier mesons. We plotted the basis function $\mathcal{F}_a(s)$ with one subtraction for $\omega \to 3\pi$ and $\phi \to 3\pi$ after each iteration step in Fig. 4.4. Convergence in the case of $\omega \to 3\pi$ is reached fast, with $\mathcal{F}_a(s)$ all but indistinguishable from the final result after two iterations, similarly to what we observed for $\eta' \to \eta\pi\pi$. The iteration still proceeds to the final result swiftly for $\phi \to 3\pi$, although one more iteration step is required indicating that the larger the decay region the more iteration steps are required for convergence. We point out that in both cases the difference between the final result and the starting point is significant: since our starting point is the Omnès function that resums rescattering between two pions only, this hints at sizeable crossed-channel effects in the decay region.

We observe that the ρ peak in $\omega \to 3\pi$ is slightly enhanced and shifted toward lower energies. Even though the peak is not part of the physical decay region and this shift therefore not observable directly, the somewhat steeper rise should leave its imprint on the Dalitz plot. The $\phi \to 3\pi$ amplitude exhibits a similar shift of the ρ peak toward smaller energies. In contrast to the ω decay, the peak here is attenuated, which should certainly have an impact on the Dalitz plot distribution, since it is part of the physical region. We reiterate that the

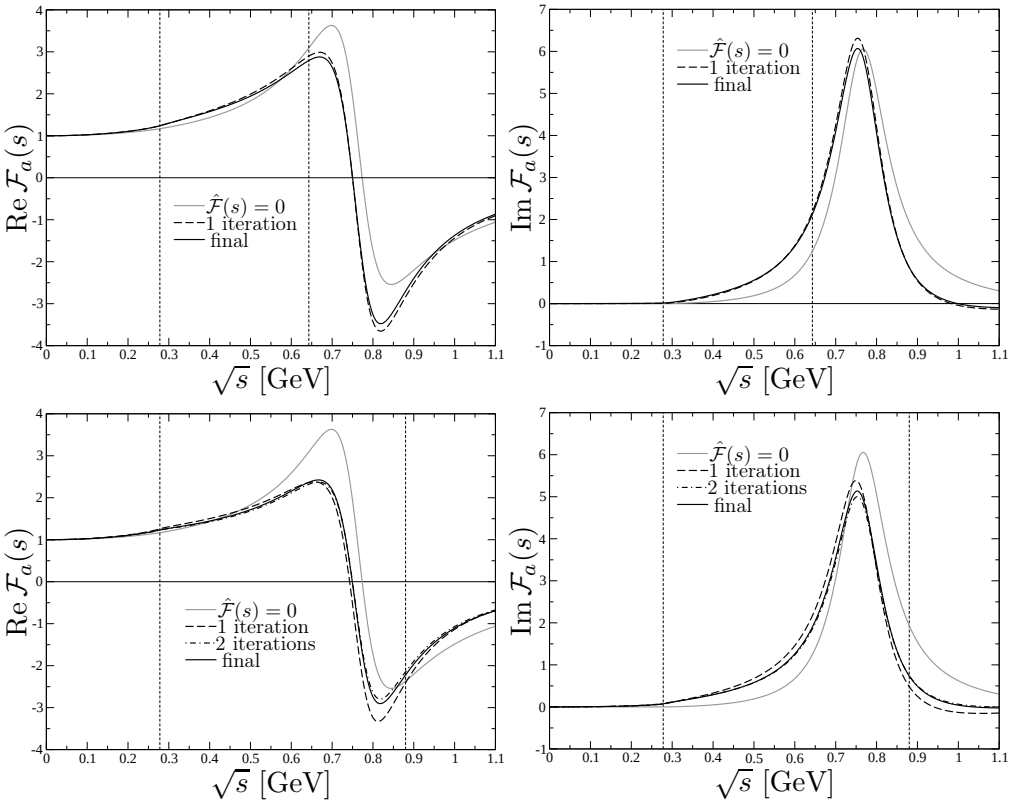

Figure 4.4: Successive iteration steps of real (left panel) and imaginary (right panel) part of the amplitude $\mathcal{F}_a(s)$ for $\omega \to 3\pi$ (top) and $\phi \to 3\pi$ (bottom) with one subtraction. The vertical dashed lines denote the physical region of the decay.

modifications we observe due to three-particle rescattering lead to non-negligible effects on the amplitude. In the following section we shall discuss how our observations translate to the actual Dalitz plot distributions.

4.4.3 Dalitz plot distributions and crossed-channel rescattering

The Dalitz plot for the $V \to 3\pi$ decay is studied in terms based of two kinematic variables, which we define analogously to before as

$$x = \frac{t-u}{\sqrt{3}R_V} \ , \quad y = \frac{s_0 - s}{R_V} \ , \tag{4.29}$$

where $R_V = \frac{2}{3}M_V(M_V - 3M_\pi)$.

In Fig. 4.5 we show the Dalitz plot distribution divided by the P-wave phase-space factor given in Eq. (4.4) and normalized to 1 in the center of the Dalitz plot. Figure 4.5 is thus a pure prediction: it is free from any input aside from the $\pi\pi$ P-wave phase shift, which is well-established up to at least 1.15 GeV, thus covering the entire physical range for both processes.

The $\omega \to 3\pi$ Dalitz plot exhibits a relatively smooth distribution, which rises from the center to its outer borders with a maximum increase of roughly 20% with respect to the center. The available phase space is not sufficient to contain the ρ resonance. This behavior

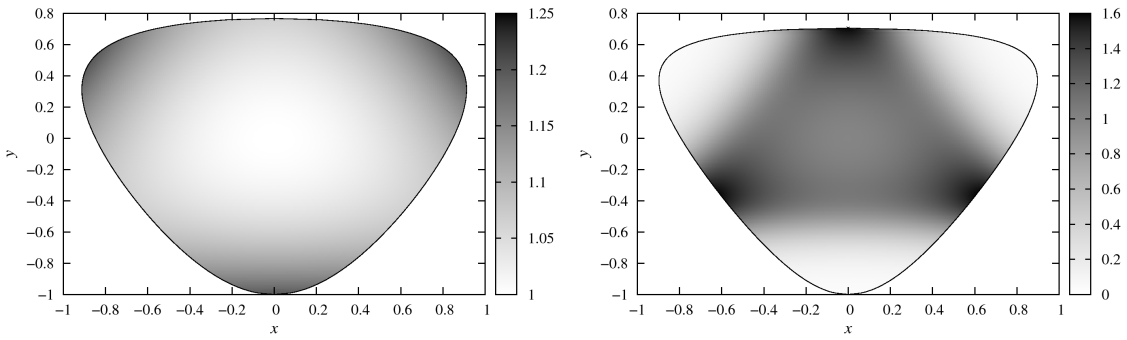

Figure 4.5: Dalitz plots for $\omega \to 3\pi$ (left panel) and $\phi \to 3\pi$ (right panel), normalized by the P-wave phase space.

unambiguously fixes the sign of the leading slope parameter in a possible Dalitz plot parameter representation to be *positive*, see Section 4.5.3 for a detailed discussion and numerical results.

The $\phi \to 3\pi$ Dalitz plot in contrast shows significantly more structure, since the physical region encompasses the ρ resonance: the resonance bands of the ρ^0 and $\rho^\pm$ are clearly visible in Fig. 4.5. From its center, the Dalitz plot distribution rises towards these bands with a maximum enhancement of roughly 60% at the peak, and then steeply falls off, showing almost complete depletion towards the outer corners.

In order to illustrate effects of crossed-channel rescattering on the Dalitz plot distribution, we study the phase-space corrected Dalitz plot after the iteration procedure ($|\mathcal{F}_{\text{full}}|^2$), divided by the same quantity before the iterations, corresponding to $\hat{\mathcal{F}} = 0$, i.e. the sum of pure Omnès solutions ($|\mathcal{F}_{\hat{\mathcal{F}}=0}|^2$). We devise two approaches of fixing the subtraction constants. First we assume that the subtraction constant is given by some independent method, and we are interested in what bearings the crossed-channel effects have on both the overall shape of the Dalitz plot and the partial decay width. The quantity $|\mathcal{F}_{\text{full}}|^2/|\mathcal{F}_{\hat{\mathcal{F}}=0}|^2$ is then independent of the specific choice of the subtraction constant. For the sake of the argument we fix the subtraction constant from the experimental decay width for $\hat{\mathcal{F}} = 0$ and then run the iteration procedure. Our second approach is to readjust the subtraction constant in such a way as to reproduce the experimental decay width in both cases, with and without crossed-channel rescattering effects included. The focus then lies exclusively on changes to the profile of the Dalitz plot distribution.

The results of both approaches are shown in Fig. 4.6. By keeping the subtraction constant fixed we observe that crossed-channel rescattering enhances the $\omega \to 3\pi$ partial width by roughly 20%. This qualitative behavior translates to the Dalitz plot, where the enhancement of the distribution ranges between 10% on the borders and 24% in the center. The $\phi \to 3\pi$ partial width in contrast sees a decrease by likewise roughly 20%. The decrease across the Dalitz plot is stronger, with 60% on the border, than in the center where it amounts to roughly 10%. Fixing the subtraction constant before *and* after the iteration procedure, the effects due to crossed-channel rescattering are to a large degree absorbed in the partial width in both decays. Indeed, the remaining effect on the $\omega \to 3\pi$ Dalitz plot amounts to an 8% decrease that is alleviated towards the central region, where one observes a slight increase of roughly 3%. The same qualitative behavior is observed in $\phi \to 3\pi$, only quantitatively stronger: the 50% suppression on the border is counterbalanced by a 20% enhancement in the center. The ρ bands are left unscathed by the iteration procedure.

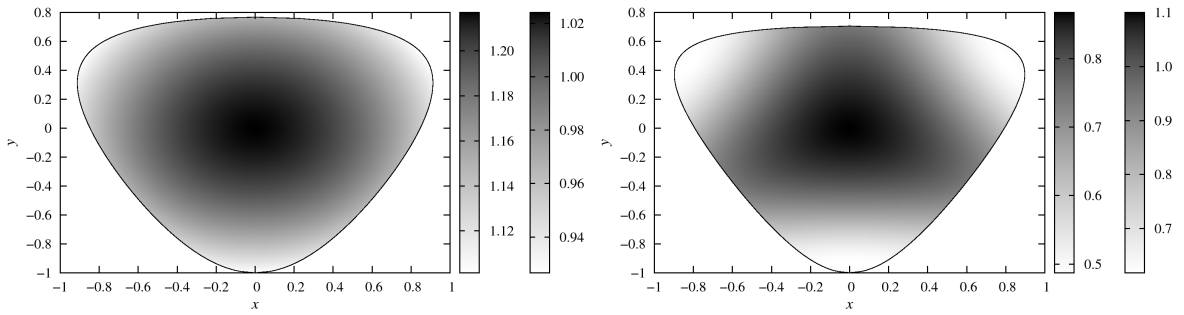

Figure 4.6: $|\mathcal{F}_{\text{full}}|^2/|\mathcal{F}_{\hat{\mathcal{F}}=0}|^2$ for $\omega \to 3\pi$ (left panel) and $\phi \to 3\pi$ (right panel). The two different scales next to the plots correspond to two different methods of fixing the subtraction constants: a is fixed to reproduce the decay width before the iteration only (left scales), or it is fixed to reproduce the decay width before and after the iteration (right scales).

Overall, we find that crossed-channel rescattering leaves a significant imprint on the Dalitz plot distribution. However, before checking how our approach to those three-particle effects holds up against experimental scrutiny, we study whether the size of the effects even withstands the uncertainties of our input parameters in the following section.

4.4.4 Error discussion

As we stated in the previous sections our results are—aside from the subtraction constant—fully constrained by the $\pi\pi$ P-wave phase shift. The parameterizations of the phase shift we use are very accurate in the low-energy regime; in this section we only briefly discuss the influence of uncertainties that are mainly due to the high-energy behavior and different methods to assess it. A more detailed study is to be found in Ref. [174].

Using a twice-subtracted Omnès function is a means to suppress the high-energy behavior of the phase-shift input. If we naively plug our central parameter set into Eq. (4.21) we obtain

$$\langle r^2_{\text{sum}}\rangle^V_\pi \simeq 0.415\,\text{fm}^2 \ , \tag{4.30}$$

which lies somewhat below a next-to-next-to-leading order chiral perturbation theory analysis [176],

$$\langle r^2_{\text{ChPT}}\rangle^V_\pi = 0.452 \pm 0.013\,\text{fm}^2 \ , \tag{4.31}$$

and the current particle-data-group average [87]. Dispersive analyses of $e^+e^- \to \pi^+\pi^-$ data [52, 53] point towards a value closer to Eq. (4.30), with central values of the order of $\langle r^2\rangle^V_\pi \simeq 0.43\,\text{fm}^2$; however, we consider the variation between a once-subtracted and twice-subtracted Omnès function, using the phenomenological radius in the latter, a conservative estimate of the uncertainty. This variation is actually the dominant uncertainty in our analysis.

The phase-shift solutions referred to as the "Bern" [39] and "Madrid" [41] parameterizations in the following, are very accurate, especially in the low-energy regime. We address these errors by varying between two different parameterizations. Next to the number of subtractions in the Omnès function these are the second largest uncertainties. We have also checked how higher resonances ($\rho'(1450)$ and $\rho''(1700)$) can modify the phase shift (beyond the range of the Roy analyses) and hence our results. This aspect is described in greater detail in Appendix B.5; the impact on the decay amplitudes in the physical region however turns out to be negligible.

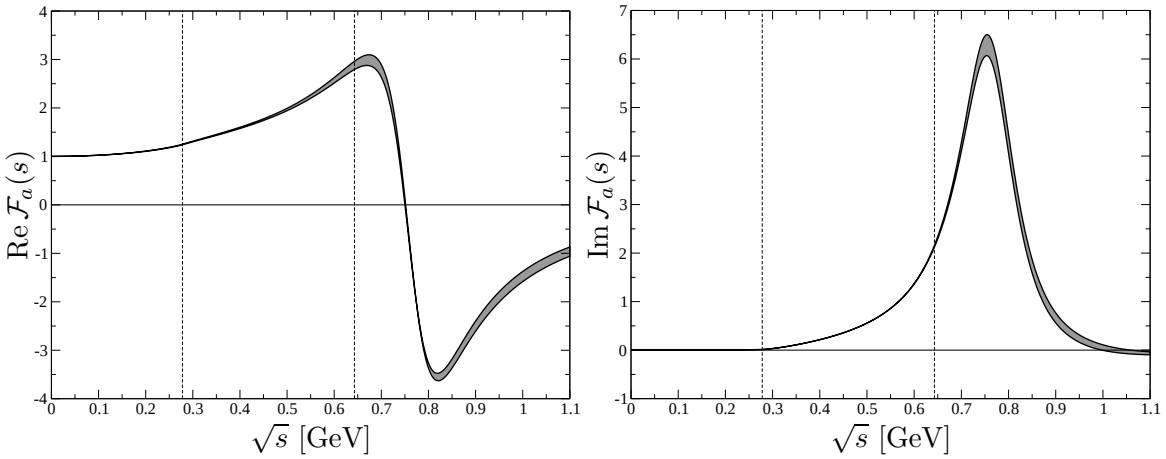

Figure 4.7: Real (left panel) and imaginary (right panel) part of the amplitude $\mathcal{F}_a(s)$ for $\omega \to 3\pi$. The vertical dashed lines denote the physical region of the decay. The shaded curve represents the uncertainty generated by upper and lower boundary of our solution (see text).

We have varied the point beyond which the phase shift $\delta(s)$ is set to a constant, and the effects of leading $\delta(s)$ smoothly to π only to find that these negligible next to the two uncertainties described above.

We tried to estimate the effects of inelasticities in the $\pi\pi$ P wave by incorporating them in a simplified fashion, following the method proposed in Ref. [122]. Bestowing the exponential of the phase shift with an inelasticity parameter $\eta(s) \doteq \eta_1^1(s)$,

$$t_1^1(s) = \frac{\eta(s)e^{2i\delta(s)} - 1}{2i} \,, \tag{4.32}$$

leads to modified dispersion integrals (see Ref. [122] and Appendix B.6),

$$\mathcal{F}(s) = a\,\xi(s)\Xi(s)\Omega(s)\left\{1 + \frac{s}{2\pi i}\int_{4M_\pi^2}^{\infty} \frac{ds'}{s'} \frac{\left[e^{i\delta(s')} - \eta(s')e^{-i\delta(s')}\right]\hat{\mathcal{F}}(s')}{\sqrt{\eta(s')}\Xi(s')|\Omega(s')|(s'-s)}\right\}, \tag{4.33}$$

where

$$\xi(s) = \begin{cases} \eta^{-1/2}(s) & \text{above the cut,} \\ \eta^{1/2}(s) & \text{below the cut,} \\ 1 & \text{elsewhere,} \end{cases} \tag{4.34}$$

and

$$\Xi(s) = \exp\left\{\frac{is}{2\pi}\,\mathcal{P}\int_{16M_\pi^2}^{\infty} ds' \frac{\log\eta(s')}{s'(s'-s)}\right\} \,, \tag{4.35}$$

where $\mathcal{P}$ denotes the principal value integral, and we assume that inelasticities set in at the four-pion threshold. The inelasticity starts showing major deviations from unity only above roughly 1 GeV (see also Section 4.7). Consequently the effects of using such a simplified model for the inelasticity show little impact on our final result.

We add one final remark on the integral cutoff in the dispersion integral of the full amplitude, Eq. (4.23). This cutoff has been fixed to 2 GeV and *not* varied. The reason for this is that

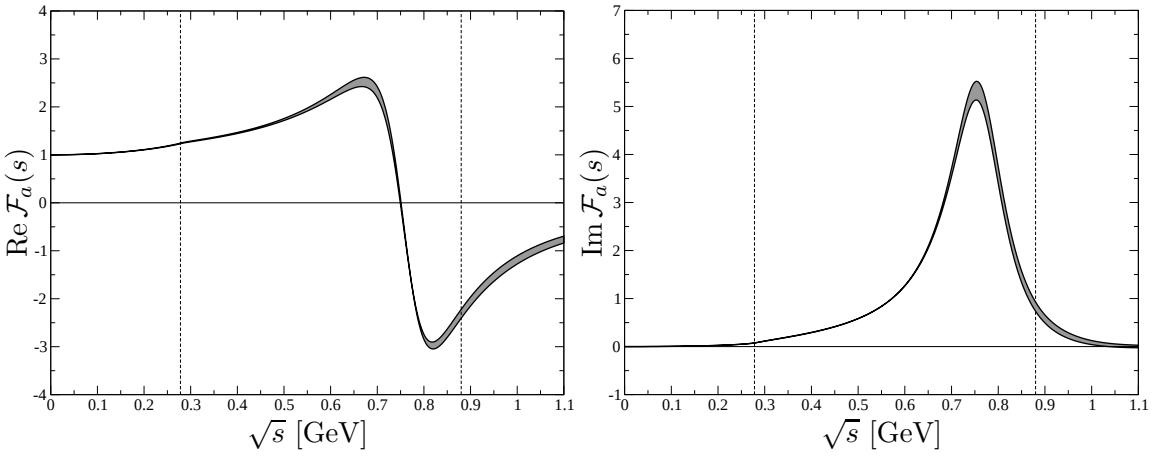

Figure 4.8: Real (left panel) and imaginary (right panel) part of the amplitude $\mathcal{F}_a(s)$ for $\phi \to 3\pi$. The vertical dashed lines denote the physical region of the decay. The shaded curve represents the uncertainty generated by upper and lower boundary of our solution (see text).

it is merely a "numerical" cutoff: the kinematic range of validity is fixed by the $\pi\pi$ phase-shift parameterization. The dispersion integral has no physical content beyond that point; we just need to ensure that the integral cutoff is large enough so as not to produce numerical artifacts. We found that this is the case at 2 GeV. As a side remark, we have checked that lowering the integral cutoff as far as to 1.3 GeV still affects the amplitudes in the physical region by less than the main sources of uncertainty discussed above.

After identifying the charge radius in the twice-subtracted Omnès function and the phase-shift parameterization as the main *single* error sources, we will now briefly study their combined error. It turns out that we can identify certain parameter sets as upper and lower boundaries of the amplitude for that purpose. The combination of the Bern parameterization along with a once-subtracted Omnès function will serve as the lower boundary, whereas the upper boundary is given by the Madrid phase together with a twice-subtracted Omnès function and the determination of the pion charge radius from Ref. [176]. The uncertainty bands generated between these boundaries are shown for $\omega \to 3\pi$ and $\phi \to 3\pi$ in Figs. 4.7 and 4.8. The maximum uncertainty of the amplitude in the physical region amounts to roughly 8% in both cases.

To rule out that interference of the crossed channels amplifies the uncertainties, we also analyze how the errors develop across the Dalitz plot. For that purpose, we study the following quantity:

$$\frac{|\mathcal{F}_u|^2 - |\mathcal{F}_l|^2}{|\mathcal{F}_u|^2 + |\mathcal{F}_l|^2} \,, \tag{4.36}$$

where $\mathcal{F}_{u/l}$ denotes the normalized amplitude on the upper/lower boundary. We find that for $\omega \to 3\pi$ the error in the Dalitz plot is even slightly decreased with respect to the amplitude, the maximal uncertainties amount to 1.4% towards the corners of the Dalitz plot. For $\phi \to 3\pi$ we observe the largest uncertainties in the outer edges of the Dalitz plot, where the Dalitz plot strength itself is strongly suppressed. So while the relative error there rises up to 8%, the absolute error is very small.

Comparing to our results in Section 4.4.3 we clearly see that crossed-channel contributions are sizable enough to outweigh the uncertainties. Again we point to Ref. [174] for a more

detailed assessment of the uncertainties. In the following section we will analyze whether crossed-channel effects are actually observable in experiment.

4.5 Comparison to experiment

4.5.1 Fit to the $\phi \to 3\pi$ Dalitz plot: single subtraction

We now wish to compare our theoretical predictions to the experimental results for the $\phi \to 3\pi$ Dalitz plot measurements by the KLOE [169] and CMD-2 [170] collaborations. The former has significantly larger statistics (almost 2×10^6 events in the Dalitz plot) than the latter (close to 8×10^4 events); furthermore, the energy resolution in the KLOE measurement was significantly better than the bin size (in the range 1–2 MeV compared to a bin size of 8.75 MeV), such that smearing effects were found to be negligible, and we could fit our amplitudes to efficiency-corrected data directly (with purely statistical errors based on data and Monte Carlo statistics), while for the comparison with the CMD-2 data, they had to be convoluted with efficiency matrices by the collaboration before. While consistency with both data sets is clearly desirable, we will present the comparison to the KLOE data in some more detail in the following.

Our first goal is to perform a fit to the Dalitz plot distribution with our most predictive theoretical representation, Eq. (4.23), employing a single subtraction, such that the normalization is the only free parameter of the fit. The shape of the Dalitz plot is thus purely a prediction, and we can compare the χ^2 of the fit with and without crossed-channel rescattering. There are two caveats to this procedure, which we need to discuss beforehand.

First, our calculations are performed in the isospin limit of equal charged and neutral pion masses; we use the *charged* pion mass, not least for consistency reasons due to the fact that the $\pi\pi$ phase shifts are only available in the isospin limit, with the charged pion mass used as the reference quantity. The effect of this approximation on the amplitude is expected to be small (compare e.g. Chapter 2), with the main difference due to different charged and neutral pion masses showing up in the available phase space: the true physical Dalitz plot is slightly larger than in our calculation. To account for this dominant isospin-breaking correction, we therefore multiply the amplitude (squared) with the physical phase-space factor:

$$|\mathcal{M}_{\phi\to 3\pi}(s,t,u)|^2 = \frac{s}{16}\kappa_0^2(s)\sin^2\theta_0 |\mathcal{F}(s,t,u)|^2 \ , \tag{4.37}$$

where in contrast to Eq. (4.4) we have $\cos\theta_0 = (t-u)/\kappa_0(s)$ and

$$\kappa_0(s) = \sqrt{1 - \frac{4M_{\pi^\pm}^2}{s}}\lambda^{1/2}(M_\phi^2, M_{\pi^0}^2, s) \ . \tag{4.38}$$

Numerically, we employ $M_{\pi^0} = 134.98\,\text{MeV}$ as before.

Furthermore, in order to avoid distortions due to threshold effects in the decay amplitude, we omit data bins that cross the boundary of the Dalitz plot, see Fig. 4.9, thereby ensuring that our amplitude is never evaluated below the isospin-symmetric threshold, that is, for $(M_{\pi^\pm} + M_{\pi^0})^2 \leq t,\, u \leq 4M_{\pi^\pm}^2$.

The second caveat, discussed in Ref. [169], concerns the fact that the ϕ is produced in e^+e^- collisions at DAΦNE, $e^+e^- \to \phi \to \pi^+\pi^-\pi^0$, which allows for the background process $e^+e^- \to \omega\pi^0 \to \pi^+\pi^-\pi^0$, the $\omega\pi^0$ invariant mass equaling the mass of the ϕ, with the

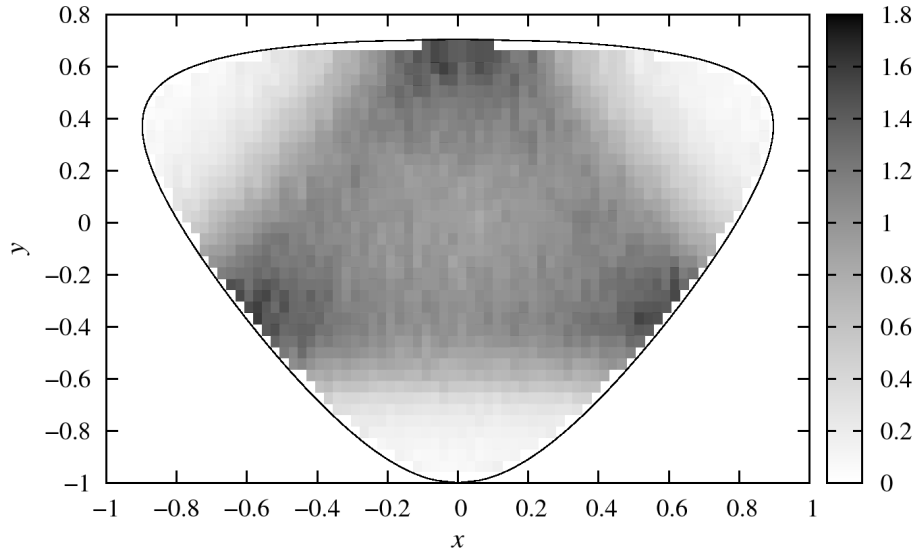

Figure 4.9: Selected data from the KLOE measurement [169]. Shown is the efficiency-corrected number of counts in the respective bin, divided by the phase-space factor in Eq. (4.37) and normalized to 1 in the Dalitz plot center.

ω subsequently decaying into $\pi^+\pi^-$. As the decay $\omega \to \pi^+\pi^-$ violates isospin, with the branching fraction suppressed to the percent level [87], the overall modification of the Dalitz plot is small.[#3] However, it is entirely concentrated in the narrow band $s = M_\omega^2$, and leaves a visible effect there. There are two possible strategies to deal with this issue: one could simply omit the corresponding horizontal band in a fit of the Dalitz plot; or, alternatively, add a resonance term of the form (see Ref. [169])

$$\mathcal{A}_{\omega\pi}(s) = a \times a_\omega e^{i\phi_\omega} \frac{M_\omega^2}{M_\omega^2 - i\sqrt{s}\Gamma_\omega - s} \tag{4.39}$$

to Eq. (4.9) after the iteration. (Note that we have factored out the normalization constant a for reasons of comparison with the fit results in Ref. [169].) M_ω and Γ_ω are fixed to the particle-data-group values [87], and a_ω and ϕ_ω are dimensionless fitting parameters. We follow the latter strategy, in particular since the resonance term also has a small impact on bins adjacent to the horizontal band at 83.7 MeV.

Our standard χ^2 fit is performed with 1834 data points and three free parameters. We perform separate fits for the upper and lower boundaries of the theoretical uncertainty band as discussed in Section 4.4.4, both with and without crossed-channel rescattering effects included. The results are listed in Table 4.2. The data set fitted to is given in arbitrary normalization, such that the constant $\tilde{a}$ does not correspond to the real subtraction constant a and is only shown for comparison of the changes between different fits. We notice that the fit quality considerably improves once crossed-channel rescattering is taken into account. This indicates that crossed-channel effects lead to modifications that are not only non-negligible, but even

[#3] Note that this is an isospin-violating effect specific for the 3π production in e^+e^- collisions. If we interpret the decay $\omega \to \pi^+\pi^-$ in terms of a ρ–ω mixing angle $\theta_{\rho\omega}$ (see e.g. Ref. [177]), this effect is *linear* in $\theta_{\rho\omega}$ due to the fact that the photon has both isoscalar and isovector components. In contrast, isospin breaking due to ρ–ω mixing in $\pi\pi$ scattering is necessarily suppressed to second order in $\theta_{\rho\omega}$ and hence irrelevant.

	$\mathcal{F}_l$ (full)	$\mathcal{F}_u$ (full)	$\mathcal{F}_l$ ($\hat{\mathcal{F}} = 0$)	$\mathcal{F}_u$ ($\hat{\mathcal{F}} = 0$)
χ^2/ndof	1.50	1.17	1.71	2.06
$\tilde{a} \times \text{GeV}^3$	228.6 ± 0.2	216.6 ± 0.2	200.2 ± 0.2	187.6 ± 0.2
$a_\omega \times 10^3$	7.9 ± 0.5	7.4 ± 0.5	10.9 ± 1.0	12.6 ± 1.2
ϕ_ω	-0.30 ± 0.11	-0.10 ± 0.11	0.87 ± 0.06	0.95 ± 0.06

Table 4.2: Fit results to the KLOE data for $\phi \to 3\pi$, using the once-subtracted dispersive representation. Shown are the outcomes of the fits for upper and lower boundaries of the theoretical uncertainty band, with and without crossed-channel rescattering included. The normalization of $\tilde{a}$ is arbitrary, such that only the relative changes in $\tilde{a}$ between different fits are significant, not the absolute values. The uncertainties quoted refer to the errors of the fit.

observable in the structure of the Dalitz plot. It is also observed, however, that the precision of the data is such that the variation of the χ^2/ndof within the theoretical uncertainty is quite non-negligible: the upper boundary yields a considerably better fit than the lower boundary for the full crossed-channel analysis, while the opposite holds for the pure Omnès solutions. The a_ω coupling is found to be in the 1% range, the expected order of magnitude; its numerical value determined together with the full dispersive solution is in slightly better agreement with what is found in Ref. [169]. The best χ^2/ndof of 1.17 of our fits is not quite as good as it is in Ref. [169], and it needs to be pointed out that due to the high number of degrees of freedom, the p-value characterizing the goodness of the fit is still rather low even in the best case, $p(\chi^2 = 1.17) = 3 \times 10^{-7}$. However, this fit quality is achieved with less degrees of freedom: apart from the $\omega\pi^0$ background term (which has nothing to do with the genuine $\phi \to 3\pi$ Dalitz plot), this is a one-parameter fit, the shape of the Dalitz plot in our case is a pure prediction. In Ref. [169] there are two additional degrees of freedom by fitting the (complex) "background" term. From the construction of our dispersive amplitude, it is obvious that in this form, such an independent background term is inconsistent with the requirements of analyticity and unitarity. Furthermore, in Appendix B.5 we show that a simplified approach to including higher resonances does not allow for an improvement of the fit as opposed to claims made for the nature of the background term being due to ρ' effects. It seems that crossed-channel effects saturate the background term in the KLOE data to a large degree.

Figure 4.10 shows slices of constant y through the Dalitz plot, where the number of events per bin divided by the bin efficiency is plotted against the bin number (note that this is not the same as Fig. 5 in Ref. [169], where slices of constant x are shown). Our fit results are displayed as error bands. The full solution (blue band) gives a better description of the data than the sum of three Omnès functions (red band), particularly in the central region of the Dalitz plot.

These conclusions on the significance of rescattering effects are not immediately substantiated by the comparison to the CMD-2 data [170]. The fits performed by the collaboration seem to lead to the almost opposite result: a fit based on the sum of Omnès functions leads to a very good χ^2/ndof of about 1.0 for both variants of the Omnès function discussed; while the full amplitudes yield bad fit qualities of $\chi^2/\text{ndof} = 1.5 \ldots 1.8$. We note, however, that due to the significantly smaller number of degrees of freedom (ndof = 197), the p-value for

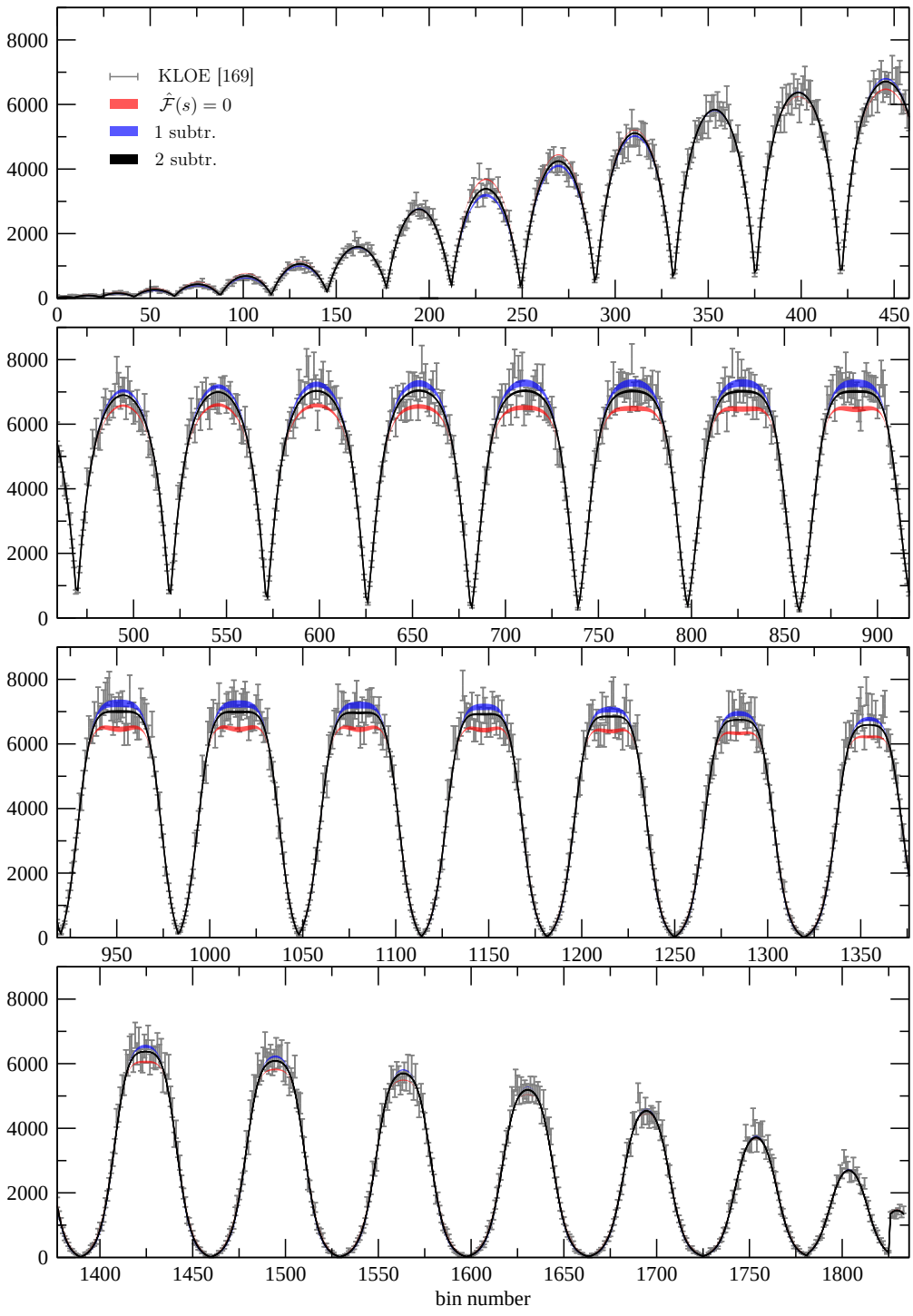

Figure 4.10: Efficiency-corrected number of events per bin plotted against bin number for slices of constant y. Every peak corresponds to one slice/one specific value of y, progressing from negative to positive x, and slices are ordered from negative to positive y. Our fit results are plotted for the sum of Omnès functions $\hat{\mathcal{F}} = 0$ (red band), for the full solution of the once-subtracted ansatz (blue band), and for the full solution in the twice-subtracted variant (black band), together with the KLOE data [169].

	Bern [39]	Madrid [41]
χ^2/ndof	1.02	1.03
$\tilde{a} \times \text{GeV}^3$	207.6 ± 1.4	207.1 ± 1.5
(sum rule)	228.6	225.4
$\lvert b\rvert \times \text{GeV}^{-2}$	0.97 ± 0.03	0.94 ± 0.03
(sum rule)	0.72	0.75
$\arg b$	0.52 ± 0.03	0.42 ± 0.03
(sum rule)	0.73	0.70
$a_\omega \times 10^3$	7.3 ± 0.6	7.5 ± 0.6
ϕ_ω	0.40 ± 0.10	0.33 ± 0.10

Table 4.3: Fit results to the KLOE data for $\phi \to 3\pi$, using the twice-subtracted dispersive representation. Shown are the outcomes of the fits using the phase parameterization of the Bern [39] and Madrid [41] groups. The "sum rule" entries for modulus and phase of b refer to the evaluation of Eq. (4.25) with the once-subtracted dispersive representation; the "sum rule" entry for a just serves as a reminder that also the normalization of the amplitude changes significantly between the two fits. For $\tilde{a}$, the same remark holds as in Table 4.2. The uncertainties quoted refer to the errors of the fit.

the CMD-2 fit of the full $\mathcal{F}_u$ solution, $p(\chi^2 = 1.50) = 7 \times 10^{-6}$, is even better than the best KLOE fit in Table 4.2. Still, this is a surprising result in different respects: primarily, as the phenomenological fits of Breit–Wigner ρ resonance terms plus a constant "background" amplitude yield perfectly compatible results in both experiments; secondly, as Ref. [170] cites the significance for a non-vanishing background term at 3.3σ, it is somewhat unexpected that simply replacing the Breit–Wigner ρ by an Omnès function is already sufficient to yield a good description of the data.

4.5.2 Fit to the $\phi \to 3\pi$ Dalitz plot: two subtractions

In order to understand the situation of the two $\phi \to 3\pi$ data sets better, we attempt a description with the (more flexible) twice-subtracted representation Eqs. (4.26), (4.27). Due to the equivalence with the once-subtracted form in case the additional parameter b fulfills the sum rule Eq. (4.25), the fits can only improve: the hope is to find an acceptable fit also to the CMD-2 data that is compatible with the fundamental principles underlying the dispersive representation. We refrain from employing the two different variants of the Omnès function defined earlier; we expect the second subtraction in the dispersion integral to render the second subtraction inside the Omnès function redundant, and therefore only use the standard form (4.19). We perform the fit of this representation with the two different $\pi\pi$ P-wave phase parameterizations [39, 41] to check the consistency of the outcome.

The results of the fits to the KLOE data are shown in Table 4.3. The resulting values for a and b are compared to the ones obtained from the fit of the once-subtracted representation, see the previous section, via the sum rule (4.25). For both phases, excellent fits of χ^2/ndof close to 1.0 are obtained ($p(\chi^2) = 0.22 \ldots 0.24$). Closer comparison shows that $\text{Im}\, b$ in fact stays

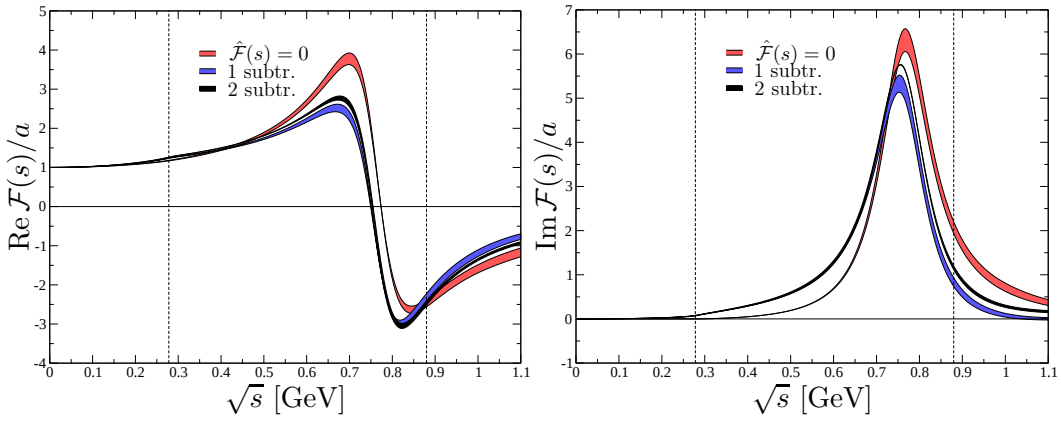

Figure 4.11: Real (left panel) and imaginary (right panel) part of the amplitude $\mathcal{F}(s)$ (normalized with $a = 1$) for $\phi \to 3\pi$, comparing the fit of the twice-subtracted dispersive representation to the KLOE data to the once-subtracted $\mathcal{F}(s)$ as well as the Omnès solution. All curves are shown with the uncertainty bands attached as discussed in the text.

very close to its sum-rule value (in particular for the Bern phase parameterization), while $\mathrm{Re}\, b$ is shifted (enlarged) more significantly, at the expense of a somewhat reduced normalization $\tilde{a}$. We compare the resulting function $\mathcal{F}_a(s) + b\mathcal{F}_b(s)$ to the once-subtracted $\mathcal{F}(s)$ as well as the Omnès function in Fig. 4.11. We see that, indeed, the difference to the once-subtracted $\mathcal{F}(s)$ is small compared to the latter's error band, let alone the difference to the Omnès function. We also display the fit result in comparison to the KLOE data in Fig. 4.10 as the black band. Note that as we now optimize the additional parameter through the fit routine and only vary between the two different phase parameterizations, the band is significantly narrower than the other two. While the deviation from the once-subtracted fit results seems to be really minor, the overall improvement in the χ^2/ndof is significant.

Fits to the CMD-2 data have again been performed by the collaboration. This time, they result in a χ^2/ndof of 0.96 and 0.94 (with associated p-values of $0.64 \ldots 0.71$), using the Bern and Madrid phases, finding

$$\begin{aligned} |b| &= \left\{0.97^{+0.16}_{-0.13}\,,\, 0.95^{+0.15}_{-0.12}\right\}\,, \\ \arg b &= \left\{0.00 \pm 0.16\,,\, -0.18 \pm 0.18\right\}\,, \end{aligned} \tag{4.40}$$

respectively. While the modulus of b therefore agrees perfectly with the fit to the KLOE data, the phase seems to prefer a *real* b, in contradistinction to the sum-rule prediction. Only the KLOE data therefore yield a high significance for a non-vanishing phase of the parameter b. We have not investigated systematic uncertainties in the determination of b from data.

4.5.3 $\omega \to 3\pi$ Dalitz plot parameterization

Since there is currently no precise data available on the $\omega \to 3\pi$ Dalitz plot, we will now discuss the issue whether it is feasible to use a parameterization of the Dalitz plot in terms of a polynomial in a precision determination, and if so, with how many terms necessary. This is common practice for decays with final-state particles at low energies, such as $K \to 3\pi$, $\eta \to 3\pi$, or $\eta' \to \eta\pi\pi$. Since the Dalitz plot for $\omega \to \pi^+\pi^-\pi^0$ is relatively smooth, we expect that a similar description should be possible here, even though the phase space available is

somewhat larger. Moreover, as opposed to e.g. the decays $K^\pm \to \pi^0\pi^0\pi^\pm$, $\eta \to 3\pi^0$, and $\eta' \to \eta\pi^0\pi^0$, one does not face the issue of cusp effects [25, 26, 29, 33] in the decay region that give rise to possibly large non-analytic structures.

The $\omega \to 3\pi$ decay amplitude is fully symmetric under exchange of s, t, and u, see Eq. (4.9), such that the Dalitz plot description is formally similar to the one in $\eta \to 3\pi^0$. For a parameterization in terms of a polynomial, it is therefore convenient to rewrite the Dalitz plot variables in Eq. (4.29) in polar coordinates, namely

$$y \doteq \sqrt{z}\sin\phi \ , \quad x \doteq \sqrt{z}\cos\phi \ . \tag{4.41}$$

We can parameterize the amplitude squared in terms of z and ϕ according to

$$|\mathcal{F}_{\rm pol}(z,\phi)|^2 = |\mathcal{N}|^2\Big\{1 + 2\alpha z + 2\beta z^{3/2}\sin 3\phi + 2\gamma z^2 + 2\delta z^{5/2}\sin 3\phi + \mathcal{O}\big(z^3\big)\Big\} \ , \tag{4.42}$$

where $\mathcal{N}$ is the normalization and α, β, γ, δ are the Dalitz plot parameters, in strict analogy to $\eta \to 3\pi^0$, see Chapter 2. Note in particular that we attempt to parameterize $|\mathcal{F}|^2$ in polynomial form, not $|\mathcal{M}|^2$: the trivial kinematic factor due to the P-wave characteristic of the vector-meson decay should always be retained exactly. In the following, we study whether such a parameterization makes sense when trying to quantitatively describe the $\omega \to 3\pi$ Dalitz plot, and give predictions for the parameters.

We perform a fit of the polynomial Dalitz plot representation $|\mathcal{F}_{\rm pol}(z,\phi)|^2$ to our theoretically determined amplitude $|\mathcal{F}_{\rm th}(z,\phi)|^2$, minimizing the function

$$\begin{aligned}\chi^2 &= \frac{1}{\mathcal{N}_\mathcal{D}}\int_\mathcal{D} dz d\phi \left[\left(1 - \frac{3z(3s_0 - R_\omega\sqrt{z}\sin 3\phi)}{(M_\omega + 3M_\pi)^2}\right)\frac{|\mathcal{F}_{\rm pol}(z,\phi)|^2 - |\mathcal{F}_{\rm th}(z,\phi)|^2}{|\mathcal{N}|^2}\right]^2 \ , \\ \mathcal{N}_\mathcal{D} &= \int_\mathcal{D} dz d\phi \ ,\end{aligned} \tag{4.43}$$

where $\mathcal{D}$ denotes the area of the Dalitz plot. The normalization of Eq. (4.43) is chosen such that $\sqrt{\chi^2}$ denotes the average deviation of the polynomial parameterization in $|\mathcal{M}(s,t,u)|^2$, relative to the Dalitz plot center. The prefactor (in round brackets) corresponds to the kinematic factor relating $|\mathcal{M}(s,t,u)|^2$ to $|\mathcal{F}(s,t,u)|^2$ in Eq. (4.4), rewritten in terms of z and ϕ, and normalized to 1 in the center of the Dalitz plot. We decide to include the kinematic phase-space factor in the minimization in order to give less weight to the outer parts of the Dalitz plot, which are expected to also contribute statistically less in an experimental determination.

We start with the singly subtracted dispersive representation, where the Dalitz plot shape is a full-fledged prediction. Our results are summarized in Table 4.4, where again we vary the amplitude between upper and lower error boundary of the once-subtracted solution, and also compare to the pure Omnès solution without rescattering effects. We observe that for the full amplitude, a fit with two parameters (the normalization is not counted as a fit quantity) already gives a very good description of the theoretical data: compared to the one-parameter fit, the $\sqrt{\chi^2}$ is improved by roughly a factor of 15, the maximum relative deviation across the Dalitz plot, i.e. the quantity $|\mathcal{F}_{\rm pol}(z,\phi)|^2/|\mathcal{F}_{\rm th}(z,\phi)|^2 - 1$ at any point, is improved by approximately a factor of 10 from 4% to 0.3%. When increasing the number of Dalitz plot parameters beyond 2, the changes in the parameters themselves as well as the quality of the fit are rather small, and quite probably beyond the reach even of a precision experiment. Note that the maximum deviation between two and three parameters is approximately the same, however the value of $\sqrt{\chi^2}$ is significantly reduced. The reason for this is that the contributions

	$\lvert\mathcal{N}\rvert \times \mathrm{GeV}^3$	$\alpha \times 10^3$	$\beta \times 10^3$	$\gamma \times 10^3$	$\delta \times 10^3$	$\sqrt{\chi^2} \times 10^3$	max dev.$\times 10^3$
full	1451 ... 1447	84 ... 96 (102)	—	—	—	0.9 ... 1.1	40
	1453 ... 1449	74 ... 84 (90)	24 ... 28 (30)	—	—	0.052 ... 0.078	3
	1453 ... 1449	73 ... 81 (86)	24 ... 28 (29)	3 ... 6 (8)	—	0.038 ... 0.047	3
	1453 ... 1449	74 ... 83 (88)	21 ... 24 (25)	0 ... 2 (3)	7 ... 8 (9)	0.012 ... 0.011	2
$\hat{\mathcal{F}} = 0$	1433 ... 1429	137 ... 148	—	—	—	1.1 ... 1.3	50
	1435 ... 1431	125 ... 135	29 ... 33	—	—	0.25 ... 0.29	20
	1436 ... 1433	113 ... 120	26 ... 29	24 ... 27	—	0.036 ... 0.045	4
	1436 ... 1433	114 ... 122	23 ... 25	20 ... 23	7 ... 8	0.002 ... 0.003	0.3

Table 4.4: Fit results for the Dalitz plot parameters with (above) and without (below) crossed-channel effects included. We show the Dalitz plot parameters along with the values for $\sqrt{\chi^2}$ as defined in the text. "max dev." is the maximum deviation at any point across the Dalitz plot between the full solution and the polynomial fit. The numbers in brackets for the full solution refer to the extension of the parameter ranges considering the twice-subtracted dispersion relation; for details, see main text.

with stronger deviation are pushed toward the outer boundary of the Dalitz plot, owing to the phase-space factor in Eq. (4.43).

The Omnès solution shows a slightly different behavior: a good fit quality is reached only with three parameters, and the third parameter γ is found to be significantly larger. Deviations across the Dalitz plot with only two terms are still substantial at 2% and probably within reach of an experimental determination. Also the parameters α and β still see changes in the 10% range. The comparison of our predictions of the Dalitz plot parameters between the full and the Omnès solution hints at a significant influence of crossed-channel rescattering. Note that, beyond the precise values of the Dalitz plot parameters, the sign of the leading parameter α is unambiguously fixed in $\omega \to 3\pi$ as discussed before (see Section 4.4.3).

Given our comparison to the experimental $\phi \to 3\pi$ Dalitz plots, we may still wonder how reliable these predictions of $\omega \to 3\pi$ Dalitz plot parameters are. It is obvious that as soon as we switch to the twice-subtracted dispersive representation, we cannot strictly predict all of these any more: at least α would have to be an input quantity. In order to estimate the potential effects, we resort to the following procedure: we assume the deviations of the second subtraction constant b from the sum-rule result to be moderate; as these should be due to imperfectly understood high-energy behavior of the amplitudes, we take the *relative* deviation in the corresponding $\phi \to 3\pi$ subtraction constant as an upper limit on what we deem acceptable for $\omega \to 3\pi$. The sum-rule values for b, see Eq. (4.25), in $\omega \to 3\pi$ are

$$b_{\mathrm{sum}} = \left\{0.54\, e^{0.14i}\,,\, 0.56\, e^{0.13i}\right\} \tag{4.44}$$

for the Bern and Madrid $\pi\pi$ phase solutions, respectively. Note that the phase $\arg b$ is significantly smaller for the ω decay compared to the ϕ: the imaginary part in the subtraction constant is a three-particle-cut effect and as such proportional to the phase space available for the three pions in the corresponding decays. Enlarging b by the same factors as required in the fits to the KLOE $\phi \to 3\pi$ data, compare Table 4.3, we evaluate the twice-subtracted $\omega \to 3\pi$ amplitude with

$$b = \left\{0.83\, e^{0.09i}\,,\, 0.83\, e^{0.07i}\right\} \tag{4.45}$$

instead. The results for the Dalitz plot parameters tend to lie only slightly above the ranges of variation found within the uncertainty band for the once-subtracted representation; they are quoted in brackets for the full solution in Table 4.4.

We conclude that we need at least two parameters to obtain a polynomial parameterization of the $\omega \to 3\pi$ Dalitz plot at the 1% level accuracy, and thus directional information (owing to the ϕ-dependence) is required. Let us compare this situation to the $\eta \to 3\pi^0$ Dalitz plot, which has the same three-fold symmetry and therefore a Dalitz plot distribution that is almost flat. The slope parameter is now measured to excellent precision to be $\alpha(\eta \to 3\pi^0) = -0.0315 \pm 0.0015$ [87]; we predict $\alpha(\omega \to 3\pi)$ to be about 2.5 times as large, and of opposite sign. No higher-order Dalitz parameters have ever been determined for $\eta \to 3\pi^0$; we predicted $\beta(\eta \to 3\pi^0) = (-4.2 \pm 0.7) \times 10^{-3}$, $\gamma(\eta \to 3\pi^0) = (1.3 \pm 0.4) \times 10^{-3}$ in Chapter 2, hence these terms beyond the linear term in z will modify the Dalitz plot density only at the few-permille level ($z \leq 1$). In contrast, $\beta(\omega \to 3\pi)$ is larger than $\beta(\eta \to 3\pi^0)$ by almost an order of magnitude, see Table 4.4, and hence expected to be significantly more important/more likely to be determined experimentally.

As a final remark on potential uncertainties in the Dalitz plot parameters, we note that in an experimental investigation of $\omega \to 3\pi$, the invariant mass of the detected three pions is going to vary within the natural width of the ω. We have checked that taking this variation into account in the calculation of the decay amplitude the two leading Dalitz plot parameters α and β change at the permille level, hence way below the level of uncertainty of our prediction, and probably also significantly below the accuracy of any experimental determination in the near future. Note that M_ω is *not* changed in the definition of the Dalitz plot variables, Eq. (4.41).

4.6 Analytic structure of the $V \to 3\pi$ partial-wave amplitude

In this section we wish to briefly discuss the analytic structure of the integrand of the dispersion integral in Eq. (4.23) (minus the $1/(s-s')$ piece), as well as of the partial-wave amplitude,

$$f_1(s) = \mathcal{F}(s) + \hat{\mathcal{F}}(s) \; . \tag{4.46}$$

The integrand is of interest since it is essentially the discontinuity, and we can compare the analytic structure ensued by three-particle effects in a dispersive framework with the two-loop calculation in a perturbative approach that we discussed in Section A.1.2. The partial-wave amplitude on the other hand is an important ingredient of our determination of the $V \to \pi^0\gamma^*$ transition form factors that will be studied in the following Chapter.

The non-trivial analytic structure is generated by the angular integral $\hat{\mathcal{F}}(s)$, which contains the left-hand-cut contributions due to crossed-channel singularities. Notice, that in the case at hand, the left-hand cut overlaps with the right-hand one, as for $M_V > 3M_\pi$, s, t, and u can be simultaneously larger than $4M_\pi^2$, which they are inside the physical decay region. Let us rewrite the angular integral in the form

$$\langle z^n \mathcal{F}(s) \rangle = \frac{1}{\kappa(s)} \int_{s_(s)}^{s_+(s)} ds' \Big(\frac{2s' - 3s_0 + s}{\kappa(s)} \Big)^n \mathcal{F}(s') \; . \tag{4.47}$$

We already noted that the evaluation of this term proceeds completely analogously to what we presented in Section 3.3.4 with the obvious replacements $M_{\eta'} \to M_V$ and $M_\eta \to M_{\pi^0}$. The analytic structure of the integrand is fully determined by the properties of the function $\kappa(s)$

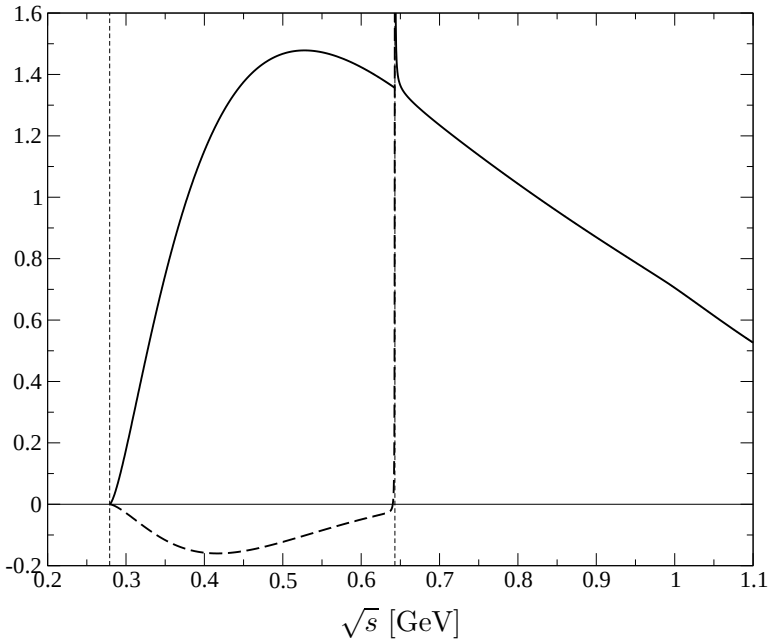

Figure 4.12: Real (solid curve) and imaginary (dashed curve) part of the integrand as a function of $\sqrt{s}$. The occurrence of the singularities at the pseudo-threshold (dashed vertical line) is explained in the text.

and its zeros. The latter are the two-particle scattering thresholds $4M_\pi^2$ and $(M_V + M_\pi)^2$, and the pseudo-threshold $(M_V - M_\pi)^2$.

Due to the particular structure of the angular integral in Eq. (4.47) the zeros of $\kappa(s)$ in principle give rise to singularities of square-root order. However, the physical thresholds at $s = 4M_\pi^2$ and $s = (M_V + M_\pi)^2$ do not contribute to the angular integration since the integration path is shrunk to a point. This is not the case at the pseudo-threshold. Due to the cut generated by the two-pion threshold and the resulting path deformation the integral gives rise to a non-vanishing contribution and thus to the aforementioned singularity. As explained in the previous section the path deformation adheres to the ability of the vector particle to decay into the final-state particles, that is $M_V > 3M_\pi$. In Fig. 4.12 we display the integrand of the dispersion integral.

Notice that our observation is in complete agreement with our study on the properties of the non-trivial relativistic two-loop graph given in Section A.1.2, see also Ref. [33], and what is found in other dispersive approaches [74]. There the singularity was explained with a deformation of the path of the angular integration to infinity as s approaches the pseudo-threshold.

In Fig. 4.13 we display the modulus and phase of the partial-wave amplitude both for $\omega \to 3\pi$ and $\phi \to 3\pi$, as derived from the numerical results of the previous section, compared to the Omnès function (whose phase of course is just $\delta(s)$). We note that the partial waves bear very little similarity to the Omnès function: there is a strong enhancement in the threshold region below the ρ resonance, a large part of which can be thought of as the partial-wave-projected t- and u-channel ρ exchanges in a VMD picture [178]. Furthermore, we note that the phase of $f_1(s)$ also does not follow $\delta(s)$: Watson's theorem does not hold due to three-pion-cut effects, see Fig. 4.14, which in particular allow for a non-vanishing imaginary part of $f_1(s)$

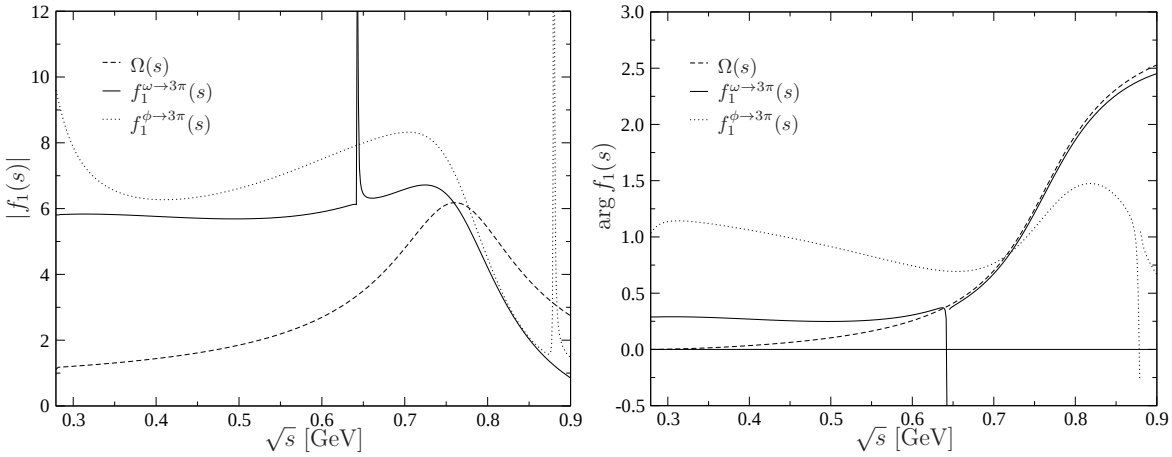

Figure 4.13: Modulus (left panel) and phase (right panel) of the P partial wave $f_1(s)$, both for $\omega \to 3\pi$ (full curve) and $\phi \to 3\pi$ (dotted curve), in comparison to the Omnès function (dashed curve). We refrain from devising error bands and fix the input for the phase according to Ref. [39] and the integral cutoff in Eq. (4.22) to $\Lambda = 2.5$ GeV. The normalization constant a is set to 1.

already at $\pi\pi$ threshold.

4.7 $\pi\pi$ P-wave inelasticity

It is well known that $K\bar{K}$ intermediate states play the dominant role in the generation of inelastic effects in the $\pi\pi$ isospin $I = 0$ S partial wave, where the $K\bar{K}$ threshold almost coincides with the position of the $f_0(980)$ resonance, up to at least 1.3 GeV. In contrast, the contribution of $K\bar{K}$ to the $\pi\pi$ $I = 1$ P-wave inelasticity η_1^1 is almost negligible, and η_1^1 is believed to be dominated by 4π contributions. Phenomenologically, one finds that the onset of this inelasticity happens roughly at $\sqrt{s} \simeq M_\omega + M_\pi \simeq 0.922\,\text{GeV}$, such that it is a natural question to ask whether $\omega\pi$ intermediate states as an effective two-body description of four pions give an adequate description of the $\pi\pi$ P-wave inelasticity, at least in a certain energy region above threshold. This requires knowledge of the inelastic scattering amplitude $\pi\pi \to \omega\pi$ in the P wave—precisely the crossed process of $\omega \to 3\pi$. The inelasticity parameter η_1^1 can be

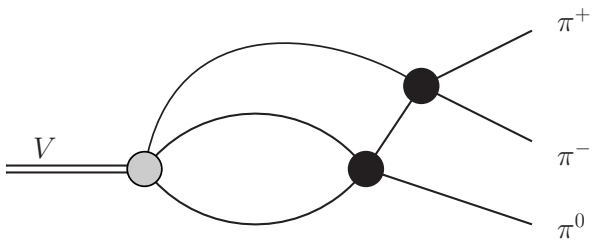

Figure 4.14: Two-loop diagram contributing to the $V \to 3\pi$ decay amplitude, which has a singular discontinuity at the pseudothreshold $s = (M_V - M_\pi)^2$ and leads to a non-vanishing phase/ imaginary part of the corresponding partial wave $f_1(s)$ at threshold $s = 4M_\pi^2$.

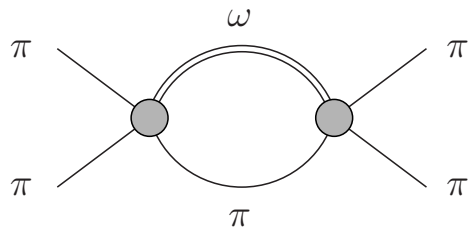

Figure 4.15: Contribution to the $\pi\pi$ P-wave inelasticity due to $\omega\pi$ intermediate states. Each gray blob corresponds to an $\omega \to 3\pi$ amplitude, analytically continued to the scattering region.

calculated from the cut contribution shown in Fig. 4.15, yielding

$$\eta_1^1(s) = \sqrt{1 - \frac{q_{\pi\pi}^3(s) q_{\omega\pi}^3(s)}{144\pi^2} \big|f_1(s)\big|^2 \theta(s - (M_\omega + M_\pi)^2)} \,, \tag{4.48}$$

where $q_{ab}^2(s) = \lambda(s, M_a^2, M_b^2)/4s$, and $f_1(s) = \mathcal{F}(s) + \hat{\mathcal{F}}(s)$ is the P-wave projection of the $\pi\pi \to \omega\pi$ amplitude.

The resulting inelasticity is shown in Fig. 4.16, up to $\sqrt{s} = 1.3\,\text{GeV}$, and for the uncertainty band in the $\omega \to 3\pi$ amplitude discussed in Section 4.4.4. It is seen that this error grows rapidly with energy. Phenomenological determinations of $\eta_1^1(s)$ are also plagued by rather large uncertainties [39, 41]; Fig. 4.16 shows that the $\omega\pi$ intermediate state seems to provide most of the inelasticity given as the central value of the analysis in Ref. [39]. There is seemingly a difference in the threshold behavior, with the $\omega\pi$ contribution rising more slowly near threshold; this is due to the fact that our $\pi\pi \to \omega\pi$ partial wave $f_1(s)$ happens to have almost a zero around 1 GeV. We hasten to add that $\omega\pi$ is not the only way to cluster four pions into an effective two-body P-wave state; other possibilities like $\rho\sigma$ would just be expected to set in at an even higher effective mass.

For comparison, we also plot the inelasticity contribution from $K\bar{K}$ intermediate states, derived from the parameterization of the $\pi\pi \to K\bar{K}$ partial wave $g_1^1(s)$ given in Ref. [179, 180] (see there for definitions), based on the data from Ref. [181]. This yields a $\pi\pi$ P-wave inelasticity contribution according to

$$\eta_1^1(s)_{K\bar{K}} = \sqrt{1 - \frac{16}{s} q_{\pi\pi}^3(s) q_{KK}^3(s) \big|g_1^1(s)\big|^2 \theta(s - 4M_K^2)} \,, \tag{4.49}$$

which, in Fig. 4.16, is indeed seen to be very small, and actually remains so up to at least $\sqrt{s} \simeq 2\,\text{GeV}$.

4.8 Summary and conclusions

In this Chapter we have performed a dispersive analysis of the decays $\omega \to 3\pi$ and $\phi \to 3\pi$. This framework allows for a treatment of crossed-channel two-body rescattering effects fully consistent with analyticity and unitarity. It contains the three-particle cuts generated by $M_V > 3M_\pi$, thus going fundamentally beyond an isobar-like description that has been state-of-the-art up to this point. We have shown that crossed-channel rescattering produces a significant effect on the Dalitz plot clearly exceeding uncertainties generated by the phenomenological input for the P-wave phase shift, discontinuities in higher partial waves, and elastic P-wave resonances other than the $\rho(770)$.

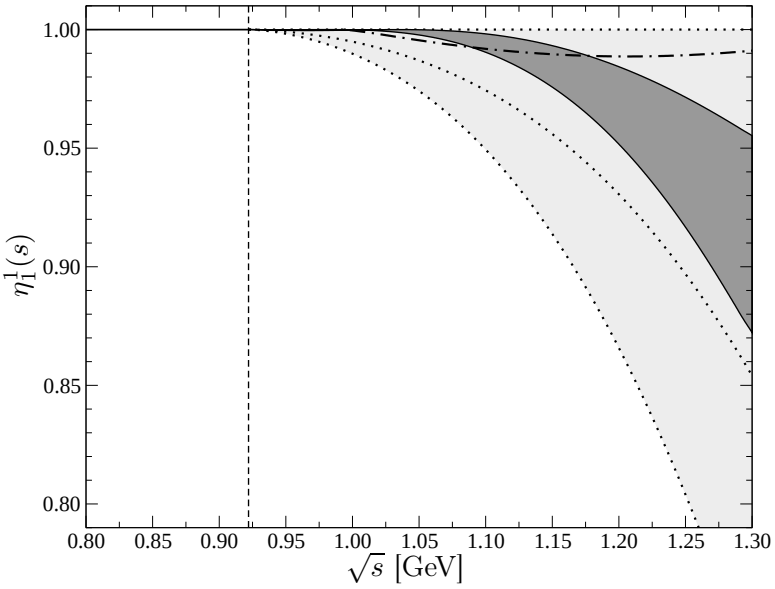

Figure 4.16: Inelasticity in the $\pi\pi$ P wave as a function of $\sqrt{s}$. The dark gray band represents the contribution of $\omega\pi$ intermediate states (within our theoretical uncertainty); the light gray band shows the error range of the phenomenological determination of Ref. [39], with the central value and error limits given by the dotted curves. The dash-dotted curve shows the inelasticity contribution of the $K\bar{K}$ intermediate state for comparison. The vertical dashed line denotes the $\omega\pi$ threshold.

Comparing to the very precise measurements of the $\phi \to 3\pi$ Dalitz plot by the KLOE collaboration, we have found indications for these rescattering effects. Indeed, we obtain a considerably improved χ^2 with the full dispersion calculation with one subtraction compared to an isobar-like description by Omnès functions. Performing a fit of a more flexible, yet less predictive twice-subtracted dispersion calculation, we can achieve an excellent description with high probability of both the KLOE and the CMD-2 data sets, with the more precise KLOE data suggesting a significant deviation of the second subtraction constant from its sum-rule value.

For $\omega \to 3\pi$ we give predictions for the Dalitz plot parameters for the full dispersion calculation as well as neglecting crossed-channel effects. A precise measurement of these parameters that is to be expected from upcoming experimental analyses by KLOE and WASA should be able to distinguish between both approaches. Moreover we have observed that a polynomial fit to the $\omega \to 3\pi$ Dalitz plot at percent-level precision should require at least two parameters, in contrast e.g. to the decay $\eta \to 3\pi^0$ that displays a similarly symmetric Dalitz plot. The sign of the leading polynomial term is constrained by the ρ peak to be positive.

The inelasticity of the $\pi\pi$ P wave is dominated by 4π intermediate states, which can be effectively approximated by a two-body description as $\omega\pi$. We have found that the inelasticity obtained from the analytic continuation of our $\omega \to 3\pi$ amplitude is in reasonable agreement with the not very well-constrained phenomenological determination.

Finally, we wish to remark that it has become amply clear in the course of this Chapter that the treatment of both decays, $\omega \to 3\pi$ and $\phi \to 3\pi$, runs strictly in parallel and shows no formal difference other than the mass of the decaying vector meson, and the overall normalization of

the Dalitz plot, which relates to the (partial) decay widths. Obviously, the very same formalism can also be applied to the Dalitz plot description of $e^+e^- \to 3\pi$ at arbitrary invariant mass of the electron–positron pair $\sqrt{s_{e^+e^-}}$, which replaces the vector mass M_V. It only has to be kept in mind that this would involve an $s_{e^+e^-}$-dependent normalization—dispersion theory does not allow us to predict the energy-dependence of the $e^+e^- \to 3\pi$ total cross section. Given that we have shown that crossed-channel rescattering effects differ in a non-trivial way for the ω and ϕ decays, it may still be interesting to investigate the $s_{e^+e^-}$-dependence of these corrections in a systematic way. Ultimately, for such a task it might be useful to strive for a combination of dispersion theory with microscopic models that can provide parameterizations for the energy-dependent subtraction constants. Finally, we note that a very similar analysis has been performed on the anomalous process $\gamma\pi \to \pi\pi$ [182] to provide a framework to extract the chiral anomaly.

In the following Chapter we will use the results for the $\omega/\phi \to 3\pi$ partial-wave amplitude for a dispersive analysis of the $\omega/\phi \to \pi^0\gamma^*$ transition form factor.

Chapter 5

$\omega \to \pi^0\gamma^*$ and $\phi \to \pi^0\gamma^*$ transition form factors in dispersion theory[#1]

5.1 Introduction

In recent years, there has been intense renewed interest in light-meson transition form factors due to their potential role in the theoretical determinations of the anomalous magnetic moment of the muon (see Ref. [184] for a review). With more and more exclusive channels contributing to the hadronic vacuum polarization measured experimentally with unprecedented precision, it is believed that the hadronic contribution to light-by-light scattering may soon constitute the dominant uncertainty [185]. While a full determination of the light-by-light scattering tensor remains a formidable task, a combination of experimental data and theoretical analyses may help to constrain one of the most important contributions (and one of the few that are model-independently accessible), namely the pseudoscalar ($P = \pi^0$, η, η') pole terms. Their strength is determined e.g. for the π^0 pole contribution by the decay $\pi^0 \to \gamma^*\gamma^*$, given in terms of the doubly-virtual form factor $F_{\pi^0\gamma^*\gamma^*}(M_{\pi^0}^2, q_1^2, q_2^2)$ (see e.g. Ref. [184] for precise definitions), where $q_{1/2}^2$ denote the two photon virtualities. As these doubly-virtual form factors, that are to be measured in the rare decays $P \to \ell^+\ell^-\ell'^+\ell'^-$ (with branching ratios of the order of 10^{-5}), are difficult to determine precisely in experiment, it is useful to note that they are intimately linked (for specific values of one of the photon virtualities) to vector-meson conversion decays: e.g., the form factor $F_{\pi^0\gamma^*\gamma^*}(M_{\pi^0}^2, q^2, M_\omega^2)$ determines the dilepton spectrum in $\omega \to \pi^0\ell^+\ell^-$, the form factor $F_{\eta\gamma^*\gamma^*}(M_\eta^2, q^2, M_\phi^2)$ can be measured in $\phi \to \eta\ell^+\ell^-$ etc.

The interactions of hadrons with (real and virtual) photons are often thought to be described at least to good approximation in the picture of vector-meson dominance (VMD): the q^2-dependence of the form factors above should largely be given by the propagator of a light intermediate vector meson (ρ, ω, ϕ), see e.g. Refs. [164, 167, 186, 187]. What is interesting about the vector-meson conversion decays is that they show a very clear deviation from such a simple VMD picture, as has been established in the decay $\omega \to \pi^0\mu^+\mu^-$ [188–190], and also in $\phi \to \eta e^+e^-$ [191, 192].

In this Chapter, we will analyze two such vector-meson transition form factors with the method of dispersion relations, concentrating on $\omega \to \pi^0\gamma^*$ and $\phi \to \pi^0\gamma^*$ (the latter being rarer due to the implied violation of the Okubo–Zweig–Iizuka rule; see Ref. [193] for a recent

[#1] The contents of this Chapter have been published in [183].

theoretical work). One specific theoretical advantage of vector-meson conversion decays, as opposed to the pseudoscalar Dalitz decays, is that the isospin of the virtual photon is fixed (in the approximation that isospin is conserved). In the cases at hand, it needs to be an iso*vector* photon, hence the lowest-lying intermediate states to contribute in a dispersion relation are 2π, 4π etc. only, and experience with pion–pion P-wave interactions suggests that the 2π intermediate state will already saturate the dispersion relation to a large degree. As we will demonstrate below, a dispersive reconstruction of the 2π contribution requires two amplitudes as input: the corresponding $V \to \pi^+\pi^-\pi^0$ decay amplitude (in the appropriate partial wave), and the pion (electromagnetic) vector form factor.

An analysis of the $\omega \to \pi^0\gamma^*$ transition form factor using dispersion theory has already been performed decades ago [178] (although phenomenologically the focus of that work lay more on the $e^+e^- \to \omega\pi^0$ production cross section). The reasons to take up this subject again are manifold: we now have much more accurate experimental as well as theoretical input at our disposal, both for the pion vector form factor and the required pion–pion phase shifts; furthermore, we have introduced a dispersive analysis of the three-pion decays of both ω and ϕ that treats final-state interactions between all three pions rigorously in the previous Chapter. It can now serve as the consistent input to the investigation of the transition form factors. All these ingredients will be reviewed as they apply to our analysis below.

As a final introductory remark, we note that in this Chapter, we concentrate our analysis of the transition form factors on the kinematical region accessible in the corresponding vector-meson *decays*. We are aiming for a precision analysis and only very briefly touch upon the processes $e^+e^- \to \pi^0\omega$ [194–196]. We will not consider $e^+e^- \to \pi^0\phi$ [197], as we expect it to be significantly more dependent on information from the excited-resonance region.

The outline of this Chapter is as follows. We introduce the necessary definitions concerning kinematics and partial-wave decomposition in Section 5.2. We discuss the dispersion relation for the transition form factors in Section 5.3, including the two main elements required as input: the pion vector form factor and the $V \to \pi^+\pi^-\pi^0$ partial-wave amplitude. Numerical results for form factors, decay spectra, and branching ratios are presented in Section 5.4, before we summarize in Section 5.5.

5.2 Kinematics and partial-wave decomposition

We consider the decays of the lightest isoscalar vector mesons into a π^0 and a dilepton pair,

$$V(p_V) \to \pi^0(p_0)\ell^+(p_{\ell^+})\ell^-(p_{\ell^-})\,,\ V = \omega/\phi\,,\ \ell = e/\mu\,. \tag{5.1}$$

The amplitude of this decay can be written as [198]

$$\mathcal{M}_{V\pi^0}(s, m^2_{V\ell^+}, m^2_{V\ell^-}) = ie^2\epsilon_{\mu\nu\alpha\beta}n^\mu p_0^\nu q^\alpha \frac{f_{V\pi^0}(s)}{s}\bar{u}_r(p_{\ell^-})\gamma^\beta v_{r'}(p_{\ell^+})\,, \tag{5.2}$$

where $q = p_{\ell^+} + p_{\ell^-}$, $s = (p_V - p_0)^2$, n^μ is the polarization vector of the vector meson, $r(r')$ is the spin of the outgoing (anti-)lepton, and $f_{V\pi^0}(s)$ is the *electromagnetic transition form factor* of the vector meson. We will also discuss the corresponding normalized form factor,

$$F_{V\pi^0}(s) = \frac{f_{V\pi^0}(s)}{f_{V\pi^0}(0)}\,. \tag{5.3}$$

The double-differential decay rate of a particle with mass M_V in terms of this amplitude is given as

$$\frac{d\Gamma_{V\to\pi^0\ell^+\ell^-}}{ds\,dm^2_{V\ell^+}} = \frac{1}{(2\pi)^3}\frac{1}{32M_V^3}\overline{|\mathcal{M}_{V\pi^0}|^2}\ , \tag{5.4}$$

where we defined the center-of-mass energies of the $\ell^\pm\pi^0$ subsystems as $m^2_{V\ell^\pm} = (p_V - p_{\ell^\pm})^2$, average over the polarizations of the vector particle and sum over the spins of the outgoing leptons,

$$\overline{|\mathcal{M}_{V\pi^0}|^2} = \frac{1}{3}\sum_{r,r'} e^4\epsilon_{\mu\nu\alpha\beta}\epsilon^{\mu}{}_{\bar\nu\bar\alpha\bar\beta}p_0^\nu q^\alpha p_0^{\bar\nu}q^{\bar\alpha}\,\bar u_r(p_{\ell^-})\gamma^\beta v_{r'}(p_{\ell^+})\bar v_{r'}(p_{\ell^+})\gamma^{\bar\beta}u_r(p_{\ell^-})\,\frac{|f_{V\pi^0}(s)|^2}{s^2}\ . \tag{5.5}$$

The polarization sum has already been evaluated yielding $\sum_{\text{pol.}} n^{\bar\mu}n^\mu = -g^{\mu\bar\mu}$. Using

$$\sum_{r,r'}\bar u_r(p_{\ell^-})\gamma^\beta v_{r'}(p_{\ell^+})\bar v_{r'}(p_{\ell^+})\gamma^{\bar\beta}u_r(p_{\ell^-}) = 4p^\beta_{\ell^-}p^{\bar\beta}_{\ell^+} + 4p^{\bar\beta}_{\ell^-}p^\beta_{\ell^+} - 4(m_\ell^2 + p_{\ell^-}p_{\ell^-})g^{\beta\bar\beta}\ , \tag{5.6}$$

and contracting the Levi-Civita symbols the double-differential decay rate can be cast into the form

$$\frac{d\Gamma_{V\to\pi^0\ell^+\ell^-}}{ds\,dm^2_{V\ell^+}} = \frac{2\alpha^2}{\pi}\frac{P}{32M_V^3}\frac{|f_{V\pi^0}(s)|^2}{s^2}\ , \tag{5.7}$$

with the fine-structure constant $\alpha = e^2/4\pi$. The phase-space factor can be evaluated to

$$P = \frac{4}{3}s\,q^2_{V\pi^0}(s)\big[s - 2q^2_{\ell\ell}(s)(1 - z^2_{V\ell^+})\big]\ , \tag{5.8}$$

where $z_{V\ell^+} = \cos\theta_{V\ell^+}$ is the center-of-mass scattering angle of the $\ell^-\pi^0$ subsystem and the center-of-mass momenta are given as

$$q^2_{AB}(s) = \frac{\lambda(M_A^2, M_B^2, s)}{4s}\ , \tag{5.9}$$

where $\lambda(x,y,z) = x^2 + y^2 + z^2 - 2(xy + yz + xz)$ is used with the slight notational abuse $M_\ell \doteq m_\ell$ implied. Eventually, integrating over $m^2_{V\ell^+}$, we obtain the differential decay width in the $\ell^+\ell^-$ center-of-mass system,

$$\frac{d\Gamma_{V\to\pi^0\ell^+\ell^-}}{ds} = \frac{2\alpha^2}{9\pi M_V^3}\left(1 + \frac{2m_\ell^2}{s}\right)q_{\ell\ell}(s)q^3_{V\pi^0}(s)|f_{V\pi^0}(s)|^2. \tag{5.10}$$

Radiative corrections to Eq. (5.10) have been calculated in Ref. [199]: they require a careful selection of kinematic cuts on the additional soft-photon radiation for the e^+e^- final state, and are small everywhere except near threshold for $\mu^+\mu^-$, where the Coulomb pole is significant. The above relation for the $V\to\pi^0\ell^+\ell^-$ spectrum is completely determined by $f_{V\pi^0}(s)$ aside from a kinematical factor that is determined by the photon propagator and phase space. Note finally that the same exercise for the corresponding *real-photon* total decay rate yields

$$\Gamma_{V\to\pi^0\gamma} = \frac{\alpha(M_V^2 - M_{\pi^0}^2)^3}{24M_V^3}|f_{V\pi^0}(0)|^2\ . \tag{5.11}$$

In establishing a dispersion relation for the $V\to\pi^0\gamma^*$ transition form factors, the corresponding three-pion decays $V(p_V)\to\pi^+(p_+)\pi^-(p_-)\pi^0(p_0)$ play a central role. We use the

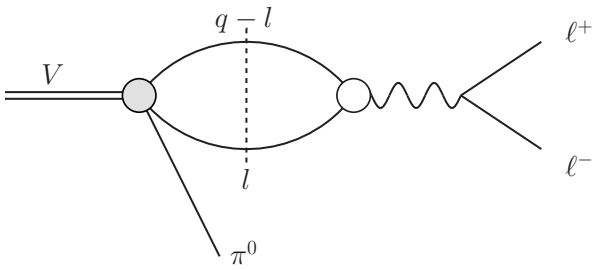

Figure 5.1: Diagrammatic representation of the discontinuity of the $V \to \pi^0\ell^+\ell^-$ transition form factor. The gray circle denotes the $V \to 3\pi$ amplitude, whereas the white circle represents the pion vector form factor.

same set of definitions from before with $s = (p_V - p_0)^2$, $t = (p_V - p_+)^2$, $u = (p_V - p_-)^2$, and $3s_0 \doteq s + t + u = M_V^2 + 3M_\pi^2$. The amplitude of $V \to 3\pi$ is used in the form of Eq. (4.3). As before the decay is treated in the isospin limit and we neglect discontinuities from F and higher partial waves. In particular the partial-wave projection of the amplitude (4.8), the analytic structure of which was discussed in some detail in Section 4.6, will be instrumental to our analysis.

5.3 Dispersion relation for the transition form factor

In the following section we will present how to set up dispersion relations for the $V \to \pi^0\gamma^*$ transition form factor. We start out deriving the unitarity relation by evaluating the discontinuity of the pertinent diagram, and subsequently present the integral equation that solves the unitarity relation. We follow up by briefly discussing the main ingredients – the pion vector form factor and the partial-wave amplitude. Since these two topics have been discussed elaborately throughout this work we shall only discuss some of the specifics of the form factor analysis.

5.3.1 Unitarity relation and integral equation

To set up the dispersion relation for the transition form factor, we calculate the two-pion discontinuity of the diagram shown in Fig. 5.1. We have

$$\begin{aligned}\operatorname{disc}\epsilon_{\mu\nu\alpha\beta}n^\mu p_0^\nu q^\alpha f_{V\pi^0}(s) = i\int\frac{d^4l}{(2\pi)^4}\epsilon_{\mu\nu\alpha\gamma}n^\mu(q-l)^\nu l^\alpha p_0^\gamma\mathcal{F}(s,t',u')\,(q-2l)_\beta F_\pi^{V*}(s)\\ \times(2\pi)\delta(l^2-M_\pi^2)(2\pi)\delta((q-l)^2-M_\pi^2)\,,\end{aligned}\tag{5.12}$$

where $\mathcal{F}(s,t,u)$ is the scalar $V \to 3\pi$ amplitude defined in Eq. (4.3) and $F_\pi^{V*}(s)$ is the pion vector form factor that we discussed in Section 1.2.2. Due to the anti-symmetry of the Levi-Civita symbol the terms $\propto l^\nu$ vanish. For similar reasons the terms $\propto q^\beta$ may be discarded: the only available Lorentz structures with one Lorentz index are the momenta of the decaying vector meson, of the π^0 and of the virtual photon, although only two of them are independent due to momentum conservation. We thus have three independent Lorentz structures (taking the polarization vector of vector particle into account) that have to be contracted with the

Levi-Civita symbol. For the remaining integral we may use the decomposition

$$\int d^4l\, l^\alpha l_\beta(\ldots) = g^\alpha_\beta \mathcal{I}_1 + q^\alpha q_\beta \mathcal{I}_2 + \mathcal{I}_3 \Delta^\alpha \Delta_\beta + \mathcal{I}_4 \Delta^\alpha q_\beta \ , \tag{5.13}$$

where $\Delta_\mu = (p_{\ell^+} - p_{\ell^-})_\mu$. Contracting with g^β_α, $q_\alpha q^\beta$, $\Delta_\alpha \Delta^\beta$, and $\Delta_\alpha q^\beta$ we can determine the integrals $\mathcal{I}_i$. We note, however, that due to the anti-symmetry of the ϵ tensor only the term $\propto \mathcal{I}_1$ remains, so that

$$\int d^4l\, l^\alpha l_\beta(\ldots) = \frac{g^\alpha_\beta}{3} \int d^4l\, l^2 (1 - z_s'^2)(\ldots) \ , \tag{5.14}$$

where $z_s' = \cos\theta_s'$ is the center-of-mass scattering angle between the initial and intermediate state. Carrying out the momentum integration in the dilepton center-of-mass frame leads to

$$\epsilon_{\mu\nu\alpha\beta} n^\mu p_0^\nu q^\alpha \text{disc}\, f_{V\pi^0}(s) = \epsilon_{\mu\nu\alpha\beta} n^\mu p_0^\nu q^\alpha \frac{i q_{\pi\pi}^3(s)}{8\pi\sqrt{s}} F_\pi^{V*}(s) \int_{-1}^1 dz_s' (1 - z_s'^2) \mathcal{F}(s, t', u') \ . \tag{5.15}$$

Finally, we use the definition of the partial-wave amplitude in Eq. (4.8), to arrive at the unitarity relation of the transition form factor [178],

$$\text{disc}\, f_{V\pi^0}(s) = \frac{i\, q_{\pi\pi}^3(s)}{6\pi\sqrt{s}} F_\pi^{V*}(s) f_1(s)\, \theta\big(s - 4M_\pi^2\big) \ , \tag{5.16}$$

Corrections to Eq. (5.16) stem from heavier intermediate states of the appropriate quantum numbers (isospin 1 P-wave states): 4π, $K\bar{K}$, ..., which are expected to be suppressed significantly due to phase space and their higher masses. We therefore neglect these contributions in our analysis and resort to elastic $\pi\pi$ final states only. Given our standard assumptions on the asymptotic high-energy behavior of the pion form factor, $F_\pi^V(s) \simeq 1/s$ (modulo logarithms), and the $V \to 3\pi$ partial wave, $f_1(s) \simeq 1/s$ (see previous Chapter), Eq. (5.16) allows for an unsubtracted dispersion relation [178]. As our analysis, however, is confined to two-pion intermediate states and neglects any higher contributions, we decide to employ a once-subtracted solution of Eq. (5.16) instead,

$$f_{V\pi^0}(s) = f_{V\pi^0}(0) + \frac{s}{12\pi^2} \int_{4M_\pi^2}^\infty ds' \frac{q_{\pi\pi}^3(s') F_\pi^{V*}(s') f_1(s')}{s'^{3/2}(s' - s)} \ , \tag{5.17}$$

in order to suppress inelastic contributions. For the predictions of the s-dependence of the form factor, we fix the subtraction constant $f_{V\pi^0}(0)$ to reproduce the $V \to \pi^0\gamma$ partial width according to Eq. (5.11). Assuming the validity of an unsubtracted dispersion relation, the subtraction constant and therefore the $V \to \pi^0\gamma$ partial width can be calculated by means of a sum rule,

$$f_{V\pi^0}(0) = \frac{1}{12\pi^2} \int_{4M_\pi^2}^\infty ds' \frac{q_{\pi\pi}^3(s')}{s'^{3/2}} F_\pi^{V*}(s') f_1(s') \ , \tag{5.18}$$

which is expected to show a more problematic convergence behavior than the form-factor dispersion relation. We will quote results for this sum rule in Section 5.4 in order to quantify the potential role of heavier intermediate states in the transition form factor. Nevertheless, Eq. (5.18) is a remarkable result: in the elastic approximation the pion vector form factor is entirely given in terms of the $\pi\pi$ P-wave phase shift $\delta_1^1(s)$, which also determines the $V \to 3\pi$

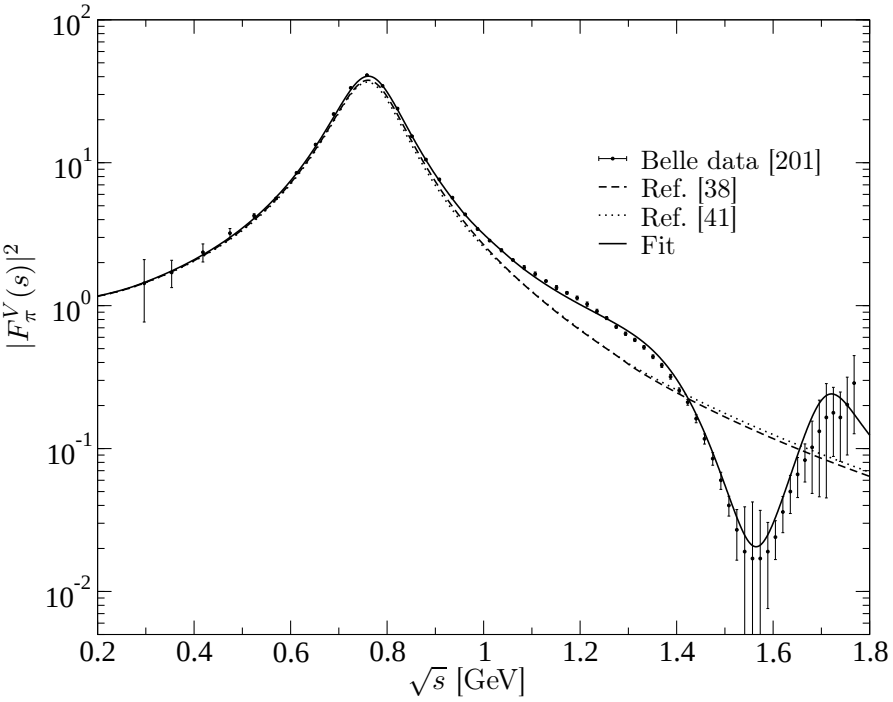

Figure 5.2: Pion vector form factor fit using a phase shift incorporating elastic ρ', ρ'' resonances (solid curve) and solutions of the Roy equations of Refs. [39, 41] (dashed and dotted curves), in comparison to the experimental data of Ref. [201]. For details, see main text.

partial wave up to a single subtraction constant that can be written as an overall normalization. This means that the ratio of branching ratios $\mathcal{B}(V \to \pi^0\gamma)/\mathcal{B}(V \to 3\pi)$ is entirely determined by $\delta_1^1(s)$, up to inelastic corrections. This result is reminiscent of the relation between these two decay modes utilized in Refs. [160, 161] as the leading order of a Lagrangian framework for vector mesons.

In the following we will briefly revisit the two ingredients to the dispersion integral, the pion vector form factor $F_\pi^V(s)$ and the $V \to 3\pi$ partial-wave amplitude $f_1(s)$.

5.3.2 Pion vector form factor and $V \to 3\pi$ partial-wave amplitude

We represent the pion vector form factor as discussed in Section 1.2.2 by the Omnès function,

$$F_\pi^V(s) = \Omega(s) = \exp\left\{\frac{s}{\pi}\int_{4M_\pi^2}^{\infty} ds' \frac{\delta(s')}{s'(s'-s)}\right\}, \tag{5.19}$$

normalized to $\Omega(0) = 1$. The omission of a polynomial in s multiplying the Omnès function relies on the absence of zeros in the form factor, see Ref. [200]. In a precision analysis of the form factor extending beyond 1 GeV, one has to account for the onset of inelasticities (dominantly 4π intermediate states), and, as far as data extracted from $e^+e^- \to \pi^+\pi^-$ is concerned, ρ–ω mixing. As we do not have a consistent treatment of inelasticity effects in the $V \to 3\pi$ partial wave $f_1(s)$ at our disposal (let alone isospin breaking), we refrain from doing so.

In this Chapter we use the following approach to estimate uncertainties generated by the input for the parameterization of the phase shift. On the one hand we will again use

the parameterizations derived from the two different solutions of the pion–pion Roy equations [38, 39, 41], which are valid roughly up to 1.3 GeV. Experimentally, the pion form factor is known to excellent precision well beyond that energy (see Refs. [201–203] for just the most recent experimental results), indicating in particular contributions from the excited resonances $\rho'(1450)$ and $\rho''(1700)$. To incorporate these higher resonance states we use the phenomenological form factor that was already discussed in the context of the previous Chapter. In the present analysis we strive for a representation of the form factor that resembles the accurate data sets as closely as possible, which is why we fit the parameters of the representation to the experimental data of Ref. [201], extract the corresponding phase, and match it smoothly to the phase-shift solution of Ref. [39] below 1 GeV, see Appendix B.5 for the pertinent fit parameters. The aforementioned procedure treats the higher resonances ρ' and ρ'' as purely elastic, which they clearly are not (compare the more sophisticated form factor representation of Ref. [204]); we merely use the phase thus obtained as an indicator for uncertainties generated in the energy range between roughly 1.3 GeV and 1.9 GeV.

As the Omnès representation requires the $\pi\pi$ P-wave phase shift up to infinity, we again have to make assumptions about its asymptotic behavior. In contrast to the previous chapter we choose to smoothly guide $\delta(s)$ to π, see Eq. (3.81), so that we guarantee the correct asymptotic behavior of $F_\pi^V(s) \to s^{-1}$ for $s \to \infty$. The point beyond which the asymptotic behavior sets in is chosen to be $\Lambda_\delta = 1.3$ GeV for the Roy-equation analyses [39,41], and $\Lambda_\delta = 1.9$ GeV for the phase derived from the form factor. The resulting form factors corresponding to the different phases are shown in Fig. 5.2, compared to the data of Ref. [201].

We would like to also add some comments on the $V \to 3\pi$ partial-wave amplitude in the context of our transition form factor study. When discussing the topic in some detail in Section 4.6, we observed a violation of Watson's theorem: due to three-pion cut effects the phase of the partial-wave amplitude $f_1(s)$ does not follow $\delta(s)$ since a non-vanishing imaginary part is allowed already below the $\pi\pi$ threshold. This complication does not occur in the treatment of the partial-wave amplitude that is used to calculate the transition form factor in Ref. [178] due to the approximation of the left-hand-cut contributions by ρ poles only, neglecting the effects of the two-pion cut starting at t, $u = 4M_\pi^2$. As only the transition form factor of the ω and not the one of the ϕ is considered in Ref. [178], the ρ poles in the t-/u-channel lie outside the integration range that affects the partial-wave projection. Thus the singular behavior of $f_1(s)$ at the pseudothreshold $s = (M_V - M_\pi)^2$ does not occur in that analysis. It should be noted, however, that these singularities in the discontinuity do *not* translate into singular behavior of the form factor itself when evaluated at the upper rim of the unitarity cut. In particular, the irregular phase in the vicinity of the pseudothreshold is an artifact as a consequence of the different divergences of real and imaginary parts from below and above, and has no physical significance.

In Section 4.5.2 we found that oversubtracting the dispersion integral we were able to achieve a perfect representation of the very precise KLOE data, using the additional subtraction constant as a fit parameter. Obviously it is very desirable to use such a representation as input for the partial-wave amplitude (at least for the $\phi \to \pi^0\gamma^*$ transition form factor owing to the lack of highly desirable $\omega \to 3\pi$ data). However, since the fitted value for b differs from a sum rule, as suggested by demanding the representations (4.22) and (4.24) to be equal, the latter integral equation does not satisfy the high-energy behavior for the partial-wave amplitude $f_1(s)$, which therefore tends asymptotically towards a constant instead of s^{-1}; consequently, the integral (5.18) does not converge, and we will not evaluate the sum rule for $f_{\phi\pi^0}(0)$ for the twice-subtracted solution of $f_1(s)$.

We will in general stabilize the high-energy behavior of our dispersion integrals by manually leading $\mathcal{F}(s)$ to $\Lambda^2\mathcal{F}(\Lambda^2)/s$ beyond a certain cutoff Λ^2. There is no obvious prescription as to when exactly the amplitude or the form factor should show this asymptotic behavior; we choose the point up to where we have adjusted our form factor representation to data, that is $\Lambda = 1.8$ GeV, and incorporate a variation of the cutoff up to $\Lambda = 2.5$ GeV in our error considerations. This prescription assures that we have a precision representation for the amplitude in the low-energy regime as well as the correct high-energy behavior. By varying the cutoff we assure that the intermediate-energy regime is sufficiently suppressed so as not to taint our numerical results, which we present in the following section.

5.4 Numerical results

For the numerical evaluation, we use the different parameterizations of the phase shift described in Section 5.3.2; the same parameterization is always used consistently for both pion form factor and $V \to 3\pi$ partial wave. We vary the cutoff of the dispersion integrals in Eqs. (5.17), (5.18), and (4.22) (beyond which the assumed asymptotic behavior is enforced by hand) between $\Lambda = 1.8$ GeV and $\Lambda = 2.5$ GeV as detailed above. We note that it does not make sense to vary the cutoff of the aforementioned integrals individually: the uncertainties in our treatment are related to our lack of knowledge concerning final-state interactions in the intermediate energy range, and thus apply equally to all considered dispersion integrals. The subtraction constants of the $V \to 3\pi$ amplitudes are fixed by the total widths $\Gamma_\omega = 8.49 \pm 0.08$ MeV and $\Gamma_\phi = 4.26 \pm 0.04$ MeV together with the $V \to 3\pi$ branching ratios $\mathcal{B}^{\exp}(\omega \to 3\pi) = 0.892 \pm 0.007$, $\mathcal{B}^{\exp}(\phi \to 3\pi) = 0.153 \pm 0.003$, the uncertainties of which we will always neglect in the following. It turns out that for all of our evaluations of the *once-subtracted* dispersion relation in Eq. (5.17), a variation of the phase between the parameterization of Ref. [41] and the one derived from the form factor spectrum along with an integral cutoff of $\Lambda = 1.8$ GeV gives rise to an enveloping uncertainty band.

For the following $V \to \pi^0\gamma$ branching ratios determined from Eq. (5.11) and the *unsubtracted* dispersion relation (5.18), the parameterization of Ref. [39] and the one from the form factor spectrum together with an integral cutoff of $\Lambda = 2.5$ GeV give rise to limiting values. We find

$$\begin{aligned} \mathcal{B}(\omega \to \pi^0\gamma) &= (7.48 \ldots 7.75) \times 10^{-2} \,, \\ \mathcal{B}(\phi \to \pi^0\gamma) &= (1.28 \ldots 1.37) \times 10^{-3} \,, \end{aligned} \tag{5.20}$$

which is to be checked against the experimental averages $\mathcal{B}^{\exp}(\omega \to \pi^0\gamma) = (8.28 \pm 0.28) \times 10^{-2}$, $\mathcal{B}^{\exp}(\phi \to \pi^0\gamma) = (1.27 \pm 0.06) \times 10^{-3}$ [87]. We observe that the $\phi \to \pi^0\gamma$ partial width compares favorably to experiment, whereas the result for $\omega \to \pi^0\gamma$ turns out to be slightly too low; even then, the 2π intermediate state seems to saturate more than 90% of the sum rule for this partial width. We note that the most precise individual measurement of $\mathcal{B}(\omega \to \pi^0\gamma)$ actually determines the ratio of branching ratios $\mathcal{B}^{\exp}(\omega \to \pi^0\gamma)/\mathcal{B}^{\exp}(\omega \to 3\pi) = (8.97 \pm 0.16) \times 10^{-2}$ [196], which is precisely the ratio we argued in Section 5.3 to be a pure prediction due to the $\pi\pi$ P-wave phase shift, independent of any subtraction constant; for this quantity, our numerical result amounts to

$$\frac{\mathcal{B}(\omega \to \pi^0\gamma)}{\mathcal{B}(\omega \to 3\pi)} = (8.39 \ldots 8.69) \times 10^{-2} \,, \tag{5.21}$$

hence suggesting a saturation of the sum rule even at the 95% level.

We stress, however, that because of the slow convergence behavior of the integrand in Eq. (5.18), we do not consider the sum-rule results to be extremely reliable: they depend rather strongly on the assumed intermediate and high-energy behavior of the $\pi\pi$ phase shift. For example, using a cutoff of $\Lambda = 1.8$ GeV in the dispersion integral (5.18) beyond which the asymptotic fall-off is enforced by hand, we find that this asymptotic region $s > \Lambda^2$ still yields a 10% correction to the $\omega \to \pi^0\gamma$ branching ratio. We therefore rather take these as benchmark values to test the accuracy of the approximation of using only two-pion intermediate states in the dispersion relation: we expect this to work *better* in the description of the s-dependence of the transition form factor, in which we choose the subtraction constant in Eq. (5.17) fixed to the experimental values of the $V \to \pi^0\gamma$ partial widths. The errors on these values contribute a large part to the uncertainty of the transition form factor and the differential $V \to \pi^0\ell^+\ell^-$ decay width, which we will present in the following.

5.4.1 $\omega \to \pi^0 \ell^+ \ell^-$

We start off by considering $V = \omega$. In Fig. 5.3 we compare the absolute value squared of the $\omega \to \pi^0\gamma^*$ transition form factor (left panel) and the differential $\omega \to \pi^0\ell^+\ell^-$ decay widths (right panel) calculated in our approach, standard VMD with a finite energy-dependent width,[#2] and a chiral Lagrangian treatment with light vector mesons from Refs. [205, 207], to data from Refs. [188–190]. The dispersive approach leads to a significant enhancement of the transition form factor over the pure VMD result, which in turn results in an improved description of the data. Part of this enhancement is even present if we use a simplified, VMD-inspired $\omega \to 3\pi$ partial wave $f_1(s) = a\,\Omega(s)$ inside the dispersion integral. As Fig. 4.13 suggests, using the correct full $\omega \to 3\pi$ P wave mainly leads to a further enhancement for invariant masses of the lepton pair near and slightly above the two-pion threshold. We note that using the slightly smaller sum-rule value for the normalization of the form factor (instead of the one determined from the experimental $\omega \to \pi^0\gamma$ width) would further enhance $|F_{\omega\pi^0}(s) - 1|^2$ by 5–10%, albeit at the expense of a significantly enlarged uncertainty. However, we also find that our analysis cannot account for the steep rise towards the end of the decay region, which is somewhat better described by the calculation in Refs. [205, 207]. The size of the discrepancy for large invariant masses is surprising (note that the form factor in Fig. 5.3 is shown on a logarithmic scale), in particular given the level of agreement found in the sum rule for the $\omega \to \pi^0\gamma$ branching ratio that should converge rather worse. Within the dispersive framework it is therefore hard to think of a plausible explanation for such a steep rise. We note that in contrast to $\phi \to 3\pi$, we have not yet been able to test the $\omega \to 3\pi$ decay amplitude against experimental precision studies of the Dalitz plot, so a remaining deficit in our input for $f_1(s)$ cannot rigorously be excluded. Still, given the analogy to the $\phi \to 3\pi$ study, it is implausible that this can account for the size of the difference.

The transition form factors are often characterized by their slope at $s = 0$:

$$b_{V\pi^0} = \left.\frac{dF_{V\pi^0}(s)}{ds}\right|_{s=0} . \tag{5.22}$$

We quote this slope in units of M_ρ^{-2} (where we use $M_\rho = 775.5$ MeV), such that VMD suggests

[#2] This produces an almost negligible effect for $V = \omega$, but guarantees sensible results for $V = \phi$.

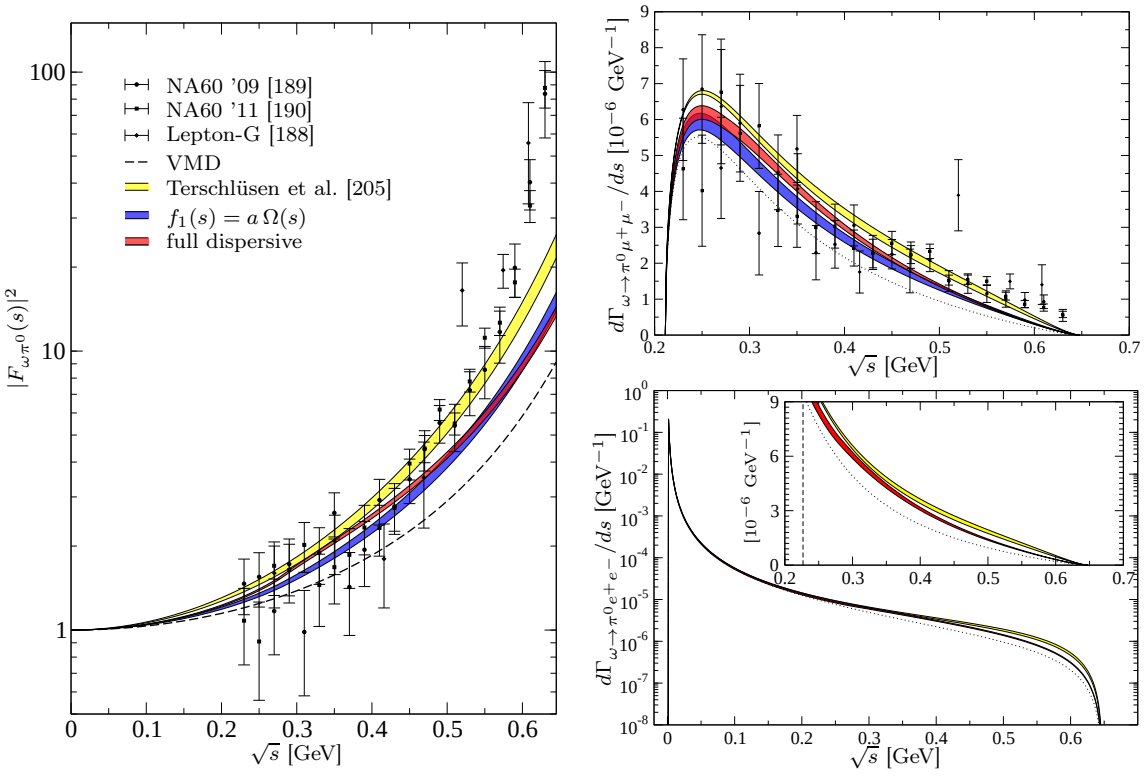

Figure 5.3: Left panel: numerical results for the $\omega \to \pi^0\gamma^*$ transition form factor. Top, right panel: differential $\omega \to \pi^0\mu^+\mu^-$ decay width. Bottom, right panel: differential $\omega \to \pi^0 e^+e^-$ decay width. Data for the transition form factor and the differential $\omega \to \pi^0\mu^+\mu^-$ width is taken from Refs. [188–190] (we have not included the data set from Ref. [206] due to its fairly low statistics). We show pure VMD (dashed curve), the results of a chiral Lagrangian treatment with explicit vector mesons [207] (yellow shaded curve), and the dispersive solution for $f_1(s) = a\,\Omega(s)$ (blue shaded curve) as well as the full dispersive solution (red shaded curve). For $\omega \to \pi^0 e^+e^-$ we do not display the pure Omnès solution, since it is virtually indistinguishable from the full dispersive result due to the strongly dominating kinematical factor in Eq. (5.10). The inset magnifies the region above the two-muon threshold (vertical dashed line).

$b_{\omega\pi^0} = 1\,M_\rho^{-2}$. Our dispersive analysis yields

$$b_{\omega\pi^0} = (1.41\ldots1.45)\,M_\rho^{-2}\ , \tag{5.23}$$

therefore a significant enhancement with respect to the VMD value, yet not as large as the theoretical value found in Refs. [205, 207], $b_{\omega\pi^0} \approx 2\,M_\rho^{-2}$, and significantly smaller than the experimental determinations $b_{\omega\pi^0} = (3.72 \pm 0.10 \pm 0.03)\,M_\rho^{-2}$ [189], $b_{\omega\pi^0} = (3.73 \pm 0.04 \pm 0.05)\,M_\rho^{-2}$ [190]. We note, however, that the latter experimental extractions are in principle model-dependent, as they rely on a monopole parameterization.

In order to improve on the comparison of our form-factor description to the data, one may think of subtracting Eq. (5.17) once more and treating the additional subtraction constant as a free parameter, at the expense of spoiling the high-energy behavior of the transition form factor. The difference between the once- and twice-subtracted representation amounts to an additive term $\Delta b_{\omega\pi^0} \times s$, and it is rather obvious that this term cannot account for the strong

curvature in the form factor at higher energies, such that the overall picture is not drastically improved. Furthermore, the value given in Eq. (5.23) amounts to a value for the slope given by a sum rule, which would be expected to converge much better than the one for $f_{\omega\pi^0}(0)$ in Eq. (5.18), yet it yields a result ostensibly off by a large factor.

The differential decay width for $\omega \to \pi^0\mu^+\mu^-$ (top right panel in Fig. 5.3) is calculated according to Eq. (5.10).[#3] We observe that the values of the form factor close to the end of the decay region are actually strongly suppressed by phase space. From that vantage point the situation does not look as dire as when the form factor is considered directly; however, due to the smallness of the errors of those values our solution still deviates by several σ. The integration of the spectrum yields

$$\mathcal{B}(\omega \to \pi^0\mu^+\mu^-) = (0.94 \ldots 1.00) \times 10^{-4} \,, \tag{5.24}$$

which agrees with the experimental average $\mathcal{B}^{\text{exp}}(\omega \to \pi^0\mu^+\mu^-) = (1.3 \pm 0.4) \times 10^{-4}$ [87] within errors. This is not surprising: as the largest deviations from the experimental form factor are strongly suppressed by phase space, they do not have a large influence on the partial width.

We also display the $\omega \to \pi^0 e^+ e^-$ differential decay width (bottom right panel in Fig. 5.3), which has not been measured yet. Phase space combined with the $1/s$ behavior of the virtual photon lead to a strong enhancement near threshold and a variation of the spectrum over many orders of magnitude; we therefore only display the full dispersive result, since it is almost indistinguishable from $f_1(s) = a\,\Omega(s)$ on this scale. For better comparison to $\omega \to \pi^0\mu^+\mu^-$, we also show this spectrum restricted to energies $\sqrt{s} \geq 2m_\mu$. As can be seen in Fig. 5.3, both leptonic final states yield very similar amounts of events in this energy range, where form-factor effects (deviations from pure QED) are felt most strongly. The integrated spectrum for $\omega \to \pi^0 e^+ e^-$ yields

$$\mathcal{B}(\omega \to \pi^0 e^+ e^-) = (7.6 \ldots 8.1) \times 10^{-4} \,, \tag{5.25}$$

where the uncertainty is dominated by the normalization given by $\mathcal{B}(\omega \to \pi^0\gamma)$—the s-dependent e^+e^- spectrum is largely given by pure QED. Equation (5.25) is in perfect agreement with the experimental value $\mathcal{B}^{\text{exp}}(\omega \to \pi^0 e^+ e^-) = (7.7 \pm 0.6) \times 10^{-4}$ within uncertainties.

5.4.2 $\phi \to \pi^0 \ell^+ \ell^-$

Next we consider $V = \phi$. The results are displayed in Fig. 5.4 for the absolute value squared of the $\phi \to \pi^0\gamma^*$ transition form factor (left panel) and the differential $\phi \to \pi^0\ell^+\ell^-$ decay widths (right panel). There are no experimental data in any of the decay channels yet. For the $\phi \to \pi^0\gamma^*$ transition form factor we observe a similar behavior as for the ω: in the full decay region, the form factor calculated with the dispersive approach is enhanced compared to the pure VMD result; in addition, we observe the two-pion-threshold enhancement of the full dispersive result with respect to $f_1(s) = a\,\Omega(s)$. Due to the strong rise of the full solution for $f_1(s)$ towards this threshold, see Fig. 4.13, the corresponding $F_{\phi\pi^0}(s)$ almost approaches a cusp-like behavior at $s = 4M_\pi^2$. Since the ϕ as opposed to the ω transition form factor encompasses the ρ resonance region, we can also observe that the full solution for $f_1(s)$ slightly reduces the height of the resonance peak with respect to the simplified assumption

[#3] The normalization of the VMD prediction is obtained from the experimental $\omega \to \pi^0\gamma$ partial width, similar to the dispersive calculation. We refrain from displaying errors on the VMD calculation thus induced, since it merely serves illustrative purposes.

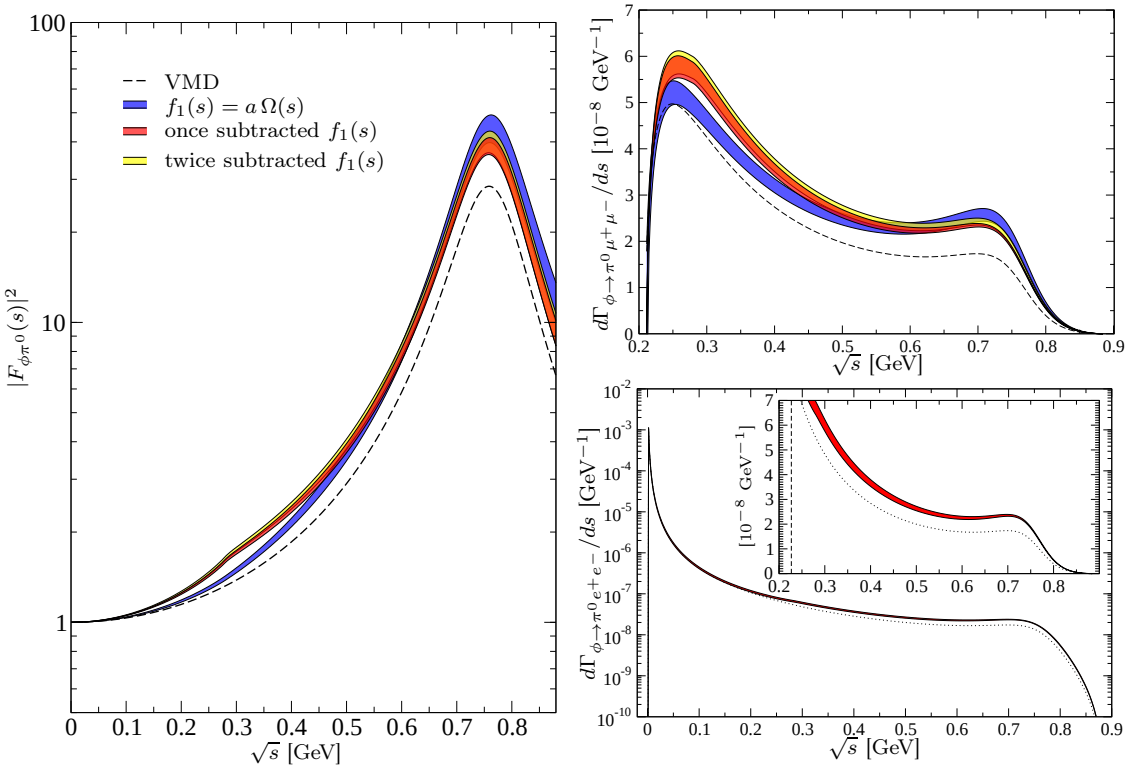

Figure 5.4: Left panel: numerical results for the $\phi \to \pi^0\gamma^*$ transition form factor. Top, right panel: differential $\phi \to \pi^0\mu^+\mu^-$ decay width. Bottom, right panel: differential $\phi \to \pi^0 e^+e^-$ decay width. We show pure VMD (dashed curve), the dispersive solution for $f_1(s) = a\,\Omega(s)$ (blue shaded curve), and the full dispersive solution with one subtraction (red shaded curve) and two subtractions (yellow shaded curve) in the $\phi \to 3\pi$ partial wave. For $\phi \to \pi^0 e^+e^-$ we only show the once-subtracted dispersive solution, since again neither the Omnès solution nor the twice-subtracted one is visibly distinguishable from the once-subtracted result on the scale shown. The inset magnifies the region above the two-muon threshold (vertical dashed line).

$f_1(s) = a\,\Omega(s)$, which agrees with our observations in Section 4.4. We note that using a twice-subtracted dispersion relation for the partial-wave amplitude $f_1(s)$, with the additional subtraction constant fitted to the $\phi \to 3\pi$ Dalitz plot of Ref. [169], does not change our results by all that much: the differences are smaller than the overall uncertainty in our transition-form-factor prediction. This corroborates our skepticism that an imperfect determination of the $\omega \to 3\pi$ P wave is the likely source of the discrepancy seen in the ω transition-form-factor data.

Again, we also quote the derivative of the form factor at $s = 0$:

$$b_{\phi\pi^0} = (1.52 \ldots 1.61)\, M_\rho^{-2} \,, \tag{5.26}$$

which is still somewhat larger than $b_{\omega\pi^0}$, see Eq. (5.23), but again not nearly as large as the slopes found experimentally in other vector-meson conversion decays.

The observations above concerning the differences of the various theoretical predictions translate directly to the $\phi \to \pi^0\mu^+\mu^-$ differential decay spectrum (top, right panel of Fig. 5.4). We find that the ρ resonance leaves a clear imprint on the spectrum, as one observes a second

peak structure that counterbalances the drop-off of the phase-space factor. The integrated spectrum yields

$$\begin{aligned} \mathcal{B}^{\text{once}}(\phi \to \pi^0 \mu^+ \mu^-) &= (3.7 \ldots 4.0) \times 10^{-6} \,, \\ \mathcal{B}^{\text{twice}}(\phi \to \pi^0 \mu^+ \mu^-) &= (3.8 \ldots 4.1) \times 10^{-6} \,, \end{aligned} \tag{5.27}$$

for the once- and twice-subtracted $\phi \to 3\pi$ partial-wave amplitudes, respectively, perfectly compatible within the error ranges. There is currently no experimental measurement of the partial width to be compared with.

As for the corresponding ω decay, the differential $\phi \to \pi^0 e^+ e^-$ decay width is enhanced for small s by several orders of magnitude; for this reason, we only display the full dispersive solution based on the once-subtracted $\phi \to 3\pi$ partial wave $f_1(s)$, the alternatives being indistinguishable on this scale. Again, an insert concentrates on energies above the two-muon threshold for better comparison of the expected event rates in both final states. The results for the integrated spectra are

$$\begin{aligned} \mathcal{B}^{\text{once}}(\phi \to \pi^0 e^+ e^-) &= (1.39 \ldots 1.51) \times 10^{-5} \,, \\ \mathcal{B}^{\text{twice}}(\phi \to \pi^0 e^+ e^-) &= (1.40 \ldots 1.53) \times 10^{-5} \,, \end{aligned} \tag{5.28}$$

for both of the full solutions, respectively. Compared with the experimental value of $\mathcal{B}^{\text{exp}}(\phi \to \pi^0 e^+ e^-) = (1.12 \pm 0.28) \times 10^{-5}$ [87], we find agreement within uncertainties.

We wish to emphasize the significance of an experimental investigation of the $\phi \to \pi^0 \gamma^*$ transition form factor. Deviations from the VMD picture now seem to be well-established in $\omega \to \pi^0 \gamma^*$; strikingly enough, both this and the latest measurement of the transition form factor in $\phi \to \eta \gamma^*$ [192], when parametrized in terms of a monopole form factor, yield monopole mass parameters significantly below the scale of the physical vector mesons, but (of course) too large to be accessible within the physical decay region. This is different in $\phi \to \pi^0 \gamma^*$: the ρ resonance can be measured in this decay; if there systematically is a steep form factor rise as seen in $\omega \to \pi^0 \gamma^*$, mapping it out in full in $\phi \to \pi^0 \gamma^*$ will help clarify its origin. From the theoretical side, our dispersive analysis for this process is based on a very precisely measured $\phi \to 3\pi$ Dalitz plot, such that we are very confident about the reliability of our prediction. We thus strongly advocate an experimental analysis of the $\phi \to \pi^0 \gamma^*$ form factor to the best possible precision.

As a final illustration, we show the (experimentally unobservable) phases of the $V \to \pi^0 \gamma^*$ transition form factors, both for ω and ϕ, in Fig. 5.5. We calculate these from the *unsubtracted* solution to the discontinuity equation (5.16), as we can only fix the modulus of the subtraction constant $f_{V\pi^0}(0)$ by means of the $V \to \pi^0 \gamma$ partial width, not its phase, which is non-vanishing due to the complex discontinuity of the $V \to 3\pi$ partial-wave amplitude $f_1(s)$. Only the phases of the full dispersive calculations, as compared to the $\pi\pi$ P-wave phase shift, are displayed. We refrain from showing the (small) error bands and fix the input in complete analogy to Fig. 4.13. An additional consequence of the complex discontinuity of the $V \to 3\pi$ partial-wave amplitude is that Watson's final-state theorem also does not apply to the transition form factors, and their phases are *different* from $\delta(s)$: three-pion-cut effects, see Fig. 5.6, produce non-vanishing imaginary parts/non-vanishing phases of the transition form factors also below the $\pi\pi$ threshold, $s < 4M_\pi^2$. We observe the transition-form-factor phases to be significantly larger than $\delta(s)$ above the two-pion threshold, and a tendency to small negative values below.

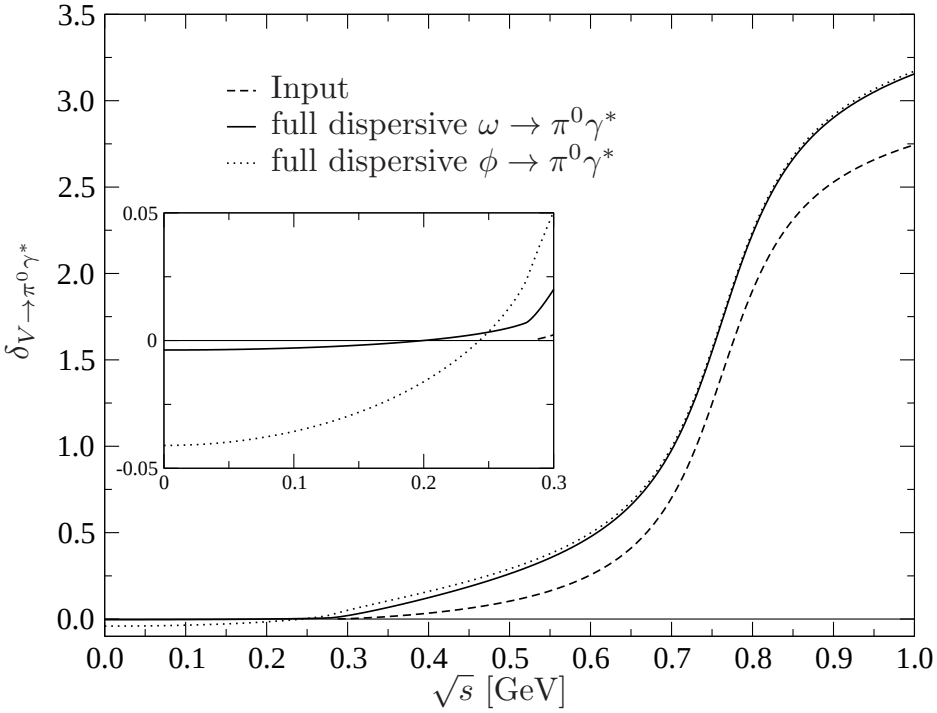

Figure 5.5: Phase of the electromagnetic transition form factor for $\omega \to \pi^0\gamma^*$ (solid curve) and $\phi \to \pi^0\gamma^*$ (dotted curve) together with the input phase-shift parameterization (dashed curve). The inset shows a magnification of the region below the two-pion threshold.

5.4.3 The $\omega \to \pi^0\gamma^*$ transition form factor beyond the $\omega\pi$ threshold

In this section we have a quick glance at the transition form factor beyond the $\omega\pi$ scattering threshold. This analysis should be taken with a grain of salt, however: to perform a fully consistent analysis of $e^+e^- \to \omega\pi^0$ one would have to solve a coupled-channel problem that also incorporates $\omega\pi \to \omega\pi$ scattering. Since there is currently no analysis, let alone data, available for this channel to perform such a treatment, we just display the analytic continuation of the form factor through the ρ resonance to the $\omega\pi$ production region in Fig. 5.7. We have only taken cross section data from Ref. [195] into account. Note that the cross section displayed there is actually $e^+e^- \to \omega\pi^0 \to \pi^0\pi^0\gamma$, so that in order to extract the transition form factor

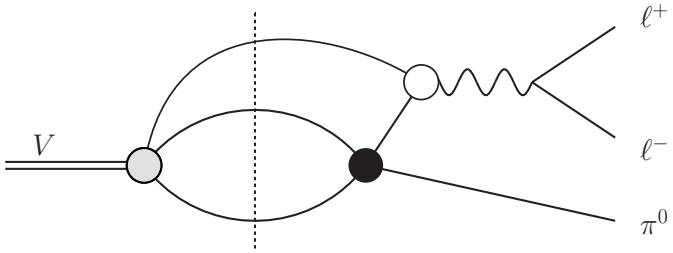

Figure 5.6: Three-pion-cut contribution to the $V \to \pi^0\ell^+\ell^-$ transition vector form factor, inducing an imaginary part also for $s < 4M_\pi^2$.

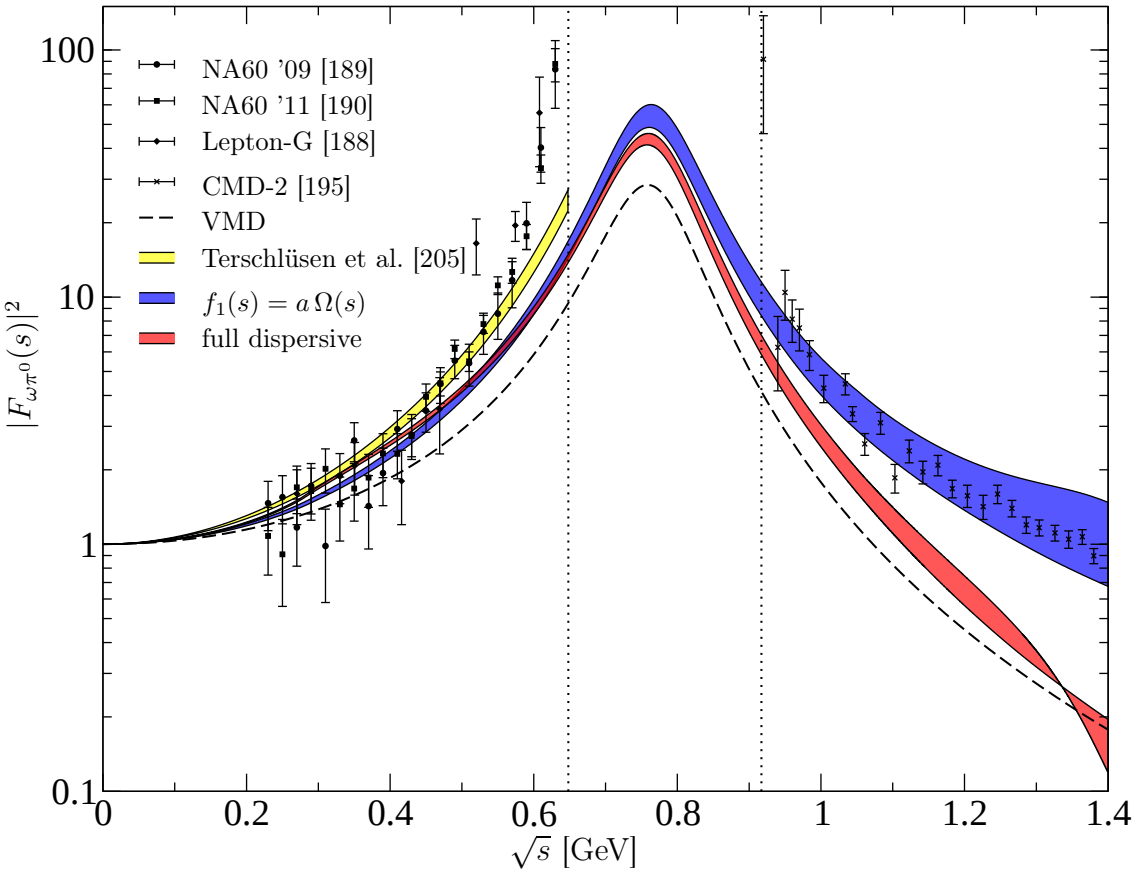

Figure 5.7: The transition form factor beyond the $\omega\pi$ threshold. We show pure VMD (dashed curve), the dispersive solution for $f_1(s) = a\,\Omega(s)$ (blue shaded curve), and the full dispersive solution with one subtraction (red shaded curve). The solution by Terschlüsen *et al.* (yellow shaded curve) cannot by continued beyond the decay region, since the transition form factor has the wrong higher-energy behavior: it tends to a constant instead of falling off. We only compare to data from Ref. [195] above $\sqrt{s} = M_\omega + M_\pi$.

we have to modify the data points according to [178]

$$|f_{\omega\pi^0}(s)|^2 = \frac{3s^{3/2}}{4\pi\alpha^2 q^3_{\omega\pi^0}(s)} \frac{\sigma_{e^+e^-\to\omega\pi^0\to\pi^0\pi^0\gamma}(s)}{\mathcal{B}(\omega\to\pi^0\gamma)} \,, \tag{5.29}$$

where the $\omega \to \pi^0\gamma$ branching ratio is given as $\mathcal{B}(\omega \to \pi^0\gamma) = 8.28 \pm 0.28\%$ [87]. To obtain normalized form factor data we divide by $f_{\omega\pi^0}(0)$ as it is determined from the dispersive analysis. Note that Eq. (5.29) is an approximation that breaks down close to threshold. The first data point just above the $\omega\pi$ threshold should thus not be taken too seriously.

We observe that the transition form factor calculated by a full dispersive analysis is significantly lower than the data points, especially at higher energies. The pure Omnès solution on the other hand reproduces the data points reasonably well. We reiterate that we have not solved a coupled-channel problem for the full dispersive analysis. It is not unreasonable to assume that this could in principle account for the deviations. Also the effects of inelasticities are stronger at higher energies. Fig. 5.7 allows for another interesting observation: in order to

accommodate the data points below $\sqrt{s} = M_\omega - M_\pi$ and above $\sqrt{s} = M_\omega + M_\pi$ the transition form factor has to drop off very steeply after crossing the ρ peak. This can certainly not by explained by a simple resonance or pole structure.

5.5 Summary

In this Chapter, we have analyzed the $\omega/\phi \to \pi^0\gamma^*$ electromagnetic transition form factors by means of a dispersive analysis. It requires the corresponding P-wave projection of the $\omega/\phi \to \pi^+\pi^-\pi^0$ decay amplitudes, and the pion vector form factor as input, both of which depend on the pion–pion P-wave scattering phase shift as input and are otherwise predictions up to a subtraction constant determining the overall normalization of the $\omega/\phi \to 3\pi$ amplitudes. The consistent treatment of crossed-channel effects in the $\omega/\phi \to 3\pi$ partial-wave amplitudes, incorporating three-particle cuts, leads to a non-trivial analytic structure for the transition form factors, in particular its phase does not follow the $\pi\pi$ P-wave phase.

We have calculated the real-photon $\omega/\phi \to \pi^0\gamma$ branching ratios using a sum rule, which yields good agreement with the experimental $\phi \to \pi^0\gamma$ branching ratio and indicates that the sum rule for $\omega \to \pi^0\gamma$ (which is much more precisely determined experimentally) is saturated roughly at the 90%–95% level by two-pion intermediate states. To lessen the dependence on medium-to-high-energy input, we have oversubtracted the dispersion relation for the form factors and used the real-photon partial widths as input for the subtraction constant. We found that this approach leads to an enhancement compared to a pure VMD calculation and thus to an improved description of experimental data from NA60 for the $\omega \to \pi^0\mu^+\mu^-$ channel. Three-pion effects in particular lead to an enhancement in the two-pion-threshold region.

We are unable to solve the puzzle of the steep rise in the $\omega \to \pi^0\gamma^*$ transition form factor data close to the end of the decay region. In order to try to better understand the physical mechanism behind this enhancement, we strongly advocate a measurement of the $\phi \to \pi^0\gamma^*$ transition form factor: the fact that the physical region of the decay goes beyond that of the corresponding ω decay and incorporates the ρ resonance peak suggests that it should give some clues about the nature of this rise.

While our predictions for branching ratios of the various $V \to \pi^0\ell^+\ell^-$ channels are in good agreement with experimental determinations, data on decay spectra only exists for $\omega \to \pi^0\mu^+\mu^-$. It would certainly be helpful, especially in light of a theoretical analysis of contributions to light-by-light scattering, if precision data for additional channels could be obtained [208].

Chapter 6

Summary and Outlook

In this thesis we have studied two methods to perform precision analysis of hadronic three-body decays and transition form factors: a perturbative modified non-relativistic effective field theory and non-perturbative dispersion relations. Applying the non-relativistic effective field theory to the decay $\eta \to 3\pi$ proved to be very successful: on the one hand we were able to predict a slope parameter of the $\eta \to 3\pi^0$ Dalitz plot that is fairly close to the experimental value, on the other hand, and perhaps more importantly, we could analyze and explain why Chiral Perturbation Theory, which has been successfully applied in other low-energy hadronic processes – especially in the SU(2) sector –, falls short to accommodate the correct value. We have shown that it is not a failure of Chiral Perturbation Theory itself, but rather that the expansion in terms of small momenta *and* the pion mass is disadvantageous.

The path to success as far as this analysis is concerned was to exploit the synergies between Chiral Perturbation Theory, a non-perturbative determination of the scattering threshold parameters, and the modified non-relativistic effective field theory: Chiral Perturbation Theory is used on the one hand to fix the low-energy constants of the non-relativistic theory and on the other hand it helps to constrain the scattering parameters extracted for a non-perturbative Roy equation analysis. While the former has still room for improvement (by matching, for example to higher orders in the chiral expansion), the latter has already lead to an unprecedented precision in the scattering parameters (see Refs. [38,41]), from which the non-relativistic effective field theory undoubtedly draws great profits.

It has become unequivocally clear in our study of $\eta' \to \eta\pi\pi$ that a similar level of understanding of the interplay between a low-energy effective field theory, in this case Chiral Perturbation Theory at large-N_C, and dispersion relations of hadronic three-body decays has to be the ultimate goal. Even in $\eta \to 3\pi$, where the picture should be much clearer since no complications due to the heavy η' arise, there are still difficulties to understand the precise connection between the two theories [76,77,103]. We have shown that a perfect representation of the data samples can be obtained by fitting the subtraction constants, however, since the Dalitz plot is more or less flat across the physical region this representation does not really allow for conclusive insights as to the theory and the nature of the final-state interactions: information on $\pi\eta$ scattering is completely absorbed in a redefinition of the subtraction polynomial. One thus has to arrive at the rather unsatisfactory conclusion that $\eta' \to \eta\pi\pi$ is not an ideal testing ground for a dispersive analysis.

The picture cleared up substantially in our analysis of $\omega/\phi \to 3\pi$, not least due to the fact that the dispersive representation converges without any subtractions. Comparing with a very

precise measurement of $\phi \to 3\pi$ by the KLOE collaboration, we found that data is reproduced reasonably well. Oversubtracting the dispersion relations and fitting the additional subtraction constant we found a perfect representation of the data. This is reassuring considering that the Dalitz plot cannot be parametrized by a polynomial due to the non-trivial band structures induced by the ρ resonance. It remains to test the theory against experimental data on $\omega \to 3\pi$ that will hopefully become available in the near future.

The analysis of $\phi \to 3\pi$ has highlighted dispersion theory as a strong tool to analyze hadronic three-body decays of heavier mesons, which exceed the applicability range of established low-energy effective field theories. Especially with the investigation of CP violation in hadronic decays of D and B mesons in mind dispersive analyses may be exploited to their full potential. The general idea behind these studies is that in many cases the branching fractions are significantly larger than for the CP violating two-hadron decays. Additionally, the Dalitz plot is strongly perturbed by resonances, which are believed to enhance small CP phases [209,210]. First evidence from B factories points to the complex phase in the Cabibbo-Kobayashi-Maskawa matrix [211, 212] as the dominant source of CP violation. In order to extract other (smaller) sources of CP violation that are triggered by physics beyond the Standard Model extremely accurate measurements and precision analysis tools are essential. It has been indicated [209,210,213] that a theory-guided analysis of experimental data leads to a more precise extraction of the CP-violating phase than brute-force subtraction of Dalitz plot bins as suggested in Refs. [214–217]. A concerted effort to improve the understanding of these processes from a theoretical and experimental point of view is part of the informal *Les Nabis* network [218].

Needless to say that dispersion relations are a prime candidate for such analyses. However, many obstacles have to be overcome before precision extractions can be realized: inelastic channels, higher resonances, coupling of decay channels, and so forth are expected to play a more crucial role due to the large available phase space and a plethora of allowed decay modes. On the bright side the Dalitz plot of these processes is significantly more structured by resonance bands, thus allowing one to test the dispersive amplitudes more rigorously. A dispersive analysis of $D^+ \to K^-\pi^+\pi^+$ that may serve as a stepping stone towards the investigation of CP-violating decay processes is currently a work in progress [210, 219].

Finally, we have extended our framework to perform a dispersion-theory analysis of the transition form factor $\omega/\phi \to \pi^0\gamma^*$. The partial-wave amplitude of $\omega/\phi \to 3\pi$ and the pion vector form factor served as an input. The integral equation of the transition form factor only contained one subtraction constant, which we fixed by matching to the $\omega/\phi \to \pi^0\gamma$ decay width. Comparing to $\omega \to \pi^0\gamma^*$ data we found significant deviations towards the end of the physical region. Aside from fundamental concepts of unitarity and analyticity the only approximation made in our analysis is the suppression of inelastic channels, which we proved to be decent by calculating the $\omega \to \pi^0\gamma$ partial width via a sum rule. The transition form factor is thus completely determined by the scattering phase shift of the isospin-1 $\pi\pi$ partial-wave and the experimental value of the real-photon partial width, which is why the strong deviations that we found in our analysis are rather puzzling. We put forth the argument that a measurement of the corresponding $\phi \to \pi^0\gamma^*$ transition form factor may shed some light on the disagreement between theory and data.

It is blatantly obvious, however, that the puzzle must be solved, especially if one endeavors to perform a dispersive analysis of the doubly-virtual form factor of $\pi^0 \to \gamma^*\gamma^*$, which is instrumental to unlocking the light-by-light contribution to the $(g-2)_\mu$. The next step that has to be taken in that regard is to connect different physical regions by performing an

analytic continuation in the vector meson mass. A full analysis of $e^+e^- \to \pi^0\gamma^*$ is not easily performed, since it necessitates input of $e^+e^- \to 3\pi$ partial waves. These cannot be predicted in our framework thus far: note that we had to fix the subtraction constant to the $\omega/\phi \to 3\pi$ partial widths.

The last example is yet another indicator that a lot of progress has to be made to improve our understanding of the strong interactions at low energies. Experiments are pushing the frontier of precision physics in a quest to unlock the intricacies of the force that constitutes matter. Similarly, new analysis tools as they have been presented in this thesis must be developed and improved to keep up with the progress on the theoretical side. After all, only an intimate interplay of theory and experiment will eventually lead one to the promised land.

Appendix

Appendix A

Perturbative methods: Non-relativistic effective field theory

A.1 Loop calculations and analytic structure of NREFT diagrams

In this Appendix we outline to some extent the methods that go along with loop calculations in the non-relativistic effective field theory and the analytic structure that these ensue. We shall start with a look at one-loop diagrams, before taking on the more complicated non-trivial two-loop diagrams. The discussion of these structures can also be found in Refs. [33, 115]

A.1.1 One-loop diagrams

We start out our discussion by considering a diagram of the type shown in Fig. A.1. Incidentally, the precise diagram shown there produces the cusp effect at the charged pion threshold in the invariant $\pi^0\pi^0$-spectrum of the neutral decay channel. It has been used to extract $\pi\pi$ scattering lengths with great precision, see Refs. [25, 26, 33]. We will, however, discuss the integral on more general terms with loop masses $M_{a/b}$, and masses $M_{c/d}$ of the resulting pion pair. Under these circumstances the integral can be written as

$$J_{ab}(s) = \int \frac{d^D l}{(2\pi)^D i} S_a(\mathbf{l}) S_b(\mathbf{P}-\mathbf{l}) \ , \tag{A.1}$$

where

$$S_a(\mathbf{p}) := \frac{1}{2w_a(\mathbf{p})(w_a(\mathbf{p}) - p_0 - i\epsilon)} \tag{A.2}$$

is the momentum space propagator of the particle in the modified non-relativistic framework, and $\mathbf{P} = \mathbf{p}_1 + \mathbf{p}_2$. After performing the integration over l^0 by closing the integration contour in the lower half of the complex l^0-plane we arrive at

$$J_{ab}(s) = \int \frac{d^d l}{(2\pi)^d} \frac{1}{2w_a(\mathbf{l}) 2w_b(\mathbf{P}-\mathbf{l})} \frac{1}{(w_a(\mathbf{l}) + w_b(\mathbf{P}-\mathbf{l}) - P^0 - i\epsilon)} \ , \tag{A.3}$$

where $d = D - 1$. One can show algebraically that

$$\frac{1}{4w_a w_b} \frac{1}{(w_a + w_b - P^0 - i\epsilon)} = \frac{1}{2P^0} \frac{1}{\mathbf{q}^2 - (\mathbf{qP}/P^0)^2 - q_{ab}^2(s) - i\epsilon} \tag{A.4}$$

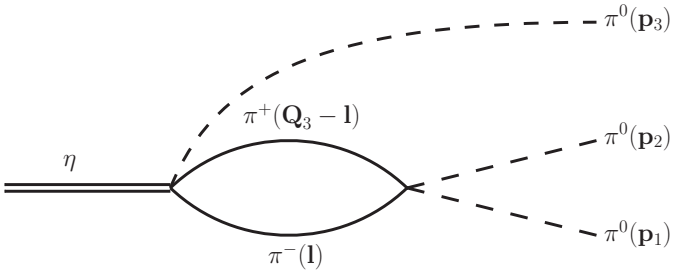

Figure A.1: One-loop diagram with $\pi^+\pi^- \to \pi^0\pi^0$ final-state interaction. The double line denotes the η, single full lines represent charged pions $\pi^\pm$, while dashed lines denote neutral pions π^0

$$+\frac{1}{4w_aw_b}\Big\{\frac{1}{P^0+w_a+w_b}-\frac{1}{P^0+w_a-w_b}-\frac{1}{P^0-w_a+w_b}\Big\}\ ,$$

where $\mathbf{q}=\mathbf{l}-\frac{1}{2}(1+\delta_{ab})\mathbf{P}$ and $\delta_{ab}=-\frac{\Delta_{ab}}{s}$. The final three terms are regular at threshold. If one performs an expansion in small momenta one arrives at so-called "no-scale integrals"

$$\sum_n A_n\int\frac{d^dl}{(2\pi)^d}l^{2(n+\alpha)}=0\ , \tag{A.5}$$

where A_n is some prefactor independent of the integration momenta and α is an arbitrary real number. One can show that the contribution of these integrals vanishes in dimensional regularization [220].

Upon performing a transformation of the integration variable

$$\mathbf{l}\to\mathbf{l}+\left(\frac{\mathbf{lP}}{\mathbf{P}^2}\Big(\frac{P^0}{\sqrt{s}}-1\Big)+\frac{1+\delta_{ab}}{2}\right)\mathbf{P}\ ,$$

we obtain

$$J_{ab}(s)=\frac{1}{2\sqrt{s}}\int\frac{d^dl}{(2\pi)^d}\frac{1}{\mathbf{l}^2-q_{ab}^2(s)-i\epsilon}\ , \tag{A.6}$$

where $q_{ab}^2(s)=\frac{\lambda(s,M_a^2,M_b^2)}{4s}$ is the center-of-mass three-momentum. The above is a standard loop integral in dimensional regularization and can be calculated explicitly in terms of the Gamma function,

$$J_{ab}(s)=\frac{\Gamma(1-d/2)}{(4\pi)^{d/2}}\frac{(-q_{ab}^2(s)-i\epsilon)^{d/2-1}}{2\sqrt{s}}\ . \tag{A.7}$$

Since dimensional regularization does not keep track of linear divergences, we can directly perform the limit $d\to 3$ and arrive at the *finite* result

$$J_{ab}(s)=\frac{iq_{ab}(s)}{8\pi\sqrt{s}}\ . \tag{A.8}$$

Returning to the special case of Fig. A.1 we have

$$J_{+-}(s_3)=\frac{iq_{+-}(s_3)}{8\pi\sqrt{s_3}}=\frac{i}{16\pi}\sqrt{1-\frac{4M_\pi^2}{s_3}}\ . \tag{A.9}$$

It is immediately clear that this loop function contributes to a cusp effect in the decay spectrum: the charged pion threshold lies in the physical decay region of $\eta \to 3\pi^0$ (see also Fig. 2.1) and perturbs the full spectrum by interference of real and imaginary part.

Derivative couplings

Derivative couplings in higher-order calculations play a very important role in analyzing rescattering. We will briefly outline the general technique for the effective range couplings, which hints at how these integrals can be solved also for other cases. A more detailed discussion can be found in Ref. [115]. Let us consider the integral

$$\begin{aligned}\mathcal{J}(s) = &\int \frac{d^D l}{(2\pi)^D i} S_a(\mathbf{l}) S_b(\mathbf{P}-\mathbf{l}) \\ &\times \Big(w_c(\mathbf{p}_m) w_d(\mathbf{p}_n) - \mathbf{p}_m \mathbf{p}_n + w_a(\mathbf{l}) w_b(\mathbf{P}-\mathbf{l}) - \mathbf{l}(\mathbf{P}-\mathbf{l}) - h_i \Big) \ ,\end{aligned} \tag{A.10}$$

where $M_{a/b}$ are the masses of the pions in the loop and $M_{c/d}$ are the respective final-state pions. Again we start off by performing the integration over l^0, so that the propagator piece reduces to (A.3). We can add a term $-\frac{1}{2}(w_a(\mathbf{l}) + w_b(\mathbf{P}-\mathbf{l}) - P^0)(w_a(\mathbf{l}) + w_b(\mathbf{P}-\mathbf{l}) + P^0)$ inside the brackets, since it cancels the non-regular piece of the denominator, so that what is left amounts to no-scale integrals in dimensional regularization. Using the simple algebraic relation

$$\begin{aligned}w_a(\mathbf{l}) w_b(\mathbf{P}-\mathbf{l}) - \mathbf{l}(\mathbf{P}-\mathbf{l}) - \frac{1}{2}(w_a(\mathbf{l}) + w_b(\mathbf{P}-\mathbf{l}) - P^0)(w_a(\mathbf{l}) + w_b(\mathbf{P}-\mathbf{l}) + P^0) \\ = \frac{1}{2}(P^2 - M_a^2 - M_b^2) \ ,\end{aligned}$$

along with

$$w_c(\mathbf{p}_m) w_d(\mathbf{p}_n) - \mathbf{p}_m \mathbf{p}_n = \frac{1}{2}(P^2 - M_c^2 - M_d^2) \ , \tag{A.11}$$

where $P^2 = (P^0)^2 - \mathbf{P}^2$. We finally arrive at

$$\mathcal{J}(s) = (s - s_i^{\text{thr}}) J_{ab}(s) \ , \tag{A.12}$$

where we have used $P^2 = s$. This is certainly the result one would have expected from momentum conservation at the vertex.

A.1.2 Two-loop diagrams

In this section we will discuss the relevant two-loop diagrams present in the non-relativistic theory, see Fig. A.2. In principle there is also a contribution by the so-called sunset graph that has a six-particle vertex. The contribution of this diagram that renormalizes the imaginary part of the low-energy tree-level coupling for six-particle exchange is sufficiently small, see the discussion in Ref. [33] and Appendix A.4. Additionally, we will entirely focus this discussion on the non-trivial two-loop diagram, Fig. A.2B, since the two-loop bubble diagram is merely proportional to a product of two one-loop diagrams,

$$\mathcal{M}^A(s) \propto J_{ab}(s) J_{cd}(s) \ . \tag{A.13}$$

The second diagram provides a much bigger challenge. We will begin by deriving an integral representation of the diagram and discuss the ensuing analytic properties before performing the non-relativistic expansion of the loop function to arrive at an analytic representation. Finally we give a brief glimpse on how to incorporate derivative couplings.

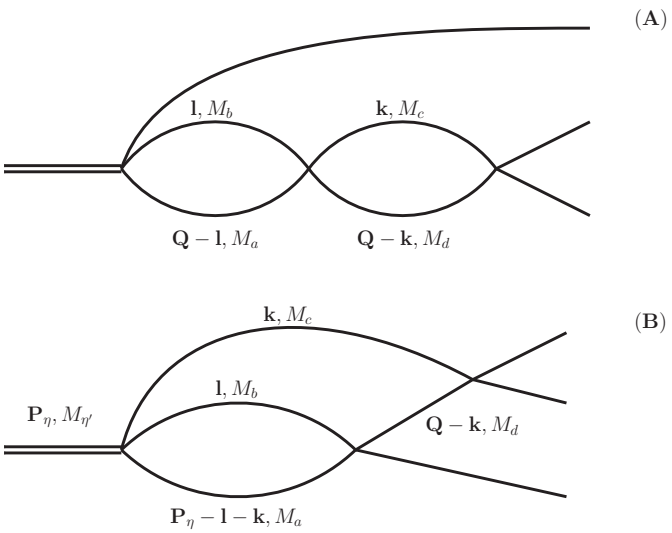

Figure A.2: The two distinct graphs at two-loop level.

Integral representation

Let us start off by noting that the diagram is given in terms of the propagators as

$$\mathcal{M}_F(s) = \int \frac{d^D l}{(2\pi)^D i} \frac{d^D k}{(2\pi)^D i} S_a(\mathbf{P}_\eta - \mathbf{k} - \mathbf{l}) S_b(\mathbf{l}) S_c(\mathbf{k}) S_d(\mathbf{Q} - \mathbf{k}) \ , \tag{A.14}$$

which upon performing the integration over l^0 and k^0 as before turns into

$$\mathcal{M}_F(s) = \int \frac{d^d k}{(2\pi)^d} \frac{1}{2w_c(\mathbf{k}) 2w_d(\mathbf{Q} - \mathbf{k})} \frac{J_{ab}(M_\eta - w_c(\mathbf{k}), -\mathbf{k})}{w_c(\mathbf{k}) + w_d(\mathbf{Q} - \mathbf{k}) - Q^0 - i\epsilon} \ , \tag{A.15}$$

where

$$J_{ab}(L_0, \mathbf{L}) = \int \frac{d^d l}{(2\pi)^d} \frac{1}{2w_a(\mathbf{L} - \mathbf{l}) 2w_b(\mathbf{l})} \frac{1}{w_a(\mathbf{L} - \mathbf{l}) + w_b(\mathbf{l}) - L^0 - i\epsilon} \ , \tag{A.16}$$

is the "inner one-loop diagram" and we have used $L^0 = M_\eta - w_c(\mathbf{k})$ and $\mathbf{L} = -\mathbf{k}$. Proceeding in an analogous fashion to Section A.1.1 we find

$$\begin{aligned} J_{ab}(s) &= \frac{1}{2\sqrt{s}} \int \frac{d^d l}{(2\pi)^d} \frac{1}{\mathbf{l}^2 - A(\Delta^2 - \mathbf{k}^2) - i\epsilon} \\ &= \frac{1}{2\sqrt{s}} \int \frac{d^d l}{(2\pi)^d} \frac{A^{d/2-1}}{\mathbf{l}^2 + \mathbf{k}^2 - \Delta^2 - i\epsilon} \ , \end{aligned} \tag{A.17}$$

where $s = M_\eta^2 + M_c^2 - 2M_\eta w_c(\mathbf{k})$, $\Delta^2 = \lambda(M_\eta^2, M_c^2, (M_a + M_b)^2)/4M_\eta^2$ and

$$A = \frac{M_\eta^2}{2(M_\eta^2 + M_c^2) - (M_a + M_b)^2 - s} \Big(1 - \frac{(M_a - M_b)^2}{s}\Big) \ , \tag{A.18}$$

and in the second line we rescaled $\mathbf{l} \to (A)^{1/2}\mathbf{l}$. Next, we perform the expansion of the outer loop in a similar fashion to Eq. (A.4). As opposed to our discussion in the previous section

the integration over the last three term does not vanish right away, since the inner loop has a singularity in $\mathbf{k}^2$. Nevertheless we can perform an expansion of all terms except the singular piece $(\mathbf{k}^2+\mathbf{l}^2-\Delta^2-i\epsilon)^{-1}$ about threshold and subsequently integrate the remainder. The result will be a function of the form $P(s)=\tilde{P}(s)(-\Delta^2-i\epsilon)$, where $\tilde{P}(s)$ is a polynomial in s with real coefficients. The real part of $P(s)$, which is ultraviolet divergent at $d=3$, can be absorbed in a redefinition of the low-energy couplings L_i, K_i. The imaginary part on the other hand is finite at $d=3$ and it can furthermore be shown that it does not contribute at the accuracy of our representation: the imaginary part of $P(s)$ starts to perturb the spectrum at $\mathcal{O}(a^3)$. Thus in the following we will simply disregard these contributions. Consequently, we find

$$\mathcal{M}_F(s)=\frac{1}{2Q^0}\int\frac{d^dk}{(2\pi)^d}\frac{d^dl}{(2\pi)^d}\frac{A^{d/2-1}}{2\sqrt{s}}\frac{1}{\mathbf{p}^2-(\mathbf{pQ}/Q^0)^2-q_{cd}^2(s)-i\epsilon}\frac{1}{\mathbf{l}^2+\mathbf{k}^2-\Delta^2-i\epsilon}\,, \tag{A.19}$$

where $\mathbf{p}=\mathbf{k}-\frac{1}{2}(1+\delta_{cd})\mathbf{Q}$ and $\delta_{cd}=\frac{M_c^2-M_d^2}{s}$. We perform a change of the integration variable according to

$$\mathbf{k}\to\mathbf{k}+\left(\frac{\mathbf{kQ}}{\mathbf{Q}^2}\left(\frac{Q^0}{\sqrt{s}}-1\right)+\frac{1+\delta_{cd}}{2}\right)\mathbf{Q}\,, \tag{A.20}$$

so that Eq. (A.19) reduces to

$$\mathcal{M}_F(s)=\frac{1}{2\sqrt{s}}\int\frac{d^dk}{(2\pi)^d}\frac{d^dl}{(2\pi)^d}\frac{1}{\mathbf{k}^2-q_{cd}^2(s)-i\epsilon}\frac{N(x)}{\mathbf{l}^2+\frac{(1+\delta_{cd})^2}{4}\mathbf{Q}^2+x-\Delta^2-i\epsilon}\,, \tag{A.21}$$

where we defined

$$\begin{aligned} x&=\mathbf{k}^2+\frac{(\mathbf{kQ})^2}{s}+\frac{\mathbf{kQ}}{\sqrt{s}}Q^0(1+\delta_{cd})\,, & N(x)&=\frac{A^{d/2-1}(s(x))}{2\sqrt{s(x)}}\,,\\ s(x)&=M_\eta^2+M_c^2-2M_\eta w_c(x)\,, & w_c(x)&=\left(M_c^2+\frac{(1+\delta_{cd})^2}{4}\mathbf{Q}^2+x\right)^{1/2}. \end{aligned} \tag{A.22}$$

The variable x is of $\mathcal{O}(\epsilon^2)$. For an explicit calculation one expands the numerator function $N(x)$ about $x=0$ and uses standard Feynman parameterization to combine the two denominators to obtain

$$\mathcal{M}_F(s)=\frac{1}{2\sqrt{s}}\sum_{n=0}^{\infty}\frac{1}{n!}\frac{d^n}{dx^n}N(x)\bigg|_{x=0}J_n(s)+\ldots \tag{A.23}$$

with

$$\begin{aligned} J_n(s)&=\int\frac{d^dkd^dl}{(2\pi)^{2d}}\int_0^1dy\frac{x^n}{\Big[(1-y)\big(\mathbf{k}^2-q_{cd}^2(s)\big)+y\big(\mathbf{l}^2+\frac{(1+\delta_{cd})^2}{4}\mathbf{Q}^2+x-\Delta^2\big)-i\epsilon\Big]^2}\\ &=\int_0^1dy\int\frac{d^2p}{(2\pi)^{2d}}\,y^{-d/2}\left(1+y\frac{\mathbf{Q}^2}{s}\right)^{1/2}\frac{f_d^{(n)}(y,\mathbf{k}^2)}{[\mathbf{p}^2+g(y,s)-i\epsilon]^2}\,, \end{aligned} \tag{A.24}$$

where $\mathbf{p^2}=\mathbf{l}^2+\mathbf{k}^2$. In the second line we rescaled $\mathbf{l}\to y^{-1/2}\mathbf{l}$ and used

$$\mathbf{k}\to\mathbf{k}-\left\{\frac{yQ^0}{2\sqrt{s}}\frac{1+\delta_{cd}}{1+y\frac{\mathbf{Q}^2}{s}}+\frac{\mathbf{kQ}}{\mathbf{Q}^2}\left(1+\left(1+y\frac{\mathbf{Q}^2}{s}\right)^{-1/2}\right)\right\}\mathbf{Q}\,, \tag{A.25}$$

so that we obtain

$$g(y,s) = -(1-y)q_{cd}^2(s) - y\Delta^2 + \frac{y}{4}\frac{(1-y)(1+\delta_{cd})^2\mathbf{Q}^2}{1+y\frac{\mathbf{Q}}{s}} \ . \tag{A.26}$$

The function $f_d^{(n)}(y,\mathbf{k}^2)$ denotes the appropriate rescaling of the term x^n. Performing the momentum integration we obtain

$$J_n(s) = \frac{\Gamma(2-d)}{(4\pi)^d}\int_0^1 dy\, y^{-d/2}\Big(1+y\frac{\mathbf{Q}^2}{s}\Big)^{-1/2} f_d^{(n)}(y,s)(g(y,s)-i\epsilon)^{d-2} \ , \tag{A.27}$$

where for the first orders in n we have

$$\begin{aligned}
f_d^{(0)}(y,s) &= 1 \ , \\
f_d^{(1)}(y,s) &= g(y,s)\frac{d}{2(1-d)}\Big(1+\frac{\mathbf{Q}^2\alpha}{ds}\Big) + \gamma \ , \\
f_d^{(2)}(y,s) &= -g^2(y,s)\frac{(2+d)}{4(1-d)}\Big(1+2\frac{\mathbf{Q}^2\alpha}{ds}+\frac{3\mathbf{Q}^4\alpha^2}{d(d+2)s^2}\Big) \\
&\quad + g(y,s)\frac{d}{2(1-d)}\Big(2\gamma+\frac{\mathbf{Q}^2(2\alpha\gamma+\beta^2 s)}{ds}\Big)+\gamma^2 \ ,
\end{aligned} \tag{A.28}$$

with

$$\begin{aligned}
\alpha &= \frac{1-y}{1+y\frac{\mathbf{Q}}{s}} \ , \qquad \beta = \frac{\alpha Q^0}{\sqrt{s}}(1+\delta_{cd})\frac{1}{\sqrt{1+\frac{y\mathbf{Q}^2}{s}}} \ , \\
\gamma &= -\frac{\mathbf{Q}^2(Q^0)^2}{2s}y(1+\delta_{cd})^2\frac{1-\frac{y}{2}\Big(1-\frac{\mathbf{Q}^2}{s}\Big)}{\Big(1+\frac{y\mathbf{Q}^2}{s}\Big)^2} \ .
\end{aligned} \tag{A.29}$$

The singularity at $y=0$ in Eq. (A.27) can be removed by a partial integration. The ensuing surface term is a polynomial in s and can be discarded. Performing the limit $d\to 3$ we arrive at the integral representation of the genuine two-loop function

$$F(M_a,M_b,M_c,M_d,s) = \frac{1}{256\pi^3\sqrt{s}}\int_0^1\frac{dy}{\sqrt{y}}\mathcal{F}(y,s)\big(\log g(y,s)-\log g(y,s^t)\big) \ , \tag{A.30}$$

where made use of the definitions

$$\begin{aligned}
\mathcal{F}(y,s) &= \sum_{n=0}^{\infty}\mathcal{F}_n(y,s) \ , \qquad \mathcal{F}_n(y,s) = \frac{4}{n!}\frac{d^n}{dx^n}N(x)\Big|_{x=0}\frac{d}{dy}\frac{g(y,s)f^n(y,s)}{\sqrt{1+\frac{y\mathbf{Q}^2}{s}}} = \mathcal{O}(\epsilon^{2n+2}) \ , \\
f^{(n)}(y,s) &= f_d^{(n)}(y,s)\Big|_{d=3} \ , \qquad s^t = (M_c+M_d)^2 \ .
\end{aligned} \tag{A.31}$$

Analytic properties of the integral representation

We want to briefly analyze the analytic properties of the integral representation, specifically the behavior of the discontinuity of the two-loop diagram at the pseudo-threshold. The latter

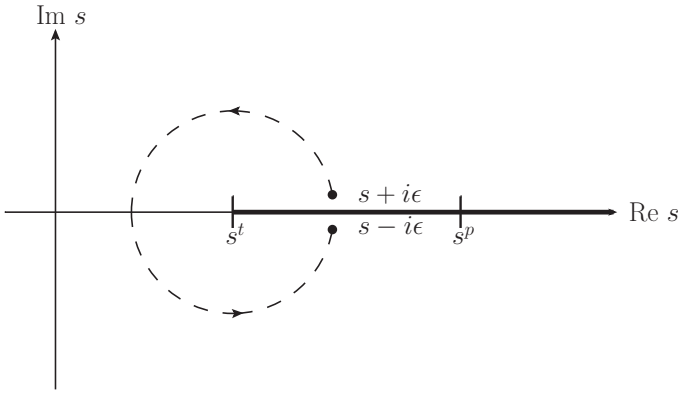

Figure A.3: Path of s in the analytic continuation given by Eq. (A.33). The function $F(s)$ is defined on the upper rim of the two-pion cut.

is a very interesting aspect of our analysis since it gives us some insights into the properties of the two-loop graph that are reoccurring in the dispersive analysis. The function $g(y,s)$ is of central importance when analyzing the analytic structure of $F(M_a,M_b,M_c,M_d,s)$: it is the argument of the logarithm and thus singularities of the two-loop functions show up precisely at the zeros in the low-energy region of $g(y,s)$. We can rearrange Eq. (A.26) so that

$$g(y,s)=\frac{A}{1+\frac{y\mathbf{Q}}{s}}(y-y_1(s))(y-y_2(s))\ , \tag{A.32}$$

where we defined

$$y_{1,2}(s)=\frac{-B\mp\sqrt{B^2-4AC}}{2A}\ ,$$
$$A=-\frac{\mathbf{Q}^2}{s}(M_c^2+\Delta^2)\ ,\qquad B=q_{cd}^2(s)-\Delta^2+\frac{\mathbf{Q}}{s}M_c^2\ ,\qquad C=-q_{cd}^2(s)\ .$$

In the following we consider the isospin symmetric case, $F(M_\pi,M_\pi,M_\pi,M_\pi,s)\doteq F(s)$, exclusively, since precisely this case is relevant for the dispersive analyses. The function F as given in the integral representation (A.30) is defined above the two-pion cut in the complex s-plane, that is for $s_+=s+i\epsilon$. To calculate the discontinuity of F, however, we need to have information about the amplitude at $s_-=s-i\epsilon$, so we have to find the *correct* prescription for the analytic continuation below the cut. To that end we parametrize s according to

$$s=s^t+(s-s^t)e^{i\varphi}\ ,\qquad 0<\varphi<2\pi\ , \tag{A.33}$$

where $s^t=4M_\pi^2$ is the two-pion threshold as before. In this prescription s_- and s_+ are the endpoints for $\varphi=0$ and $\varphi=2\pi$, respectively. The path in the complex plane for arbitrary s between s^t and s^p is visualized in Fig. A.3. This has direct consequences for the position of the zeros $y_1(s)$ and $y_2(s)$ as is shown in Fig. A.4: as long as s is below the pseudo-threshold s_p the trajectories of $y_{1/2}(s)$ follow ellipses in the complex y-plane starting with a small imaginary part for $s+i\epsilon$ and finishing just above the real axis for $s-i\epsilon$.

The trajectory of $y_1(s)$ is of particular interest in this case since it crosses the path of the integration in Eq. (A.30) and draws it along to the endpoint. This has to be taken into

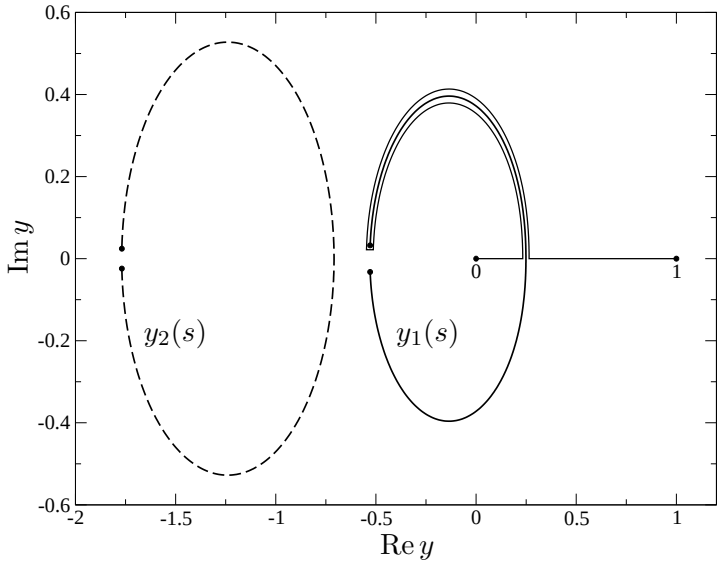

Figure A.4: Trajectories of $y_1(s)$ (solid curve) and $y_2(s)$ (dashed curve), when s is continued along a circle with parameterization, Eq. (A.33) in the complex s-plane.

account when calculating the discontinuity of the genuine two-loop function, as we shall see in the following. To ease up the discussion we will consider the following function,

$$H(s) = \int_0^1 \frac{dy}{\sqrt{y}} \Big[\frac{d}{dy}\bar{g}(y,s)\Big] \log \bar{g}(y,s) \ , \qquad \bar{g}(y,s) = (y - y_1(s))(y - y_2(s)) \ , \tag{A.34}$$

which has the same singularity structure as the two-loop function $F(s)$, but is more easily treatable. The discontinuity of $H(s)$ is given as

$$\operatorname{disc} H(s) = H(s + i\epsilon) - H(s - i\epsilon) \ . \tag{A.35}$$

$H(s-i\epsilon)$ can be calculated by deforming the integration path to $y = 0$, encircle the singularity $y_1(s - i\epsilon)$ and then back deform it back to $y = 0$. The integral piece from 0 to 1 cancels with the corresponding piece from $H(s + i\epsilon)$ and we are left with the remainder

$$\operatorname{disc} H(s) = 2\pi \int_0^{y_1(s)} \frac{dy}{\sqrt{-y}} \frac{d}{dy}\bar{g}(y,s) \ , \tag{A.36}$$

which is easily evaluated as

$$\operatorname{disc} H(s) = \frac{4\pi}{3}\sqrt{-y_1(s)}[y_1(s) + 3y_2(s)] \ . \tag{A.37}$$

This allows us to finally discuss the discontinuity at the pseudo-threshold, $s^p = (M_\eta - M_\pi)^2$. In this case we have $\lim_{s\to s^p} y_1(s) = -\infty$, while $y_2(s)$ stays finite. From Eq. (A.37) we thus find that the discontinuity diverges at the pseudothreshold. This phenomenon, that we also observe in the dispersive treatment of the decay, see Section 4.6, is thus explained by the singularity $y_1(s)$ hitting the integration paths and dragging it along to infinity.

Analytic representation

In the following we show how to arrive at an analytic representation for the two-loop diagrams. To simplify the discussion we constrict ourselves to the case $n = 0$. Note, however, that we have included contributions of $n = 1$ in Section A.3 as entailed by the accuracy we are trying to achieve with our representation. These extensions are fairly simple to include, but require some algebraic effort. Derivative couplings on the other hand merit some more discussion, and we will briefly comment on those after this section. We consider

$$\begin{aligned} F(M_a, M_b, M_c, M_d, s) &= \frac{1}{256\pi^3\sqrt{s}} \int_0^1 \frac{dy}{\sqrt{y}} \mathcal{F}_0(y,s) \log\Big(\frac{g(y,s)}{g(y,s^t)} - i\epsilon\Big) + \mathcal{O}(\epsilon^4) \ , \\ \mathcal{F}_0(y,s) &= \frac{1}{s_0} \frac{\lambda(s_0, M_a^2, M_b^2)}{\Delta^2 - \frac{\mathbf{Q}^2}{4}(1+\delta_{cd})^2} \frac{d}{dy} \frac{g(y,s)}{\sqrt{1 + \frac{y\mathbf{Q}^2}{s}}} \ , \\ s_0 &= M_\eta + M_c^2 - 2M_\eta \Big(M_c^2 + \frac{(1+\delta_{cd})^2}{4}\mathbf{Q}^2\Big)^{1/2} \ . \end{aligned} \tag{A.38}$$

Up-to-and-including $\mathcal{O}(\epsilon^2)$, we can rewrite Eq. (A.32) according to

$$g(y,s) = A(y - y_1)(y - y_2) + \mathcal{O}(\epsilon^4) \ , \tag{A.39}$$

where $y_{1/2}(s)$ are the zeros of $g(y,s)$ as defined before. This leads to

$$F(M_a, M_b, M_c, M_d, s) = \bar{\mathcal{N}} \int_0^1 \frac{dy}{\sqrt{y}} (2Ay + B) \log\Big(\frac{g(y,s)}{g(y,s^t)} - i\epsilon\Big) + \mathcal{O}(\epsilon^4) \ , \tag{A.40}$$

with

$$\bar{\mathcal{N}} = \frac{1}{256\pi^3\sqrt{s}} \frac{\lambda^{1/2}(s_0, M_a^2, M_b^2)}{s_0 \sqrt{\Delta^2 - \frac{(1+\delta)^2}{4}\mathbf{Q}^2}} \ . \tag{A.41}$$

Upon performing the integration we eventually arrive at

$$F_k(M_a, M_b, M_c, M_d, s) = \bar{\mathcal{N}}(2Af_1 + Bf_0) + \mathcal{O}(\epsilon^4) \ , \tag{A.42}$$

where we have used

$$\begin{aligned} &f_0 = 4(v_1 + v_2 - \bar{v}_2 + h) \ , \ f_1 = \frac{4}{3}(y_1(v_1 - 1) + y_2(v_2 - 1) - \bar{y}_2(\bar{v}_2 - 1) + h) \ , \\ &v_i = \sqrt{-y_i} \arctan \frac{1}{\sqrt{-y_i}} \ , \ i = 1,2 \ ; \ \bar{v}_2 = \sqrt{-\bar{y}_2} \arctan \frac{1}{\sqrt{-\bar{y}_2}} \ , \\ &\bar{y}_2 = y_2(s^t) \ , \ h = \frac{1}{2} \log\Big(\frac{1 + \mathbf{Q}^2/s}{1 + \bar{\mathbf{Q}}^2/s^t}\Big) \ , \ \bar{\mathbf{Q}}^2 = \mathbf{Q}^2(s^t) \ . \end{aligned} \tag{A.43}$$

There is a demonstrative limit of the above result when approaching the threshold $s \to s^t$, namely

$$F_k(M_a, M_b, M_c, M_d, s) \to -\frac{q_{cd}(s)}{64\pi^2\sqrt{s^t}} \frac{q_{ab}(s_0^t)}{\sqrt{s_0^t}} + \mathcal{O}(q_{cd}^2) \ , \tag{A.44}$$

where s_0^t denotes the function s_0 evaluated at threshold. The singularity is thus proportional to the one-loop function of the outer loop graph.

Derivative couplings

We will consider the effective range vertex of the inner loop diagram for illustrative purposes. Additional derivative couplings can be calculated with the same techniques. We need to determine the following quantity,

$$\int \frac{d^D l}{(2\pi)^D i}\frac{d^D k}{(2\pi)^D i} S_a(\mathbf{P}_\eta - \mathbf{k} - \mathbf{l}) S_b(\mathbf{l}) S_c(\mathbf{k}) S_d(\mathbf{Q} - \mathbf{k})(\tilde{s}_n - s_n^t) \ , \tag{A.45}$$

where we defined

$$\tilde{s}_n - s_n^t = w_c(\mathbf{Q} - \mathbf{k}) w_n(\mathbf{p}_n) - (\mathbf{Q} - \mathbf{k})\mathbf{p}_n + w_a(\mathbf{l}) w_b(\mathbf{P}_\eta - \mathbf{k} - \mathbf{l}) - \mathbf{l}(\mathbf{P}_\eta - \mathbf{k} - \mathbf{l}) - h_i \ . \tag{A.46}$$

$\tilde{s}_n$ can be treated with similar methods as in the one-loop case and be brought to a form,

$$\tilde{s}_n - s_n^t = \big(w_d(\mathbf{Q} - \mathbf{k}) + w_n(\mathbf{p}_n)\big)^2 - (\mathbf{Q} - \mathbf{k} + \mathbf{p}_n)^2 \ , \tag{A.47}$$

which after some algebraic rearrangements gives

$$\tilde{s}_n - s_n^t = M_c^2 + M_3^2 - s + \frac{M_\eta}{Q^0}(s - M_c^2 + M_d^2) - \frac{2M_\eta}{Q^0}\mathbf{k}\mathbf{Q} \ . \tag{A.48}$$

We thus need to perform the integration with an additional factor of $\mathbf{kQ}$ in the numerator. Retracing our steps in the calculation of the two-loop function, we observe that up to additional terms of $\mathcal{O}(\epsilon)$ the shifts in the integration variable amount to $\mathbf{k} \to \mathbf{k} + \frac{1-y}{2}(1+\delta)\mathbf{Q}$, and, noting that terms linear in $\mathbf{k}$ vanish, we arrive at $\mathbf{kQ} \to \frac{1-y}{2}(1+\delta)\mathbf{Q}^2$. The additional integral that has to be evaluated is thus (suppressing the mass indices)

$$\tilde{F}(s) = \frac{N(0)(1+\delta)}{256\pi^3\sqrt{s}} \int_0^1 \frac{dy}{\sqrt{y}} (2g'(y,s) - g(y,s)) \log g(y,s) \ , \tag{A.49}$$

with

$$\begin{aligned} 2g'(y,s) - g(y,s) &= 4Ay + 2B - Ay^2 - By - C \\ &= \frac{2}{5}[(10A - B)y + (5B - 2C)] + \text{reg.} \ , \end{aligned} \tag{A.50}$$

where in the second line we have used that $5Ay^2 + 3By + C$ consists only of regular terms. This can easily be confirmed, considering

$$\begin{aligned} 5Ay^2 + 3By + C &= 4A(y_1^2 v_1 + y_2^2 v_2) + 4B(y_1 v_1 + y_2 v_2) + 4C(v_1 + v_2) + \text{reg.} \\ &= 4(Ay_1^2 + By_1 + C)v_1 + 4(Ay_2^2 + By_2 + C)v_2 + \text{reg.} \\ &= 0 + \text{reg.} \end{aligned} \tag{A.51}$$

This brings us to our final result,

$$\tilde{F}(s) = \frac{\mathcal{N}(1+\delta)}{10}[(10A - B)f_1 + (5B - 2C)f_0] + \mathcal{O}(\epsilon^4) \ . \tag{A.52}$$

The additional calculations required for the full two-loop result found in Section A.3 proceed along similar lines.

A.2 Isospin-breaking corrections

A.2.1 Isospin-breaking corrections to $\pi\pi$ scattering

To calculate isospin-breaking corrections to the matching relations Eq. (2.23), we expand the ChPT amplitudes for all channels with electromagnetic corrections included [92, 93] around threshold. These contain virtual-photon exchange and real-photon radiation in the form of bremsstrahlung. For the definition of a reasonable (regular) threshold expansion, at first the divergent Coulomb pole contribution has to be subtracted. As the Coulomb pole emerges equally in the vertex correction diagram in both the NREFT and the ChPT calculation due to the same infrared properties of both theories, in a matching between them, this part drops out anyway. The determination of the scattering lengths is then relatively straightforward and has already been performed in the above references. Note, however, that in contrast to Refs. [92, 93] we expand around an isospin limit defined in terms of the *charged* pion mass. Thus, non-analytic terms $\propto \sqrt{\Delta_\pi}$ arise in the expansion of the $\pi^0\pi^0 \to \pi^0\pi^0$ channel, which are due to a cusp structure at the charged pion threshold and cancel the corresponding contribution in the expansion of $J_{+-}(s)$ in Eq. (2.19), once the correct matching is performed. We display the corrections in the form $C_i = \bar{C}_i + \Delta C_i$, where $\bar{C}_i$ denotes the corresponding coupling in the isospin limit (the $\pi^+\pi^+ \to \pi^+\pi^+$ channel is not needed in the present analysis, we just give it for completeness). For the combinations of S-wave scattering lengths, we find

$$
\begin{aligned}
\Delta C_{00} &= \frac{M_\pi^2}{F_\pi^2}\Big\{-\frac{\Delta_\pi}{M_\pi^2} + \frac{e^2}{32\pi^2}\mathcal{K}^{00} + \frac{\Delta_\pi}{32\pi^2 F_\pi^2}\big(13 - 16\bar{l}_1 - 32\bar{l}_2 + 6\bar{l}_3 - 4\bar{l}_4\big)\Big\}\,,\\
\Delta C_{x} &= \frac{M_\pi^2}{F_\pi^2}\Big\{-\frac{\Delta_\pi}{M_\pi^2} + \frac{e^2}{32\pi^2}\big(30 - 3\mathcal{K}_1^{\pm 0} + \mathcal{K}_2^{\pm 0}\big) - \frac{\Delta_\pi}{96\pi^2 F_\pi^2}\big(23 + 8\bar{l}_1 + 6\bar{l}_3 + 12\bar{l}_4\big)\Big\}\,,\\
\Delta C_{+0} &= \frac{M_\pi^2}{F_\pi^2}\Big\{\frac{\Delta_\pi}{M_\pi^2} - \frac{e^2}{32\pi^2}\big(2 + \mathcal{K}_1^{\pm 0} + \mathcal{K}_2^{\pm 0}\big) + \frac{\Delta_\pi}{96\pi^2 F_\pi^2}\big(3 - 8\bar{l}_1 - 16\bar{l}_2 + 6\bar{l}_3 + 12\bar{l}_4\big)\Big\}\,,\\
\Delta C_{+-} &= \frac{M_\pi^2}{F_\pi^2}\Big\{\frac{2\Delta_\pi}{M_\pi^2} - \frac{e^2}{16\pi^2}\big(24 - \mathcal{K}^{+-}\big) + \frac{\Delta_\pi}{8\pi^2 F_\pi^2}\big(2 + \bar{l}_3 + 2\bar{l}_4\big)\Big\}\,,\\
\Delta C_{++} &= \frac{M_\pi^2}{F_\pi^2}\Big\{\frac{2\Delta_\pi}{M_\pi^2} - \frac{e^2}{16\pi^2}\big(20 - \mathcal{K}^{++}\big) + \frac{\Delta_\pi}{16\pi^2 F_\pi^2}\big(3 + 2\bar{l}_3 + 4\bar{l}_4\big)\Big\}\,.
\end{aligned}
\tag{A.53}
$$

We note that ΔC_{00} is indeed free of non-analytic terms in Δ_π: the analytic structure of ChPT and the non-relativistic representation near threshold is the same, as it must.

The definition of effective ranges and P-wave scattering lengths is not *a priori* clear, since one has to deal with infrared divergences in the ChPT amplitudes. In calculations of, say, cross sections these divergences, which arise from virtual-photon corrections, cancel with corresponding divergences from real-photon radiation (bremsstrahlung). However, when matching the non-relativistic framework to ChPT, the explicit inclusion of bremsstrahlung is not necessary, since the virtual-photon diagrams exhibit the same infrared behavior and thus contain the same divergences (see Ref. [27]). On a rather technical note, the infrared divergences were calculated in dimensional regularization in Ref. [27], while the ChPT calculations [92, 93] use a finite photon mass m_γ as infrared regulator. The transition between both regularization schemes can be made by replacing $\log(m_\gamma^2/M_\pi^2) \to -32\pi^2\lambda_{\rm IR} - 1$. The infrared divergences then cancel, rendering the matching relations finite. We wish to emphasize that the physical reason for this cancellation is again the identical infrared behavior of both theories.

For the S-wave effective ranges, defining in analogy with the above $D_i = \bar{D}_i + \Delta D_i$, we

find the following corrections to the matching relations:

$$\begin{aligned}
\Delta D_{00} &= \frac{1}{F_\pi^2}\Big\{\frac{\Delta_\pi}{48\pi^2F_\pi^2}\big(35-8\bar{l}_1-16\bar{l}_2\big)\Big\}\,,\\
\Delta D_{x} &= \frac{1}{F_\pi^2}\Big\{\frac{e^2}{96\pi^2}\big(59-3\mathcal{K}_1^{\pm0}\big)+\frac{\Delta_\pi}{120\pi^2F_\pi^2}\big(18-5\bar{l}_1\big)\Big\}\,,\\
\Delta D_{+0} &= \frac{1}{F_\pi^2}\Big\{-\frac{e^2}{192\pi^2}\big(1+3\mathcal{K}_1^{\pm0}\big)+\frac{\Delta_\pi}{192\pi^2F_\pi^2}\big(21-4\bar{l}_1-12\bar{l}_2\big)\Big\}\,,\\
\Delta D_{+-} &= \frac{1}{F_\pi^2}\Big\{-\frac{e^2}{1152\pi^2}\Big(764-9(\mathcal{K}^{+-}-\mathcal{K}^{++})\Big)-\frac{109\Delta_\pi}{384\pi^2F_\pi^2}\Big\}\,,\\
\Delta D_{++} &= \frac{1}{F_\pi^2}\Big\{-\frac{e^2}{576\pi^2}\Big(676+9(\mathcal{K}^{+-}-\mathcal{K}^{++})\Big)+\frac{61\Delta_\pi}{192\pi^2F_\pi^4}\Big\}\,,
\end{aligned}\tag{A.54}$$

while for the two P-wave scattering lengths, we have (with $E_i=\bar{E}_i+\Delta E_i$)

$$\begin{aligned}
\Delta E_{+0} &= \frac{1}{F_\pi^2}\Big\{\frac{e^2}{64\pi^2}\big(1+3\mathcal{K}_1^{\pm0}\big)-\frac{\Delta_\pi}{192\pi^2F_\pi^2}\big(19-12\bar{l}_1+12\bar{l}_2\big)\Big\}\,,\\
\Delta E_{+-} &= \frac{1}{F_\pi^2}\Big\{\frac{3e^2}{128\pi^2}\Big(-28+\mathcal{K}^{+-}-\mathcal{K}^{++}\Big)-\frac{93\Delta_\pi}{128\pi^2F_\pi^2}\Big\}\,,
\end{aligned}\tag{A.55}$$

where the following abbreviations have been used for combinations of electromagnetic SU(2) low-energy constants $\bar{k}_i$ and $Z=\Delta_\pi/(2e^2F_\pi^2)$:

$$\begin{aligned}
\mathcal{K}^{00} &= \Big(3+\frac{4Z}{9}\Big)\bar{k}_1-\frac{40Z}{9}\bar{k}_2-3\bar{k}_3-4Z\bar{k}_4\,,\\
\mathcal{K}_1^{\pm0} &= \Big(3+\frac{4Z}{9}\Big)\bar{k}_1+\frac{32Z}{9}\bar{k}_2+3\bar{k}_3+4Z\bar{k}_4\,,\\
\mathcal{K}_2^{\pm0} &= 8Zk_2+3\bar{k}_3+4Z\bar{k}_4-2(1+8Z)\bar{k}_6-(1-8Z)\bar{k}_8\,,\\
\mathcal{K}^{+-} &= \Big(3+\frac{4Z}{9}\Big)\bar{k}_1-\frac{40Z}{9}\bar{k}_2-9\bar{k}_3+4Z\bar{k}_4+4(1+8Z)\bar{k}_6+2(1-8Z)\bar{k}_8\,,\\
\mathcal{K}^{+-}-\mathcal{K}^{++} &= 2\Big(3+\frac{4Z}{9}\Big)\bar{k}_1+\frac{208Z\bar{k}_2}{9}-18\bar{k}_3+24Z\bar{k}_4\,.
\end{aligned}\tag{A.56}$$

We refrain from calculating corrections to the shape parameters, since their intrinsic, isospin-symmetric error is much larger than what can be expected from isospin breaking.

For the numerical evaluation we express the low-energy constants $\bar{l}_1$ and $\bar{l}_2$ in terms of $\pi\pi$ D-wave scattering lengths [17], for which we use the numerical values [44]

$$a_2^0=1.75\pm0.03\times10^{-3}M_\pi^{-4}\,,\qquad a_2^2=0.170\pm0.013\times10^{-3}M_\pi^{-4}\,.\tag{A.57}$$

This way a_2^0 and a_2^2 can be independently varied according to their uncertainty, whereas $\bar{l}_1$ and $\bar{l}_2$ are correlated. For $\bar{l}_3$ we propose $\bar{l}_3=3.1\pm0.5$ as a sensible mean value from lattice simulations (see Ref. [221] for individual results of the various groups). The constant $\bar{l}_4$ is extracted from the scalar radius of the pion [44], $\bar{l}_4=4.4\pm0.2$.

For the electromagnetic SU(2) low-energy constants k_i^r we use the values given in Ref. [222]. The authors of this work have matched the two-flavor low-energy constants to their SU(3) counterparts, using numerical estimates from Refs. [223, 224]. We convert the values k_i^r given

channel	$\Delta C_i/C_i \times 10^{-2}$	$\Delta D_i/D_i \times 10^{-2}$	$\Delta E_i/E_i \times 10^{-2}$
00	-7.3 ± 0.2	-3.3 ± 0.4	–
x	2.5 ± 0.6	0.1 ± 0.6	–
$+0$	-5.2 ± 0.8	1.9 ± 0.8	0.4 ± 0.6
$+-$	6.1 ± 0.5	-0.2 ± 0.3	0.5 ± 0.4

Table A.1: Corrections to the matching relations relative to the phenomenological values.

at the mass of the ρ, $M_\rho = 0.77$ GeV, in Ref. [222] to scale-independent constants according to the standard prescription,

$$\bar{k}_i = \frac{32\pi^2}{\sigma_i} k_i^r(M_\rho) - \log \frac{M_\pi^2}{M_\rho^2} \ , \tag{A.58}$$

where the σ_i are the corresponding β-functions to be found in Ref. [92]. Numerically this results in

$$\bar{k}_1 = 1.66 \ , \quad \bar{k}_2 = 4.08 \ , \quad \bar{k}_3 = 2.28 \ , \quad \bar{k}_4 = 3.69 \ , \quad \bar{k}_6 = 4.08 \ , \quad \bar{k}_8 = 4.06 \ . \tag{A.59}$$

The uncertainties on the k_i^r are estimated analogously to Ref. [62] by their logarithmic scale variation,

$$k_i^r \to k_i^r \pm \frac{\sigma_i}{16\pi^2} \ , \tag{A.60}$$

which for the $\bar{k}_i$ translates to $\bar{k}_i \to \bar{k}_i \pm 2$. The errors on the quantities $\mathcal{K}^{00}, \mathcal{K}_i^{\pm 0}, \mathcal{K}^{+-}, \mathcal{K}^{++}$ are then calculated in a correlated fashion (i.e. $+2$ or -2 for *all* $\bar{k}_i$).

The numerical corrections are displayed in Table A.1. We find that the corrections at one-loop order are very small. The main contributions to the C_i stem from the tree-level correction factor.

A.2.2 Corrections to the $\Delta I = 1$ rule

The content of this Appendix is a subject of Ref. [225]. In the following we will briefly report some of the results of that study. At leading order p^2 in ChPT and up to next-to-leading order in the isospin-breaking parameters $m_u - m_d$ and e^2, the amplitudes for the charged and the neutral decay were already quoted in Eq. (2.7). We also hinted at the fact that in order to define the deviations from the $\Delta I = 1$ relation, Eq. (2.51), it is useful to expand the decay amplitudes for *both* channels around the point $s_3 = s_n$, $s_1 = s_2$ as shown in Eq. (2.9), so that $\Delta_{\tilde{\mathcal{N}}}$ is going to be of chiral order p^4.

The decay amplitudes at $\mathcal{O}(p^4)$ in ChPT and at $\mathcal{O}(m_d - m_u, e^2, (m_d - m_u)e^2)$ in isospin breaking are given explicitly in Ref. [62]. With minimal modifications they can be shown to be also valid up-to-and-including $\mathcal{O}((m_d - m_u)^2)$, i.e. only numerically tiny terms of $\mathcal{O}(e^4)$ are potentially neglected at second order in isospin breaking. In order to match the expanded ChPT amplitude of Ref. [62] to the polynomial part of the NREFT representation, the following steps have to be taken into account:

1. The (non-analytic) imaginary parts due to pion loops in the chiral and NREFT amplitude are identical and drop out in the matching relation.

2. For the radiative corrections due to real and virtual photons, one has to match the result of Ref. [62] to an analogous NREFT representation as in Ref. [27]. As a result, the Coulomb pole and phase have to be subtracted from the chiral representation, as well as the bremsstrahlung contributions. As in the case of radiative corrections to $\pi\pi$ scattering infrared divergences are regulated by introducing a finite photon mass m_γ in Ref. [62] and have to be treated as described in Appendix A.2.1.

As $\Delta_{\tilde{\mathcal{N}}}$ is of $\mathcal{O}(p^4)$, it is convenient to factor out the neutral normalization at leading order and quote the result as the ratio $\Delta_{\tilde{\mathcal{N}}}/\mathcal{N}_n$ below. One finds [225]

$$\begin{aligned}
\frac{\Delta_{\tilde{\mathcal{N}}}}{\mathcal{N}_n} &= 2e^2\bigg\{\frac{1-3\rho}{3\rho}G(s_n)+\frac{1}{2}\bar{J}_{\pi\pi}(s_n)+\frac{3}{32\pi^2}\left(\log\frac{M_\pi^2}{\mu^2}-1\right)-\frac{1+\rho}{1-\rho}(2K_3^r-K_4^r)\\
&\quad+\frac{8K_6^r}{3(1-\rho)}-\frac{4(3-\rho)}{1-\rho}(K_{10}^r+K_{11}^r)\bigg\}\\
&\quad+\frac{\Delta_\pi}{3(1-\rho)F_\pi^2}\bigg\{\frac{29-111\rho-9\rho^2+27\rho^3}{8(1+3\rho)}\bar{J}_{KK}(s_n)-32L_3^r\\
&\quad+\frac{3\rho(1+22\rho+9\rho^2)}{(1-9\rho)(1+3\rho)}\bar{J}_{\eta\pi}(s_n)-\frac{7+21\rho-495\rho^2+243\rho^3}{(1-9\rho)(1+3\rho)}\bar{J}_{\pi\pi}(s_n)\\
&\quad+\frac{8(3-\rho)}{1-\rho}\frac{F_\pi^2}{M_\eta^2}\Delta_F+\frac{1}{16\pi^2}\bigg[6(3-2\rho)\log\frac{M_\pi^2}{\mu^2}+\frac{2(1+2\rho-\rho^2)}{1-\rho}\log\frac{3+\rho}{4\rho}\\
&\quad-\frac{3(3-26\rho-\rho^2)}{(1-9\rho)(1-\rho)}\log\rho+\frac{53-357\rho+351\rho^2+81\rho^3}{4(1-9\rho)}\bigg]\bigg\}+\mathcal{O}\left(e^2p^2\right)\ , \qquad \text{(A.61)}\\
\Delta_{\tilde{\alpha}} &= \frac{3e^2}{(1-9\rho)^2(1-\rho)(1+3\rho)^2M_\eta^4}\bigg\{12\rho(1+63\rho^2)G(s_n)\\
&\quad-\frac{1-14\rho-138\rho^2+234\rho^3-1107\rho^4}{1-9\rho}\bar{J}_{\pi\pi}(s_n)\\
&\quad+\frac{7-102\rho-504\rho^2+1926\rho^3-3375\rho^4}{32\pi^2(1-9\rho)}\bigg\}\\
&\quad+\frac{3\Delta_\pi}{(1-\rho)(1+3\rho)^2F_\pi^2M_\eta^4}\bigg\{\frac{3(3+\rho)(957-5240\rho-1398\rho^2-288\rho^3+81\rho^4)}{4096(1+3\rho)}\bar{J}_{KK}(s_n)\\
&\quad+\frac{\rho^2(221-3612\rho+32022\rho^2-32076\rho^3-2187\rho^4)}{8(1-9\rho)^3(1+3\rho)}\bar{J}_{\eta\pi}(s_n)\\
&\quad-\frac{3\rho(3-124\rho+1794\rho^2-7596\rho^3+9315\rho^4)}{(1-9\rho)^3(1+3\rho)}\bar{J}_{\pi\pi}(s_n)\\
&\quad+\frac{1}{32768\pi^2(1-9\rho)^3}\Big(243-39737\rho+540471\rho^2-729333\rho^3\\
&\quad+3630825\rho^4-1810107\rho^5+85293\rho^6+59049\rho^7\Big)\\
&\quad-\frac{\rho^2(37+237\rho-2025\rho^2+3159\rho^3)}{128\pi^2(1-9\rho)^3(1-\rho)}\log\rho\bigg\}+\mathcal{O}\left(e^2p^{-2}\right)\ , \qquad \text{(A.62)}
\end{aligned}$$

neglecting even higher-order terms in the isospin-breaking parameters e^2 and m_d-m_u. Here, $\Delta_F=F_K/F_\pi-1$ is used (cf. Ref. [18]) and the loop functions are given as

$$G(s)=\frac{1-\sigma_\pi^2}{64\pi^2\sigma_\pi}\left\{\mathrm{Li}\left(\frac{1-\sigma_\pi}{1+\sigma_\pi}\right)-\mathrm{Li}\left(\frac{1+\sigma_\pi}{1-\sigma_\pi}\right)+\log\frac{1+\sigma_\pi}{1-\sigma_\pi}\right\}\ ,\quad \mathrm{Li}(z)=\int_1^z\frac{\log t}{1-t}dt\ ,$$

$$\bar{J}_{\pi\pi}(s) = \frac{1}{8\pi^2}\left\{1 - \frac{\sigma_\pi}{2}\log\frac{1+\sigma_\pi}{1-\sigma_\pi}\right\}, \qquad \bar{J}_{KK}(s) = \frac{1}{8\pi^2}\left\{1 - \sigma_K \operatorname{arccot}\sigma_K\right\},$$
$$\bar{J}_{\eta\pi}(s) = \frac{1}{32\pi^2}\left\{2 + \log\rho\left(\frac{M_\eta^2 - M_\pi^2}{s} - \frac{1+\rho}{1-\rho}\right) - \frac{\nu}{s}\log\frac{s - M_\eta^2 - M_\pi^2 + \nu}{s - M_\eta^2 - M_\pi^2 - \nu}\right\},$$
$$\sigma_\pi = \sqrt{1 - \frac{4M_\pi^2}{s}}, \quad \sigma_K = \sqrt{\frac{4M_K^2}{s} - 1}, \quad \nu = \lambda^{1/2}(M_\eta^2, M_\pi^2, s), \quad \rho = \frac{M_\pi^2}{M_\eta^2}. \quad \text{(A.63)}$$

$G(s)$ is the real part of the triangle loop function for the photon exchange between two charged pions (rescaled by a factor of M_π^2) with the Coulomb pole subtracted, involving Spence's function $\mathrm{Li}(z)$, and $\bar{J}_{ab}(s)$ are the usual finite and scale-independent parts of the corresponding two-meson loop functions. For the definition of the (renormalized) strong and electromagnetic SU(3) low-energy constants L_3^r and K_i^r in terms of chiral Lagrangians (not to be confused with the tree-level couplings L_i, K_i of the non-relativistic theory), see Refs. [18, 177].

Both results Eqs. (A.61) and (A.62) are divergence-free and independent of the scale μ. The scale-independence of $\Delta_{\tilde{\alpha}}$ is explicitly seen, that of $\Delta_{\tilde{\mathcal{N}}}$ can be found by using the scale variation of the electromagnetic constants K_i^r as given in Ref. [177]. Both corrections turn out to be completely of electromagnetic origin. For the numerical evaluation one makes use of the same estimates and variations of the low-energy constants as described in Appendix A.2.1 and explained in more detail in Refs. [62, 225]; their uncertainties completely dominate the error on $\Delta_{\tilde{\mathcal{N}}}/\mathcal{N}_n$. As $\Delta_{\tilde{\alpha}}$ is free of low-energy constants at this order, it is a pure loop effect and a prediction in terms of well-known parameters. Here we quote an uncertainty solely due to the use of the Gell-Mann–Okubo relation for the masses, using either the mass of the η directly, or the same expressed in terms of pion and kaon masses. We consider the error thus obtained rather underestimated. In total, we find

$$\frac{\Delta_{\tilde{\mathcal{N}}}}{\mathcal{N}_n} = (-0.7 \pm 1.5)\%, \qquad \Delta_{\tilde{\alpha}} = 0.035 \pm 0.003\ \mathrm{GeV}^{-4}. \quad \text{(A.64)}$$

A.3 NREFT representation including isospin breaking

A.3.1 $\eta \to 3\pi$ amplitudes up to two loops

For the representation of the $\eta \to 3\pi$ decay amplitudes at one-loop order, we find (see also Ref. [26])

$$\mathcal{M}_n^{\text{1-loop}}(s_1,s_2,s_3) = \Big\{C_{00}(s_1)K(s_1)J_{00}(s_1) + 2C_x(s_1)L(s_1)J_{+-}(s_1) + (s_1 \leftrightarrow s_2) + (s_1 \leftrightarrow s_3)\Big\},$$
$$\mathcal{M}_c^{\text{1-loop}}(s_1,s_2,s_3) = C_x(s_3)K(s_3)J_{00}(s_3) + 2C_{+-}(s_3)L(s_3)J_{+-}(s_3) + \Big\{\Big[2C_{+0}(s_1)L'(s_1) - \tilde{E}_{+0}(s_1,s_2,s_3)\tilde{L}(s_1)\Big]J_{+0}(s_1) + (s_1 \leftrightarrow s_2)\Big\}. \quad \text{(A.65)}$$

The pertinent diagrams for the two-loop calculations are shown in Figs. A.5 and A.6. For the two-loop amplitudes at the order discussed in Section 2.3.5, we obtain

$$\mathcal{M}_n^{\text{2-loops}} = \Big\{\mathcal{M}_n^A(s_1,s_2,s_3) + \mathcal{M}_n^B(s_1,s_2,s_3) + (s_1 \leftrightarrow s_2) + (s_1 \leftrightarrow s_3)\Big\},$$
$$\mathcal{M}_c^{\text{2-loops}} = \mathcal{M}_c^A(s_1,s_2,s_3) + \mathcal{M}_n^B(s_1,s_2,s_3), \quad \text{(A.66)}$$

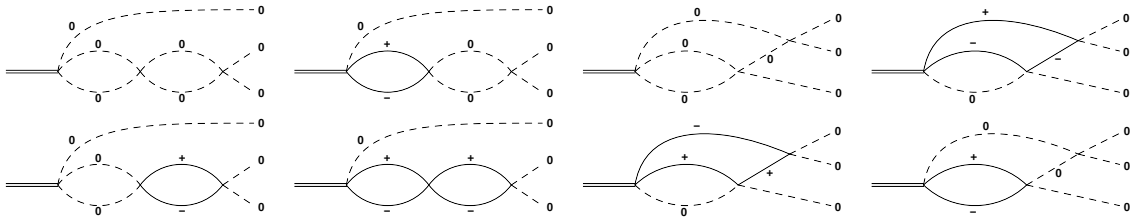

Figure A.5: Two-loop diagrams contributing to $\eta \to 3\pi^0$. Dashed lines correspond to neutral pions, solid lines to charged pion. The double line represents the η particle. Diagrams obtained by permutation of identical particles are not shown.

where

$$\begin{aligned}
\mathcal{M}_n^A &= 2K_0 C_{00}(\tilde{s}_1^{00}) C_{00}(s_1) F_0(M_{\pi^0}, M_{\pi^0}, M_{\pi^0}, M_{\pi^0}, s_1) \\
&\quad - 4M_\eta K_0 D_{00} C_{00}(s_1) \frac{\mathbf{Q}_1^2}{Q_1^0} F_0^{(1)}(M_{\pi^0}, M_{\pi^0}, M_{\pi^0}, M_{\pi^0}, s_1) \\
&\quad + 8\Big[L'''_{+0}(s_1) C_{+0}(\tilde{s}_1^{+-}) \\
&\qquad - \frac{\Delta_\pi}{4M_{\pi^0}}\Big(\frac{s_1 + 2\mathbf{Q}_1^2}{2Q_1^0} - p_1^0\Big) L_0 E_{+0}\Big] C_x(s_1) F_0(M_{\pi^0}, M_\pi, M_\pi, M_\pi, s_1) \\
&\quad - 8\Big[\frac{1}{2} L_1 C_{+0}(\tilde{s}_1^{+-}) + 2M_\eta L'''_{+0}(s_1) D_{+0} \\
&\qquad - \frac{\Delta_\pi}{4M_{\pi^0}} L_0 E_{+0}\Big] C_x(s_1) \frac{\mathbf{Q}_1^2}{Q_1^0} F_0^{(1)}(M_{\pi^0}, M_\pi, M_\pi, M_\pi, s_1) \\
&\quad + 8M_\eta L_1 D_{+0} C_x(s_1) \frac{\mathbf{Q}_1^4}{(Q_1^0)^2} F_0^{(2)}(M_{\pi^0}, M_\pi, M_\pi, M_\pi, s_1) \\
&\quad + 4L''(s_1) C_x(\tilde{s}_1^{00}) C_{00}(s_1) F_0(M_\pi, M_\pi, M_{\pi^0}, M_{\pi^0}, s_1) \\
&\quad + 4\Big[L_1 C_x(\tilde{s}_1^{00}) - 2M_\eta L''(s_1) D_x\Big] C_{00}(s_1) \frac{\mathbf{Q}_1^2}{Q_1^0} F_0^{(1)}(M_\pi, M_\pi, M_{\pi^0}, M_{\pi^0}, s_1) \\
&\quad - 8M_\eta L_1 D_x C_{00}(s_1) \frac{\mathbf{Q}_1^4}{(Q_1^0)^2} F_0^{(2)}(M_\pi, M_\pi, M_{\pi^0}, M_{\pi^0}, s_1) \ , \qquad \text{(A.67)}
\end{aligned}$$

$$\begin{aligned}
\mathcal{M}_n^B &= K(s_1) C_{00}(s_1)^2 J_{00}^2(s_1) + 2\Big[L(s_1) C_x(s_1) C_{00}(s_1) + K(s_1) C_x^2(s_1)\Big] J_{00}(s_1) J_{+-}(s_1) \\
&\quad + 4L(s_1) C_{+-}(s_1) C_x(s_1) J_{+-}^2(s_1) \ , \qquad \text{(A.68)}
\end{aligned}$$

and

$$\begin{aligned}
\mathcal{M}_c^A &= \Big\{ 4\Big[L'''_{+0}(s_1^+) C_{+0}(\tilde{s}_1^{+0})\Big(C_{+0}(s_1) - E_{+0}^+(s_1, s_2, s_3)\Big) \\
&\qquad + \frac{\Delta_\pi}{4M_{\pi^0}}\Big(\frac{s_1 + 2\mathbf{Q}_1^2 - \Delta_\pi}{2Q_1^0} - p_1^0\Big) L_0 E_{+0} C_{+0}(s_1)\Big] F_+(M_\pi, M_{\pi^0}, M_\pi, M_{\pi^0}, s_1) \\
&\quad - 4\Big[\Big(\frac{1}{2} L_1 C_{+0}(\tilde{s}_1^{+0}) + 2M_\eta L'''_{+0}(s_1^+) D_{+0}\Big)\Big(C_{+0}(s_1) - E_{+0}^+(s_1, s_2, s_3)\Big) \frac{\mathbf{Q}_1^2}{Q_1^0} \\
&\qquad + \frac{\Delta_\pi}{4M_{\pi^0}} L_0 E_{+0} C_{+0}(s_1) \frac{\mathbf{Q}_1^2}{Q_1^0}
\end{aligned}$$

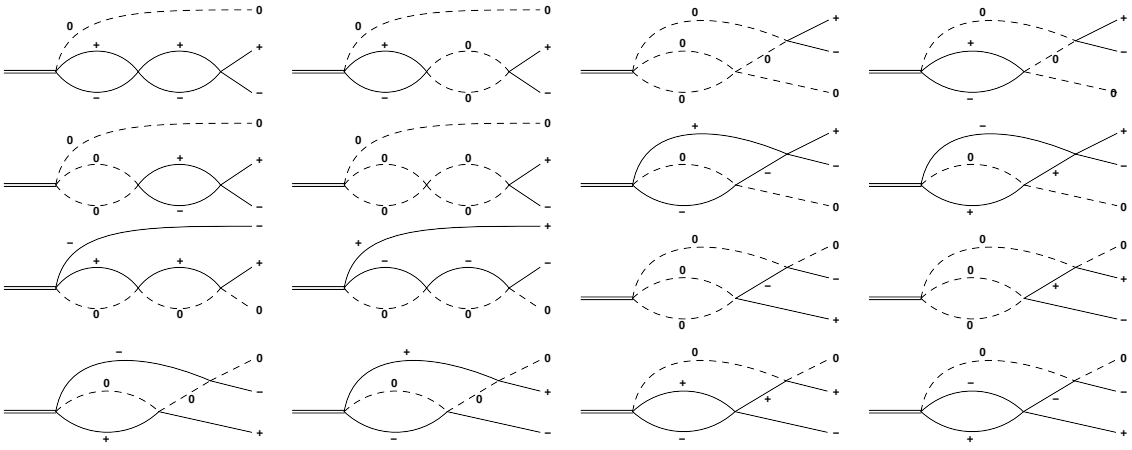

Figure A.6: Two-loop diagrams contributing to $\eta \to \pi^+\pi^-\pi^0$. Dashed lines correspond to neutral pions, solid lines to charged pion. The double line represents the η particle.

$$
\begin{aligned}
&\quad - 2L'''_{+0}(s_1^+)C_{+0}(\tilde{s}_1^{+0})E_{+0}(s_1,s_2,s_3)\Big]F_+^{(1)}(M_\pi,M_{\pi^0},M_\pi,M_{\pi^0},s_1)\\
&+ 4\Big[M_\eta L_1 D_{+0}\Big(C_{+0}(s_1) - E_{+0}^+(s_1,s_2,s_3)\Big)\frac{\mathbf{Q}_1^4}{(Q_1^0)^2} - \Big(L_1 C_{+0}(\tilde{s}_1^{+0})\\
&\qquad + 4M_\eta L'''_{+0}(s_1^+)D_{+0}\Big)E_{+0}(s_1,s_2,s_3)\frac{\mathbf{Q}_1^2}{Q_1^0}\Big]F_+^{(2)}(M_\pi,M_{\pi^0},M_\pi,M_{\pi^0},s_1)\\
&+ 8M_\eta L_1 D_{+0}E_{+0}(s_1,s_2,s_3)\frac{\mathbf{Q}_1^4}{(Q_1^0)^2}F_+^{(3)}(M_\pi,M_{\pi^0},M_\pi,M_{\pi^0},s_1)\\
&+ 4L''(s_1^-)C_{+-}(\tilde{s}_1^{0+})\Big(C_{+0}(s_1) + E_{+0}^-(s_1,s_2,s_3)\Big)F_+(M_\pi,M_\pi,M_{\pi^0},M_\pi,s_1)\\
&+ 4\Big[\Big(L_1 C_{+-}(\tilde{s}_1^{0+}) - 2M_\eta L''(s_1^-)D_{+-}\Big)\Big(C_{+0}(s_1) + E_{+0}^-(s_1,s_2,s_3)\Big)\frac{\mathbf{Q}_1^2}{Q_1^0}\\
&\quad - 2L''(s_1^-)C_{+-}(\tilde{s}_1^{0+})E_{+0}(s_1,s_2,s_3)\Big]F_+^{(1)}(M_\pi,M_\pi,M_{\pi^0},M_\pi,s_1)\\
&- 8\Big[M_\eta L_1 D_{+-}\Big(C_{+0}(s_1) + E_{+0}^-(s_1,s_2,s_3)\Big)\frac{\mathbf{Q}_1^4}{(Q_1^0)^2} + \Big(L_1 C_{+-}(\tilde{s}_1^{0+})\\
&\qquad - 2M_\eta L''(s_1^-)D_{+-}\Big)E_{+0}(s_1,s_2,s_3)\frac{\mathbf{Q}_1^2}{Q_1^0}\Big]F_+^{(2)}(M_\pi,M_\pi,M_{\pi^0},M_\pi,s_1)\\
&+ 16M_\eta L_1 D_{+-}E_{+0}(s_1,s_2,s_3)\frac{\mathbf{Q}_1^4}{(Q_1^0)^2}F_+^{(3)}(M_\pi,M_\pi,M_{\pi^0},M_\pi,s_1)\\
&+ 2K_0 C_x(\tilde{s}_1^{0+})\Big(C_{+0}(s_1) + E_{+0}^-(s_1,s_2,s_3)\Big)F_+(M_{\pi^0},M_{\pi^0},M_{\pi^0},M_\pi,s_1)\\
&- 4K_0\Big[M_\eta D_x\Big(C_{+0}(s_1) + E_{+0}^-(s_1,s_2,s_3)\Big)\frac{\mathbf{Q}_1^2}{Q_1^0} + C_x(\tilde{s}_1^{0+})E_{+0}(s_1,s_2,s_3)\Big]\\
&\quad \times F_+^{(1)}(M_{\pi^0},M_{\pi^0},M_{\pi^0},M_\pi,s_1)\\
&\quad + 8M_\eta K_0 D_x E_{+0}(s_1,s_2,s_3)\frac{\mathbf{Q}_1^2}{Q_1^0}F_+^{(2)}(M_{\pi^0},M_{\pi^0},M_{\pi^0},M_\pi,s_1) + (s_1 \leftrightarrow s_2)\Big\}\\
&+ 2K_0 C_{00}(\tilde{s}_3^{00})C_x(s_3)F_0(M_{\pi^0},M_{\pi^0},M_{\pi^0},M_{\pi^0},s_3)
\end{aligned}
$$

$$
\begin{aligned}
&- 4M_\eta K_0 D_{00} C_x(s_3) \frac{\mathbf{Q}_3^2}{Q_3^0} F_0^{(1)}(M_{\pi^0}, M_{\pi^0}, M_{\pi^0}, M_{\pi^0}, s_3) \\
&+ 4L''(s_3) C_x(\tilde{s}_3^{00}) C_x(s_3) F_0(M_\pi, M_\pi, M_{\pi^0}, M_{\pi^0}, s_3) \\
&+ 4\Big[L_1 C_x(\tilde{s}_3^{00}) - 2M_\eta L''(s_3) D_x\Big] C_x(s_3) \frac{\mathbf{Q}_3^2}{Q_3^0} F_0^{(1)}(M_\pi, M_\pi, M_{\pi^0}, M_{\pi^0}, s_3) \\
&- 8M_\eta L_1 D_x C_x(s_3) \frac{\mathbf{Q}_3^4}{(Q_3^0)^2} F_0^{(2)}(M_\pi, M_\pi, M_{\pi^0}, M_{\pi^0}, s_3) \\
&+ 8\Big[L'''_{+0}(s_3) C_{+0}(\tilde{s}_3^{+-}) \\
&\quad - \frac{\Delta_\pi}{4M_{\pi^0}}\Big(\frac{s_3 + 2\mathbf{Q}_3^2}{2Q_3^0} - p_3^0\Big) L_0 E_{+0}\Big] C_{+-}(s_3) F_0(M_\pi, M_{\pi^0}, M_\pi, M_\pi, s_3) \\
&- 8\Big[\frac{1}{2} L_1 C_{+0}(\tilde{s}_3^{+-}) + 2M_\eta L'''_{+0}(s_3) D_{+0} \\
&\quad - \frac{\Delta_\pi}{4M_{\pi^0}} L_0 E_{+0}\Big] C_{+-}(s_3) \frac{\mathbf{Q}_3^2}{Q_3^0} F_0^{(1)}(M_\pi, M_{\pi^0}, M_\pi, M_\pi, s_3) \\
&+ 8M_\eta L_1 D_{+0} C_{+-}(s_3) \frac{\mathbf{Q}_3^4}{(Q_3^0)^2} F_0^{(2)}(M_\pi, M_{\pi^0}, M_\pi, M_\pi, s_3) \ , \qquad \text{(A.69)}
\end{aligned}
$$

$$
\begin{aligned}
\mathcal{M}_c^B = &\Big\{4L'(s_1) C_{+0}^2(s_1) J_{+0}^2(s_1) + (s_1 \leftrightarrow s_2)\Big\} + K(s_3) C_{00}(s_3) C_x(s_3) J_{00}^2(s_3) + 2\Big[L(s_3) C_x^2(s_3) \\
&+ K(s_3) C_x(s_3) C_{+-}(s_3)\Big] J_{+-}(s_3) J_{00}(s_3) + 4L(s_3) C_{+-}^2(s_3) J_{+-}^2(s_3) \ . \qquad \text{(A.70)}
\end{aligned}
$$

We have used the following abbreviations:

$$
\begin{aligned}
J_{ab}(s_i) &= \frac{i q_{ab}(s_i)}{8\pi\sqrt{s_i}} \ , \qquad q_{ab}^2(s_i) = \frac{\lambda(s_i, M_a^2, M_b^2)}{4s_i} \ , \\
C_n(s_i) &= C_n + D_n\big(s_i - s_n^{\rm thr}\big) + F_n\big(s_i - s_n^{\rm thr}\big) \ , \\
\tilde{s}_i^{cd} &= M_c^2 + M_i^2 - s_i + \frac{M_\eta}{Q_i^0}\big(s_i + 2\mathbf{Q}_i^2 - M_c^2 + M_d^2\big) \ , \\
\tilde{E}_{+0}(s_1,s_2,s_3) &= E_{+0} \frac{q_{+0}^2(s_1)}{3s_1 M_\eta}\Big(s_1(s_3 - s_2) + \Delta_\pi(M_\pi^2 - M_\eta^2)\Big) \ , \\
E_{+0}^{(\pm)}(s_1,s_2,s_3) &= E_{+0}\left[\frac{(s_1(\pm\Delta_\pi))(s_3 - s_2 + \Delta_\pi)}{2M_\eta Q_1^0} - \Delta_\pi\right] \ , \\
E_{+-}(s_1,s_2,s_3) &= E_{+-}\, \frac{s_3(s_1 - s_2)}{2M_\eta Q_3^0} \ , \\
K(s_i) &= K_0 + K_1\Big[\big(p_i^0 - M_{\pi^0}\big)^2 + 2\left(\frac{Q_i^0}{2} - M_{\pi^0}\right)^2 + \frac{\mathbf{Q}_i^2}{6}\left(1 - \frac{4M_{\pi^0}^2}{s_i}\right)\Big] \ , \\
L(s_i) &= L_0 + L_1\big(p_i^0 - M_{\pi^0}\big) + L_2\big(p_i^0 - M_{\pi^0}\big)^2 + L_3 \frac{\mathbf{Q}_i^2}{3}\left(1 - \frac{4M_\pi^2}{s_i}\right) \\
\tilde{L}(s_i) &= L_1 + 2L_2\left[\frac{Q_i^0}{2}\Big(1 - \frac{\Delta_\pi}{s_i}\Big) - M_{\pi^0}\right] + 2L_3\left[p_i^0 - \frac{Q_i^0}{2}\Big(1 + \frac{\Delta_\pi}{s_i}\Big)\right] \\
L'(s_i) &= L_0 + L_1\Big(\frac{Q_i^0}{2}\Big(1 - \frac{\Delta_\pi}{s_i}\Big) - M_{\pi^0}\Big) + L_2\left[\Big(\frac{Q_i^0}{2}\Big(1 - \frac{\Delta_\pi}{s_i}\Big) - M_{\pi^0}\Big)^2 + \frac{\mathbf{Q}_i^2}{3s_i}\, q_{+0}^2(s_i)\right]
\end{aligned}
$$

$$
\begin{aligned}
&\quad + L_3\Big[\Big(\frac{Q_i^0}{2}\Big(1+\frac{\Delta_\pi}{s_i}\Big)-p_i^0\Big)^2+\frac{\mathbf{Q}_i^2}{3s_i}\,q_{+0}^2(s_i)\Big]\,,\\
L''\big(s_i^{(\pm)}\big) &= L_0+L_1\Big(\frac{s_i(\pm\Delta_\pi)}{2Q_i^0}-M_{\pi^0}\Big)\,,\\
L'''_{ab}\big(s_i^{(\pm)}\big) &= L_0+L_1\Big(\frac{1}{2}(M_\eta-M_a-M_b)-\frac{s_i(\pm\Delta_\pi)}{4Q_i^0}\Big)\,.
\end{aligned}
\tag{A.71}
$$

In the notation, it is understood that the shape parameter term F_n is omitted in the polynomials $C_n(\tilde{s}_i^{cd})$ inside the "genuine" two-loop graphs. There is a subtlety with regard to the neutral Dalitz plot couplings in the irreducible two-loop graphs: since we included these couplings only up to $\mathcal{O}(\epsilon^2)$, the $\Delta I = 1$ rule is only fulfilled up that same order. Eq. (2.15), however, is valid up to $\mathcal{O}(\epsilon^4)$, so that we have to replace $K_0 \to \bar{K}_0 = -(3L_0 + L_1 Q_n)$ in $\mathcal{M}_n^A$ and $\mathcal{M}_c^A$ above or simply $\bar{K}_0 = \tilde{\mathcal{N}}_n(1 - \frac{4}{9}\tilde{b}M_\eta^2 Q_n^2)$. The numerical effects of this replacement are small.

$F_i(\ldots;s)$, $F_i^{(k)}(\ldots;s)$, $k = 1, 2, 3$, stand for the integral representations of the functions $F(\ldots;s)$, $F^{(k)}(\ldots;s)$, evaluated at $\mathbf{Q}_i^2 = \lambda(M_\eta^2, M_i^2, s_i)/4M_\eta^2$, with $i = 1, 2, 3$. The analytic expression for these two-loop functions read

$$
\begin{aligned}
F(M_a,M_b,M_c,M_d,s) &= \mathcal{N}\Big[2A\,f_1+B\,f_0-\frac{3\mathbf{Q}^2}{10s}(B\,f_1+2C\,f_0)\\
&\quad +\mathcal{K}(X_3f_3+X_2f_2+X_1f_1+X_0f_0)\Big]\,,\\
F^{(1)}(M_a,M_b,M_c,M_d,s) &= \frac{\mathcal{N}}{10}(1+\delta)\big[(10A-B)f_1+(5B-2C)f_0\big]+\mathcal{O}(\epsilon^4)\,,\\
F^{(2)}(M_a,M_b,M_c,M_d,s) &= \frac{\mathcal{N}}{2}\Big[-\frac{1}{\mathbf{Q}^2}\Big(2A^2f_3+3ABf_2+(B^2-2AC)f_1+BCf_0\Big)\\
&\quad +\frac{(1+\delta)^2}{4}\Big(Af_3+(B-2A)f_2+(4A-2B+C)f_1+2(B-C)f_0\Big)\Big]+\mathcal{O}(\epsilon^4)\,,\\
F^{(3)}(M_a,M_b,M_c,M_d,s) &= \frac{\mathcal{N}(1+\delta)}{16}\Big[\frac{3}{\mathbf{Q}^2}\Big(A^2f_4+2A(B-4A)f_3\\
&\quad +(2AC+B^2-12AB)f_2+(2BC-8AC-4B^2)f_1+(C^2-4BC)f_0\Big)\\
&\quad -(1+\delta)^2\Big(Af_4+(B-3A)f_3+(3A-3B+C)f_2\\
&\quad +(3B-4A-3C)f_1+(3C-2B)f_0\Big)\Big]+\mathcal{O}(\epsilon^4)\,,
\end{aligned}
\tag{A.72}
$$

with

$$
\begin{aligned}
&f_2=-\frac{1}{5A}\,(3Bf_1+Cf_0)\,,\qquad f_3=-\frac{1}{7A^2}\Big[3(AC-B^2)f_1-BCf_0\Big]\,,\\
&f_4=\frac{1}{9A^2}\Big[3(ABC+5BC-5B^3)f_1-5(B^2C-C^2)f_0\Big]\,,\\
&X_0=HBC-RC\,,\quad X_1=H(2AC+B^2)-R(2B-C)\,,\quad X_2=3HAB-R(3A-\frac{3}{2}\,B)\,,\\
&X_3=2HA^2+2AR\,,\quad H=-\frac{3}{2}\left(1+\frac{\mathbf{Q}^2}{3s}\right),\quad R=\frac{\mathbf{Q}^2Q_0^2}{2s}\,(1+\tilde{\delta})^2\,.
\end{aligned}
\tag{A.73}
$$

and

$$
\begin{aligned}
\mathcal{N} &= \frac{1}{256\pi^3\sqrt{s}}\,\frac{\lambda^{1/2}(s_0,M_a^2,M_b^2)}{s_0\sqrt{\Delta^2-\frac{(1+\tilde\delta)^2}{4}\,\mathbf{Q}^2}}\;,\\
\mathcal{K} &= \left[\frac{1}{2(M_\eta^2+M_c^2)-(M_a+M_b)^2-s_0}+\frac{1}{s_0-(M_a-M_b)^2}-\frac{2}{s_0}\right]\frac{M_\eta^2}{s_0-M_\eta^2-M_c^2}\;,\\
f_0 &= 4\big(v_1+v_2-\bar v_2+h\big)\;,\\
f_1 &= \frac{4}{3}\left(y_1(v_1-1)+y_2(v_2-1)-\bar y_2(\bar v_2-1)+h\right)\;,\\
h &= \frac{1}{2}\ln\!\left(\frac{1+\mathbf{Q}^2/s}{1+\bar{\mathbf{Q}}^2/\bar s}\right)\;,\quad \bar{\mathbf{Q}}^2=\mathbf{Q}^2(\bar s)\;,\quad \bar s=(M_c+M_d)^2\;,\\
v_i &= \sqrt{-y_i}\,\arctan\frac{1}{\sqrt{-y_i}}\;,\quad i=1,2\;;\quad \bar v_2=\sqrt{-\bar y_2}\,\arctan\frac{1}{\sqrt{-\bar y_2}}\;,\\
y_{1,2} &= \frac{-B\mp\sqrt{B^2-4AC}}{2A}\;,\quad \bar y_2=y_2(\bar s)\;,\\
A &= -\frac{\mathbf{Q}^2}{s}\,(M_c^2+\Delta^2)\;,\quad B=q_0^2-\Delta^2+\frac{\mathbf{Q}^2}{s}\,M_c^2\;,\quad C=-q_0^2\;,\\
s_0 &= M_\eta^2+M_c^2-2M_\eta\left(M_c^2+\frac{\mathbf{Q}^2(1+\tilde\delta)^2}{4}\right)^{1/2}\;,\quad q_0^2=\frac{\lambda(s,M_c^2,M_d^2)}{4s}\;,\\
\Delta^2 &= \frac{\lambda(M_\eta^2,M_c^2,(M_a+M_b)^2)}{4M_\eta^2}\;,\quad \tilde\delta=\frac{M_c^2-M_d^2}{s}\;.
\end{aligned}
\tag{A.74}
$$

A.3.2 Resummed amplitudes

In order to estimate the effects of higher-order corrections we iterate the bubble diagrams and the external vertex of the non-trivial two-loop graph. A diagrammatic expression of this iteration is shown in Fig. 2.3. Here we show the results including isospin violation. For the bubble chain a coupled-channel resummation can be performed analogously to Ref. [226]. We obtain

$$
\begin{aligned}
\mathcal{M}_n^{\mathrm{u}}(s_1,s_2,s_3) &= \frac{2L(s_1)C_x(s_1)J_{+-}(s_1)+K(s_1)\Big[C_{00}(s_1)J_{00}(s_1)-2\chi(s_1)J_{+-}(s_1)J_{00}(s_1)\Big]}{1-2C_{+-}(s_1)J_{+-}(s_1)-C_{00}(s_1)J_{00}(s_1)+2\chi(s_1)J_{+-}(s_1)J_{00}(s_1)}\\
&\quad+(s_1\leftrightarrow s_2)+(s_1\leftrightarrow s_3)\;,\\
\mathcal{M}_c^{\mathrm{u}}(s_1,s_2,s_3) &= \frac{2C_{+0}(s_1)J_{+0}(s_1)L'(s_1)}{1-2C_{+0}(s_1)J_{+0}(s_1)}-\frac{\tilde E'_{+0}(s_1,s_2,s_3)\tilde L(s_1)J_{+0}(s_1)}{1-E_{+0}(s_1)J_{+0}(s_1)}+(s_1\leftrightarrow s_2)\\
&\quad+\frac{2L(s_3)\Big[C_{+-}(s_3)J_{+-}(s_3)-2\chi(s_3)J_{+-}(s_3)J_{00}(s_3)\Big]+K(s_3)C_x(s_3)J_{00}(s_3)}{1-2C_{+-}(s_3)J_{+-}(s_3)-C_{00}(s_3)J_{00}(s_3)+2\chi(s_3)J_{+-}(s_3)J_{00}(s_3)}\;,
\end{aligned}
\tag{A.75}
$$

where

$$
\begin{aligned}
\chi(s_i) &= C_{+-}(s_i)C_{00}(s_i)-C_x(s_i)^2\;,\\
\tilde E'_{+0}(s_1,s_2,s_3) &= \Big[E_{+0}+G_{+0}(s_i-s_{+0}^{\mathrm{thr}})\Big]\frac{q_{+0}^2(s_1)}{3s_1M_\eta}\Big(s_1(s_3-s_2)+\Delta_\pi(M_\pi^2-M_\eta^2)\Big)\;,
\end{aligned}
$$

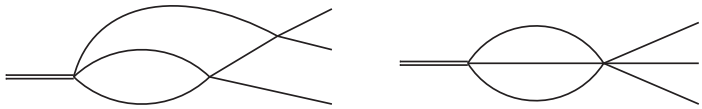

Figure A.7: Two-loop graphs with three-particle cuts in the physical region.

$$E_{+0}(s_i) = \frac{4q_{+0}^2(s_i)}{3}\Big[E_{+0} + G_{+0}(s_i - s_{+0}^{\rm thr})\Big] \ , \qquad G_{+0} = 3\pi b_1 \ , \tag{A.76}$$

and b_1 is the P-wave effective range. Additionally, we performed a resummation of the external vertex of the non-trivial two-loop diagram. This can be achieved by replacing the outer vertex in Eqs. (A.68) and (A.70) according to

$$\begin{aligned}
C_{00}(s_i) &\to \frac{C_{00}(s_i) - 2\chi(s_i)J_{+-}(s_i)}{1 - C_{00}(s_i)J_{00}(s_i) - 2C_{+-}(s_i)J_{+-}(s_i) + 2\chi(s_i)J_{+-}(s_i)J_{00}(s_i)} \ , \\
C_x(s_i) &\to \frac{C_x(s_i)}{1 - C_{00}(s_i)J_{00}(s_i) - 2C_{+-}(s_i)J_{+-}(s_i) + 2\chi(s_i)J_{+-}(s_i)J_{00}(s_i)} \ , \\
C_{+0}(s_i) &\to \frac{C_{+0}(s_i)}{1 - 2C_{+0}(s_i)J_{+0}(s_i)} \ , \qquad E_{+0}^{(\pm)}(s_1,s_2,s_3) \to \frac{E'^{(\pm)}_{+0}(s_1,s_2,s_3)}{1 - E_{+0}(s_1)J_{+0}(s_1)} \ , \\
C_{+-}(s_i) &\to \frac{C_{+-}(s_i) - \chi(s_i)J_{00}(s_i)}{1 - C_{00}(s_i)J_{00}(s_i) - 2C_{+-}(s_i)J_{+-}(s_i) + 2\chi(s_i)J_{+-}(s_i)J_{00}(s_i)} \ ,
\end{aligned} \tag{A.77}$$

with

$$E'^{(\pm)}_{+0}(s_1,s_2,s_3) = \Big[E_{+0} + G_{+0}(s_i - s_{+0}^{\rm thr})\Big]\left[\frac{(s_1(\pm\Delta_\pi))(s_3 - s_2 + \Delta_\pi)}{2M_\eta Q_1^0} - \Delta_\pi\right] . \tag{A.78}$$

A.4 Comment on imaginary parts of two-loop diagrams

In our analysis of the non-relativistic $\eta \to 3\pi$ decay amplitude, we have neglected the imaginary parts of the non-trivial two-loop graphs, see Fig. A.7 (left). The loop function $F(s)$ (in the simplified notation introduced for the equal-mass case in Section 2.4) given in Appendix A.3.1 strictly speaking only corresponds to the *real* part of this diagram. At leading order in the ϵ expansion, its *imaginary* part is given by

$$\mathrm{Im}\, F(s) = -\frac{1}{\sqrt{3}(32\pi)^2}\frac{(M_\eta - 3M_\pi)^2}{M_\pi^2} + \mathcal{O}(\epsilon^6) \ . \tag{A.79}$$

We therefore confirm that $\mathrm{Im}\, F(s) = \mathcal{O}(\epsilon^4)$, while the real part of the same diagram already starts at $\mathcal{O}(\epsilon^2)$. The imaginary part is due to the three-pion cut and only arises because the η is unstable, $M_\eta > 3M_\pi$. It stems from a part of the non-relativistic loop integral in which one of the propagators is non-singular, and therefore yields a result very similar to that of the sunset graph Fig. A.7 (right), which in the non-relativistic framework can only arise when introducing (very small) six-pion vertices [25, 33]. The three-pion cut causes a non-vanishing imaginary part of the isospin amplitudes $\mathcal{M}_I(s)$ already at threshold $s = 4M_\pi^2$.

It is obvious that $\mathrm{Im}\, F(s)$ can only contribute to the amplitude's squared modulus at $\mathcal{O}(a_{\pi\pi}^3\epsilon^5)$ via interference with one-loop terms, and is therefore naturally suppressed compared to the real part at two-loop order. What is less clear is its relative importance compared to

the imaginary parts generated at three loops by the unitarization prescription Eq. (2.44). The latter contributes to $|\mathcal{M}|^2$ at $\mathcal{O}(a_{\pi\pi}^4\epsilon^4)$, i.e. it is suppressed in powers of $a_{\pi\pi}$, but enhanced in ϵ. By investigating the imaginary part of the dominant isospin $I = 0$ amplitude $\mathcal{M}_0(s)$, with Eq. (A.79) added appropriately to the representation Eq. (2.39), we find that the two-loop imaginary part is suppressed by more than a factor of 30 relative to the one-loop piece at the center of the Dalitz plot, and by roughly a factor of 2 relative to the three-loop part. This suppression grows even stronger when considering derivatives of the amplitude, as s-dependence in $\operatorname{Im} F(s)$ is even further suppressed in ϵ, see Eq. (A.79). We therefore neglect these terms of $\mathcal{O}(ia_{\pi\pi}^2\epsilon^4)$ in our analysis, and consider their effects to be safely included in our error estimates due to partial higher-order resummation. The smallness of the imaginary parts due to three-pion cuts is in accordance with findings from ChPT at two loops [60] as well as from dispersion relations [76].

Appendix B

Non-perturbative methods: Dispersion relations

B.1 On the uniqueness of the amplitude decomposition

In the following we will show that the decomposition of the $\eta' \to \eta\pi\pi$ amplitude Eq. (3.25) is not unique. In fact, we claim that it will remain invariant under the transformation (3.61), which has rather severe consequences on the number of the independent subtraction constants: we can eliminate two of these so that the system is significantly more constrained. We will follow a very similar argument for $\eta \to 3\pi$ from Ref. [227] and define the following functions,

$$\begin{aligned} \mathcal{M}_0^{\text{inv}}(s) &= c_1 + c_2(s - s_{\eta'}) \ , \\ \mathcal{M}_0^{\pi\eta,\text{inv}}(t) &= -\frac{c_1}{2} + c_2(t - s_{\eta'}) \ , \end{aligned} \tag{B.1}$$

which plugged into Eq. (3.49) fulfill

$$\hat{\mathcal{M}}_0^{\text{inv}}(s) = -\mathcal{M}_0^{\text{inv}}(s) \ , \qquad \hat{\mathcal{M}}_0^{\pi\eta,\text{inv}}(t) = -\mathcal{M}_0^{\pi\eta,\text{inv}}(t) \ . \tag{B.2}$$

This is hardly surprising since a polynomial function has of course a vanishing discontinuity. Cast into the Omnès form of the dispersion relations Eq. (3.56) we can write

$$\begin{aligned} \frac{\mathcal{M}_0^{\text{inv}}(s)}{\Omega_0(s)} &= P_0(s) - \frac{s^4}{\pi}\int\limits_{s_0}^{\infty} \frac{d\mu_0(s')}{s'(s'-s)}\mathcal{M}_0^{\text{inv}}(s') \ , \\ \frac{\mathcal{M}_0^{\pi\eta,\text{inv}}(t)}{\Omega_0^{\pi\eta}(t)} &= P_0^{\pi\eta}(t) - \frac{t^3}{\pi}\int\limits_{t_0}^{\infty} \frac{d\mu_0^{\pi\eta}(t')}{t'(t'-t)}\mathcal{M}_0^{\pi\eta,\text{inv}}(t') \ , \end{aligned} \tag{B.3}$$

where we defined

$$d\mu_0(s') = ds' \frac{\sin\delta_0(s')}{|\Omega_0(s')|s'^3} \ , \qquad d\mu_0^{\pi\eta}(t') = dt' \frac{\sin\delta_0^{\pi\eta}(t')}{|\Omega_0^{\pi\eta}(t')|t'^2} \ . \tag{B.4}$$

We have to find a suitable representation of the inverse of the Omnès function $\Omega(s)$. For that we calculate its discontinuity,

$$\text{disc}\,\frac{1}{\Omega(s)} = \frac{\Omega(s-i\epsilon) - \Omega(s+i\epsilon)}{\Omega(s+i\epsilon)\Omega(s-i\epsilon)} = -\frac{\sin\delta(s)}{|\Omega(s)|} \ , \tag{B.5}$$

where we used $\Omega(s \pm i\epsilon) = |\Omega(s)|e^{\pm i\delta(s)}$. We can now write down a dispersion relation for the inverse Omnès function. To that end we note that since $\Omega_0(s)$ behaves as s^{-2}, the inverse Omnès function has to be quadratic in s. This suggests a dispersion relation with three subtractions, which can be fixed by the value of the Omnès function and its first and second derivative at the origin. We thus obtain

$$\frac{1}{\Omega_0(s)} = 1 - \omega_0 s - \tilde{\omega}_0 s^2 - \frac{s^3}{\pi}\int_{s_0}^{\infty} \frac{d\mu_0(s')}{s'-s} \,, \tag{B.6}$$

with

$$\omega_0 = \frac{1}{\pi}\int_{s_0}^{\infty} ds' \frac{\delta_0(s')}{s'^2} \,, \qquad \tilde{\omega}_0 = \frac{1}{\pi}\int_{s_0}^{\infty} ds' \frac{\delta_0(s')}{s'^3} - \frac{\omega_0^2}{2} \,. \tag{B.7}$$

The $\pi\eta$ Omnès function goes as $1/t$ for $t \to \infty$ and thus the inverse is linear in t, so that

$$\frac{1}{\Omega_0^{\pi\eta}(t)} = 1 - \omega_0^{\pi\eta} t - \frac{t^2}{\pi}\int_{t_0}^{\infty} \frac{d\mu_0^{\pi\eta}(t')}{t'-t} \,, \tag{B.8}$$

with

$$\omega_0^{\pi\eta} = \frac{1}{\pi}\int_{t_0}^{\infty} dt' \frac{\delta_0^{\pi\eta}(t')}{t'^2} \,. \tag{B.9}$$

Inserting Eqs. (B.6) and (B.8) in Eq. (B.3), we find

$$\begin{aligned}
(1 - \omega_0 s - \tilde{\omega}_0 s^2)\mathcal{M}_0^{\text{inv}}(s) &= P_0(s) - \frac{s^3}{\pi}\int_{s_0}^{\infty} d\mu_0(s')\left\{\frac{\mathcal{M}_0^{\text{inv}}(s') - \mathcal{M}_0^{\text{inv}}(s)}{s'-s} - \frac{\mathcal{M}_0^{\text{inv}}(s')}{s'}\right\} \,, \\
(1 - \omega_0^{\pi\eta} t)\mathcal{M}_0^{\pi\eta,\text{inv}}(t) &= P_0^{\pi\eta}(t) - \frac{t^2}{\pi}\int_{t_0}^{\infty} d\mu_0^{\pi\eta}(t')\left\{\frac{\mathcal{M}_0^{\pi\eta,\text{inv}}(t') - \mathcal{M}_0^{\pi\eta,\text{inv}}(t)}{t'-t} - \frac{\mathcal{M}_0^{\pi\eta,\text{inv}}(t')}{t'}\right\} \,.
\end{aligned} \tag{B.10}$$

With Eq. (B.1) this leads to

$$\begin{aligned}
P_0(s) &= m_0 + (c_2 - m_0\omega_0)s - (c_2\omega_0 + m_0\tilde{\omega}_0)s^2 - (c_2\tilde{\omega}_0 + m_0\tau_0)s^3 \,, \\
P_0^{\pi\eta}(t) &= m_0^{\pi\eta} + (c_2 - m_0^{\pi\eta}\omega_0^{\pi\eta})t - (c_2\omega_0^{\pi\eta} + m_0^{\pi\eta}\tau_0^{\pi\eta})t^2 \,,
\end{aligned} \tag{B.11}$$

where we defined the constants

$$m_0 = c_1 - c_2 s_{\eta'} \,, \quad \tau_0 = \frac{1}{\pi}\int_{s_0}^{\infty} \frac{d\mu_0(s')}{s'} \,, \quad m_0^{\pi\eta} = -\frac{c_1}{2} - c_2 s_{\eta'} \,, \quad \tau_0^{\pi\eta} = \frac{1}{\pi}\int_{t_0}^{\infty} \frac{d\mu_0^{\pi\eta}(t')}{t'} \,. \tag{B.12}$$

We can thus absorb the additional polynomial contributions in the subtraction constants of $P_0(s)$ and $P_0^{\pi\eta}(t)$. The dispersion integrals therefore remain invariant under this transformation. The above discussion also has ramifications for $\omega/\phi \to 3\pi$: naively one might expect that the additional subtraction constant can be eliminated by virtue of Eq. (4.2). However, the above discussion implies that in order to eliminate the second subtraction constant, one has to introduce a third one. It is thus justified to use a system with two independent subtraction constants in $\omega/\phi \to 3\pi$.

B.2 Analytic structure of the inhomogeneities

In this section we discuss the analytic structure of the remaining angular integrals of Section 3.3.4. The discussion is largely analogous, however, in this channel it turns out that the most convenient way to proceed is to separate integration over the amplitudes $M_0(s')$ and $M_0^{\pi\eta}(u')$. Performing a change of the integration variable according to

$$\begin{aligned} z'_t &= -\frac{1}{\kappa_{\pi\eta}(t)}\Big(2s' - 3s_{\eta'} + t + \frac{\Delta_{\eta'\pi}\Delta_{\eta\pi}}{t}\Big) \,, \\ z'_t &= \frac{1}{\kappa_{\pi\eta}(t)}\Big(2u' - 3s_{\eta'} + t - \frac{\Delta_{\eta'\pi}\Delta_{\eta\pi}}{t}\Big) \,, \end{aligned} \tag{B.13}$$

for $\langle \mathcal{M}_0 \rangle^-$ and $\langle \mathcal{M}_0^{\pi\eta} \rangle^+$, respectively, neglecting again the $\pi\eta$ P wave, leads to

$$\hat{\mathcal{M}}_0^{\pi\eta}(t) = \frac{1}{\kappa_{\pi\eta}(t)}\Big\{ \int_{\mathcal{C}'_s} ds' \mathcal{M}_0(s') + \int_{\mathcal{C}'_u} du' \mathcal{M}_0^{\pi\eta}(u') \Big\} \,, \tag{B.14}$$

where $\mathcal{C}'_s$ is the integration contour in the complex s'-plane with endpoints

$$s'_\pm(t) = \frac{1}{2}\Big(3s_{\eta'} - t - \frac{\Delta_{\eta'\pi}\Delta_{\eta\pi}}{t} \mp \kappa_{\pi\eta}(t)\Big) \,,$$

and $\mathcal{C}'_u$ is the integration contour in the complex u'-plane with endpoints

$$u'_\pm(t) = \frac{1}{2}\Big(3s_{\eta'} - t + \frac{\Delta_{\eta'\pi}\Delta_{\eta\pi}}{t} \pm \kappa_{\pi\eta}(t)\Big) \,. \tag{B.15}$$

The endpoints are displayed in Figs. B.1 and B.2. The correct analytic continuation of the integration contour for $\mathcal{C}'_s$ is given as:

I) $(M_\eta + M_\pi)^2 < t < (M_{\eta'}^2 + M_\eta^2 - 2M_\pi^2)/2$: $\kappa_{\pi\eta}(t)$ is purely real. The integration contour runs infinitesimally above the two-pion cut from $s_+(t)$ to $s_-(t)$,

$$\begin{aligned} s_+(t) &= \frac{1}{2}\big(3s_{\eta'} - t - \Delta_{\eta'\pi}\Delta_{\eta\pi} - \tilde{\kappa}_{\pi\eta}(t)\big) + i\epsilon \,, \\ s_-(t) &= \frac{1}{2}\big(3s_{\eta'} - t - \Delta_{\eta'\pi}\Delta_{\eta\pi} + \tilde{\kappa}_{\pi\eta}(t)\big) + i\epsilon \,. \end{aligned} \tag{B.16}$$

II) $(M_{\eta'}^2 + M_\eta^2 - 2M_\pi^2)/2 < t < (M_{\eta'} - M_\pi)^2$: $s_+(t)$ runs smoothly around the two-pion threshold into the lower half of the complex t-plane and continues infinitesimally below the cut. $s_-(t)$ stays above the cut. We have

$$\begin{aligned} s_+(t) &= \frac{1}{2}\big(3s_{\eta'} - t - \Delta_{\eta'\pi}\Delta_{\eta\pi} - \tilde{\kappa}_{\pi\eta}(t)\big) - i\epsilon \,, \\ s_-(t) &= \frac{1}{2}\big(3s_{\eta'} - t - \Delta_{\eta'\pi}\Delta_{\eta\pi} + \tilde{\kappa}_{\pi\eta}(t)\big) + i\epsilon \,. \end{aligned} \tag{B.17}$$

III) $(M_{\eta'} - M_\pi)^2 < t < (M_{\eta'} + M_\pi)^2$: $\kappa_{\pi\eta}(t)$ is purely imaginary. The endpoints have to follow the trajectory according to

$$\begin{aligned} s_+(t) &= \frac{1}{2}\big(3s_{\eta'} - t - \Delta_{\eta'\pi}\Delta_{\eta\pi} - i\tilde{\kappa}_{\pi\eta}(t)\big) \,, \\ s_-(t) &= \frac{1}{2}\big(3s_{\eta'} - t - \Delta_{\eta'\pi}\Delta_{\eta\pi} + i\tilde{\kappa}_{\pi\eta}(t)\big) \,. \end{aligned} \tag{B.18}$$

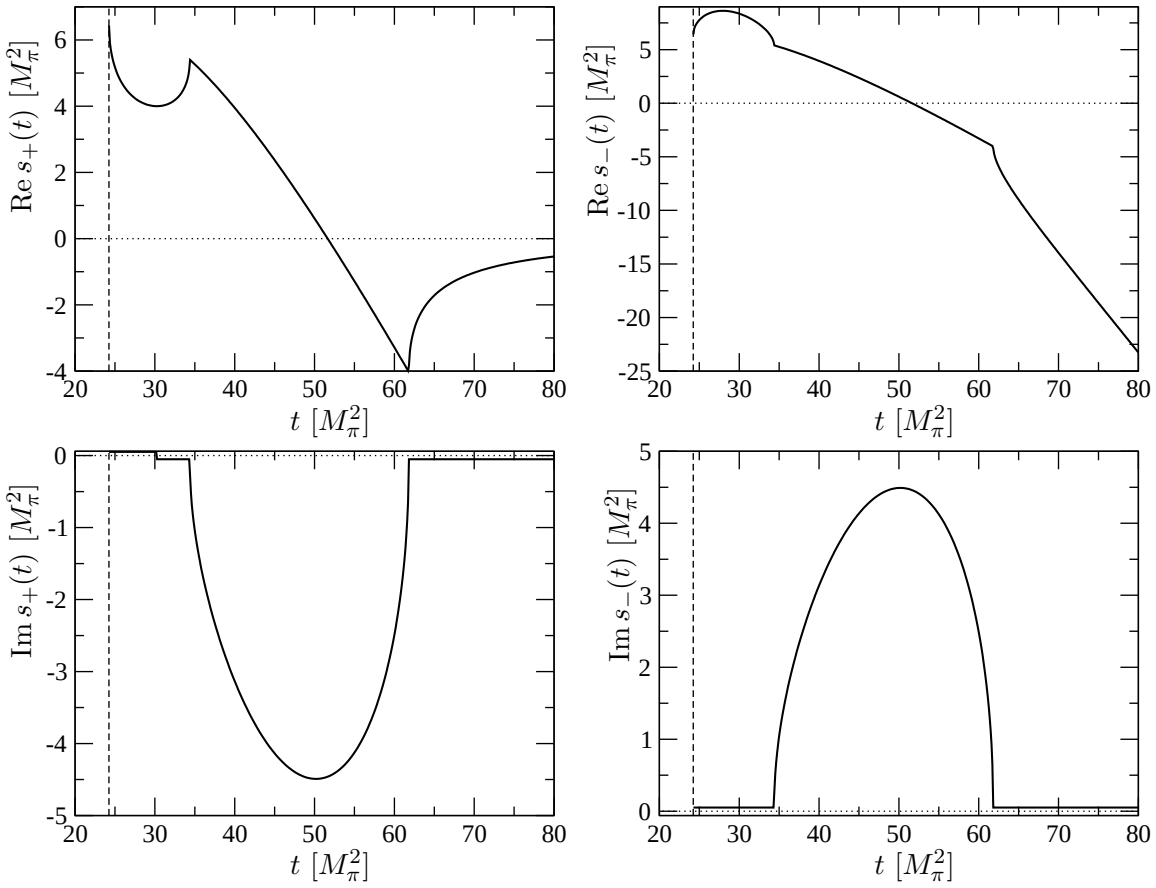

Figure B.1: Real (top) and imaginary (bottom) part of the endpoints $s_\pm(t)$ of the integration contour $\mathcal{C}'_s$. The dashed vertical line denotes the threshold $t = (M_\eta + M_\pi)^2$.

IV) $(M_{\eta'} + M_\pi)^2 < t$: $\kappa_{\pi\eta}(t)$ is again purely real and the endpoints follow the trajectories

$$s_+(t) = \frac{1}{2}\big(3s_{\eta'} - t - \Delta_{\eta'\pi}\Delta_{\eta\pi} + \tilde{\kappa}_{\pi\eta}(t)\big) \ ,$$
$$s_-(t) = \frac{1}{2}\big(3s_{\eta'} - t - \Delta_{\eta'\pi}\Delta_{\eta\pi} - \tilde{\kappa}_{\pi\eta}(t)\big) \ . \tag{B.19}$$

The contour in the complex s'-plane is completely analogous to Fig. 3.4 with the only exception that $s_+(t)$ and $s_-(t)$ have to be interchanged, and the threshold starts at $s = 4M_\pi^2$. For $\mathcal{C}'_u$ we have:

I) $(M_\eta+M_\pi)^2 < t < (M_\eta\Delta_{\eta'\pi}-M_\pi\Delta_{\eta\pi})/(M_\eta+M_\pi)$: $\kappa_{\pi\eta}(t)$ is purely real. The integration contour runs infinitesimally above the $\pi\eta$ cut from $u_-(t)$ to $u_+(t)$,

$$u_+(t) = \frac{1}{2}\big(3s_{\eta'} - t + \Delta_{\eta'\pi}\Delta_{\eta\pi} + \tilde{\kappa}_{\pi\eta}(t)\big) + i\epsilon \ ,$$
$$u_-(t) = \frac{1}{2}\big(3s_{\eta'} - t + \Delta_{\eta'\pi}\Delta_{\eta\pi} - \tilde{\kappa}_{\pi\eta}(t)\big) + i\epsilon \ . \tag{B.20}$$

II) $(M_\eta\Delta_{\eta'\pi} - M_\pi\Delta_{\eta\pi})/(M_\eta + M_\pi) < t < (M_{\eta'} - M_\pi)^2$: $u_-(t)$ continues smoothly around the $\pi\eta$ threshold into the lower half of the complex t-plane and continues below the cut.

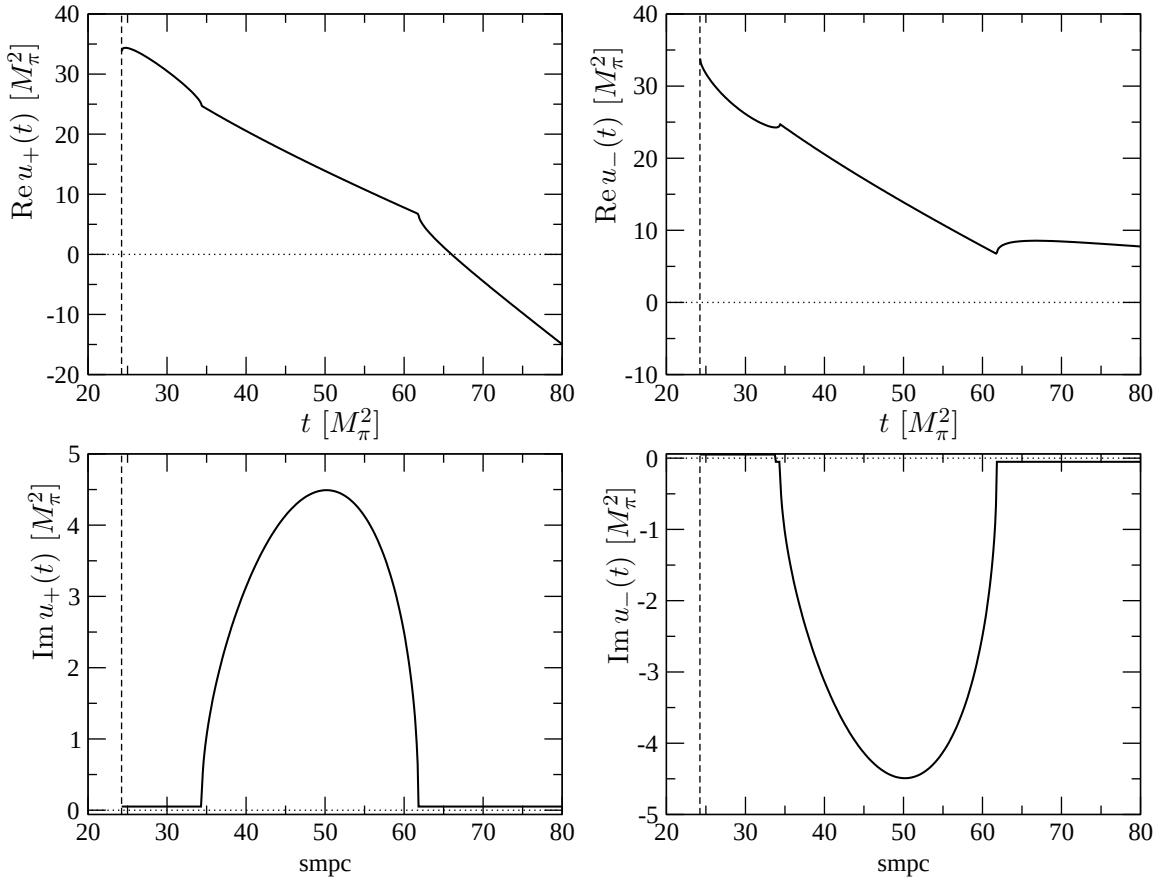

Figure B.2: Real (top) and imaginary (bottom) part of the endpoints $u_\pm(t)$ of the integration contour $\mathcal{C}'_u$. The dashed vertical line denotes the threshold $t = (M_\eta + M_\pi)^2$.

$u_+(t)$ stays above the cut. One finds

$$u_+(t) = \frac{1}{2}\big(3s_{\eta'} - t + \Delta_{\eta'\pi}\Delta_{\eta\pi} + \tilde{\kappa}_{\pi\eta}(t)\big) + i\epsilon \ ,$$
$$u_-(t) = \frac{1}{2}\big(3s_{\eta'} - t + \Delta_{\eta'\pi}\Delta_{\eta\pi} - \tilde{\kappa}_{\pi\eta}(t)\big) - i\epsilon \ . \tag{B.21}$$

III) $(M_{\eta'} - M_\pi)^2 < t < (M_{\eta'} + M_\pi)^2$: $\kappa_{\pi\eta}(t)$ is purely imaginary. The endpoints are given as

$$u_+(t) = \frac{1}{2}\big(3s_{\eta'} - t + \Delta_{\eta'\pi}\Delta_{\eta\pi} + i\tilde{\kappa}_{\pi\eta}(t)\big) \ ,$$
$$u_-(t) = \frac{1}{2}\big(3s_{\eta'} - t + \Delta_{\eta'\pi}\Delta_{\eta\pi} - i\tilde{\kappa}_{\pi\eta}(t)\big) \ . \tag{B.22}$$

IV) $(M_{\eta'} + M_\pi)^2 < t$: $\kappa_{\pi\eta}(t)$ is purely real and the endpoints follow the trajectories

$$u_+(t) = \frac{1}{2}\big(3s_{\eta'} - t + \Delta_{\eta'\pi}\Delta_{\eta\pi} - \tilde{\kappa}_{\pi\eta}(t)\big) \ ,$$
$$u_-(t) = \frac{1}{2}\big(3s_{\eta'} - t + \Delta_{\eta'\pi}\Delta_{\eta\pi} + \tilde{\kappa}_{\pi\eta}(t)\big) \ . \tag{B.23}$$

The trajectories in the complex u-plane are again completely analogous to Fig. 3.4.

B.3 Numerical treatment of the P-wave dispersion integral

In this section we resume the discussion of Section 3.4.3 about the numerical treatment of the dispersion integral Eq. (3.91) and consider the case $n = 1$. This is relevant for the calculations performed in Chapters 4 and 5. Obviously the case $s' = a$ merits some additional discussion. While the integrand itself is still diverging as $1/(a - s')$, we now have to find a way to amend the factor of $1/(a - s')^{3/2}$ in the numerator. We proceed exactly as before with a case-by-case study.

- $s_0 < s < b$: s is part of the integration interval, and again we split the integration interval further:

  - $s < a$: we need to take care of the singularity $s' = s$ in the integration interval from s_0 to p, and of $s' = a$ in the interval from p to b. One finds

$$\begin{aligned}\mathcal{I}(s) = &\int_{s_0}^{p} ds' \frac{\mathcal{H}(s') - \mathcal{H}(s)}{s'^m(s' - s)} + \mathcal{H}(s)\mathcal{R}(s, s_0, p) \\ &+ \int_{p}^{b} ds' \frac{\mathcal{G}(s') - \mathcal{G}(a) - (s' - a)\mathcal{G}'(a)}{(a - s')^{3/2}(s' - s)} \\ &+ \frac{\mathcal{G}(a)}{s - a}\Big(\frac{2}{\sqrt{a - p}} + \frac{2i}{\sqrt{b - a}} - \mathcal{Q}(s, a, p, b)\Big) + \mathcal{G}'(a)\mathcal{Q}(s, a, p, b) \\ &+ \int_{b}^{\Lambda^2} ds' \frac{\mathcal{G}(s')}{(a - s')^{3/2}(s' - s)} \,, \end{aligned} \tag{B.24}$$

    where we have added and subtracted $\mathcal{H}(s)$ and $\mathcal{G}(a) + (s' - a)\mathcal{G}'(a)$ in the respective integrals, $\mathcal{R}(s, x, y)$ and $\mathcal{Q}(s, a, x, y)$ are defined in Eqs. (3.96) and (3.97), and the additional terms are obtained from evaluating

$$\int_{x}^{y} ds' \frac{1}{(a - s)^{3/2}(s' - s)} = \frac{1}{s - a}\Big(\frac{2}{\sqrt{a - x}} + \frac{2i}{\sqrt{y - a}} - \mathcal{Q}(s, a, x, y)\Big) \,. \tag{B.25}$$

    The remaining integrals may again be solved numerically. The procedure is similar to the one in Section 3.4.3, only now we represent $\mathcal{G}(s')$ as

$$\mathcal{G}(s') \simeq \mathcal{G}(a) + \mathcal{G}'(a)(a - s') + g_0(a - s')^{3/2} + g_1(a - s')^2 + g_2(a - s')^{5/2} + \dots \,. \tag{B.26}$$

    Since the numerical determination of the derivative $\mathcal{G}'(a)$ is not well behaved, we choose to use $\mathcal{G}'(a)$ as an additional coefficient that is fitted along with g_0, g_1. The ratio thus becomes

$$\frac{\mathcal{G}(s') - \mathcal{G}(a) - \mathcal{G}'(a)(a - s')}{(a - s')^{3/2}} \simeq g_0 + g_1(a - s')^{1/2} + g_2(a - s') + \dots \,, \tag{B.27}$$

    and is necessarily finite.

  - $s > a$: the singularity $s' = s$ lies in the integration interval from p to b, and $s' = a$ in the interval s_0 to p. We thus have

$$\mathcal{I}(s) = \int_{s_0}^{p} ds' \frac{\mathcal{G}(s') - \mathcal{G}(a) - (s' - a)\mathcal{G}'(a)}{(a - s')^{3/2}(s' - s)}$$

$$+\frac{\mathcal{G}(a)}{s-a}\Big(\frac{2}{\sqrt{a-s_0}}+\frac{2i}{\sqrt{p-a}}-\mathcal{Q}(s,a,s_0,p)\Big)+\mathcal{G}'(a)\mathcal{Q}(s,a,s_0,p)$$
$$+\int_p^b ds'\frac{\mathcal{H}(s')-\mathcal{H}(s)}{s'^m(s'-s)}+\mathcal{H}(s)\mathcal{R}(s,p,b)+\int_b^{\Lambda^2} ds'\frac{\mathcal{G}(s')}{(a-s')^{3/2}(s'-s)}\ . \tag{B.28}$$

- $s>b$: $s'-s$ is located in the integration interval from b to Λ^2, and we find

$$\mathcal{I}(s)=\int_{s_0}^b ds'\frac{\mathcal{G}(s')-\mathcal{G}(a)-(s'-a)\mathcal{G}'(a)}{(a-s')^{3/2}(s'-s)}$$
$$+\frac{\mathcal{G}(a)}{s-a}\Big(\frac{2}{\sqrt{a-s_0}}+\frac{2i}{\sqrt{b-a}}-\mathcal{Q}(s,a,s_0,b)\Big)+\mathcal{G}'(a)\mathcal{Q}(s,a,s_0,b)$$
$$+\int_b^{\Lambda^2} ds'\frac{\mathcal{H}(s')-\mathcal{H}(s)}{s'^m(s'-s)}+\mathcal{H}(s)\mathcal{R}(s,b,\Lambda^2)\ . \tag{B.29}$$

- $s<s_0$ and s complex: s is not port of the integration interval and we only have to amend the singularity at $s'=a$, thus

$$\mathcal{I}(s)=\int_{s_0}^b ds'\frac{\mathcal{G}(s')-\mathcal{G}(a)-(s'-a)\mathcal{G}'(a)}{(a-s')^{3/2}(s'-s)}$$
$$+\frac{\mathcal{G}(a)}{s-a}\Big(\frac{2}{\sqrt{a-s_0}}+\frac{2i}{\sqrt{\Lambda^2-a}}-\mathcal{Q}(s,a,s_0,\Lambda^2)\Big)+\mathcal{G}'(a)\mathcal{Q}(s,a,s_0,\Lambda^2)\ . \tag{B.30}$$

B.4 On the size of higher partial waves in $\omega \to 3\pi$

In this Appendix, we investigate the potential uncertainty in our amplitude solution due to the omission of discontinuities in higher partial waves for $\omega \to 3\pi$, the next higher one being the F wave. We wish to emphasize to begin with that higher partial waves do not vanish for the solution $\mathcal{F}(s,t,u)$: projecting onto the F wave (in the s-channel)

$$f_3(s)=-\frac{7}{16}\int_{-1}^1 dz_s\big(5z_s^4-6z_s^2+1\big)\mathcal{F}(s,t,u)\ , \tag{B.31}$$

where $z_s=\cos\theta_s=(t-u)/\kappa(s)$, yields contributions from the t- and u-channel P-wave amplitudes. $f_3(s)$ thus calculated just happens to be *real*. To generalize our approach and also include F-wave discontinuities, we may amend the decomposition (4.9) according to

$$\mathcal{F}(s,t,u)=\mathcal{F}(s)+\mathcal{F}(t)+\mathcal{F}(u)+P_3'(z_s)\mathcal{G}(s)+P_3'(z_t)\mathcal{G}(t)+P_3'(z_u)\mathcal{G}(u)\ , \tag{B.32}$$

where $\mathcal{G}(s)$ again only has a right-hand cut, and $z_t=(s-u)/\kappa(t)$, $z_u=(s-t)/\kappa(u)$. The discontinuities of P and F wave are expressed by the relations

$$\begin{aligned}\operatorname{disc} f_1(s)&=\operatorname{disc}\mathcal{F}(s)=2i\big(\mathcal{F}(s)+\hat{\mathcal{F}}(s)\big)\theta(s-4M_\pi^2)\sin\delta_1^1(s)e^{-i\delta_1^1(s)}\ ,\\ \operatorname{disc} f_3(s)&=\operatorname{disc}\mathcal{G}(s)=2i\big(\mathcal{G}(s)+\hat{\mathcal{G}}(s)\big)\theta(s-4M_\pi^2)\sin\delta_3^1(s)e^{-i\delta_3^1(s)}\ ,\end{aligned} \tag{B.33}$$

where $\delta_3^1(s)$ is the $\pi\pi$ F-wave phase shift, and the inhomogeneities are now given by

$$\hat{\mathcal{F}}(s)=3\langle(1-z_s^2)(\mathcal{F}+P_3'\mathcal{G})\rangle(s)\ ,$$

$$\hat{\mathcal{G}}(s) = -\frac{7}{4}\langle\big(5z_s^4 - 6z_s^2 + 1\big)(\mathcal{F} + P_3'\mathcal{G})\rangle(s) \ . \tag{B.34}$$

Note that, in Eq. (B.34), the notation of angular averaging $\langle\ldots\rangle$ is generalized compared to Eq. (4.18) in the sense that the argument of P_3' is taken to be z_t, reexpressed in terms of s and z_s. We will now proceed to estimate the potential size of the F-wave discontinuity contribution $\mathcal{G}(s)$ by calculating the effects of the $\rho_3(1690)$ resonance.

B.4.1 The $\boldsymbol{\rho_3(1690)}$

The spin-3 resonance $\rho_3(1690)$ is described in terms of a totally symmetric third-rank tensor field $\boldsymbol{\rho}_{\mu\nu\lambda} = \rho^a_{\mu\nu\lambda}\tau^a$ (of isospin $I = 1$), which is subject to the constraints

$$\partial^\mu \boldsymbol{\rho}_{\mu\nu\lambda} = 0 \ , \qquad g^{\mu\nu}\boldsymbol{\rho}_{\mu\nu\lambda} = 0 \ . \tag{B.35}$$

The numerator of its propagator in momentum space involves the polarization sum [228]

$$\begin{aligned} P^{\nu_1\nu_2\nu_3}_{\mu_1\mu_2\mu_3} &= \frac{1}{6}\sum_{P\{\nu_1\nu_2\nu_3\}}\bigg\{X^{\nu_1}_{\mu_1}X^{\nu_2}_{\mu_2}X^{\nu_3}_{\mu_3} - \frac{1}{5}\Big(X_{\mu_1\mu_2}X^{\nu_1\nu_2}X^{\nu_3}_{\mu_3} \\ &\qquad + X^{\nu_1}_{\mu_1}X_{\mu_2\mu_3}X^{\nu_2\nu_3} + X_{\mu_1\mu_3}X^{\nu_2}_{\mu_2}X^{\nu_1\nu_3}\Big)\bigg\} \ , \\ X_{\alpha\beta} &= -g_{\alpha\beta} + \frac{p_\alpha p_\beta}{M^2_{\rho_3}} \ , \end{aligned} \tag{B.36}$$

where the sum runs over all possible permutations of the indices $\{\nu_1, \nu_2, \nu_3\}$. The simplest ρ_3 interaction Lagrangians with $\pi\pi$ and $\pi\omega$ are given by

$$\mathcal{L}_{\rho_3} = \frac{g_{\rho_3\pi\pi}}{4F_\pi^2}\langle\boldsymbol{\rho}_{\mu\nu\lambda}\big[\partial^\mu\boldsymbol{\pi}, \partial^\nu\partial^\lambda\boldsymbol{\pi}\big]\rangle + \frac{g_{\rho_3\pi\omega}}{2F_\pi}\epsilon^{\lambda\alpha\beta\gamma}\langle\boldsymbol{\rho}_{\mu\nu\lambda}\partial^\mu\partial_a\boldsymbol{\pi}\rangle\partial^\nu\partial_\beta\omega_\gamma \ , \tag{B.37}$$

where $\boldsymbol{\pi} = \pi^a\tau^a$ denotes the isotriplet of pion fields, and ω_μ the isosinglet ω vector field. From Eq. (B.37), we can calculate the partial decay widths of the ρ_3 into $\pi\pi$ and $\pi\omega$ to be

$$\begin{aligned} \Gamma(\rho_3 \to \pi\pi) &= \frac{g^2_{\rho_3\pi\pi}}{4480\pi F_\pi^4 M^2_{\rho_3}}\big(M^2_{\rho_3} - 4M^2_\pi\big)^{7/2} \ , \\ \Gamma(\rho_3 \to \pi\omega) &= \frac{g^2_{\rho_3\pi\omega}}{13440\pi F_\pi^2 M^7_{\rho_3}}\lambda\big(M^2_{\rho_3}, M^2_\omega, M^2_\pi\big)^{7/2} \ , \end{aligned} \tag{B.38}$$

which show the expected phase-space dependence for the decay of a spin-3 particle. From $M_{\rho_3} = (1688.8 \pm 2.1)\,\text{MeV}$, $\Gamma_{\rho_3} = (161 \pm 10)\,\text{MeV}$, $\mathcal{B}(\rho_3 \to \pi\pi) = (23.6 \pm 1.3)\%$, $\mathcal{B}(\rho_3 \to \pi\omega) = (16 \pm 6)\%$, and $F_\pi = 92.2\,\text{MeV}$ [87], we therefore deduce

$$|g_{\rho_3\pi\pi}| = 0.056 \pm 0.005 \, , \quad |g_{\rho_3\pi\omega}| = (1.2 \pm 0.5)\,\text{GeV}^{-2} \, . \tag{B.39}$$

Having fixed the coupling constants of the Lagrangian (B.37), we can proceed to calculate the impact of the ρ_3 resonance on the decay $\omega \to 3\pi$. The exchange of a ρ_3 in the s-channel, see Fig. B.3, yields a contribution to $\mathcal{G}(s)$ as defined in Eq. (B.32) according to

$$\mathcal{G}_{\rho_3}(s) = C_F\,\frac{M^2_{\rho_3}}{M^2_{\rho_3} - s}\frac{\kappa^2(s)}{M^4_\omega} \ , \quad C_F = \frac{g_{\rho_3\pi\pi}g_{\rho_3\pi\omega}M^4_\omega}{60F_\pi^3 M^2_{\rho_3}} \ . \tag{B.40}$$

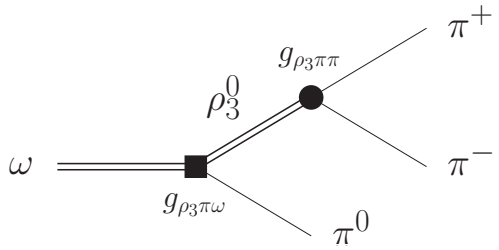

Figure B.3: Feynman diagram for the $\rho_3(1690)$-exchange contribution to $\omega \to 3\pi$ (in the s-channel).

$\kappa^2(s)/M_\omega^4$ is a dimensionless kinematic factor characteristic for the F wave. The remaining effective coupling C_F is numerically evaluated from the above to be

$$|C_F| \approx (1.4 \pm 0.5) \times 10^{-4}\, F_\pi^{-3} \ . \tag{B.41}$$

For illustration, we compare this to the simplified P-wave amplitude $\mathcal{F}(s)$ as given by vector-meson dominance, e.g. according to the hidden-local-symmetry (HLS) formalism [229, 230],

$$\mathcal{F}_{\rm HLS}(s) = C_P\, \frac{M_\rho^2}{M_\rho^2 - s} \ , \quad C_P = \frac{N_c\, g}{8\pi^2 F_\pi^3} \ , \tag{B.42}$$

where $N_c = 3$ is the number of colors, $g \approx 5.8$ is the universal vector coupling, and we have used the simplest choice for the anomalous HLS couplings, $c_1 - c_2 = c_3 = 1$ [165, 166, 230]. In this case, the effective coupling constant is

$$C_P \approx 0.22\, F_\pi^{-3} \ . \tag{B.43}$$

Comparing Eqs. (B.41) and (B.43), we see that the coupling constant alone, i.e. before application of the F-wave phase-space factors, suppresses the F-wave vs. the P-wave contribution by three orders of magnitude.

B.4.2 The $\omega \to 3\pi$ F wave

We therefore have strong indication that the $\omega \to 3\pi$ F wave $f_3(s) = \mathcal{G}(s) + \hat{\mathcal{G}}(s)$ is dominated by the term in $\hat{\mathcal{G}}(s)$ given by the projection of the crossed-channel P-wave terms. With the simplified amplitude (B.42), we can calculate this contribution even analytically, eschewing all complications of path deformation in the complete description. The result is

$$\begin{aligned} \hat{\mathcal{G}}_{\rm HLS}(s) &= -C_P \frac{2M_\rho^2}{M_\rho^2 - \frac{1}{2}(3s_0 - s)} \frac{7}{8\bar{\kappa}^4} \left(\frac{5 - 6\bar{\kappa}^2 + \bar{\kappa}^4}{2\bar{\kappa}} \log\frac{1+\bar{\kappa}}{1-\bar{\kappa}} - \frac{15 - 13\bar{\kappa}^2}{3} \right) , \\ \bar{\kappa} &= \frac{\kappa(s)}{2M_\rho^2 - 3s_0 + s} \ . \end{aligned} \tag{B.44}$$

In Fig. B.4, we plot the function $C_P^{-1} M_\omega^4 \kappa^{-2}(s) \times \hat{\mathcal{G}}_{\rm HLS}(s)$, which is seen to vary between 0.53 and 0.14 in the physical region $2M_\pi \le \sqrt{s} \le M_\omega - M_\pi$. In view of Eq. (B.40), this is to be compared to the scale $C_F/C_P \approx 10^{-3}$ for the ρ_3-induced F-wave contribution. The conclusion is that we expect neglected terms to yield only percent-level corrections even to the $\omega \to 3\pi$ F wave.

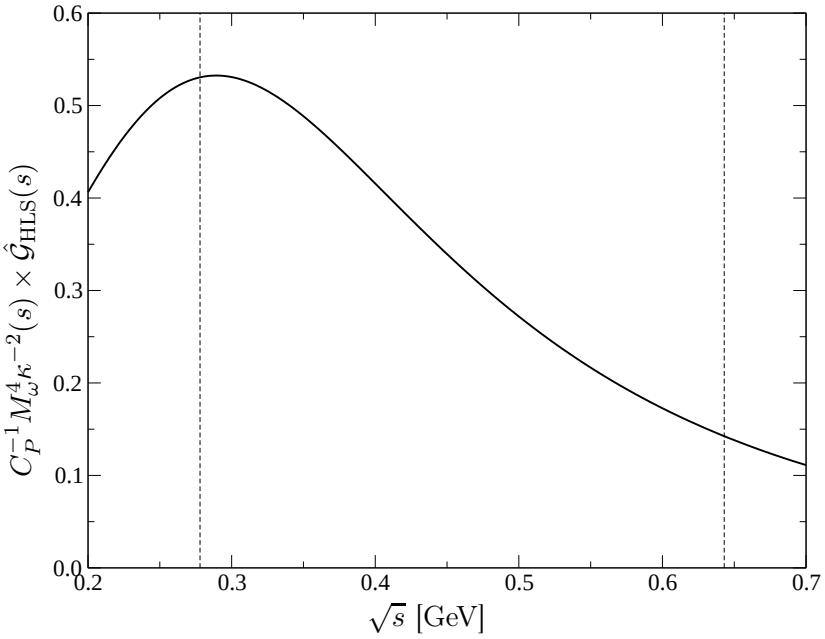

Figure B.4: The function $C_P^{-1} M_\omega^4 \kappa^{-2}(s) \times \hat{\mathcal{G}}_{\rm HLS}(s)$, characterizing the F-wave projection of the t- and u-channel P-wave amplitudes; for details, see text. The vertical dashed lines indicate the boundaries of the physical region for $\omega \to 3\pi$.

It remains to ask to what extent the assumption of the F wave being purely real is justified. Ref. [41] provides a simple analytic parameterization of the $\pi\pi$ F-wave phase shift, according to which we find, at the upper limits of the phase space accessible in $\omega \to 3\pi$ and $\phi \to 3\pi$,

$$\begin{aligned} \delta_3^1\big(s = (M_\omega - M_\pi)^2\big) &\approx 1 \times 10^{-4} \ , \\ \delta_3^1\big(s = (M_\phi - M_\pi)^2\big) &\approx 7 \times 10^{-4} \ , \end{aligned} \tag{B.45}$$

which corresponds to 0.06° and 0.4°, respectively. The F-wave phase is tiny in all the accessible phase space; neglecting the imaginary part is an approximation way below the accuracy of our decay amplitude representation.

B.4.3 Comparison to the pion–pion F wave

Finally, we wish to briefly point out that the hierarchy suggested for the $\omega \to 3\pi$ F wave—complete dominance of t-channel exchange over the s-channel resonance tail at low energies—should not come as a big surprise, looking at the comparable situation in pion–pion scattering. The ρ_3 contribution to the $\pi\pi$ F wave that follows from the Lagrangian (B.37) is given by

$$t_3^1(s)_{\rho_3} = \frac{g_{\rho_3\pi\pi}^2}{8960\pi F_\pi^4} \frac{(s - 4M_\pi^2)^3}{M_{\rho_3}^2 - s} \ . \tag{B.46}$$

This yields a contribution to the F-wave scattering length according to

$$(a_3^1)_{\rho_3} = \frac{g_{\rho_3\pi\pi}^2}{140\pi F_\pi^4 M_{\rho_3}^2} \approx 2.6 \times 10^{-7} M_\pi^{-6} \ , \tag{B.47}$$

to be compared with a phenomenological value of $a_3^1 \approx 5.4\times10^{-5} M_\pi^{-6}$ [37]: the ρ_3 contribution to the scattering length is suppressed by more than two orders of magnitude. The leading-order prediction in chiral perturbation theory at one loop, in contrast, yields [16]

$$a_3^1 = \frac{11}{94080\pi^3 F_\pi^4 M_\pi^2} + \mathcal{O}(M_\pi^0) \approx 2.0 \times 10^{-5} M_\pi^{-6} \,, \tag{B.48}$$

which is entirely given by (t- and u-channel) loop effects.

B.5 Contribution from higher resonances

In order to estimate the potential influence of higher P-wave resonances ($\rho'(1450)$, $\rho''(1700)$) on the $V \to 3\pi$ decays, we follow an approach recently suggested in connection with the pion vector form factor [231]. There, the following form factor representation has been fitted to the high-precision data for $\tau^- \to \pi^-\pi^0\nu_\tau$ from Belle [201]:

$$\begin{aligned} F_\pi^V(s) = {} & \frac{M_\rho^2 + s(\gamma\, e^{i\phi_1} + \delta\, e^{i\phi_2})}{M_\rho^2 - s - iM_\rho\Gamma_\rho(s)} \exp\left\{-\frac{sA_\pi(s)}{96\pi^2 F_\pi^2}\right\} \\ & - \frac{\gamma\, s\, e^{i\phi_1}}{M_{\rho'}^2 - s - iM_{\rho'}\Gamma_{\rho'}(s)} \exp\left\{-\frac{s\Gamma_{\rho'} A_\pi(s)}{\pi M_{\rho'}^3 \sigma_\pi^3(M_{\rho'}^2)}\right\} \\ & - \frac{\delta\, s\, e^{i\phi_2}}{M_{\rho''}^2 - s - iM_{\rho''}\Gamma_{\rho''}(s)} \exp\left\{-\frac{s\Gamma_{\rho''} A_\pi(s)}{\pi M_{\rho''}^3 \sigma_\pi^3(M_{\rho''}^2)}\right\}, \end{aligned} \tag{B.49}$$

where

$$\begin{aligned} A_\pi(s) &= \log\frac{M_\pi^2}{M_\rho^2} + \frac{8M_\pi^2}{s} - \frac{5}{3} + \sigma_\pi^3(s)\log\frac{1+\sigma_\pi(s)}{1-\sigma_\pi(s)}\,, \\ \Gamma_\rho(s) &= \frac{M_\rho s}{96\pi F_\pi^2}\sigma_\pi^3(s)\,, \\ \Gamma_{\rho',\rho''}(s) &= \frac{M_{\rho',\rho''}}{\sqrt{s}}\left(\frac{s-4M_\pi^2}{M_{\rho',\rho''}^2 - 4M_\pi^2}\right)^{3/2}\Gamma_{\rho',\rho''}\,. \end{aligned} \tag{B.50}$$

We have omitted a kaon-loop contribution to $\Gamma_\rho(s)$ (which also affects the real exponential multiplying the ρ propagator in Eq. (B.49)) that is retained in Ref. [231]: it does not have a large effect on the form factor, and we want to translate the above representation into a single-channel Omnès form with only elastic $\pi\pi$ rescattering included; Eq. (B.49) treats the ρ' and ρ'' as purely elastic resonances anyway. Besides, inelasticities in the $\pi\pi$ P wave in general, and in these higher P-wave resonances in particular, are expected to be dominated by 4π rather than $K\bar{K}$. Furthermore, our form of Eq. (B.49) is only valid above threshold, $s \geq 4M_\pi^2$.

Given the treatment of ρ', ρ'' as *elastic* resonances, we implement these into our formalism by just modifying the $\pi\pi$ P-wave phase shift accordingly and using the phase of the form factor in Eq. (B.49) as the input for a modified Omnès function. More precisely, we employ a phase identical to the one of Ref. [38] below $\sqrt{s} = 1.1\,\text{GeV}$, guide this smoothly to the phase of the form factor, which is used up to $\sqrt{s} = 1.8\,\text{GeV}$ (roughly the kinematic range accessible in $\tau^- \to \pi^-\pi^0\nu_\tau$ and therefore fitted in Ref. [231]), before guiding the phase smoothly to π. This phase, calculated for the central parameter values of the fit to the Belle data [201]

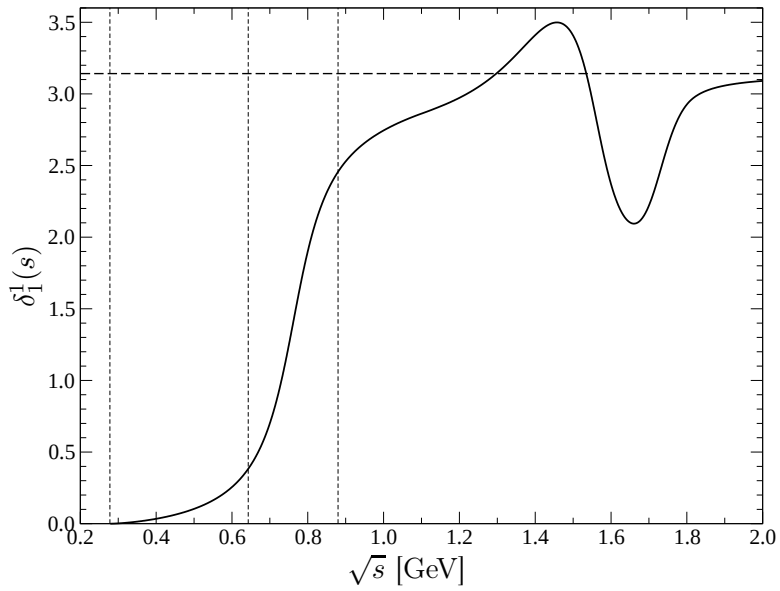

Figure B.5: Alternative P-wave phase shift $\delta_1^1(s)$ including the effects of $\rho'(1450)$ and $\rho''(1700)$ resonances; see text for details. The horizontal dashed line denotes the assumed asymptotic phase of π, the vertical dashed lines show the boundaries of the physical region for the two decays at $\sqrt{s} = 2M_\pi$, $M_\omega - M_\pi$, $M_\phi - M_\pi$.

given by $M_{\rho'} = 1.461\,\text{GeV}$, $\Gamma_{\rho'} = 0.353\,\text{GeV}$, $M_{\rho''} = 1.732\,\text{GeV}$, $\Gamma_{\rho''} = 0.141\,\text{GeV}$, $\gamma = 0.088$, $\delta = -0.024$, $\phi_1 = 0.6$, $\phi_2 = 0.8$ [232], is shown in Fig. B.5.

We refrain from investigating the variation within the error ranges on these parameters determined in Ref. [231]: we regard our estimate of higher-resonance contributions as indicative rather (and, as such, they will turn out to be entirely negligible) than as a precision study; which, as we will argue below, it cannot be as a matter of principle. We would like to point out that the form factor representation (B.49) allows to lead the phase smoothly to π: the higher resonances only induce "wiggles" in the phase. This is in contrast to the (weighted) sum of Breit–Wigner or Gounaris–Sakurai [233] functions as employed in the data fit in Ref. [201], which makes the phase rise by π for each resonance, leading to an asymptotic phase of rather 3π in the case at hand.

It turns out that the effect of using an alternative Omnès function, based on the phase shown in Fig. B.5, as the starting point for our dispersive representation of the $V \to 3\pi$ Dalitz plots is totally negligible: it changes the Dalitz plot distributions by less than 1%, and is therefore smaller than the other uncertainty sources identified in the main text. Figure B.5 makes this rather plausible: the deviations due to the two high-mass resonances show up only significantly above the energy range accessible in the ω and ϕ decays; furthermore, in the integral, the two "wiggles" of opposite sign tend to cancel out. Indeed, calculating e.g. the sum-rule value for the pion charge radius according to Eq. (4.21), we find

$$\langle r^2_{\text{sum}(\rho',\rho'')}\rangle^V_\pi \simeq 0.420\ \text{fm}^2\ , \tag{B.51}$$

very close to the value $0.415\ \text{fm}^2$ found with our "standard phase".

We need to recall the rather indicative nature of this investigation. We employ information on the ρ' and ρ'' resonances gained experimentally from the pion form factor measurement in

$\tau^- \to \pi^-\pi^0\nu_\tau$ [201]; it might be possible that they couple particularly strongly to $\omega\pi$, and thus have a more pronounced impact on $\omega \to 3\pi$. However, phenomenological information does not seem to support this: if we compare the pion form factor fit of Ref. [201] with an experimental analysis of $e^+e^- \to \omega\pi^0$ [195], both employing weighted sums of Breit–Wigner or Gounaris–Sakurai resonance propagators as fit functions, the pion form factor suggests a (modulus of the) coupling strength of the ρ' relative to the ρ of the order of 15%, while the $\omega\pi$ production measurement suggests a ρ'-to-ρ ratio of the order of 10% (despite the fact that here, the ρ is obviously sub-threshold, and phase space tends to emphasize the higher-resonance contributions in the cross section).

We therefore conclude that the influence of higher-mass P-wave resonance states on the $V \to 3\pi$ decays seems to be very small, and well contained in the uncertainty estimate we have performed in the main text.

Since the transition form factor is more sensitive to the precise shape of the pion vector form factor we have chosen to account for omitting the Kaon loop effects by performing the fit again using the various masses, widths, and coupling constants as fit parameters. We use the $\tau^- \to \pi^-\pi^0\nu_\tau$ data set of Ref. [201] thus avoiding additional complications arising from ρ–ω mixing and obtain

$$\begin{aligned} M_{\rho'} &= 1.44 \pm 0.01 \text{ GeV} , & \Gamma_{\rho'} &= 0.34 \pm 0.03 \text{ GeV} , \\ \gamma &= 0.097 \pm 0.009 , & \phi_1 &= 0.5 \pm 0.2 , \\ M_{\rho''} &= 1.71 \pm 0.05 \text{ GeV} , & \Gamma_{\rho''} &= 0.13 \pm 0.03 \text{ GeV} , \\ \delta &= -0.02 \pm 0.02 , & \phi_2 &= 1.1 \pm 0.6 . \end{aligned} \tag{B.52}$$

As expected our fit values are slightly different as compared to before, however the resonance parameters are still plausible.

B.6 Inelasticity parameter

In this appendix, we wish to briefly derive Eq. (4.33), following Ref. [122]. We introduce an inelasticity parameter $\eta(s)$ in the parameterization of the $\pi\pi$ P-wave amplitude (see Eq. (4.32)) according to

$$\sin\delta(s) e^{-i\delta(s)} \to \frac{1}{2i}\big(1 - \eta(s) e^{-2i\delta(s)}\big) . \tag{B.53}$$

Thus the unitarity relation for $\mathcal{F}(s)$ takes the following modified form

$$\operatorname{disc}\mathcal{F}(s) = \big(\mathcal{F}(s) + \hat{\mathcal{F}}(s)\big)\theta(s - 4M_\pi^2)\Big(1 - \eta(s) e^{-2i\delta(s)}\Big) . \tag{B.54}$$

For the homogeneous case $\hat{\mathcal{F}}(s) = 0$, we take the logarithm

$$\operatorname{disc}\log\mathcal{F}(s) = 2i\,\delta(s) - \log\eta(s) , \tag{B.55}$$

which leads to the modified Omnès solution

$$\begin{aligned} \tilde{\Omega}(s) &= \Omega(s) \exp\left\{ \frac{is}{2\pi} \int\limits_{16M_\pi^2}^{\infty} ds' \frac{\log\eta(s')}{s'(s'-s)} \right\} \\ &= \xi(s)\Xi(s)\Omega(s) , \end{aligned} \tag{B.56}$$

with

$$\xi(s) = \begin{cases} \eta^{-1/2}(s) & \text{above the cut,} \\ \eta^{1/2}(s) & \text{below the cut,} \\ 1 & \text{elsewhere,} \end{cases} \tag{B.57}$$

and

$$\Xi(s) = \exp\left\{ \frac{is}{2\pi} \int\limits_{16M_\pi^2}^{\infty} ds' \frac{\log \eta(s')}{s'(s'-s)} \right\} . \tag{B.58}$$

For the full solution of the unitarity relation (B.54) we use the product ansatz $\mathcal{F}(s) = \tilde{\Omega}(s)\psi(s)$ to obtain

$$\operatorname{disc} \psi(s) = \frac{\hat{\mathcal{F}}(s)\big(e^{i\delta(s)} - \eta(s)e^{-i\delta(s)}\big)}{\sqrt{\eta(s)}\Xi(s)|\Omega(s)|} . \tag{B.59}$$

Rewriting $\psi(s)$ into a dispersion relation finally leads to the full solution quoted in Eq. (4.33).

Bibliography

[1] S. Glashow, *Partial symmetries of weak interactions*, *Nucl.Phys.* **22** (1961) 579–588.

[2] S. Weinberg, *A model of leptons*, *Phys.Rev.Lett.* **19** (1967) 1264–1266.

[3] A. Salam and J. C. Ward, *Electromagnetic and weak interactions*, *Phys.Lett.* **13** (1964) 168–171.

[4] G. 't Hooft and M. Veltman, *Regularization and renormalization of gauge fields*, *Nucl.Phys.* **B44** (1972) 189–213.

[5] ATLAS Collaboration, G. Aad et al., *Observation of a new particle in the search for the Standard Model Higgs boson with the ATLAS detector at the LHC*, *Phys.Lett.* **B716** (2012) 1–29, [arXiv:1207.7214].

[6] CMS Collaboration, S. Chatrchyan et al., *Observation of a new boson at a mass of* 125 *GeV with the CMS experiment at the LHC*, *Phys.Lett.* **B716** (2012) 30–61, [arXiv:1207.7235].

[7] P. W. Higgs, *Broken symmetries, massless particles and gauge fields*, *Phys.Lett.* **12** (1964) 132–133.

[8] F. Englert and R. Brout, *Broken Symmetry and the Mass of Gauge Vector Mesons*, *Phys.Rev.Lett.* **13** (1964) 321–323.

[9] G. Guralnik, C. Hagen, and T. Kibble, *Global Conservation Laws and Massless Particles*, *Phys.Rev.Lett.* **13** (1964) 585–587.

[10] H. Fritzsch, M. Gell-Mann, and H. Leutwyler, *Advantages of the color octet gluon picture*, *Phys.Lett.* **B47** (1973) 365–368.

[11] S. Bethke, *The 2009 world average of* α_s, *Eur.Phys.J.* **C64** (2009) 689–703, [arXiv:0908.1135].

[12] M. Gell-Mann and F. Low, *Quantum electrodynamics at small distances*, *Phys.Rev.* **95** (1954) 1300–1312.

[13] D. Gross and F. Wilczek, *Ultraviolet behavior of nonabelian gauge theories*, *Phys.Rev.Lett.* **30** (1973) 1343–1346.

[14] H. D. Politzer, *Reliable perturbative results for strong interactions?*, *Phys.Rev.Lett.* **30** (1973) 1346–1349.

[15] S. Weinberg, *Phenomenological lagrangians*, *Physica* **A96** (1979) 327.

[16] J. Gasser and H. Leutwyler, *Low-energy theorems as precision tests of QCD*, *Phys.Lett.* **B125** (1983) 325.

[17] J. Gasser and H. Leutwyler, *Chiral perturbation theory to one loop*, *Annals Phys.* **158** (1984) 142.

[18] J. Gasser and H. Leutwyler, *Chiral perturbation theory: expansions in the mass of the strange quark*, *Nucl.Phys.* **B250** (1985) 465.

[19] J. Bijnens, G. Ecker, and J. Gasser, *Chiral perturbation theory*, `hep-ph/9411232`.

[20] G. Colangelo and G. Isidori, *An introduction to ChPT*, `hep-ph/0101264`.

[21] S. Scherer, *Introduction to chiral perturbation theory*, *Adv.Nucl.Phys.* **27** (2003) 277, [`hep-ph/0210398`].

[22] V. Bernard and U.-G. Meißner, *Chiral perturbation theory*, *Ann.Rev.Nucl.Part.Sci.* **57** (2007) 33–60, [`hep-ph/0611231`].

[23] B. Kubis, *An introduction to chiral perturbation theory*, `hep-ph/0703274`.

[24] W. Heisenberg and H. Euler, *Consequences of Dirac's theory of positrons*, *Z.Phys.* **98** (1936) 714–732, [`physics/0605038`].

[25] G. Colangelo, J. Gasser, B. Kubis, and A. Rusetsky, *Cusps in $K \to 3\pi$ decays*, *Phys.Lett.* **B638** (2006) 187–194, [`hep-ph/0604084`].

[26] M. Bissegger, A. Fuhrer, J. Gasser, B. Kubis, and A. Rusetsky, *Cusps in $K_L \to 3\pi$ decays*, *Phys.Lett.* **B659** (2008) 576–584, [`arXiv:0710.4456`].

[27] M. Bissegger, A. Fuhrer, J. Gasser, B. Kubis, and A. Rusetsky, *Radiative corrections in $K \to 3\pi$ decays*, *Nucl.Phys.* **B806** (2009) 178–223, [`arXiv:0807.0515`].

[28] C.-O. Gullström, A. Kupść, and A. Rusetsky, *Predictions for the cusp in $\eta \to 3\pi^0$ decay*, *Phys.Rev.* **C79** (2009) 028201, [`arXiv:0812.2371`].

[29] B. Kubis and S. P. Schneider, *The cusp effect in $\eta' \to \eta\pi\pi$ decays*, *Eur.Phys.J.* **C62** (2009) 511–523, [`arXiv:0904.1320`].

[30] A. Fuhrer, *Pion photoproduction in a nonrelativistic theory*, *Phys.Lett.* **B683** (2010) 172–177, [`arXiv:0909.3121`].

[31] A. Fuhrer, *Pion electroproduction in a nonrelativistic theory*, *Phys.Lett.* **B692** (2010) 130–135, [`arXiv:1007.0031`].

[32] B. Kubis, *Cusp effects in meson decays*, *EPJ Web Conf.* **3** (2010) 01008, [`arXiv:0912.3440`].

[33] J. Gasser, B. Kubis, and A. Rusetsky, *Cusps in $K \to 3\pi$ decays: a theoretical framework*, *Nucl.Phys.* **B850** (2011) 96–147, [`arXiv:1103.4273`].

[34] J. Gasser, V. Lyubovitskij, and A. Rusetsky, *Hadronic atoms in QCD + QED*, *Phys.Rept.* **456** (2008) 167–251, [arXiv:0711.3522].

[35] R. J. Eden, P. V. Landshoff, D. I. Olive, and J. C. Polkinghorne, *The analytic S-matrix*. Cambridge University Press, 1966.

[36] R. J. Eden, *Threshold behaviour in quantum field theory*, *Proc.Roy.Soc. A* **210** (1952) 388–404.

[37] B. Ananthanarayan, G. Colangelo, J. Gasser, and H. Leutwyler, *Roy equation analysis of $\pi\pi$ scattering*, *Phys.Rept.* **353** (2001) 207–279, [hep-ph/0005297].

[38] I. Caprini, G. Colangelo, and H. Leutwyler, *Regge analysis of the $\pi\pi$ scattering amplitude*, *Eur.Phys.J.* **C72** (2012) 1860, [arXiv:1111.7160].

[39] I. Caprini, G. Colangelo, and H. Leutwyler, *in preparation*, .

[40] R. Kamiński, J. Peláez, and F. Ynduráin, *The pion–pion scattering amplitude. III. Improving the analysis with forward dispersion relations and Roy equations*, *Phys.Rev.* **D77** (2008) 054015, [arXiv:0710.1150].

[41] R. García-Martín, R. Kamiński, J. Peláez, J. Ruiz de Elvira, and F. Ynduráin, *The Pion-pion scattering amplitude. IV: improved analysis with once subtracted Roy-like equations up to* 1100 *MeV*, *Phys.Rev.* **D83** (2011) 074004, [arXiv:1102.2183].

[42] C. Ditsche, M. Hoferichter, B. Kubis, and U.-G. Meißner, *Roy-Steiner equations for pion-nucleon scattering*, *JHEP* **1206** (2012) 043, [arXiv:1203.4758].

[43] M. Hoferichter, C. Ditsche, B. Kubis, and U.-G. Meißner, *Dispersive analysis of the scalar form factor of the nucleon*, *JHEP* **1206** (2012) 063, [arXiv:1204.6251].

[44] G. Colangelo, J. Gasser, and H. Leutwyler, *$\pi\pi$ scattering*, *Nucl.Phys.* **B603** (2001) 125–179, [hep-ph/0103088].

[45] M. Froissart, *Asymptotic behavior and subtractions in the Mandelstam representation*, *Phys.Rev.* **123** (1961) 1053–1057.

[46] A. Martin, *Unitarity and high-energy behavior of scattering amplitudes*, *Phys.Rev.* **129** (1963) 1432–1436.

[47] R. Cutkosky, *Singularities and discontinuities of Feynman amplitudes*, *J.Math.Phys.* **1** (1960) 429–433.

[48] K. M. Watson, *Some general relations between the photoproduction and scattering of π mesons*, *Phys.Rev.* **95** (1954) 228–236.

[49] R. Omnès, *On the solution of certain singular integral equations of quantum field theory*, *Nuovo Cim.* **8** (1958) 316–326.

[50] J. Gasser and U.-G. Meißner, *Chiral expansion of pion form-factors beyond one loop*, *Nucl.Phys.* **B357** (1991) 90–128.

[51] J. De Trocóniz and F. Ynduráin, *Precision determination of the pion form-factor and calculation of the muon $g-2$*, *Phys.Rev.* **D65** (2002) 093001, [hep-ph/0106025].

[52] H. Leutwyler, *Electromagnetic form-factor of the pion*, hep-ph/0212324.

[53] G. Colangelo, *Hadronic contributions to a_μ below one GeV*, *Nucl.Phys.Proc.Suppl.* **131** (2004) 185–191, [hep-ph/0312017].

[54] S. P. Schneider, B. Kubis, and C. Ditsche, *Rescattering effects in $\eta \to 3\pi$ decays*, *JHEP* **1102** (2011) 028, [arXiv:1010.3946].

[55] D. Sutherland, *Current algebra and the decay $\eta \to 3\pi$*, *Phys.Lett.* **23** (1966) 384.

[56] J. Bell and D. Sutherland, *Current algebra and $\eta \to 3\pi$*, *Nucl.Phys.* **B4** (1968) 315–325.

[57] J. A. Cronin, *Phenomenological model of strong and weak interactions in chiral $U(3) \times U(3)$*, *Phys.Rev.* **161** (1967) 1483–1494.

[58] H. Osborn and D. Wallace, *$\eta - \eta'$ mixing, $\eta \to 3\pi$ and chiral Lagrangians*, *Nucl.Phys.* **B20** (1970) 23–44.

[59] J. Gasser and H. Leutwyler, *$\eta \to 3\pi$ to One Loop*, *Nucl.Phys.* **B250** (1985) 539.

[60] J. Bijnens and K. Ghorbani, *$\eta \to 3\pi$ at Two Loops In Chiral Perturbation Theory*, *JHEP* **0711** (2007) 030, [arXiv:0709.0230].

[61] R. Baur, J. Kambor, and D. Wyler, *Electromagnetic corrections to the decays $\eta \to 3\pi$*, *Nucl.Phys.* **B460** (1996) 127–142, [hep-ph/9510396].

[62] C. Ditsche, B. Kubis, and U.-G. Meißner, *Electromagnetic effects in $\eta \to 3\pi$*, *PoS* **CD09** (2009) 043, [arXiv:0910.0210].

[63] Crystal Ball Collaboration, W. Tippens et al., *Determination of the quadratic slope parameter in $\eta \to 3\pi^0$ decay*, *Phys.Rev.Lett.* **87** (2001) 192001.

[64] Crystal Barrel Collaboration, A. Abele et al., *Decay dynamics of the process $\eta \to 3\pi^0$*, *Phys.Lett.* **B417** (1998) 193–196.

[65] Serpukhov-Brussels-Annecy(LAPP) and Soviet-CERN Collaboration, D. Alde et al., *Neutral decays of the η meson*, *Z.Phys.* **C25** (1984) 225–229.

[66] KLOE Collaboration, F. Ambrosino et al., *Measurement of the $\eta \to 3\pi^0$ slope parameter α with the KLOE detector*, *Phys.Lett.* **B694** (2010) 16–21, [arXiv:1004.1319].

[67] Crystal Ball at MAMI, TAPS, and A2 Collaboration, M. Unverzagt et al., *Determination of the Dalitz plot parameter α for the decay $\eta \to 3\pi^0$ with the Crystal Ball at MAMI-B*, *Eur.Phys.J.* **A39** (2009) 169–177, [arXiv:0812.3324].

[68] Crystal Ball at MAMI and A2 Collaboration, S. Prakhov et al., *Measurement of the slope parameter α for the $\eta \to 3\pi^0$ decay with the Crystal Ball at MAMI-C*, *Phys.Rev.* **C79** (2009) 035204, [arXiv:0812.1999].

[69] M. Achasov et al., *Dynamics of $\eta \to 3\pi^0$ decay*, *JETP Lett.* **73** (2001) 451–452.

[70] M. Bashkanov et al., *Measurement of the slope parameter for the $\eta \to 3\pi^0$ decay in the $pp \to pp\eta$ reaction*, *Phys.Rev.* **C76** (2007) 048201, [arXiv:0708.2014].

[71] WASA-at-COSY Collaboration, C. Adolph et al., *Measurement of the $\eta \to 3\pi^0$ Dalitz Plot Distribution with the WASA Detector at COSY*, *Phys.Lett.* **B677** (2009) 24–29, [arXiv:0811.2763].

[72] A. Neveu and J. Scherk, *Final-state interaction and current algebra in $K \to 3\pi$ and $\eta \to 3\pi$ decays*, *Annals Phys.* **57** (1970) 39–64.

[73] C. Roiesnel and T. N. Truong, *Resolution of the $\eta \to 3\pi$ problem*, *Nucl.Phys.* **B187** (1981) 293.

[74] J. Kambor, C. Wiesendanger, and D. Wyler, *Final state interactions and Khuri-Treiman equations in $\eta \to 3\pi$ decays*, *Nucl.Phys.* **B465** (1996) 215–266, [hep-ph/9509374].

[75] A. Anisovich and H. Leutwyler, *Dispersive analysis of the decay $\eta \to 3\pi$*, *Phys.Lett.* **B375** (1996) 335–342, [hep-ph/9601237].

[76] G. Colangelo, S. Lanz, and E. Passemar, *A New Dispersive Analysis of $\eta \to 3\pi$*, *PoS* **CD09** (2009) 047, [arXiv:0910.0765].

[77] G. Colangelo, S. Lanz, H. Leutwyler, and E. Passemar, *Determination of the light quark masses from $\eta \to 3\pi$*, *PoS* **EPS-HEP2011** (2011) 304.

[78] M. Zdráhal, K. Kampf, M. Knecht, and J. Novotný, *Analytical dispersive construction of $\eta \to 3\pi$ amplitude: first order in isospin breaking*, *Phys.Rev.* **D84** (2011) 114015, [arXiv:1103.0982].

[79] J. Bijnens and J. Gasser, *η decays at and beyond p^4 in chiral perturbation theory*, *Phys.Scripta* **T99** (2002) 34–44, [hep-ph/0202242].

[80] B. Borasoy and R. Nißler, *Hadronic η and η' decays*, *Eur.Phys.J.* **A26** (2005) 383–398, [hep-ph/0510384].

[81] M. Kolesár, *$\eta \to 3\pi$ in resummed χPT, talk given at: EuroFlavour2010, Munich, Germany, September 8–10, 2010.*

[82] KLOE Collaboration, F. Ambrosino et al., *Determination of $\eta \to \pi^+\pi^-\pi^0$ Dalitz plot slopes and asymmetries with the KLOE detector*, *JHEP* **0805** (2008) 006, [arXiv:0801.2642].

[83] P. Adlarson, *Studies of the decay $\eta \to \pi^+\pi^-\pi^0$ with WASA-at-COSY*, *PhD thesis, Uppsala University* (2012).

[84] Crystal Ball at MAMI Collaboration, M. Unverzagt, *η and η' Physics at MAMI*, *Nucl.Phys.Proc.Suppl.* **198** (2010) 174–181, [arXiv:0910.1331].

[85] N. Brambilla, E. Epelbaum, H.-W. Hammer, and U.-G. Meißner, *talk by Descotes-Genon in Strong interactions: From methods to structures*, arXiv:1104.0847.

[86] U.-G. Meißner, G. Müller, and S. Steininger, *Virtual photons in $SU(2)$ chiral perturbation theory and electromagnetic corrections to $\pi\pi$ scattering*, *Phys.Lett.* **B406** (1997) 154–160, [hep-ph/9704377].

[87] Particle Data Group, K. Nakamura et al., *Review of particle physics*, *J.Phys.* **G37** (2010) 075021.

[88] J. Stern, H. Sazdjian, and N. Fuchs, *What $\pi\pi$ scattering tells us about chiral perturbation theory*, *Phys.Rev.* **D47** (1993) 3814–3838, [hep-ph/9301244].

[89] M. Knecht, B. Moussallam, J. Stern, and N. Fuchs, *The low-energy $\pi\pi$ amplitude to one and two loops*, *Nucl.Phys.* **B457** (1995) 513–576, [hep-ph/9507319].

[90] H. Leutwyler, *Physics of the light quarks*, arXiv:0808.2825.

[91] J. Batley, A. Culling, G. Kalmus, C. Lazzeroni, D. Munday, et al., *Determination of the S-wave $\pi\pi$ scattering lengths from a study of $K^{\pm} \to \pi^{\pm}\pi^0\pi^0$ decays*, *Eur.Phys.J.* **C64** (2009) 589–608, [arXiv:0912.2165].

[92] M. Knecht and R. Urech, *Virtual photons in low-energy $\pi\pi$ scattering*, *Nucl.Phys.* **B519** (1998) 329–360, [hep-ph/9709348].

[93] M. Knecht and A. Nehme, *Electromagnetic corrections to charged pion scattering at low-energies*, *Phys.Lett.* **B532** (2002) 55–62, [hep-ph/0201033].

[94] Crystal Barrel Collaboration, A. Abele et al., *Momentum dependence of the decay $\eta \to \pi^+\pi^-\pi^0$*, *Phys.Lett.* **B417** (1998) 197–201.

[95] J. Layter, J. Appel, A. Kotlewski, W. Lee, S. Stein, and J. Thaler, *Study of dalitz-plot distributions of the decays $\eta \to \pi^+\pi^-\pi^0$ and $\eta \to \pi^+\pi^-\gamma$*, *Phys.Rev.* **D7** (1973) 2565–2568.

[96] R. Barlow, *Asymmetric systematic errors*, physics/0306138.

[97] G. D'Ambrosio, G. Isidori, A. Pugliese, and N. Paver, *Strong rescattering in $K \to 3\pi$ decays and low-energy meson dynamics*, *Phys.Rev.* **D50** (1994) 5767, [hep-ph/9403235].

[98] P. Adlarson, *private communication*.

[99] M. Gormley, E. Hyman, W.-Y. Lee, T. Nash, J. Peoples, C. Schultz, and S. Stein, *Experimental determination of the Dalitz plot distribution of the decays $\eta \to \pi^+\pi^-\pi^0$ and $\eta \to \pi^+\pi^-\gamma$, and the branching ratio $\eta \to \pi^+\pi^-\gamma/\eta \to \pi^+\pi^-\pi^0$*, *Phys.Rev.* **D2** (1970) 501–505.

[100] G. Amelino-Camelia, F. Archilli, D. Babusci, D. Badoni, G. Bencivenni, et al., *Physics with the KLOE-2 experiment at the upgraded DAϕNE*, *Eur.Phys.J.* **C68** (2010) 619–681, [arXiv:1003.3868].

[101] CLAS Collaboration, M. Amaryan et al., *Photoproduction and decay of light mesons*, *CAA-HS12-01, October 2012*.

[102] N. Khuri and S. Treiman, *Pion–pion Scattering and $K^{\pm} \to 3\pi$ decay*, *Phys.Rev.* **119** (1960) 1115–1121.

[103] S. Lanz, *Determination of the quark mass ratio Q from $\eta \to 3\pi$*, *PhD thesis, University of Bern* (2012).

[104] R. Kaiser and H. Leutwyler, *Large N_C in chiral perturbation theory*, *Eur.Phys.J.* **C17** (2000) 623–649, [hep-ph/0007101].

[105] R. Escribano, P. Masjuan, and J. J. Sanz-Cillero, *Chiral dynamics predictions for $\eta' \to \eta\pi\pi$*, *JHEP* **1105** (2011) 094, [arXiv:1011.5884].

[106] Riazuddin and S. Oneda, *Some remarks on the $(3, 3^*) \times (3^*, 3)$ breaking of chiral symmetry*, *Phys.Rev.Lett.* **27** (1971) 548–552.

[107] N. G. Deshpande and T. N. Truong, *Resolution of the $\eta' \to \eta\pi\pi$ puzzle*, *Phys.Rev.Lett.* **41** (1978) 1579.

[108] C. Singh and J. Pasupathy, *On the decay modes of the meson $\eta'(958)$ and chiral symmetry breaking*, *Phys.Rev.Lett.* **35** (1975) 1193–1195.

[109] A. H. Fariborz and J. Schechter, *$\eta' \to \eta\pi\pi$ decay as a probe of a possible lowest lying scalar nonet*, *Phys.Rev.* **D60** (1999) 034002, [hep-ph/9902238].

[110] N. Beisert and B. Borasoy, *The $\eta' \to \eta\pi\pi$ decay in $U(3)$ chiral perturbation theory*, *Nucl.Phys.* **A705** (2002) 433–454, [hep-ph/0201289].

[111] N. Beisert and B. Borasoy, *Hadronic decays of η and η' with coupled channels*, *Nucl.Phys.* **A716** (2003) 186–208, [hep-ph/0301058].

[112] R. Nißler, *Topics in three-flavour chiral dynamics*, *PhD thesis, University of Bonn* (2007).

[113] A. Blik, A. Gorin, S. Donskov, V. Kolosov, A. Lednev, et al., *Measurement of the matrix element for the decay $\eta' \to \eta\pi^0\pi^0$ with the GAMS-4π spectrometer*, *Phys.Atom.Nucl.* **72** (2009) 231–236.

[114] S. P. Schneider and B. Kubis, *Cusps in $\eta' \to \eta\pi\pi$ decays*, *PoS* **CD09** (2009) 120, [arXiv:0910.0200].

[115] S. P. Schneider, *The cusp effect in $\eta' \to \eta\pi\pi$ decays*, *Diploma thesis, University of Bonn* (2009).

[116] BESIII Collaboration, M. Ablikim et al., *Measurement of the Matrix Element for the Decay $\eta' \to \eta\pi^+\pi^-$*, *Phys.Rev.* **D83** (2011) 012003, [arXiv:1012.1117].

[117] V. Dorofeev et al., *Study of $\eta' \to \eta\pi^+\pi^-$ Dalitz plot*, *Phys.Lett.* **B651** (2007) 22–26, [hep-ph/0607044].

[118] G. R. Kalbfleisch, *Comments on the $\eta'(958)$: Branching ratio, linear matrix element and Dipion phase shift*, *Phys.Rev.* **D10** (1974) 916.

[119] CLEO Collaboration, R. A. Briere et al., *Rare decays of the η'*, *Phys.Rev.Lett.* **84** (2000) 26–30, [hep-ex/9907046].

[120] E. Byckling and K. Kajantie, *Particle Kinematics*. John Wiley & Sons Ltd, 1973.

[121] M. Zdráhal and J. Novotný, *Dispersive Approach to Chiral Perturbation Theory*, *Phys.Rev.* **D78** (2008) 116016, [arXiv:0806.4529].

[122] M. Walker, $\eta \to 3\pi$, *Master thesis, University of Bern* (1998).

[123] T. A. Lähde and U.-G. Meißner, *Improved analysis of J/ψ decays into a vector meson and two pseudoscalars*, *Phys.Rev.* **D74** (2006) 034021, [hep-ph/0606133].

[124] U.-G. Meißner and J. Oller, *$J/\psi \to \phi\pi\pi$ ($K\bar{K}$) decays, chiral dynamics and OZI violation*, *Nucl.Phys.* **A679** (2001) 671–697, [hep-ph/0005253].

[125] A. Vainshtein and V. I. Zakharov, *Remarks on Electromagnetic Form-Factors of Hadrons in the Quark Model*, *Phys.Lett.* **B72** (1978) 368.

[126] B. Moussallam, *N_f dependence of the quark condensate from a chiral sum rule*, *Eur.Phys.J.* **C14** (2000) 111–122, [hep-ph/9909292].

[127] V. Bernard, N. Kaiser, and U.-G. Meißner, *$\pi\eta$ scattering in QCD*, *Phys.Rev.* **D44** (1991) 3698–3701.

[128] M. Kolesár and J. Novotný, *$\pi\eta$ scattering and the resummation of vacuum fluctuation in three-flavour ChPT*, *Eur.Phys.J.* **C56** (2008) 231–266, [arXiv:0802.1289].

[129] C. Hanhart, B. Kubis, and J. Peláez, *Investigation of $a_0 - f_0$ mixing*, *Phys.Rev.* **D76** (2007) 074028, [arXiv:0707.0262].

[130] A. Gómez Nicola and J. Peláez, *Meson–meson scattering within one loop chiral perturbation theory and its unitarization*, *Phys.Rev.* **D65** (2002) 054009, [hep-ph/0109056].

[131] J. Oller, E. Oset, and J. Peláez, *Meson–meson interaction in a nonperturbative chiral approach*, *Phys.Rev.* **D59** (1999) 074001, [hep-ph/9804209].

[132] V. Baru, J. Haidenbauer, C. Hanhart, A. E. Kudryavtsev, and U.-G. Meißner, *Flatte-like distributions and the $a_0(980)/f_0(980)$ mesons*, *Eur.Phys.J.* **A23** (2005) 523–533, [nucl-th/0410099].

[133] J. Schwinger, *Chiral transformations*, *Phys.Rev.* **167** (1968) 1432–1436.

[134] P. Di Vecchia, F. Nicodemi, R. Pettorino, and G. Veneziano, *Large N, Chiral approach to pseudoscalar masses, mixings and decays*, *Nucl.Phys.* **B181** (1981) 318.

[135] S. Fajfer and J. Gérard, *Hadronic decays of η and η' in the large-N limit*, *Z.Phys.* **C42** (1989) 431.

[136] P. Herrera-Siklódy, *η and η' hadronic decays in $U(3)_L \times U(3)_R$ chiral perturbation theory*, hep-ph/9902446.

[137] J. Schechter and Y. Ueda, *General treatment of the breaking of chiral symmetry and scale invariance in the SU(3) sigma model*, *Phys.Rev.* **D3** (1971) 2874–2893.

[138] G. Ecker, *Chiral perturbation theory*, *Prog.Part.Nucl.Phys.* **35** (1995) 1–80, [hep-ph/9501357].

[139] J. Bijnens, E. Gámiz, E. Lipartia, and J. Prades, *QCD short distance constraints and hadronic approximations*, *JHEP* **0304** (2003) 055, [hep-ph/0304222].

[140] A. Pich, *Low-energy constants from resonance chiral theory*, *PoS* **CONFINEMENT8** (2008) 026, [arXiv:0812.2631].

[141] H. Leutwyler, *On the $1/N$ expansion in chiral perturbation theory*, *Nucl.Phys.Proc.Suppl.* **64** (1998) 223–231, [hep-ph/9709408].

[142] R. Kaiser and H. Leutwyler, *Pseudoscalar decay constants at large N_c*, hep-ph/9806336.

[143] S. L. Adler, *Consistency conditions on the strong interactions implied by a partially conserved axial vector current*, *Phys.Rev.* **137** (1965) B1022–B1033.

[144] S. L. Adler, *Consistency conditions on the strong interactions implied by a partially conserved axial-vector current. II*, *Phys.Rev.* **139** (1965) B1638–B1643.

[145] G. Ecker, J. Gasser, A. Pich, and E. de Rafael, *The Role of Resonances in Chiral Perturbation Theory*, *Nucl.Phys.* **B321** (1989) 311.

[146] G. Ecker, J. Gasser, H. Leutwyler, A. Pich, and E. de Rafael, *Chiral Lagrangians for Massive Spin 1 Fields*, *Phys.Lett.* **B223** (1989) 425.

[147] V. Cirigliano, G. Ecker, M. Eidemuller, R. Kaiser, A. Pich, et al., *Towards a consistent estimate of the chiral low-energy constants*, *Nucl.Phys.* **B753** (2006) 139–177, [hep-ph/0603205].

[148] V. Bernard, N. Kaiser, and U.-G. Meißner, *Chiral perturbation theory in the presence of resonances: Application to $\pi\pi$ and πK scattering*, *Nucl.Phys.* **B364** (1991) 283–320.

[149] J. Pelaez, *On the Nature of light scalar mesons from their large-N_C behavior*, *Phys.Rev.Lett.* **92** (2004) 102001, [hep-ph/0309292].

[150] G. Rios, C. Hanhart, and J. Pelaez, *N_C and M_π dependence of rho and sigma mesons from unitarized Chiral Perturbation Theory*, *AIP Conf.Proc.* **1322** (2010) 452–456, [arXiv:1101.1766].

[151] A. Kupść *private communication.*

[152] Z.-H. Guo and J. J. Sanz-Cillero, *$\pi\pi$ scattering lengths at $\mathcal{O}(p^6)$ revisited*, *Phys.Rev.* **D79** (2009) 096006, [arXiv:0903.0782].

[153] M. Jamin, J. A. Oller, and A. Pich, *S-wave $K\pi$ scattering in chiral perturbation theory with resonances*, *Nucl.Phys.* **B587** (2000) 331–362, [hep-ph/0006045].

[154] B. Moussallam, *Improved evaluation of the second class decay $\tau \to \eta\pi\nu_\tau$ in the standard model, talk given at: tau2012, Nagoya, Japan, September 8–10, 2010.*

[155] F. Niecknig, B. Kubis, and S. P. Schneider, *Dispersive analysis of $\omega \to 3\pi$ and $\phi \to 3\pi$ decays*, *Eur.Phys.J.* **C72** (2012) 2014, [arXiv:1203.2501].

[156] J. Bijnens, P. Gosdzinsky, and P. Talavera, *Vector meson masses in chiral perturbation theory*, *Nucl.Phys.* **B501** (1997) 495–517, [hep-ph/9704212].

[157] J. Bijnens, P. Gosdzinsky, and P. Talavera, *Matching the heavy vector meson theory*, *JHEP* **9801** (1998) 014, [hep-ph/9708232].

[158] J. Bijnens, P. Gosdzinsky, and P. Talavera, *Chiral corrections to vector meson decay constants*, *Phys.Lett.* **B429** (1998) 111–120, [hep-ph/9801418].

[159] P. C. Bruns and U.-G. Meißner, *Infrared regularization for spin-1 fields*, *Eur.Phys.J.* **C40** (2005) 97–119, [hep-ph/0411223].

[160] M. Lutz and S. Leupold, *On the radiative decays of light vector and axial-vector mesons*, *Nucl.Phys.* **A813** (2008) 96–170, [arXiv:0801.3821].

[161] S. Leupold and M. Lutz, *Hadronic three-body decays of light vector mesons*, *Eur.Phys.J.* **A39** (2009) 205–212, [arXiv:0807.4686].

[162] D. Djukanovic, J. Gegelia, A. Keller, and S. Scherer, *Complex-mass renormalization in chiral effective field theory*, *Phys.Lett.* **B680** (2009) 235–238, [arXiv:0902.4347].

[163] K. Kampf, J. Novotný, and J. Trnka, *Renormalization and additional degrees of freedom within the chiral effective theory for spin-1 resonances*, *Phys.Rev.* **D81** (2010) 116004, [arXiv:0912.5289].

[164] F. Klingl, N. Kaiser, and W. Weise, *Effective Lagrangian approach to vector mesons, their structure and decays*, *Z.Phys.* **A356** (1996) 193–206, [hep-ph/9607431].

[165] M. Benayoun, P. David, L. DelBuono, and O. Leitner, *A global treatment of VMD physics up to the ϕ: I. e^+e^- annihilations, anomalies and vector meson partial widths*, *Eur.Phys.J.* **C65** (2010) 211–245, [arXiv:0907.4047].

[166] M. Benayoun, P. David, L. DelBuono, and F. Jegerlehner, *Upgraded breaking of the HLS model: a full solution to the $\tau^- e^+ e^-$ and ϕ decay issues and its consequences on $g-2$ VMD estimates*, *Eur.Phys.J.* **C72** (2012) 1848, [arXiv:1106.1315].

[167] U.-G. Meißner, *Low-energy hadron physics from effective chiral Lagrangians with vector mesons*, *Phys.Rept.* **161** (1988) 213.

[168] I. Aitchison and R. Golding, *Relativistic three pion dynamics in the ω channel*, *J.Phys.* **G4** (1978) 43.

[169] KLOE Collaboration, A. Aloisio et al., *Study of the decay $\phi \to \pi^+\pi^-\pi^0$ with the KLOE detector*, *Phys.Lett.* **B561** (2003) 55–60, [hep-ex/0303016].

[170] R. Akhmetshin, V. Aulchenko, V. S. Banzarov, L. Barkov, N. Bashtovoy, et al., *Study of $\phi \to \pi^+\pi^-\pi^0$ with CMD-2 detector*, *Phys.Lett.* **B642** (2006) 203–209.

[171] WASA-at-COSY Collaboration, P. Adlarson et al., *poster contribution by L. Heijkenskjöld and S. Sawant Khan in: Proceedings of the second International PrimeNet Workshop*, arXiv:1204.5509.

[172] KLOE Collaboration, S. Giovannella, *private communication.*

[173] M. Jacob and G. Wick, *On the general theory of collisions for particles with spin*, *Annals Phys.* **7** (1959) 404–428.

[174] F. Niecknig, *Analysis of the ω and $\phi \to 3\pi$ Dalitz plot*, *Diploma thesis, University of Bonn* (2011).

[175] F.-K. Guo, C. Hanhart, F. J. Llanes-Estrada, and U.-G. Meißner, *Quark mass dependence of the pion vector form factor*, *Phys.Lett.* **B678** (2009) 90–96, [arXiv:0812.3270].

[176] J. Bijnens and P. Talavera, *Pion and kaon electromagnetic form factors*, *JHEP* **0203** (2002) 046, [hep-ph/0203049].

[177] R. Urech, *Virtual photons in chiral perturbation theory*, *Nucl.Phys.* **B433** (1995) 234–254, [hep-ph/9405341].

[178] G. Köpp, *Dispersion calculation of the transition form-factor $f_{\pi\omega\gamma}(t)$ with cut contributions*, *Phys.Rev.* **D10** (1974) 932–940.

[179] P. Büttiker, S. Descotes-Genon, and B. Moussallam, *A new analysis of πK scattering from Roy and Steiner type equations*, *Eur.Phys.J.* **C33** (2004) 409–432, [hep-ph/0310283].

[180] B. Moussallam, *private communication.*

[181] D. H. Cohen, D. Ayres, R. Diebold, S. Kramer, A. Pawlicki, et al., *Amplitude analysis of the K^-K^+ system produced in the reactions $\pi^-p \to K^-K^+n$ and $\pi^+n \to K^-K^+p$ at 6 GeV/c*, *Phys.Rev.* **D22** (1980) 2595.

[182] M. Hoferichter, B. Kubis, and D. Sakkas, *Extracting the chiral anomaly from $\gamma\pi \to \pi\pi$*, arXiv:1210.6793.

[183] S. P. Schneider, B. Kubis, and F. Niecknig, *The $\omega \to \pi^0\gamma^*$ and $\phi \to \pi^0\gamma^*$ transition form factors in dispersion theory*, *Phys.Rev.* **D86** (2012) 054013, [arXiv:1206.3098].

[184] F. Jegerlehner and A. Nyffeler, *The muon $g-2$*, *Phys.Rept.* **477** (2009) 1–110, [arXiv:0902.3360].

[185] J. Bijnens and J. Prades, *The hadronic light-by-light contribution to the muon anomalous magnetic moment: where do we stand?*, *Mod.Phys.Lett.* **A22** (2007) 767–782, [hep-ph/0702170].

[186] A. Faessler, C. Fuchs, and M. Krivoruchenko, *Dilepton spectra from decays of light unflavored mesons*, *Phys.Rev.* **C61** (2000) 035206, [nucl-th/9904024].

[187] S. Ivashyn, *Vector to pseudoscalar meson radiative transitions in chiral theory with resonances*, *Prob.Atomic Sci.Technol.* **2012N1** (2012) 179–182, [arXiv:1111.1291].

[188] R. Dzhelyadin et al., *Study of the electromagnetic transition form factor $\omega \to \pi^0\mu^+\mu^-$ decay*, *Phys.Lett.* **B102** (1981) 296.

[189] NA60 Collaboration, R. Arnaldi et al., *Study of the electromagnetic transition form-factors in $\eta \to \mu^+\mu^-\gamma$ and $\omega \to \mu^+\mu^-\pi^0$ decays with NA60*, *Phys.Lett.* **B677** (2009) 260–266, [arXiv:0902.2547].

[190] NA60 Collaboration, G. Usai, *Low mass dimuon production in proton-nucleus collisions at* 400 *GeV/c*, *Nucl.Phys.* **A855** (2011) 189–196.

[191] M. Achasov et al., *Study of conversion decays $\phi \to \eta e^+e^-$ and $\eta \to \gamma e^+e^-$ in the Experiment with SND Detector at the VEPP-2M Collider*, *Phys.Lett.* **B504** (2001) 275–281.

[192] KLOE-2 Collaboration, J. Zdebik, *Hadron physics at KLOE and KLOE-2*, *PoS* **QNP2012** (2012) 080.

[193] S. Pacetti, *Study of the $\phi - \pi^0$ transition form factor*, arXiv:0904.3684.

[194] M. Achasov et al., *The process $e^+e^- \to \omega\pi^0 \to \pi^0\pi^0\gamma$ up to* 1.4 *GeV*, *Phys.Lett.* **B486** (2000) 29–34, [hep-ex/0005032].

[195] CMD-2 Collaboration, R. Akhmetshin et al., *Study of the process $e^+e^- \to \omega\pi^0 \to \pi^0\pi^0\gamma$ in c.m. energy range* 920 *MeV* – 1380 *MeV at CMD-2*, *Phys.Lett.* **B562** (2003) 173–181, [hep-ex/0304009].

[196] KLOE Collaboration, F. Ambrosino et al., *Study of the process $e^+e^- \to \omega\pi^0$ in the ϕ-meson mass region with the KLOE detector*, *Phys.Lett.* **B669** (2008) 223–228, [arXiv:0807.4909].

[197] BABAR Collaboration, B. Aubert et al., *Measurements of $e^+e^- \to K^+K^-\eta$, $K^+K^-\pi^0$ and $K^0_S K^\pm\pi^\mp$ cross- sections using initial state radiation events*, *Phys.Rev.* **D77** (2008) 092002, [arXiv:0710.4451].

[198] L. Landsberg, *Electromagnetic decays of light mesons*, *Phys.Rept.* **128** (1985) 301–376.

[199] B. Kubis and R. Schmidt, *Radiative corrections in $K \to \pi l^+ l^-$ decays*, *Eur.Phys.J.* **C70** (2010) 219–231, [arXiv:1007.1887].

[200] B. Ananthanarayan, I. Caprini, and I. S. Imsong, *Implications of the recent high statistics determination of the pion electromagnetic form factor in the timelike region*, *Phys.Rev.* **D83** (2011) 096002, [arXiv:1102.3299].

[201] Belle Collaboration, M. Fujikawa et al., *High-statistics study of the $\tau^- \to \pi^-\pi^0\nu_\tau$ decay*, *Phys.Rev.* **D78** (2008) 072006, [arXiv:0805.3773].

[202] BABAR Collaboration, B. Aubert et al., *Precise measurement of the $e^+e^- \to \pi^+\pi^-(\gamma)$ cross section with the Initial State Radiation method at BABAR*, *Phys.Rev.Lett.* **103** (2009) 231801, [arXiv:0908.3589].

[203] KLOE Collaboration, F. Ambrosino et al., *Measurement of $\sigma(e^+e^- \to \pi^+\pi^-)$ from threshold to* 0.85 *GeV^2 using Initial State Radiation with the KLOE detector*, *Phys.Lett.* **B700** (2011) 102–110, [arXiv:1006.5313].

[204] C. Hanhart, *A new parameterization for the pion vector form factor*, *Phys.Lett.* **B715** (2012) 170–177, [arXiv:1203.6839].

[205] C. Terschlüsen and S. Leupold, *Electromagnetic transition form factors of light vector mesons*, *Phys.Lett.* **B691** (2010) 191–201, [arXiv:1003.1030].

[206] CMD-2 Collaboration, R. Akhmetshin et al., *Study of the ρ and ω meson decays into pseudoscalar meson and e^+e^- pair with the CMD-2 detector*, *Phys.Lett.* **B613** (2005) 29–38, [hep-ex/0502024].

[207] C. Terschlüsen and S. Leupold, *Electromagnetic transition form factors of mesons*, *Prog.Part.Nucl.Phys.* **67** (2012) 401–405, [arXiv:1111.4907].

[208] P. Adlarson et al., *talk by F.A. Khan in: Proceedings of the second International PrimeNet Workshop*, arXiv:1204.5509.

[209] B. Kubis, *The role of final-state interactions in Dalitz plot studies*, arXiv:1108.5866.

[210] B. Kubis, F. Niecknig, and S. P. Schneider, *On the role of final-state interactions in Dalitz plot studies*, *Nucl.Phys.Proc.Suppl.* **225-227** (2012) 75–79, [arXiv:1111.6799].

[211] N. Cabibbo, *Unitary symmetry and leptonic decays*, *Phys.Rev.Lett.* **10** (1963) 531–533.

[212] M. Kobayashi and T. Maskawa, *CP violation in the renormalizable theory of weak interaction*, *Prog.Theor.Phys.* **49** (1973) 652–657.

[213] C. Hanhart, *private communication.*

[214] S. Gardner, *Direct CP violation in untagged B meson decays*, *Phys.Lett.* **B553** (2003) 261–266, [hep-ph/0203152].

[215] S. Gardner and J. Tandean, *Observing direct CP violation in untagged B meson decays*, *Phys.Rev.* **D69** (2004) 034011, [hep-ph/0308228].

[216] I. Bediaga, I. Bigi, A. Gomes, G. Guerrer, J. Miranda, et al., *On a CP anisotropy measurement in the Dalitz plot*, *Phys.Rev.* **D80** (2009) 096006, [arXiv:0905.4233].

[217] I. Bediaga, J. Miranda, A. dos Reis, I. Bigi, A. Gomes, et al., *Second generation of 'Miranda Procedure' for CP violation in Dalitz studies of B (&D &τ) decays*, *Phys.Rev.* **D86** (2012) 036005, [arXiv:1205.3036].

[218] Les Nabis Collaboration, I. I. Bigi, S. Gardner, C. Hanhart, B. Kubis, T. Mannel, U.-G. Meißner, W. Ochs, J. A. Oller, J. R. Peláez, M. R. Pennington, A. Sibirtsev (*theory*), I. Bediaga, A. E. Bondar, A. Denig, T. J. Gershon, W. Gradl, B. T. Meadows, K. Peters, U. Wiedner, G. Wilkinson (*experiment*), et al.

[219] F. Niecknig and B. Kubis, *in preparation.*

[220] J. C. Collins, *Renormalization: An Introduction to Renormalization, the Renormalization Group and the Operator-Product Expansion (Cambridge Monographs on Mathematical Physics)*. Cambridge University Press, 1986.

[221] S. Necco, *Chiral low-energy constants from lattice QCD*, *PoS* **CONFINEMENT8** (2008) 024, [arXiv:0901.4257].

[222] C. Haefeli, M. A. Ivanov, and M. Schmid, *Electromagnetic low-energy constants in ChPT*, *Eur.Phys.J.* **C53** (2008) 549–557, [arXiv:0710.5432].

[223] B. Moussallam, *A Sum rule approach to the violation of Dashen's theorem*, *Nucl.Phys.* **B504** (1997) 381–414, [hep-ph/9701400].

[224] B. Ananthanarayan and B. Moussallam, *Four-point correlator constraints on electromagnetic chiral parameters and resonance effective Lagrangians*, *JHEP* **0406** (2004) 047, [hep-ph/0405206].

[225] C. Ditsche, *Probing quark mass effects in low-energy hadron physics*, *PhD thesis, University of Bonn* (2012).

[226] G. Colangelo, J. Gasser, and A. Rusetsky, *Isospin breaking in K_{l4} decays*, *Eur.Phys.J.* **C59** (2009) 777–793, [arXiv:0811.0775].

[227] H. Leutwyler, *private communication.*

[228] J.-J. Zhu and M.-L. Yan, *Covariant amplitudes for mesons*, hep-ph/9903349.

[229] M. Bando and K. Kugo, Taichiro waki, *Nonlinear realization and hidden local symmetries*, *Phys.Rept.* **164** (1988) 217–314.

[230] M. Harada and K. Yamawaki, *Hidden local symmetry at loop: a new perspective of composite gauge boson and chiral phase transition*, *Phys.Rept.* **381** (2003) 1–233, [hep-ph/0302103].

[231] P. Roig, *Hadronic currents for $\tau^- \to \pi^-\pi^0\nu_\tau$ and Other decays of interest in TAUOLA*, *Nucl.Phys.Proc.Suppl.* **225** (2012) 161–164, [arXiv:1112.0962].

[232] P. Roig, *private communication.*

[233] G. Gounaris and J. Sakurai, *Finite width corrections to the vector meson dominance prediction for $\rho \to e^+e^-$*, *Phys.Rev.Lett.* **21** (1968) 244–247.

Acknowledgments

At the end of a long thesis such as this and the three years of work that it took to finish it, I owe a debt of gratitude towards all the people who were (directly and indirectly) involved in this work.

First of all, I would like to thank my thesis advisor PD Bastian Kubis for pitching the ideas for the projects contained in this thesis and his continuous support and encouragement during their realization. Starting from the "two-week" $\eta \to 3\pi$ project (which turned out to be a slightly too optimistic estimate of the time frame), over the interesting and fast-progressing $\omega/\phi \to 3\pi$ and $\omega/\phi \to \pi^0\gamma^*$ analyses, up to the more taxing (for lack of nicely "representable" results) $\eta' \to \eta\pi\pi$ study, I could count on him to patiently address the countless questions and confusions on my part. Moreover, I am truly grateful for suggesting my participation in numerous international conferences and workshops that allowed me to share and broaden my view on particle physics with experts in the field and besides that spend a very enjoyable and sociable time.

I thank Prof. Ulf-G. Meißner for accepting to carefully read and assess this thesis in a very limited time frame, for reading and commenting on the various manuscripts before publication, and for sharing numerous insights on university and research politics.

I am grateful to Prof. Gilberto Colangelo for inviting me to the university of Bern for a one-month research stay and his invaluable support in the early stages of Part II of this thesis. It tremendously helped to speed up the process. I would also like to thank Stefan Lanz and Peter Stoffer for numerous useful discussions on dispersion theory and Swiss peculiarities, and finally Christof Schüpbach and Daniel Arnold for sharing lunches and spending a very enjoyable time in Bern.

Likewise, thanks go out to Christoph Ditsche, who helped with the $\eta \to 3\pi$ project, and Franz Niecknig, who I collaborated with on the various ω/ϕ decay studies. It has been a pleasure to work with you guys and share some of the frustrations and some of the more delightful moments that are inevitably intertwined with challenging research problems. Additionally, I would like to thank Patrik Adlarson, Gilberto Colangelo, Simon Eidelman, Jürg Gasser, Christoph Hanhart, Andrzej Kupść, Stefan Lanz, Stefan Leupold, Bachir Moussallam and Akaki Rusetsky for useful discussions, as well as Cesare Bini, Sanja Damjanovic, Gianluca Usai, Denis Epifanov, Simona Giovannella, and Boris Shwartz for support on various experimental data sets. I am also indebted to Andrzej for helping out with the Monte Carlo program.

Thanks to my long-term office mate Martin Hoferichter for numerous stimulating discussions "on and off the field", for sharing frustrations and solutions on LaTeX, Mathematica, and Xmgrace. I give myself some credit for pulling him into some of the intricacies of American Sports. I am also grateful to Sebastian König for the IT support and general help with programming issues. Thanks to the rest of my office mates and the whole HISKP theory group

for a very enjoyable working atmosphere.

I can never express how grateful I am to my family and friends. I thank my family for patiently listening to countless fascinating tales on particle physics... and for putting them into perspective. ("Aha,... und was kann man damit anfangen?") I am grateful to my Mom for her continued support, words of encouragement, and for always having a sympathetic ear when things did not go as planned, to my Dad for his continued words of encouragement, for gently pushing me in the right direction, and for the support without which my studies never would have been possible. Thanks to my sister Melanie, my friends, and also the 3rd and 4th team of the Bonn Capitals for letting me enjoy life outside the confines of physics.

And finally, Raquel, this would not have been possible without you. Thank you for everything!